Antibiotic-free PHA-based antibacterial materials for bone regeneration

Marcello, E.

Antibiotic-free PHA-based antibacterial materials for bone regeneration

Elena Marcello

A thesis submitted to the University of Westminster
in candidature for the award of the degree of Doctor of Philosophy

March 2020

Author's declaration

I declare that the present work was carried out in accordance with the Guidelines and Regulations of the University of Westminster. The work is original except where indicated by special reference in the text.

The submission as a whole or part is not substantially the same as any that I previously or am currently making, whether in published or unpublished form, for a degree, diploma or similar qualification at any university or similar institution.

Until the outcome of the current application to the University of Westminster is known, the work will not be submitted for any such qualification at another university or similar institution.

Any views expressed in this work are those of the author and in no way represent those of the University of Westminster.

Signed: Elena Marcello Date: March, 2020

Acknowledgements

This research project was carried out within the framework of the HyMedPoly project, funded by the EU Horizon 2020 research and innovation programme under the Marie Sklodowska-Curie actions (Grant agreement #643050).

I would firstly like to express my gratitude to my supervisor Prof. Ipsita Roy for giving me the opportunity to join her research lab and the HyMedPoly project, and for her support, motivation and encouragement throughout the course of my PhD, even during and after my secondment.

I would also like to thank Prof. Brendon Noble for becoming my supervisor during the final stage of my PhD, for his support and help.

I am extremely grateful to Dr. Pooja Basnett for her training and guidance throughout this PhD project, and for her constant emotional support and encouragement. Many thanks to Dr. Rinat Nigmatullin for his precious and invaluable advice and suggestions, and for his patience. A special thanks to Dr. Barbara Lukasiewicz for training me with fermentation techniques.

I would also like to thank all the members of the HyMedPoly project for the inspiring and challenging scientific discussions. In particular, I would like to thank Prof. Boccaccini and Dr. Muhammad Maqbool for providing me with the antibacterial hydroxyapatite used in this work.

I would also like to thank Prof. María Auxiliadora Prieto and Dr. Aranzazu Mato Aguirre of Centro de Investigaciones Biológicas for the collaboration in the production of thioester-PHAs.

Many thanks to Dr. Marguerite Clyde and her group at University College Dublin for the possibility to perform the microbiological characterization of my materials in their lab.

I would like to thank all the technical staff from the University of Westminster, especially Neville for his constant support during fermentation experiments. I would also like to acknowledge Dr. Nicola Mordan from University Collage of London for her assistance with SEM analysis.

I will be always grateful to Prof. Paola Petrini from Politecnico of Milano for introducing me to the wonderful and challenging world of research, and for her mentorship and support.

I would like to thank all the members of the lab at University of Westminster, present and past, Barbara, Hima, Sheila, Alex, and Moyin for their friendship and for the time spent together during the long days of work. A special thank you to Isabel, for being my “partner-in-crime” along the ups and downs of this PhD journey.

Many thanks to all my friends in Italy, Chiara, Serena, Irene, Ludovica and across Europe, Carola and Nico, whose friendship has been essential throughout these years. A big thank you to my housemates and friends in London, Diletta and Rossella for making me feel like at home and for all the funny moments we shared throughout these years.

Finally, I would like to dedicate this work to my family, my parents and my brother, who have always believed in me and pushed me to achieve my best. Thank you for being my constant rocks.

Abstract

The current world problem of antibacterial resistance to antibiotics has driven the need to develop new therapeutics as alternatives to antibiotic to prevent and fight infections. In the biomedical field, bone regeneration is one of the applications with the highest risk of infection. Therefore, alongside biological and functional properties, materials used for this application should be able to provide antibacterial features able to inhibit bacterial adhesion and growth. In such a scenario, this work focused on the development of novel antibiotic-free materials based on polyhydroxyalkanoates (PHAs) for bone regeneration following two strategies.

For the first strategy, inherently antibacterial PHAs, thioester containing PHAs, were produced by bacterial fermentation. Such materials exhibited antibacterial activity by contact against *S. aureus* 6538P. Physical blending of thioester-PHA with P(3HHx-co-3HO-co-3HD) was investigated and a polymer ratio of 80:20 (P(3HHx-co-3HO-co-3HD): thioester-PHA) was identified as optimal to develop handleable and processable samples possessing antibacterial and *in vitro* biocompatibility properties.

For the second strategy, novel 2D antibacterial composite materials were produced by combining P(3HB) and P(3HO-co-3HD-co-3HDD) with a novel antibacterial co-substituted hydroxyapatite, containing two therapeutic ions, selenium and strontium, conferring osteoinductive and antibacterial properties to the ceramic. The materials developed showed to be able to induce an inhibitory effect against both Gram positive and Gram negative bacteria.

The possibility of developing 3D scaffolds using melt 3D printing of mcl-PHAs was investigated in this study for the first time. The process parameters were successfully optimized to produce well-defined and reproducible 3D P(3HO-co-3HD-co-3HDD) scaffolds. 3D scaffolds with dual porosity were also developed through the combination of 3D printing with salt leaching.

Finally, the obtained 2D antibacterial films were used as starting materials for the development of 3D scaffolds for antibacterial synthetic bone substitutes using the optimized melt 3D printing process. Novel 3D composite scaffolds were produced using the 2D composite materials based on P(3HO-co-3HD-co-3HDD) and the antibacterial hydroxyapatite. Based on the antibacterial and cell compatibility studies, the composite material with 10 wt% of Se-Sr-HA as a filler was identified as the optimal candidate for the development of antibacterial scaffolds for bone regeneration. Novel inherently antibacterial scaffolds were produced by melt 3D printing of 20:80 blend films of thioester-PHA with P(3HHx-co-3HO-co-3HD). The 3D blend scaffolds showed an inhibitory effect against *S. aureus* 6538P by direct contact testing and were able to support the growth of MC3T3-E1 cells, showing potential for bone regeneration.

Table of contents

List of figures

List of tables

List of Abbreviations

ALP	Alkaline phosphatase
AMR	Antimicrobial resistance
ARS	Alizarin red S
ATH	6-acetylthiohexanoic acid
BG	Bioactive glasses
BMP	Bone morphogenic proteins
CDC	Centers for Disease Control and Prevention
CFU	Colony forming units
DCW	Dry cell weight
DMEM	Dulbecco's modified Eagle medium
DNS	Dinitrosalicylic acid assay
DOT	Dissolved oxygen tension
DSC	Differential scanning calorimetry
DWV	Dried weight variation
E	Young's modulus
ECM	Extracellular matrix
EDX	Energy Dispersive X-ray
EOs	Essential oils
FBS	Fetal bovine serum
FT-IR	Fourier-transform infrared
GC-MS	Gas Chromatography Mass Spectroscopy
GPC	Gas permeation chromatography
HA	Hydroxyapatite
ISO	International organisation for standardisation
MBC	Minimal bacteriocidal concnetration
Mcl-PHA	Medium chain length polyhydroxyalkanoate
MH broth	Mueller Hinton broth
MIC	Minimal inhibitory concentration
MSM	Mineral salt media
MW	Molecular weigth
NMR	Nuclear magnetic resonance

NPs	Nano particles
OECD	Organization for Economic Co-operation and Development
OD_x	Optical density, x represents the wavelength used
P(3HB)	Poly(3-hydroxybutyrate)
P(3HB-co-3HHx)	Poly(3-hydroxybutyrate-co-3-hydroxyhexanoate)
P(3HB-co-3HV)	Poly(3-hydroxybutyrate-co-3-hydroxyvalerate)
P(3HHx-co-3HO)	Poly(3-hydroxyhexanoate-co-3-hydroxyoctanoate)
P(3HHx-co-3HO-co-3HD)	Poly(3-hydroxyhexanoate-co-3-hydroxyoctanoate-co-3-hydroxydecanoate)
P(3HHx-co-3HO-co-3HD-co-3H4ATB-co-3H6ATH).	Poly(3-hydroxyhexanoate-co-3-hydroxyoctanoate-co-3-hydroxydecanoate-co-3-hydroxy-4-acetylthiobutanoate-co-3-hydroxy-6-acetythiolhexanoate)
P(3HO)	Poly(3-hydroxyoctanoate)
P(3HO-co-3HD)	Poly(3-hydroxyoctanoate-co-3-hydroxydecanoate)
P(3HO-co-3HD-co-3HDD)	Poly(3-hydroxyoctanoate-co-3-hydroxydecanoate-co-3-hydroxydodecanoate)
P(3HO-co-3HHx)	Poly(3-hydroxyoctanoate-co-3-hydroxyhexanoate)
P(4HB)	Poly(4-hydroxybutyrate)
P(3HB-co-3MB)	P(3-hydroxybutyrate-co-3-mercaptobutyrate)
P(3HB-co-3MP)	P(3-hydroxybutyrate-co-3-mercaptovalerate)
P(3HB-co-3MV-co-3HV)	P(3-hydroxybutyrate-co-3-mercaptovalerate-co-hydroxyvalerate)
P(3HPTB-co-3HPTHx)	Poly(3-hydroxypropylthiobutyrate-co-3-hydroxypropylthiohexanoate)
P(3HPTB-co-3HPTHx-co-3HPTO)	Poly(3-hydroxypropylthiobutyrate-co-3-hydroxypropylthiohexanoate-co-3-hydroxypropylthio-octanoate)
pNPP	p-Nitrophenyl phosphate
PBS	Phosphate buffer saline
PCL	Polycaprolactone
PDI	Polydispersity index
PEG	Polyethylene glycol

PET	Polyethylene terephthalate
PGA	Poly(glycolic acid)
PHA	Polyhydroxyalkanoate
PLA	Poly(lactic acid)
PLGA	Poly(lactic-co-glycolic acid)
QA	Quaternary ammonium groups
R	Antibacterial activity
ROS	Reactive oxygen species
S-PHAs	Sulphur containing polyhydroxyalkanoates
Se-Sr-HA	Hydroxyapatite containing selenium and strontium ions
Scl-PHA	Short chain Polyhydroxyalkanoate
SEM	Scanning electron microscopy
STD	Standard deviation
TCP	Tissue culture plastic
Thioester-PHA	Thioester containing polyhydroxyalkanoate
Tc	Crystallization temperature
Tm	Melting temperature
Tg	Glass transition temperature
Tm	Meting temperature
WHO	World Health Organization
WU	Water uptake
α-MEM	Alpha Minimum Essential Medium
ΔHm	Enthalpy of fusion
εu	Elongation at break
ε-PL	pol-ε-lysine
σu	Ultimate tensile strength
X_c%	Crystallinity of the materials

Chapter 1

Introduction

1.1. Antibiotic resistance

Antimicrobial resistance (AMR) has become a primary concern worldwide. At the World Health Assembly in 2015, it was one of the main topics of the agenda and the World Health organization (WHO) published a global action plan against AMR in 2015 (WHO, 2015). Bacterial infections pose a great threat to global health and the world economy. AMR has been listed by the Organization for Economic Co-operation and Development (OECD) as one of the top five causes of mortality (OECD, 2018). According to the Centres for Disease Control and Prevention (CDC), each year in the United States around 2.8 million people become infected with antibiotic resistant bacteria and at least 35,000 people die each year as a direct result of these infections (CDC, 2019). The situation is similar in Europe where 5–12% of hospital patients acquire an infection during their stay and an average of 33,000 people die due to resistant strains (OECD, 2018). Moreover, infections represent a problem in terms of economic costs due to a longer hospitalization period. Multidrug-resistant bacteria in the EU are estimated to cause an economic loss of more than €1.5 billion each year (WHO, 2014). The OECD predicted a worsening of the situation by 2050 in terms of both death and economic consequences (OECD, 2018).

The current misuse and overuse of antibiotics combined with an increased reduction in the number of new drugs developed have led to the aforementioned AMR crisis. Up to 50% of the current prescriptions of antibiotics are believed to be unnecessary or incorrect in terms of treatment choice or duration (Medina *et al.*, 2020). Antibiotics are in fact nowadays available worldwide at low prices, making them easy to be accessed, and in many countries they can be obtained even without a prescription despite this being an illegal practise (Auta *et al.*, 2019; Chokshi *et al.*, 2019). Simultaneously, there has been a drastic reduction in the interest

of pharmaceutical companies to produce novel antibiotics, seen as not profitable (da Cunha *et al.*, 2019). Compared to drugs used to treat chronic diseases, antibiotics are used for a limited amount of time and have usually a lower price, leading to low returns on the high capitals invested. They are also associated with a high risk as resistance might be developed easily once they are introduced in the clinic. Alternatively, if a novel drug is actually effective, it is prescribed only when established antibiotics are not effective, as a last resort (Fair and Tor, 2014; da Cunha *et al.*, 2019). As a result only two new classes of antibiotics have been commercialized in the last 30 years (Coates *et al.*, 2011; Butler *et al.*, 2013).
This scenario shows an urgent need for the prevention and treatment of infections and the need to find a solution to eradicate resistant strains.

Penicillin was firstly discovered by Alexander Fleming in 1928 and antibiotics have since then revolutionized the medical field. However, since the introduction of antibiotics in the clinics, bacteria started developing resistance mechanisms (Ventola, 2015; Medina *et al.*, 2020).
Three main mechanisms by which bacteria are able to develop resistance have been described by various researchers and are schematized in Figure 1.1 (Levy and Marshall, 2004; Blair *et al.*, 2015).

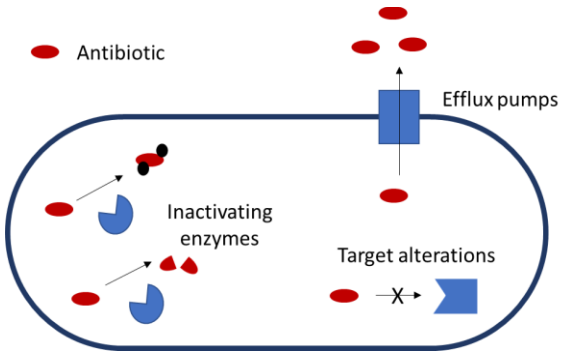

Figure 1.1 Schematic representation of the main mechanisms of antibacterial resistance.

Bacteria can target antibiotics directly via enzymes, which are able to either destroy or deactivate them. β-lactamase enzymes are able to hydrolyse the β-lactam class of antibiotics (e.g. penicillin), while aminoglycoside antibiotics are instead enzymatically modified (through N-acetylation, O-phosphorylation or O-adenylylation) preventing their binding to ribosome targets. Alternatively, bacteria can act by transportation of the drug outside the bacterial cell via efflux pumps. The resistance mechanism consists of pumping the drug out of the bacteria faster than their transportation or movement in to the bacterial cell, so it never

reaches a concentration effective enough to have an antibacterial function (Walsh, 2000; Li and Nikaido, 2004). Thirdly, bacteria can develop resistance through the modification of the antibiotic target sites, lowering the affinity of the drug for such targets. The targets can be modified by point mutations in the genes encoding the targets or by enzymatic alterations of the binding site, impairing the binding of the drug to the site (Munita and Arias, 2016).

The resistance can also be an intrinsic characteristic of the bacteria, through spontaneous mutations, or it can be acquired by horizontal gene transfer from other bacteria. In the latter case the resistance genes are transmitted among bacteria through three main mechanisms, conjugation, transformation and transduction, which are described in Figure 1.2 (Furuya and Lowy, 2006). Through the conjugation process, bacteria are able to exchange genetic material in the form of plasmids and conjugative transposons by direct contact between the two organisms through the formation of a hollow tubular structure (i.e. pilus) (Von Wintersdorff *et al.*, 2016). Transformation is characterized by a direct uptake of chromosomal DNA, plasmids, and other DNAs surrounding the bacterial cell membrane. Finally, transduction occurs when new genetic material is introduced in the bacteria through an external vector, a bacterial virus or bacteriophage. Bacteriophages use the bacterial machinery to duplicate their genetic material. During such a process, fragments of bacterial genetic material can be incorporated into the viral DNA/RNA and transferred to new infected cells (Haaber *et al.*, 2016; Furuya and Lowy, 2006).

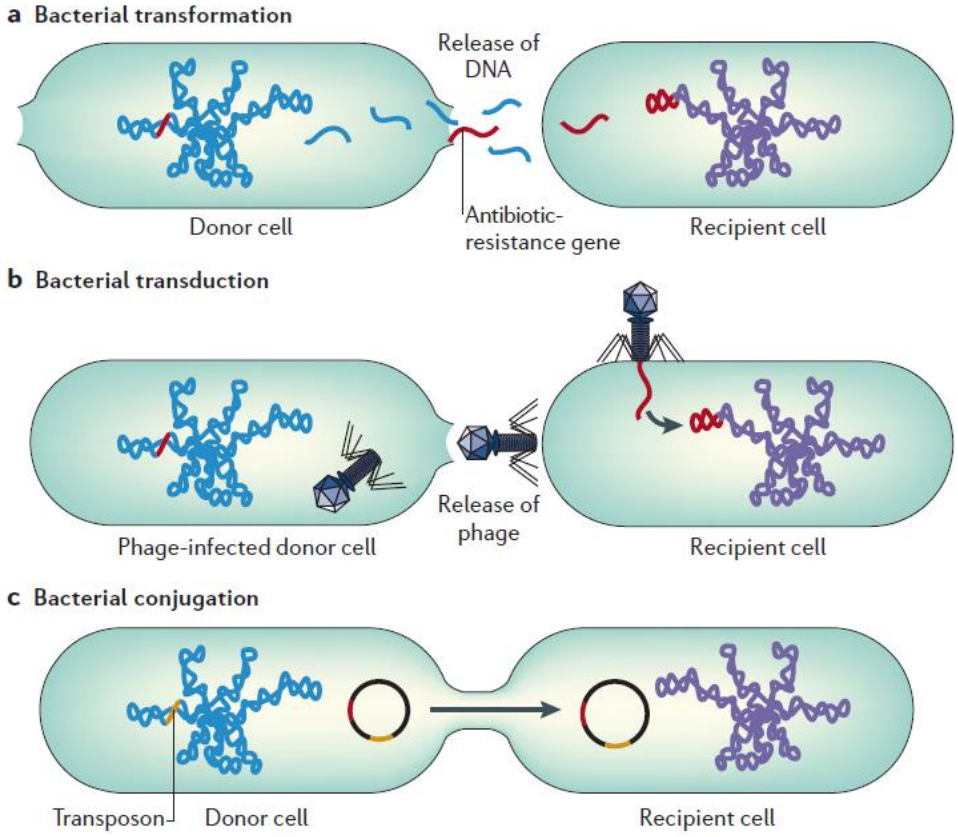

Figure 1.2 Three mechanisms of horizontal gene transfer: a) transformation, b) transduction and c) conjugation. Image reproduced from Furuya and Lowy, 2006 with permission from Springer Nature.

1.1.1. Biofilm

Another mechanism of bacterial resistance is related to biofilm formation. These are matrices composed of polysaccharides and proteins in which bacteria are embedded (Stewart and Costerton, 2001; Høiby *et al.*, 2010; Toyofuku *et al.*, 2015). The stages of biofilm formation are described in Figure 1.3. Biofilm formation begins with a reversible attachment of planktonic bacteria to the surface of materials, mediated by cell appendages (pili, flagella or fimbriae). After adhesion, gene alteration occurs characterized by the increase in secretion of extracellular polymeric substances. The binding becomes irreversible and bacteria start proliferating and forming micro-colonies. Production of the polymer matrix and its thickness increase until a mature biofilm is formed. Finally, cells can return to their planktonic phase and leave the biofilm, attaching again to other surfaces and thus restarting a new cycle.

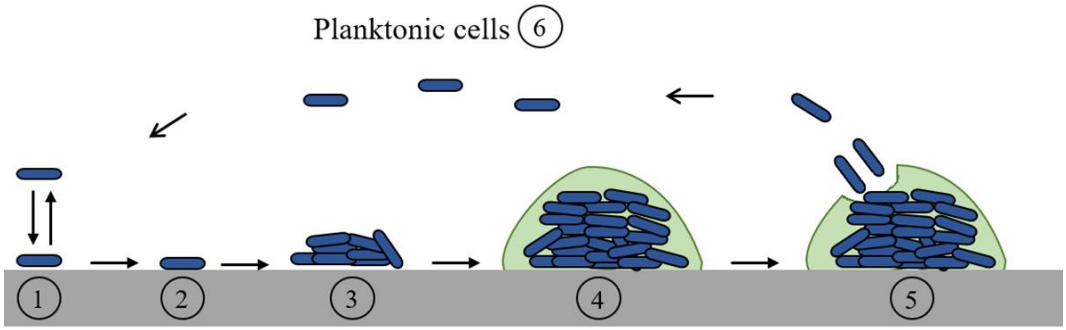

Figure 1.3 Schematic representation of the stages of biofilm formation on a surface. 1) Reversable attachment of planktonic cells, 2) Irreversible attachment, 3) Microcolony, 4)Maturation, 5) Dispersion phase with the release of planktonic bacteria that can attach to another surface and restart the cycle.

A mature biofilm provides resistance to most antibiotics (Darouiche, 2001; Stewart, 2002,Mah and O'Toole, 2001). The matrix represents a barrier to the passage of antibiotics as it is composed of several layers which can limit their diffusion. The drug transport can also be reduced by the interaction with or adsorption to slime components. As a result of this, a slow and incomplete penetration of the antibiotics occurs, especially in the centre of the biofilm. Additionally, the biofilm is a heterogeneous environment characterized by varied oxygen concentrations, pH, waste products and signalling molecules, which can modify, alter or inhibit the activity of antibiotics. For example, aminoglycosides activity is reduced by the low oxygen availability (Tack and Sabath, 1985). The presence of chemical gradients inside the matrix induces heterogeneity in the state of the bacteria, creating zones characterized by cells in the stationary phase. Many antibiotics act on growing cells and are therefore not effective in the non-growing zones. Finally, genetic material is contained in the biofilm resulting in possible horizontal gene transfer which favours the spreading of resistant bacteria, as mentioned in the above section (Flemming, 2011).

1.1.2. Device related infections

Infections caused by biofilms can be tissue-related such as chronic wounds or urinary infections or they can be device-related caused by the introduction of foreign materials inside the human body (Lebeaux *et al.*, 2014; Darouiche, 2001; Von Eiff *et al.*, 2005).

When a device is implanted or inserted in the human body, host cells should interact with the surface of the material and adhere to it, inducing the formation of new tissue (i.e. granulation tissue) and thus a successful bio-integration. Bacteria can also compete for the colonization of the surface, adhere to it, proliferate and create a biofilm. *Staphylococcus* species are the

main organisms associated with device related infections, especially *S. epidermis* and *S. aureus* (Heilmann *et al.*, 1999;Ziebuhr, 2001). Generally, if a mature biofilm is formed, the only solution available is to remove the implant which increases the patient's distress and raises the health costs due to the need of a second surgery. As described above, the biofilm confers antibiotic resistance and it also provides protection against the body's immune response. In this state bacteria are able to reduce the leukocyte mediated phagocytosis and killing capacity (Roilides *et al.*, 2015). Additionally, infections impair the formation of new tissue and thus the revascularization, reducing the delivery to the site of granulocytes and antibacterial drugs.

All medical devices can lead to infections, with different levels of impact (Darouiche, 2001; VanEpps and Younger, 2016). Bladder catheters have a high rate of infection but are associated with a low mortality rate, while heart valve implant infections are rarer but fatal. Generally, infections related to intravascular implants are high risk (Darouiche, 2001). The patient's morbidity is another aspect to be considered. Even though infections associated with joint prosthesis or fracture fixation devices possess a low risk of mortality, they can cause serious psychological damage to the patient, due to disability and scars or disfigurement (VanEpps and Younger, 2016).

1.2. Natural antibacterial polymers

Considering the problem of bacterial resistance, new therapeutics have to be discovered or developed to inhibit bacterial growth and prevent bacterial attachment on the surface of the materials thereby preventing biofilm formation. One of the main strategies investigated is the development of "antibiotic-free" antibacterial materials. To achieve this goal, researchers have focused on the use of inherently active materials, either by using materials possessing bactericidal or bacteriostatic effects or by chemical modification to introduce antibacterial groups, and on the loading of the polymers with active agents (Santos *et al.*, 2016; Muñoz-Bonilla and Fernández-García, 2015; Huang *et al.*, 2016a).

Among the polymers used for medical applications, natural polymers are being extensively researched due to their interesting properties. These includes collagen, gelatin, hyaluronic acid, fibrin, alginate, chitosan and polyhydroxyalkanoates. They are obtained from renewable resources, either by extraction from natural resources (e.g. collagen) or by fermentation

processes (e.g. polyhydroxyalkanoates). Long processes of purification are, however, required in order to obtain polymers adapted for biomedical applications. Biocompatibility is another important aspect for their biomedical application. Polymers such as collagen and gelatin are components of the extracellular matrix and possess cell adhesion peptides, such as the RGD sequence (Arg-Gly-Asp) of collagen, which promote cellular adhesion (Lee *et al.*, 2001; Rosellini *et al.*, 2009). Alginate and cellulose are characterized by a high water content and have visco-elastic properties which make them perfect substitutes for soft tissues (Czaja *et al.*, 2007; Lee and Mooney, 2013). Additionally, natural polymers are usually biodegradable with degradation products well tolerated by the human body. One of their disadvantages over synthetic polymers is that their properties can be affected by the original source of the polymer and by the extractions and purification techniques employed. Even batch-to-batch variations can occur causing limited reproducibility.

1.2.1. Intrinsically antibacterial natural polymers

1.2.1.1. Chitosan

The best-known example of an intrinsically antibacterial natural material is chitosan. This polymer is a carbohydrate obtained by deacetylation of chitin, the structural component of the crustacean exoskeleton. It consists of β(1→4) linked D-glucosamine (deacetylated unit) and N-acetyl-D-glucosamine (acetylated unit) units. The deacetylation process leads to the formation of amino groups, which are protonated at pH < 6-6.5. Commercial chitosan is characterized by a degree of deacetylation between 60% and 100%. It has been extensively used in the biomedical field, especially for wound dressing applications (Park and Kim, 2010; Zhang *et al.*, 2010). Its antibacterial properties are ascribed to a combination of several mechanisms of action (Chung and Chen, 2008; Hafdani and Sadeghinia, 2011; Kong *et al.*, 2010; No *et al.*, 2002). Firstly, electrostatic interactions between the positively charged polymer (due to the protonation of the free amino groups) and the negatively charged bacterial cell wall induce changes in its permeability, integrity and leakage of intracellular components. Several studies have confirmed this hypothesis, showing the influence of the degree of deacetylation of chitosan on its inherent antibacterial activity. A higher degree of deacetylation results in a higher number of amino-groups and therefore a higher positive charge, leading to an increase in the antimicrobial activity against *Staphylococcus aureus* and *Escherichia coli.* (Kong *et al.*, 2010; Li *et al.*, 2016a; Raafat *et al.*, 2008; Rabea *et al.*, 2003).

The changes in membrane permeability have been associated with a possible competitive mechanism between chitosan and with Ca^{2+} for negative sites on the bacterial membrane/wall (Raafat *et al.*, 2008). Chitosan has also been shown to induce degradation of teichoic acids and peptidoglycans, leading to leakage of cytosol components and eventual cell lysis (Mohammadi *et al.*, 2016). Another mechanism of action is related to the capability of low molecular weight chitosan to bind to the negatively charged microbial DNA once inside the cellular environment, leading to inhibition of DNA transcription. This mechanism has been shown in Gram negative bacteria, where low molecular weight chitosan showed higher antimicrobial effect, probably due to an increased penetration through the bacterial membrane (Raafat *et al.*, 2008; No *et al.*, 2002). Finally, the chelating capability of chitosan has also been ascribed for its antimicrobial activity, by selectively binding essential trace metals and inhibiting microbial growth (Raafat *et al.*, 2008).

Due to its antibacterial properties, chitosan has been combined with other natural polymers. Combination with alginate has been explored mainly for wound dressing applications. Alginate is an anionic linear copolymer typically extracted from brown algae. Its structure consists of 1,4-linked β-D-mannuronate (M) and α-L-guluronate (G) residues (Lee and Mooney, 2013). Alginate/chitosan sponges were obtained through lyophilization to be used as wound healing patches, showing antimicrobial activity against *E. coli* and *S. aureus* (Zhang *et al.*, 2015). Several studies investigated the production of alginate/chitosan fibres by extrusion of the blend solutions in a $CaCl_2$ coagulation, and the materials obtained showed inhibition of the growth of *S. aureus* (Fan *et al.*, 2012; Fan *et al.*, 2006; Fan *et al.*, 2012; Knill *et al.*, 2004; Fan *et al.*, 2010). Chitosan has also been coupled with collagen and gelatin to develop antibacterial materials. Collagen, a fibrous protein, is the main component of bones, skin and connective tissues. It presents a triple helix structure composed of three polypeptide chains. Each chain is characterized by the repetition of the amino acid sequence Gly-X-Y, where X is mostly proline and Y is mostly hydroxyproline (Lee *et al.*, 2001; Sionkowska *et al.*, 2017). Gelatin is the denatured form of collagen and it is obtained by the hydrolytic degradation of collagen containing tissues (Djagny *et al.*, 2001). Films and sponges based on the mix between the protein and the polysaccharide were obtained using physical blending or by chemical cross-linking with alginate dialdehyde as the crosslinker (Du *et al.*, 2016; Deng *et al.*, 2007; Ungureanu *et al.*, 2015; Wei *et al.*, 2015). An alternative approach used for the formation of gelatin/chitosan films involved a dual enzymatic cross-

linking method. Microbial transglutaminase was used for intramolecular cross-linking of gelatin, while tyrosinase catalysed the conjugation of chitosan nucleophilic amines with the oxidized tyrosine residues of gelatin (Wang *et al.*, 2015b).

1.2.1.2. Poly-ε-lysine

Another natural material with intrinsic antibacterial properties is pol-ε-lysine (ε-PL), a cationic polyamide, characterized by the repetition of units of L-lysine linked by a peptide bond between a carboxylic acid and a ε-amino group of the consecutive L-residues. This material is an extracellular product obtained through bacterial fermentation by *Streptomycetaceace* and ergot fungal species. This polymer is biodegradable, soluble in water and non-toxic and has been used in biomedical applications mainly in drug and gene delivery as a carrier. Its antibacterial activity has been associated to the non-specific electrostatic interaction between the positively charge of amino groups of ε-PL and the negatively charged phospholipids of bacterial cytoplasmatic membrane causing its permeabilization through a carpet-like mechanism (Hyldgaard *et al.*, 2014). ε-PL has shown activity against yeast, fungi and bacterial species (Hamano, 2011; Shih *et al.*, 2006; Shima *et al.*, 1984).

Preparation of ε-PL-based hydrogels for medical applications has been investigated. ε-PL-γ-PGA hydrogels for wound healing were produced through chemical crosslinking with 1-ethyl-3-(3-dimethylaminopropyl)-carbodiimide (EDC) and N-hydroxysuccinimide (Hua *et al.*, 2016; Wang *et al.*, 2016a). Antimicrobial hydrogel coatings for medical devices were produced via coupling of ε-PL with methacrylic acid (Zhou *et al.*, 2011). Enzymatic crosslinking was also explored using horseradish peroxidase (HRP)/H_2O_2 system to produce εPL-PEG conjugates and εPL-hydroxyphenyl propionic acid (Wang *et al.*, 2015a).

1.2.2. Chemical functionalization of natural polymers

Chemical functionalization of natural polymers has been investigated to enhance (e.g. for chitosan) or to introduce antibacterial properties.

The most common functionalization is based on the introduction of cationic groups. The positive charges allow electrostatic interactions with the negatively charged bacterial cell wall, leading to cell disruption and leakage of intracellular components. Gram negative bacteria are less affected by this mechanism than Gram positive due to the presence of the

outer membrane composed of lipopolysaccharides and phospholipids which protects the cytoplasmatic membrane (Timofeeva and Kleshcheva, 2011; Muñoz-Bonilla and Fernández-García, 2012). The main groups studied for the functionalization are quaternary ammonium groups (QA) and quaternary phosphonium groups (QP). QP show higher biocidal activity than QA due to a stronger polarization of phosphonium cations compared to ammonium cations (Santos *et al.*, 2016). Quaternization of chitosan nitrogen atoms has been performed in several studies to obtain antibacterial properties at neutral pH (Martins *et al.*, 2014). The activity of chitosan is pH-dependent due to the need of acidic conditions for the protonation of ammonium groups. Muzzarelli *et al.* developed the first chitosan quaternized-derivative, N,N,N-trimethyl chitosan (Muzzarelli and Tanfani, 1985). The incorporation of QA groups in chitosan was also investigated, showing antibacterial activity against *S. aureus* 6538 and *E.coli* 25922 (Zhu *et al.*, 2016). A range of quaternary ammonium salts containing epoxides have been linked to gelatin through a ring-opening reaction using base catalysis. The derivative showed excellent bacterial inhibition against a range of Gram positive and Gram negative bacteria (Jiang *et al.*, 2014; Li *et al.*, 2016b; Liu *et al.*, 2014b). Quaternary ammonium groups containing alginate materials were also produced by the reaction with a quaternary ammonium compound, 3-(trimethoxysilyl) propyl-octadecyldimethylammoniumchloride (TSA). Under acidic conditions silanol groups were formed by partial hydrolysis of TSA, which reacted with the hydroxyl groups of sodium alginate by a condensation reaction. Insoluble antibacterial beads were then obtained by ionic crosslinking with calcium chloride and showed antibacterial activity against *E.coli* 25922 and *S. aureus* 6538P (Seok *et al.*, 2007). In another approach, alginate derived cationic surfactants were obtained by esterification of the cationic surfactant N-(2-hydroxyethyl)-N,N-dimethyldodecan-1-ammonium bromide and alginic acid (Tawfik and Hefni, 2016). The complex antibacterial activity depended on the length of the hydrophobic alkyl chain, with 12 carbon atoms inducing the highest zone of inhibition (Tawfik and Hefni, 2016).

Chemical functionalization of gelatin was also investigated to obtain antibacterial properties. A range of quaternary ammonium salts containing epoxy groups were linked to gelatin through a ring-opening reaction under basic conditions. Using this method both quaternary ammonium groups (2,3-epoxypropyl trimethyl ammonium chloride (Jiang *et al.*, 2014), epoxypropyl dodecyl dimethyl ammonium chloride (Liu *et al.*, 2014b) and silicone quaternary ammonium groups (diethyl-2,3-epoxypropyl-(3-methyldimethoxyl) silpropyl

ammonium (Li *et al.*, 2016)) were grafted on the material. Antibacterial activity against both Gram positive and Gram negative bacteria was observed for all of the above- mentioned modifications of gelatin.

N-halamine groups are another class of moieties with antibacterial properties. They are characterized by the presence of nitrogen-halogen covalent bonds. The biocidal activity is due to the release of halogens (chlorine, bromine or iodine) that can oxidize thiol and amino groups present in proteins of cell receptors, leading to inhibition of the cell enzymatic activity and thus to cell death (Timofeeva and Kleshcheva, 2011; Hui and Debiemme-Chouvy, 2013). Chlorination of amino groups of chitosan films was obtained by treatment with sodium hypochlorite. The material obtained showed higher biocidal activity against *E.coli* 15597 and *S. aureus* 6538 compared to plain chitosan (Cao and Sun, 2007). The same procedure was used to chlorinate cellulose fibres grafted with methacrylamide, showing total inactivation of *E.coli* 11229 and *S. aureus* 6538P within 10 minutes of contact time (Liu *et al.*, 2016).

The introduction of sulphur-containing groups in chitosan has also been investigated. Sulfonate groups were linked to chitosan's amino groups via reaction with 1,3-propane sulfone. The materials obtained showed lower MIC values compared to plain chitosan against both *E. coli* 21524 and *S. aureus* 10384 (Sun *et al.*, 2017). Sulfonamide derivatives have also been used for the functionalization of chitosan. These compounds have shown bacteriostatic (inhibiting bacteria growth) or bactericidal (killing bacteria) effect. A range of sulfonamide-chitosan derivatives were obtained, and membranes were produced through chemical crosslinking with sodium tripolyphosphate to be used as wound dressings. The materials showed higher bacterial growth inhibition compared to plain chitosan against several Gram positive and Gram negative bacteria (Dragostin *et al.*, 2016). Chitosan was also functionalized with thio-acids of different alkyl-chain length via formation of amide bonds using a carbodiimide crosslinker. The derivatives induced higher bactericidal effect against *P. aeruginosa* 27853, *Streptococcuss obrinus* 176 and *Streptococcus mutans* 918 compared to chitosan. The antibacterial activity of the thiol-alkyl chains was hypothesized to be related to hydrophobic interaction of the alkyl chains with the bacterial cell wall components and reaction of the thiol-groups with cysteine residues, inducing membrane disruption (Croce *et al.*, 2016).

1.2.3. Loading with antimicrobial agents

The final strategy implemented for the development of natural antibacterial polymers is related to the loading of inorganic and organic active compounds.

The main class of inorganic agents is represented by metal ions, including both essential metals (e.g. Cu or Se) that are toxic at concentrations higher than their biological activity and non-essential metals (e.g. Si and Zn) active at low concentrations (Palza, 2015). A variety of mechanisms have been associated with the antibacterial activity of metal elements, depending on the type and the species investigated. One of the main modes of action involves the production of reactive oxygen species (ROS), chemically reactive species containing oxygen (e.g. superoxide anion (O2•−), hydrogen peroxide (H_2O_2) and hydroxyl radical (OH•)). At low levels ROS are involved in normal physiological processes, while at high concentrations, an imbalance state between pro-oxidant/antioxidant is achieved (i.e. oxidative stress), leading to membrane, protein and DNA damage (Ruddaraju *et al.*, 2019; Lemire *et al.*, 2013). Some metals like copper are able to produce hydroxyl radicals through Fenton-type reactions, as shown in the following equations (Grass *et al.*, 2011):

$$Cu^{+} + H_2O_2 = Cu^{2+} + OH^{-} + OH\bullet$$

Other compounds (e.g. Ag and Ga) can disrupt the iron-sulphur clusters, leading to the release of $Fe^{2+,}$ which could generate ROS species through the Fenton reaction (Lemire *et al.*, 2013; Palza, 2015). Alternatively, metals can also lead to the increase of ROS species indirectly through the oxidation of thiols and the formation of disulphide bonds, depleting the antioxidant defence system, as shown in the formula below using copper as an example (Kędziora *et al.*, 2018; Lemire *et al.*, 2013).

$$2Cu^{2+} + 2RSH = 2Cu^{+} + RSSH + 2H$$

Another antibacterial mechanism is related to the capability of certain metals to compete with other ions for active site of proteins, disrupting or inhibiting their functioning (Lemire *et al.*, 2013; Bridges and Zalups, 2010).

Metals have been coupled with natural polymers either in the form of salts (e.g. silver nitrate or copper sulphate) or as nanoparticles (NPs). Salt -compounds have been employed due to their competitive price and easiness of incorporation into the polymer matrices. Alginate and chitosan are the two bio-derived materials most investigated with such agents thanks to their

capability to form hydrogels by chelation of divalent cations, through ionic crosslinking (Gurikov and Smirnova, 2018). Once implanted or in contact with external fluids, exchange mechanisms between the incorporated ions and monovalent ones favour their release in the surrounding media (Lee and Mooney, 2013). In this way, copper (Cu^{2+} from copper sulfate) and zinc (Zn^{2+} from zinc carbonate) ions were used to develop antibacterial films (Klinkajon and Supaphol, 2014; Gritsch *et al.*, 2018; Straccia *et al.*, 2015; Wichai *et al.*, 2019) or beads (Madzovska-Malagurski *et al.*, 2016; Rui-Rodrigues and Lagoa, 2006). Alternatively, physical incorporation of silver nitrate in chitosan, cellulose and alginate matrices was studied either by immersion of the constructs in an aqueous solution containing the metal compound (exploiting the swelling capabilities of the materials) (Gupta *et al.*, 2016; Fan *et al.*, 2006; Kozicki *et al.*, 2016) or by incorporating the metal-salt compound in the polymer solution followed by production of fibres through electrospinning (Qin, 2005; Son *et al.*, 2009). Recently great attention has been posed on the use of metal-based NPs due to their high surface area to volume ratio, providing better contact with microorganisms and faster ion release kinetics compared to equivalent bulk materials (Gold *et al.*, 2018; Palza, 2015; Reidy *et al.*, 2013). When incorporated with natural polymers, the metal-NPs can be synthetized either *ex situ*, indicating that the nanoparticles are synthetized before being mixed with the matrix, or *in situ*, which refers to the fact that the synthesis of the NPs occurs in parallel with their incorporation in the construct. In the latter mechanism, NPs are obtained from a metal precursor using chemical (i.e. chemical reduction using a reducing agent) or physical stimuli (e.g. irradiation, photochemical treatment), with the polymer acting as a stabilizer or capping agents, avoiding particle aggregation and allowing the formation of nanoscale structures, or as both a stabilizing and reducing agent, due to the presence of many functional groups with reducing capability (e.g. carbonyl, alcohol, amine) (Zahran and Marei, 2019; Saldias *et al.*, 2017). To date the mechanism of action of metal NPs is still under debate. Many studies suggest that the activity is based on the release of ions, which then act in one of the ways described above leading to bacterial death (Kędziora *et al.*, 2018; Palza, 2015). Alternatively, it has been hypothesised that NPs interact with the cell membrane causing its disintegration and increased permeability (Slavin *et al.*, 2017).

Overall silver is the most investigated ion in the biomedical field and has been combined with chitosan, alginate and cellulose in the form of fibres, sponges, gauzes and pastes to developed commercial products for wound regeneration, established in clinical practice, having received FDA approval or CE certification (e.g. Suprasorb A+Ag by Lohmann &

Rauscher GmbH and Co, Acticoat* Absorbent by Smith & Nephew Ltd., Tegaderm Alginate Ag by 3M, Askina® Calgitrol® Paste by Braun, DURAFIBER Ag by Smith & Nephew Ltd., AQUACEL® Ag Dressing by ConvaTec). However, in the last decade, a variety of other metals have attracted great interest in the medical field such as copper, zinc, gallium and selenium. These compounds represent valid alternatives to the silver-based system because they possess a novel mechanism of action against bacteria and/or because they can simultaneously induce positive effects in mammalian cells (Gold *et al.*, 2018; Slavin *et al.*, 2017). For instance, Gallium (Ga^{3+}) ions can be used as "Trojan horses" as bacteria cannot differentiate between them and iron ones. Contrary to iron, gallium cannot be reduced leading to the disruption of iron metabolism, due to the inhibition of redox reactions(Goss *et al.*, 2018). Copper instead has been shown to promote angiogenesis (Xie and Kang, 2009), while selenium has shown promising results as an effective anticancer agent (Gandin *et al.*, 2018).

Plant-derived compounds represent the other major classes of active agents that has been investigated to introduce antibacterial properties in natural polymers. Such class can be divided into four groups based on the chemical structure: terpenes and terpenoids, polyphenols, alkaloids and sulphur-containing compounds. The first two categories represent the most investigated compounds as they are the main components of essential oils (EOs), liquid extracts from plants. Terpenes are simple hydrocarbons obtained by the combination of several isoprene units, while terpenoids (e.g. thymol from thyme oil and carvacrol from oregano oil) are terpenes that have modified enzymatically modified to introduce a range of functional groups (e.g. alcohols, esters and ketones). Polyphenols (e.g. curcumin from turmeric oil) are chemical compounds with an aromatic group usually link to a hydroxyl group. Phenylpropanoids (e.g. eugenol from clove oil and cinnamaldehyde from cinnamon oil) also belong to this class and are characterized by a phenol ring with a three carbon side chain. The antibacterial activity of such compounds has usually been associated with the ability to modify the integrity of the bacterial cell wall, increasing its permeability and causing membrane disruption (Khameneh *et al.*, 2019; Hyldgaard *et al.*, 2012). A range of EOs have been loaded in natural polymers to develop antibacterial materials mainly in the form of films and nanoparticles. Solvent casting was the main technique investigated for the development of antibacterial wound healing dressing containing EOs based on alginate (Liakos *et al.*, 2014), chitosan (Pereira dos Santos *et al.*, 2019; Bajić *et al.*, 2019), gelatin (Kavoosi *et al.*, 2015) or a combination of the mentioned natural polymers (i.e.

chitosan/gelatin (Kenawy *et al.*, 2019) or chitosan/alginate (Hamedi *et al.*, 2019)). Alternatively, lyophilization was also investigated to produce antimicrobial porous sponges by incorporation of curcumin into a gelatin/chitosan solution followed by freeze-drying (Nguyen *et al.*, 2013). Moreover, a spray-by-spray technique was adopted to produce tea tree oil (TTO) loaded alginate hydrogels, by spraying the TTO/alginate emulsion on a petri dish, followed by nebulization of calcium chloride solution to induce ionic cross-linking (Catanzano *et al.*, 2015). Microparticles have been produced by oil/water or oil/water/oil emulsions followed by ionic gelation (i.e. cross-linking of the polymer using ions) of cellulose (Mikulcová *et al.*, 2016), chitosan (Shetta *et al.*, 2019), alginate (Hosseini *et al.*, 2013; Lertsutthiwong *et al.*, 2008) or chitosan/alginate complexes (Natrajan *et al.*, 2015). Finally, Khajavi *et al.* produced alginate fibres containing eucalyptus essential oil by wet spinning technology, followed by ionic gelation using calcium chloride to obtain a fibrous wound healing patch (Khajavi *et al.*, 2014).

Alkaloids comprise a large class of heterocyclic compounds that contain nitrogen, which can be in the form of primary, secondary or tertiary amine (Cushnie *et al.*, 2014). Different mechanisms of action have been described depending on the specific sub-category, but overall the activity is connected to the presence of a nitrogen atom able to accept protons and one or more hydrogen atoms able to donate protons, making them highly reactive with protein and enzymes (Thawabteh *et al.*, 2019; Cushnie *et al.*, 2014). Berberine, an isoquinoline alkaloid found in roots and bark, was studied in combination with natural polymer, either by loading in sodium alginate beads (Zhang *et al.*, 2011) or by incorporation in chitosan-based coatings (Huang *et al.*, 2011).

The last class of plant-derived antimicrobial compounds consists of the sulphur containing agents. In particular allicin, obtained from garlic extracts, is the molecule that has been mainly investigated and has been incorporated into chitosan films by solvent casting (Pirak *et al.*, 2012) and into chitosan/alginate beads by ionic gelation using calcium chloride (Fakoor-Yazdan-Abad *et al.*, 2016). The activity of such compound is related to the ability of the thiosulfinate group (S-O-S) to react with the thiol moieties of intracellular enzymes, inducing their inhibition (Marchese *et al.*, 2016).

1.3. Polyhydroxyalkanoates

Polyhydroxyalkanoates (PHAs) are biological polyesters produced through microbial fermentation as intracellular components. They are normally produced under nutrient limiting conditions, in the presence of an excess of carbon source and a limitation of nutrients (nitrogen, phosphorus or potassium), and they are accumulated in granules inside the cell cytoplasm and serve as carbon-storage compounds, as shown in Figure 1.4 (Sudesh *et al.*, 2000). In case of carbon source depletion, bacteria are able to depolymerize the polymer through specific enzymes (i.e. PHAs-depolymerase) and use the degradation products as carbon resources. For a few bacterial, nutrient limitation is not essential for the accumulation of the polyester, which are produced during the exponential growth phase (de Souza and Shivakumar, 2019).

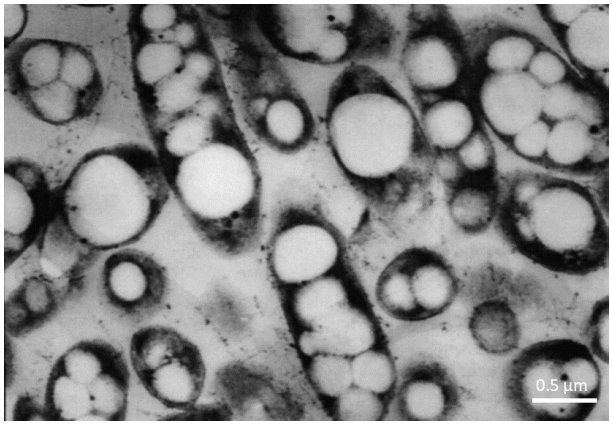

Figure 1.4 PHA granules in *P. stutzeri* 1317 grown on glucose. Image taken by Guo-Qiang *et al.*, 2001 reproduced with permission from Elsevier.

From their discovery in 1920s, PHAs have attracted great interest as a good alternative to petrol-based plastics. The increasing usage of petrochemical plastics has raised concerns regarding the limited availability and rapid depletion of fossil-fuel resources. Moreover, the accumulation of non-degradable plastic in landfills and oceans has become a world-wide concern. In this scenario, great attention has been posed on the development of alternative bio-based materials obtained from renewable feedstocks, able to be recycled or composted, and based on environmentally friendly production processes (Álvarez-Chávez *et al.*, 2012; Vu *et al.*, 2019). Among the bioplastic, PHAs represent a valid option thanks to their complete degradability in soil and marine environments and the possibility to be obtained from a wide range of renewable resources. However, one of the main limitations of their

commercialization on a large scale is their production cost, significantly higher than common plastic (Lee and Na, 2013). An average price in the range of 2–8 US$/kg has been reported for PHAs, while for instance the one for polypropylene is around 1.6 US$/kg and for high-density polyethylene is of 1.7 US$/kg (Pratt *et al.*, 2019; Kourmentza *et al.*, 2017). The high cost of the carbon sources and of the down streaming processes combined with a low PHA productivity are the main reasons for the expensive price of these polyesters (Zheng *et al.*, 2019).

1.3.1. Types and properties of PHAs

PHAs are polyhydroxyesters of usually 3-hydroxyalkanoic acids and their chemical structure is shown in Figure 1.5. A few microbial species can also produce PHAs containing 4-, 5- and 6- hydroxyalkanoic acids (Butt *et al.*, 2018). The number of monomeric units can vary between 1000 to 10000 and their pendant groups (R) are alkyl chains (C_1 to C_{13}). The backbone chiral atoms are in the R(-) configuration due to the stereo-specificity of the enzymes involved in their synthesis (i.e. PHA synthase) (Akaraonye *et al.*, 2010; Nigmatullin *et al.*, 2015). Based on the organism and the culture conditions, the molecular weight of the polymers vary from 2×10^5 to 3×10^6 Da (Khanna and Srivastava, 2005; Zinn *et al.*, 2001).

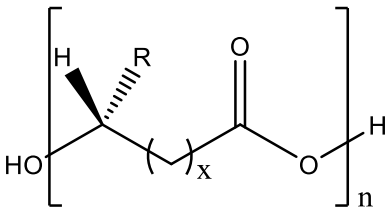

Figure 1.5 General structure of PHAs. (R = alkyl groups C1-C13, x = 1–4, n = 1000–10000).

Monomeric units with different structures and compositions can be obtained based on the producer microorganism and the carbon sources used in their production. As of now, 150 different structures have been identified and reported (Tortajada *et al.*, 2013; Hazer and Steinbüchel, 2007). PHAs can be classified based on the number of carbon atoms in the monomeric units into two classes, short chain length or scl-PHAs, with 3-5 carbon atoms, and medium chain length or mcl-PHAs, with 6-14 carbon atoms. The two classes of PHAs usually exhibit very distinct properties that have been summarised in Table 1.1. Scl- PHAs are usually highly crystalline materials, with a high melting temperature (160-180°C) and low glass transition (-4-0°C) (Możejko-Ciesielska and Kiewisz, 2016; Puppi *et al.*, 2019;

Bugnicourt *et al.*, 2014). The melting temperature of such PHAs is usually similar to its degradation temperature, limiting its processing through conventional thermal-based techniques (Li *et al.*, 2016c). Scl-PHAs possess a stiff and brittle mechanical behaviour, characterized by a high Young's modulus (0.5-4 GPa) and low elongation at break (<50%). P(4HB) represent an exception to this class, as it exhibits a lower melting temperature (50-70°C), glass transition temperature (around 50°C), and crystallinity (<40%), leading to a relatively high elastic modulus (0.15 GPa) coupled with a high elongation at break (1000%) (Puppi *et al.*, 2019; Grigore *et al.*, 2019). Mcl-PHAs are instead a more heterogenous group, where the properties are greatly influenced by the length of the side chain and the type of functional group present (Basnett, *et al.*, 2017a). Overall, it has been reported that such PHAs possess a lower crystallinity than scl-PHAs, with some polyesters showing a completely amorphous behaviour due to the presence of some functional groups preventing their crystallization (Grigore *et al.*, 2019; Rai *et al.*, 2011a). A lower melting temperature (40-60°C) and a glass transition usually below room temperature (-50-25°C) are also evidenced among this class. Such properties confer an elastomeric behaviour to mcl-PHAs, characterized by a high elongation at break (200-500%) and a lower elastic modulus (4-50 MPa) compared to scl-PHAs (Możejko-Ciesielska and Kiewisz, 2016; Rai *et al.*, 2011a; Lizarraga-Valderrama *et al.*, 2015).

Table 1.1 Comparison of the physical and mechanical properties between scl-(not including P(4HB)) and mcl-PHAs (Akaraonye *et al.*, 2010; Możejko-Ciesielska and Kiewisz, 2016; Rai *et al.*, 2011a; Grigore *et al.*, 2019).

Properties	**Scl-PHAs**	**Mcl-PHAs**
Melting temperature (°C)	160-180	40-70
Glass transition (°C)	-4-0	-50-25
Young's Modulus (MPa)	500-4000	4-50
Elongation at break (%)	<50%	200-500%

Finally, PHAs can also be classified based on the type of monomer units into homopolymers, composed of only one type of monomer unit (e.g. Poly(3-hydroxybutyrate) or P(3HB)), or heteropolymers with two or more monomer units in their molecular structure (e.g. Poly(3-

hydroxybutyrate-co-3-hydroxyvalerate) or P(3HB-co-3HV)). Copolymers of scl and mcl-PHAs can also be produced, such as poly(3-hydroxybutyrate-co-3-hydroxyhexanoate) or P(3HB-co-3HHx).

1.3.2. Biosynthesis of PHAs

The biochemical synthesis of PHAs comprises several metabolic pathways and depends on the type of carbon source and the organism used. Two types of carbon sources can be utilized: "related", possessing a structure similar to the one of the final monomers, and "unrelated", different from the final monomeric unit structure. To date, 13 pathways have been discovered for PHA biosynthesis (reported in Figure 1.6), 10 for scl-PHA synthesis (pathways A-J) and 4 for mcl-PHA synthesis (pathways J-M) (Tan *et al.*, 2014). Two main steps can be identified in PHA biosynthesis. The first one is the synthesis of (R)-3-hydroxyacyl-CoA, (R)-3-HA-CoA, the most common precursor for PHA production. Alternative precursors to (R)-3-HA-CoA have been proposed for the metabolism of cyclohexanol to 6-hydroxyhexanoyl-CoA and 4,5-alkanolactone to 4,5-hydroxyacyl-CoA (4,5-HA-CoA) (pathways L and M in Figure 4). During the second phase, (R)-3-HA-CoA units are polymerized into PHAs by the PHA synthase (Chen, 2009; Lu *et al.*, 2009). Four classes of PHA synthases have been identified based on their unit composition and the substrate specificity. Class I, III and IV are related to the polymerization of scl-PHAs, while mcl-PHAs production is catalysed by class II enzymes. Class I and II are composed of 1 unit (PhaC), while class III and IV have two subunits, PhaC-PhaE and PhaC-PhaR respectively (Basnett *et al.*, 2017a; Możejko-Ciesielska and Kiewisz, 2016).

Among the 13 pathways described in Figure 11, B, J and K are the three main pathways described in literature. Pathway B is used by *Cupriavidus necator* using unrelated carbon sources for the production of P(3HB) and is characterized by three steps. Firstly, β- ketothiolase catalyzes the formation of acetoacetyl CoA through condensation of two acetyl CoA units. (R)-3-hydroxybutyryl CoA is then formed by acetoacetyl-CoA-reductase. Finally, P(3HB) is polymerized via esterification by the PHA synthase enzyme. The importance of nutrient limitation can be highlighted in this pathway. In normal conditions, the synthesis of PHA is blocked by the formation of high amounts of coenzyme A obtained from the Krebs cycle, inhibiting β- ketothiolase. In the presence of unbalanced conditions, the level of coenzyme A does not inhibit the activity of the enzyme, enabling the synthesis of PHAs. The second and third pathway are related to the production of mcl PHAs (Lu *et al.*,

2009). Pathway J is the fatty acid β-oxidation pathway and is characterized by the production of hydroxyacyl units from structure-related carbon sources which are then polymerized by PHA synthase. Three intermediates of the metabolic process enoyl-CoA, (S)-3-hydroxyacyl-CoA and (R)-3-ketoa-cyl-CoA can be converted into the PHA precursor by a (R)-enoyl-CoA hydratase, (R)-3-hydroxyacyl-CoA epimerase, or (R)-ketoacyl-CoA reductase respectively (Tortajada *et al.*, 2013). Pathway K involves the fatty acid *de novo* pathways and is characterized by the formation of (R)-3-hydroxyacyl-CoA precursors from unrelated carbon sources. The metabolic pathway generates (R)-3-hydroxyacyl-ACP which is then converted to (R)-3-hydroxyacyl CoA by the enzyme (R)-3-hydroxyacyl-CoA-ACP transacylase (Tortajada *et al.*, 2013; Sudesh *et al.*, 2000).

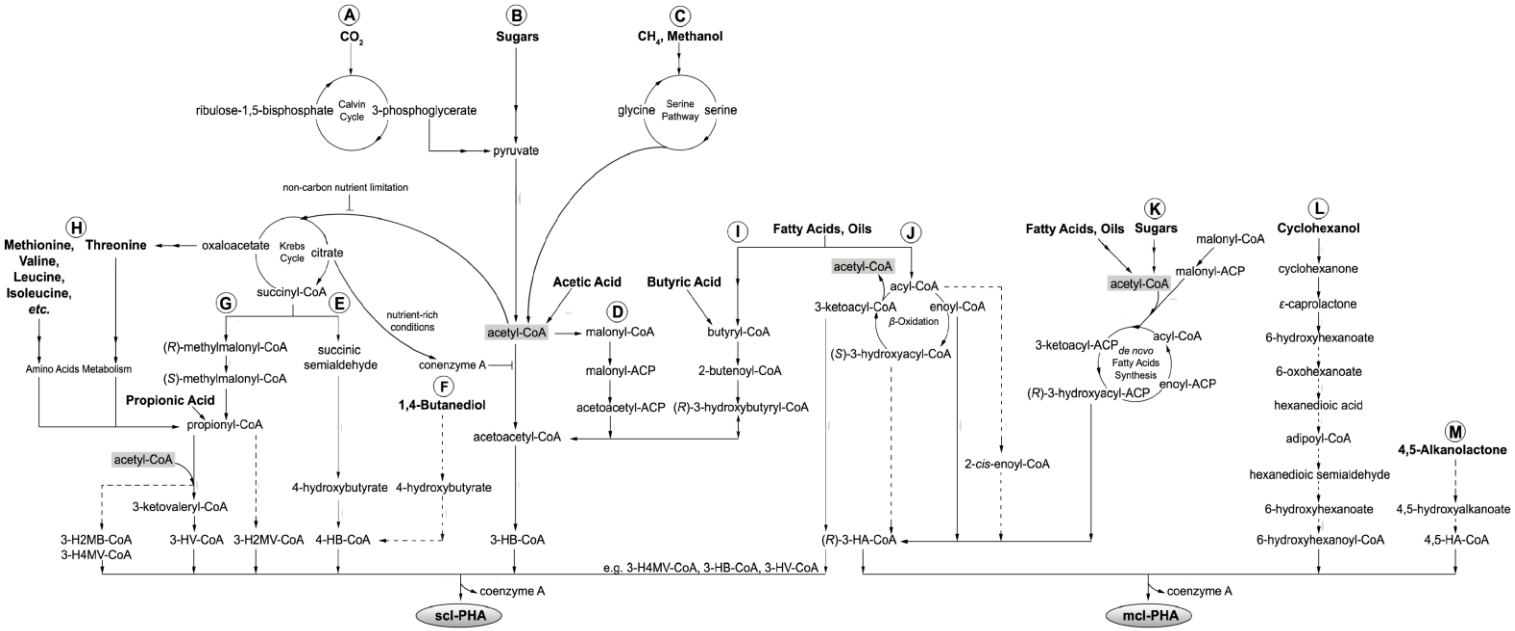

Figure 1.6 Main metabolic pathways for PHA production. The dotted lines represent putative pathways. The image was reproduced from Tan *et al.*, 2014 under Creative Commons Attribute licence.

1.3.3. Antibacterial PHAs

A few studies have been conducted on the development of antibacterial PHAs, by developing intrinsically active polymers (Sulphur containing PHAs), through chemical modification and through loading of inorganic and organic compounds.

1.3.3.1. Sulphur containing PHAs

A new family of sulphur containing PHAs (S-PHAs) has recently been discovered. This new class can be divided based on the position of sulphur in the polymer structure into S-PHAs in the backbone and S-PHAs in the side chain. The former was first discovered by Lütke-Eversloh *et al.* and it is characterized by the presence of thioester linkages. These polymers include monomers such as 3-mercaptopropionate (3MP), 3-mercaptobutyrate (3MB) or 3-mercaptovalerate (3MV), which were incorporated as comonomers with 3-hydroxybutyrate (3HB). P(3HB-co-3MP) (Figure 1.7a) was produced by *Cupriavidus necator* H16 via a co-feeding experiment using 3-mercaptopropionic acid, 3,3'-thiodipropionic acid or 3, 3'-dithiodipropionic acid, in addition to fructose or gluconic acid (Lu *et al.*, 2001). The highest molar fraction of 3MP was 54 mol% and the molecular weight of these polymers decreased with the increase of sulphur containing units (M_w 890000 Da for 10 mol % of 3MP and M_w of 150000 Da for 54 mol% of 3MP). The polythioester containing 3MB (Figure 1.7b) and 3MV (Figure 1.7 c) were obtained using the same fermentation procedure but using chemically synthesized precursor substrates (Bergander *et al.*, 2001). The highest molar fraction of 3MB was 73 mol%, while for 3MV only 5 mol% was obtained. The polymers containing 3MV showed also the presence of 3HV units which was perhaps due to the presence of a pentanoic acid contamination in the substrate solution.

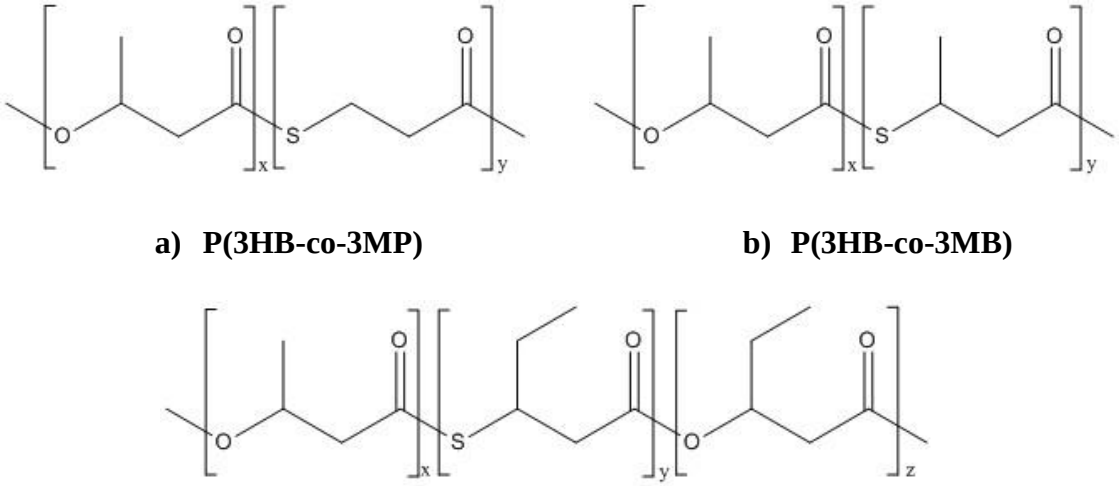

a) P(3HB-co-3MP) **b) P(3HB-co-3MB)**

c) P(3HB-co-3MV-co-3HV)

Figure 1.7 Chemical structures of a) P(3HB-co-3MP), b) P(3HB-co-3MB) and c) P(3HB-co-3MV-co-3HV)

Homopolymers of 3MP, 3MV and 3MB (Figure 1.8) were then produced using an engineered strain of *E. coli* JM109 pBPP1, which expressed a non-natural pathway for polythioester synthesis. The P(3MP) showed peculiar characteristics compared to the other polythioesters (Kawada *et al.*, 2003). It was the only homopolymer insoluble in chloroform at any temperature. Solubility in other solvents was observed at high temperatures. The copolymers obtained using *C. necator* H16 were instead soluble at room temperature in chloroform. Thermal analyses showed a higher melting temperature, 171°C, for P(3MP) compared to the oxoester analogue P(3HP), 121°C. On the contrary P(3MB) and P(3MV) showed a lower T_m, 100°C and 85°C respectively (Kawada and Marchessault, 2002).

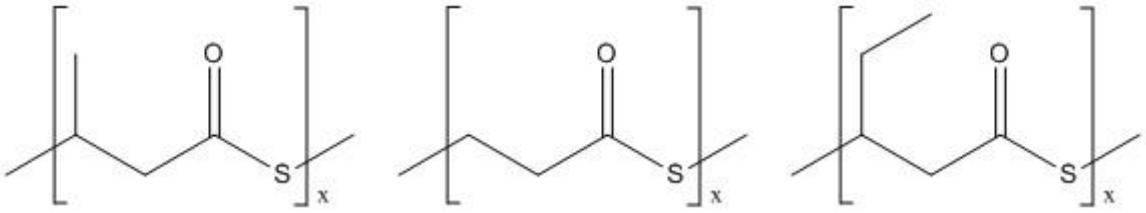

a) P(3MB) **b) P(3MP)** **c) P(3MV)**

Figure 1.8 Chemical structure of a) P(3MB), b) P(3MP) and c) P(3MV)

Regarding the S-PHAs in the side chains, both thioether and thioester linkages have been developed (Ewering *et al.*, 2002; Escapa *et al.*, 2011).

Cultivation of metabolic engineered *C. necator* H16, harbouring the PHA synthase enzyme of *P. mendocina,* with chemically synthetized alkylthioalkanoic acids lead to the production of PHAs containing thioether groups. Poly(3-hydroxypropylthiobutyrate-co-3-hydroxypropylthiohexanoate-co-3-hydroxypropylthio-octanoate) or P(3HPTB-co-3HPTHx-co-3HPTO) (Figure 1.9a) was obtained by feeding with propylthiooctanoic acid, while using propylthiohexanoic acid, Poly(3-hydroxypropylthiobutyrate-co-3-hydroxypropylthiohexanoate) or P(3HPTB-co-3HPTHx) (Figure 1.9b) was produced. The same carbon sources were utilized with a range of *Pseudomonas* species, but only *P. putida* KT2440 was able to produce sulphur containing PHAs, detected by elemental sulphur analysis. However, the chemical composition of these polymers were not evaluated (Ewering *et al.*, 2002).

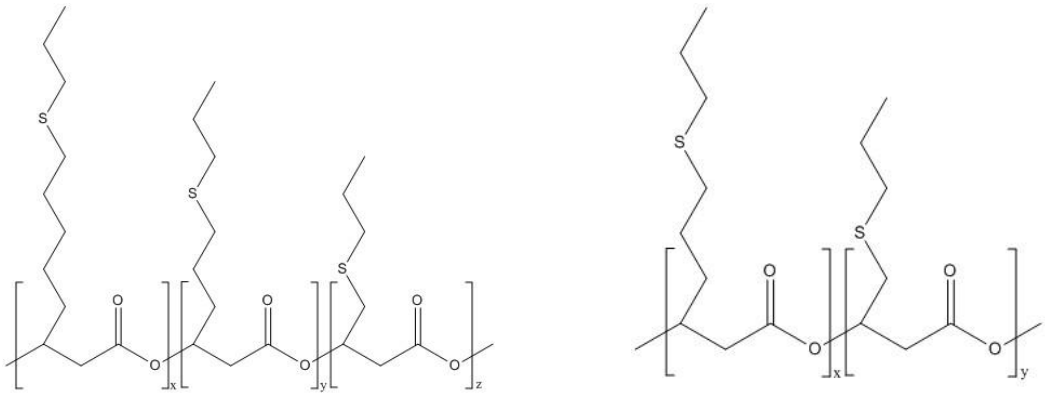

a) P(3HPTB-co-3HPTHx-co-3HPTO) **b) P(3HPTB-co-3HPTHx)**

Figure 1.9 Chemical structure of a) P(3HPTB-co-3HPTHx-co-3HPTO) and b) P(3HPTB-co-3HPTHx)

Thioester linkages were obtained via bacterial fermentation using *P. putida* KT2442 and *P. putida* KT42FadB using a co-feeding experiment with fatty acids (i.e. decanoic acid) as the "good" substrates to support bacterial growth and carbon sources containing thiol groups for polymer production (i.e. 6-acetylthiohexanoic acid) (Escapa *et al.*, 2011;Escapa *et al.*, 2013). *P. putida* KT42FadB was a genetic mutant which consisted of a knock-out of the *fadB* gene to produce PHAs with a higher fraction of monomers of long chain length. These materials were identified as PHACOS and they contained 3-hydroxy-6-acetylthiohexanoic acid and 3-hydroxy-4-acetylthiobutanoate (Figure 1.10). The wild type strain produced polymers with a higher fraction of sulphur containing monomers compared to the mutant. The mutant produced polymers with a higher content of longer monomeric units (i.e. 3-

hydroxy-decanoate and 3-hydroxy-6-acetylthiohexanoate). The thioester-PHAs were characterized in terms of antibacterial properties and showed to be inherently active, inhibiting the growth of methicillin-resistant *Staphylococcus aureus* (MRSA) both *in vitro* and *in vivo* (Dinjaski *et al.*, 2014). However, the mechanism behind the antibacterial activity was not investigated (Dinjaski *et al.*, 2014).

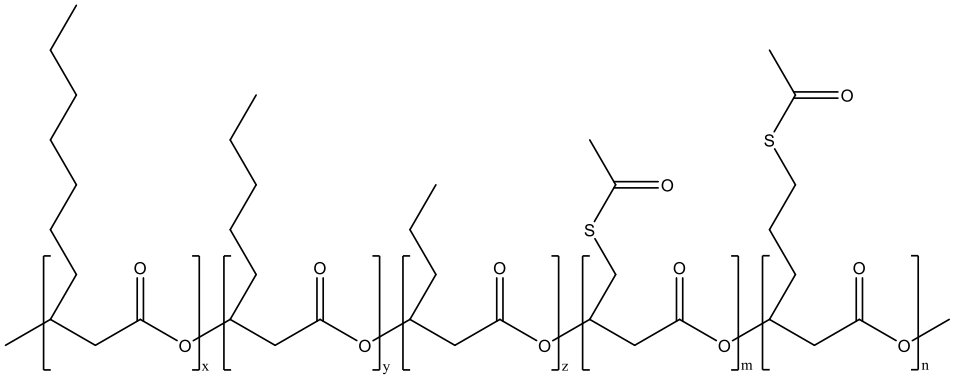

Figure 1.10 Chemical structure of thioester-PHA (i.e. PHACOS)

1.3.3.2. Chemical functionalization of PHAs

A few studies have investigated the possibility of using chemical functionalization to introduce antibacterial properties in PHAs.

Chemical functionalization of the films of P(3HB-co-3HV) was conducted by Langlois *et al.* to introduce methacrylate monomers with antibacterial properties. Surface modification with both 2-(methacryloyloxy)-ethyl-trimethylammonium and 2-(methacryloylethyl)-dimethyl-(3-sulfopropyl) ammonium was performed using UV photografting. The functionalized materials showed reduction in the number of bacterial cells for both *S. aureus* 6538 and *E. coli* 25922 compared to the non-functionalized samples (Manecka *et al.*, 2014).

N-vinylimidazole were grafted to the P(3HO) backbone using chemical grafting with benzoylperoxide as an initiator to introduce antibacterial properties. The solvent cast films produced showed bacteriostatic effect against *E. coli* 25922 and *S. aureus* 25922 (Chung *et al.*, 2012). Finally, P(3HB) was functionalized with a series of amine containing chemical groups (i.e. 1,4-butanediamine, 1,3-propanediamine, 1,2-ethylenediamine, piperazine, cyclohexylamine, 2,2′-(ethane-1,2-diylbis(oxy)) diethanamine (jeffamine EDR 148)). A transesterification reaction was firstly conducted to produce P(3HB) diols, which were then converted into P(3HB)-diacrylates by reaction with acryloyl chloride. The PHB-diacrylate were then grafted with the amino containing compounds through a Michael-addition reaction.

The materials produced showed antibacterial activity through the formation of inhibition zones against *S. aureus* 29213, *E. coli* 11105 and *P. aeruginosa* 9027 (Abdelwahab *et al.*, 2019).

Alternatively, coupling of PHAs with chitosan has also been investigated to introduce antibacterial features due to the inherently antimicrobial properties of such materials. Wu *et al.* investigated the grafting of chitosan onto a P(3HB-co-HV) membrane. To achieve the grafting, the PHA was firstly functionalized with maleic anhydride via radical polymerization using benzoyl peroxide as an initiator. The reaction introduced anhydride and carboxyl groups able to react with hydroxyl and amino groups of chitosan, producing antibacterial composite membranes (Wu *et al.*, 2015a). In another study by Hu *et al.*, ozone treatment was used to graft chitosan and chito-oligosaccharides on P(3HB-co-HV) films. The membranes were treated with ozone and acrylic acid to introduce carboxylic acid groups which then reacted with the amine groups of the polysaccharides. The produced material showed antibacterial activity against clinically isolated *S. aureus* strain, *E. coli* 43894 and *P. aeruginosa* 10145 (Hu *et al.*, 2003). Tai *et al.* produced antibacterial P(3HB)-chitosan membrane for bone regeneration. P(3HB) solvent-cast films were firstly grafted with poly(acrylic acid) using plasma irradiation and then functionalized with chitosan through the formation of an amide bond (Tai *et al.*, 2014). Physical blending was also investigated through the production of a nanofibrous mat by electrospinning of P(3HB-co-3HV) and chitosan for skin tissue engineering. The material enhanced skin tissue repair in Wistar rats promoting neo-epithelium regeneration in less than 14 days with no evidence of bacterial infection (Veleirinho *et al.*, 2012). Electrospinning was also employed for blending of P(3HB-co-3HHx) with chitosan grafted polycaprolactone (PCL). The antibacterial activity of the produced material was concentration dependent. A 30/70 blend (chitosan-PCL/PHA) did not show antibacterial activity against *E. coli* 25922 and *S. aureus* 12600. A 50/50 membrane showed activity only against Gram negative bacteria, while 70/30 were active against both species, with a higher efficacy toward *E. coli* 25922 (Díez-Pascual and Díez-Vicente, 2016).

1.3.4. Loading of antibacterial compounds

Another approach that has been investigated to produce PHAs with antibacterial properties , was the loading with natural agents such as plant-derived compounds or essential oils (Requena *et al.*, 2016).

Pramanik *et al.* developed curcumin-loaded P(3HB-co-3HV) films through solvent casting technique. The material showed wound healing properties and antibacterial activity against both Gram positive and Gram negative strains (Pramanik *et al.*, 2015). Similar results were obtained with curcumin loaded 3D scaffold of P(3HB-co-3HV) by salt leaching processing (Pramanik *et al.*, 2016). Kundrat *et al.* investigated the physical absorption of four oil extracts (i.e. cinnamon, clove, oregano and oak bark) onto P(3HB) fibres obtained through wet spinning. All the four plant extracts exhibited antibacterial activity against *Micrococcus luteus* 1569, a Gram positive bacteria, and *Serratia marcescens* 8587, a Gram negative bacteria, with clove-functionalized fibres showing the highest reduction in the bacterial cell count of both species after 24 hours of incubation in direct contact with the samples (Kundrat *et al.*, 2019). Alternatively, Figueroa-Lopez *et al.* investigated the incorporation of oregano EO and two natural extracts (rosemary and green tea extracts) in P(3HB-co-3HV) fibres by adding the active agents directly to the polymer solution prior to electrospinning. All the loaded fibrous mats developed showed antibacterial properties against *S. aureus* 6538P and *E. coli* 25922 (Figueroa-Lopez *et al.*, 2019). In another study from the same group, eugenol EO was firstly loaded onto mesoporous silica nanoparticles and then incorporated into P(3HB-co-3HV) fibres using the same technique. The encapsulation was employed to maintain and protect the antibacterial effect of the agent, as essential oils are volatile compounds. The films obtained showed antibacterial activity against the two strains mentioned above up to 15 days after day fabrication and storage in a close environment (Melendez-Rodriguez *et al.*, 2019).

Finally, incorporation of metal ions has also been investigated. Castro-Mayorga *et al.* developed a multilayer system loaded with silver nanoparticles (AgNPs). P(3HB-co-HV)/AgNP electrospun fibres were used as a coating of a P(3HB-co-HV) film, showing good antibacterial activity against *Salmonella enterica* 4300 (Castro-Mayorga *et al.*, 2016). In another study, polymethacrylic acid was grafted onto the surface of P(3HB-co-3HV) electrospun fibres to introduce carboxylic groups to be used for the *in situ* photogeneration of silver nanoparticles. The obtained material showed antibacterial activity against *S. aureus*

6538 and *E.coli* 25922, reducing bacterial adhesion by 98% and 100% respectively (Versace *et al.*, 2013). Two studies investigated the incorporation of zinc oxide nanoparticles in scl-PHA-based constructs. Díez-Pascual and Díez-Vicente incorporated nano-ZnO in P(3HB-co-3HV) by solvent casting technique. The films showed a bactericidal effect against both *S. aureus* 12600 and *E. coli* 25922, and the effect increased with the increase in loading percentage, reaching the highest reduction of the bacterial cell count for the samples containing 5 wt% of nano-ZnO (Díez-Pascual and Díez-Vicente, 2014). Another study investigated the incorporation of zinc oxide in P(3HB) fibres by electrospinning. All the three loading compositions of nano-ZnO developed (i.e. 1, 3 and 5 wt%) showed antibacterial activity against *E. coli* 25922 and *S. aureus* 29213 (Rodríguez-Tobías *et al.*, 2016). Finally, electrospinning was also employed to develop a P(3HB-co-3HV) fibres containing copper oxide (CuO) nanoparticles to be used as a coating of a fibrous mat obtained by compression moulding of P(3HB-co-3HV). The obtained nanocomposite showed high antibacterial activity against *S. enterica* 4300 and *Listeria monocytogenes* 7467, inducing a 100% reduction of the bacterial cell count after 24h of incubation of the bacterial species directly on the surface of the samples (Castro-Mayorga *et al.*, 2018).

1.3.5. Medical application of PHAs

One of the many areas of investigation of PHAs is as materials for biomedical applications. Such a high-value application area represents an attractive market for PHAs allowing to overcome their major limitation related to cost issues, as in this field the products are firstly evaluated based on their performance and secondly on their price, contrary to large-scale-low-value plastic materials (e.g. packaging material) (Koller, 2018).

The interest on the study of PHAs has particularly increased since P(4HB) received the Food and Drug Administration (FDA) approval for its use in clinical practise as material for surgical sutures (Grigore *et al.*, 2019). Devices based on this polyester currently used in the clinic include MonoMax Suture (B Braun Aesculap, Tuttlingen, Germany) (Odermatt *et al.*, 2012), GalaFLEX (Galatea Surgical, Inc., Massachusetts, USA) a macroporous monofilament meshed used for plastic and reconstructive surgery (Williams *et al.*, 2016) and Phasix and Phasix ST (C.R. Bard Inc., Murray Hill, NJ) a mesh used for hernia repair (van Rooijen *et al.*, 2018).

Biocompatibility and biodegradability are the two main properties of PHAs that make them suitable for the biomedical field (Akaraonye *et al.*, 2010; Chanprateep, 2010; Li *et al.*, 2016;

Zinn *et al.*, 2001). The former is described as "the ability of a material to perform with an appropriate host response in a specific application without having any risk of injury, toxicity, or rejection by the immune system and undesirable or inappropriate local or systemic effects" (Ghasemi-Mobarakeh *et al.*, 2019). *In vitro* and *in vivo* studies have proven the capability of PHAs to be well tolerated when used as implantable devices and to support attachment, proliferation and growth of various mammalian cells (Valappil *et al.*, 2006; Ali and Jamil, 2016; Koller, 2018). PHAs have also shown to undergo non-enzymatic and enzymatic hydrolysis *in vitro* and *in vivo* with non-toxic degradation products (Gogolewski and Dillon, 1993; Nigmatullin *et al.*, 2015; Ali and Jamil, 2016; Philip *et al.*, 2007, Freier *et al.*, 2002; Kehail *et al.*, 2017). In particular, 3-hydroxybutyric acid, the degradation product of P(3HB), is a natural metabolite of the human body , present in the blood plasma with a concentration of 30-100 µg/mL (Grigore *et al.*, 2019; Koller, 2018). Due to the wide variety of mechanical properties that that can be obtained using different carbon sources and microorganisms, PHAs are good candidates as substitutes for different human tissues. They have been investigated for a range of medical applications, including scaffolds for both hard (e.g. bone, cartilage) and soft (e.g. cardiac tissue, nerve and skin) tissue engineering and drug delivery systems (Lizarraga-Valderrama *et al.*, 2018; Butt *et al.*, 2018; Elmowafy *et al.*, 2019; Koller and Braunegg, 2018).

1.4. Bone healing and repair

Bone tissue has dynamic structure with high capacity of regeneration. In case of a fracture, two types of bone healing can occur, primary and secondary. The former usually does not happen naturally as it requires an almost no gap formation and no movement of the segments and is obtained through rigid internal fixation. It is based on the same process that characterises bone remodelling, with the action of osteoclasts, cell responsible for bone resorption, and osteoblasts, involved in new bone deposition. The osteoclast cells remove damaged bone along the fracture line, followed by refilling of new bone from the osteoblasts. If the gap between the two bone segments is less than 0.01 mm, the new tissue is placed longitudinally along the axis of the bone (i.e. contact healing), if a larger separation (e.g. < 1 mm) is obtained, a weaker tissue is firstly deposited perpendicular to the orientation of the bone, which is then replaced by tissue oriented longitudinally by a second remodelling process (i.e. gap healing) (Marsell and Einhorn, 2012; Pountos and Giannoudis, 2018).

Second (or indirect) bone healing is the process that occurs naturally after bone fracture. It is characterized by three phases, inflammatory, reparative and remodelling, which usually overlap, and are described in Figure 1.11.

After fracture, a hematoma, a blood clot, is formed, filling the fracture gap and forming the temporary scaffold and environment critical for healing. The acute inflammatory stage usually lasts up to 7 days after the injury and is characterized by the recruitment of inflammatory cells including lymphocytes, macrophages, eosinophils, and neutrophils. Such cells are responsible for the release of cytokines that have multiple effects, recruitment of other inflammatory cells and mesenchymal stem cells (MSCs), stimulating angiogenesis, osteogenic differentiation of MSCs, and extracellular matrix synthesis (Pountos and Giannoudis, 2018; Ghiasi *et al.*, 2017). The hematoma is transformed into a granulation tissue (MSCs, immune cells and endothelial cells embedded in extracellular matrix), which is then converted into a cartilaginous callus, named soft callus. Such tissue is than replaced by woven bone (i.e. hard callus) through a process called endochondral ossification, involving cartilage calcification, removal and bone deposition. The reparative stage (comprising both soft and hard callus formation) begins within days from the injury and can last up to a couple of months. Finally, during the remodelling stage the woven bone is gradually replaced with lamellar bone. This stage may take years to achieve full regeneration (Marsell and Einhorn, 2012; Marzona and Pavolini, 2009).

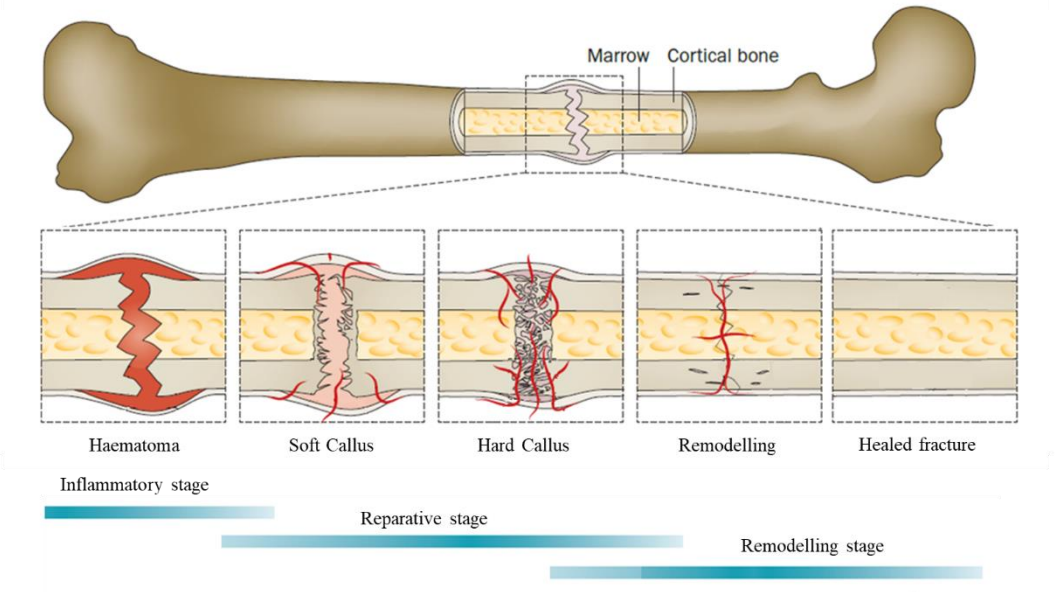

Figure 1.11 Schematic representation of the stages of secondary or indirect bone healing. From left to right: inflammatory, reparative and remodelling stage, and healed bone. The imaged is adapted from Einhorn and Gerstenfeld, 2015 with permission from Springer Nature.

Thanks to this biological process, the majority of fractures are able to self-heal. However, the healing capability is associated with the proximity of the bone segments. In case of large bone defects, they are not able to heal on their own and surgical intervention is required. The critical size of the defect impairing auto regeneration depends on the skeletal segment that is involved. For example, for the forearm a defect longer than 3 cm is considered critical, for the femur and tibia 5 cm and for the humerus 6 cm (Calori *et al.*, 2011; Lasanianos *et al.*, 2010). There are a variety of scenarios that can lead to the formation of large bone defects, including high energy trauma, tumour resection, chronic diseases (e.g. osteoporosis) and complications due to infections (i.e. osteomyelitis). Alternatively, another complication associated with bone fractures is the development of non-unions, defined as fractures that are not healed after 6 months or where no progression in the healing process has occurred over a 3-moths period (Jones and Mayo, 2005). In both cases, the use of a bone graft, a substitute to fill the gap, is usually required to restore the normal function of the tissue. The gold standard applied in clinic is the use of bone autografts. This involves the harvesting and implantation of bone from a healthy site of the patient (usually non-load bearing). The main drawback associated with this treatment is the limited availability of tissue. Additionally, the need of an extra surgery required for the harvesting can increase the patient's distress, due to possibility of complications such as haemorrhages or nerve and vascular lesions and the development of postoperative pain, and increase in costs (Leteve and Passuti, 2018). An alternative to autografts is represented by allografts, tissue obtained from individuals of the same species (e.g. cadavers). Several issues are associated with this technique, including the risk of an immune response leading to rejection and possible transmission of diseases. Moreover, limited reproducibility is also another drawback as the properties of the materials may vary depending on the site of harvesting and the health conditions of the donor and can be affected by the different treatments used for sterilization and to prolong storage time (Baldwin *et al.*, 2019; Iaquinta *et al.*, 2019). Due to the problems associated with such transplanted tissues, great interest has been brought to the development of synthetic bone substitutes as alternative therapeutic strategies to achieve bone healing, thanks to their unlimited availability and longer shelf life. One of the available options is to use a tissue engineering approach based on the combination of a scaffold (natural, synthetic or decellularized tissue) with cells and appropriate stimuli (e.g. chemical stimuli with growth factors) (Fernandez de Grado *et al.*, 2018; Hasan *et al.*, 2018).

1.4.1. Requirements for an ideal material for bone tissue engineering

One of the most important aspect of a tissue engineered construct is the scaffold, the three-dimensional substrate able to provide a suitable environment for cell anchorage and proliferation, in order to allow tissue regeneration. The requirements that a scaffold need to possess in order to develop an ideal construct for bone regeneration have been extensively investigated in literature and categorised into biological, mechanical and structural (De Witte *et al.*, 2018; Turnbull *et al.*, 2018; Haugen *et al.*, 2019; Chocholata *et al.*, 2019).

Biological requirements are key aspects of any material studied for tissue regeneration and refers to biocompatibility, degradability and non-toxicity.

Biocompatibility refers to the ability of a material to induce a specific tissue response without eliciting an adverse immune response, as mentioned in section 1.3.5. In the case of bone tissue, the desired tissue-tailored response can be described in terms of osteoconductive and osteoinductive properties. Osteoconduction refers to the ability to induce bone growth on the scaffold surface, favouring the implant osteointegration, which indicates the formation of a stable anchorage between the bone and the constructs. Among the materials used in bone regeneration, synthetic ceramics (i.e. calcium-phosphate based materials like hydroxyapatite ($Ca_{10}(PO_4)_6(OH)_2$,), (HA)) are inherently osteoconductive thanks to their chemical composition similar to the inorganic component of human bone tissue (Jeong *et al.*, 2019). Osteoinduction describes the capability of the material to induce the proliferation and differentiation of mesenchymal stem cells into osteoblasts and chondrocytes to favour the formation of new bone (Ahmed *et al.*, 2016; Albrektsson and Johansson, 2001). One of the main strategies investigated to introduce osteoinductive characteristics to scaffold is the incorporation of bioactive molecules such us bone morphogenetic proteins (BMPs), growth factors that play a fundamental role in fracture regeneration by inducing a cascade of events leading to the differentiation of MSCs into osteogenic lineage (De Witte *et al.*, 2018). However, their usage needs to be controlled as high dosages are associated with sever adverse effects. Moreover, the incorporation of BMPs can be challenging due to their rapid degradation. Finally, their high costs limit their usage in clinical practice (Oryan *et al.*, 2014; García-Gareta *et al.*, 2015). Recently, the use of metallic ions has emerged as an alternative solution to such biomolecules to confer osteoinductive properties to materials for bone

regeneration. Such inorganic materials, defined as therapeutic inorganic ions, have the advantages of being economic and stable compounds able to withstand the different processing conditions used for the development of scaffolds. Moreover, in addition to osteogenesis, several ions possess other characteristics like antibacterial (e.g. selenium, zinc or copper) and anticancer (e.g. selenium) effect or stimulation of angiogenesis (e.g. copper), allowing the incorporation of novel beneficial features in the constructs. However, their release needs to be controlled as high level of such ions might lead to toxic effects in the human body (Mouriño and Boccaccini, 2010; Glenske *et al.*, 2018).

Biodegradability is another important property for any type of tissue engineering application. The scaffold should degrade in an appropriate manner to favour the cells to produce their own extracellular matrix, replacing the construct. Moreover, the degradation product should be non-toxic and should not elicit an adverse reaction in the site of implantation. In this context biodegradable polymers have an advantage compared to other materials and their degradability can be tailored based on their physical and chemical properties, such as crystallinity, hydrophobicity/hydrophilicity, molecular weight, porosity and pore size (Yang *et al.*, 2019).

The material should also possess mechanical properties compatible with the specific anatomical site of implantation, allowing appropriate load transfer. At the early stage of implantation, sufficient mechanical stability is important to preserve the construct integrity until the newly formed tissue is able to withstand the load. However, if the material adsorbs all the stress applied, due to higher mechanical features than the natural tissue, loss of density and weakening of the bone tissue might occur (i.e. stress shielding), leading to implant failure. Natural bone is composed of two type of tissues, cortical and cancellous, showing different mechanical features. The former possess an elastic modulus (measure of the stiffness of the material) of 7–20 GPa and compressive strength (capacity to resist compressive loads) of 100-180 MPa, while for the latter the values are 0.2–2 GPa and 2–20 MPa (Bose *et al.*, 2012; Kashirina *et al.*, 2019). Metals are widely used in clinics due to their high mechanical properties and stability, making them feasible for load-bearing applications (Thandapani *et al.*, 2018). However, their Young's modulus higher than that of cortical bone, can lead to stress shielding and bone resorption (De Witte *et al.*, 2018). Ceramics possess good compressive strength but are brittle materials with a low fracture toughness. Polymers instead have a low mechanical strength and the elastic modulus

compared to cortical bone. These features limit the application of such classes of materials to bone stuffing or reconstruction of bone cancellous material in not-load bearing applications where their use needs to be combined with internal or external fixation (Blom, 2007; Gao *et al.*, 2017). Another important aspect for the mechanical properties of a scaffold for bone regeneration is the ability to be easily shaped and manipulated in the surgical operating room to better adapt to the defect to be treated (Jakus *et al.*, 2016; Turnbull *et al.*, 2018). In this context, due to their stiffness and brittleness, ceramics can be difficult to implement surgically. To aid such a disadvantage, different formulations have been developed like granules or putties, that can even be injected in the injured site. However, such systems are still associated with some drawbacks due to the possible displacement or disintegration of the paste when in contact with blood and body fluids, and potential side effects due to the exothermic properties of the hardening process of some cements (Zhang *et al.*, 2014; Jakus *et al.*, 2016). Alternatively, a wide range of composite materials have been developed based on ceramics, providing stiffness, and polymers, adding elasticity (Kashirina *et al.*, 2019; Ghassemi *et al.*, 2018).

Porosity is the main structural requirement for a construct for bone tissue engineering. An open and interconnected porous structure is essential for the diffusion of oxygen nutrients and the flow of nutrients and of wastes throughout the constructs reaching especially the central part, in the case where blood supply has not been engineered (Turnbull *et al.*, 2018). Moreover, it allows cell seeding, proliferation and migration through the scaffold, favouring tissue ingrowth. Osteointegration is also facilitated by a porous construct, favouring implant stability by allowing interlocking between the tissue and the scaffold (De Witte *et al.*, 2018; Hannink and Arts, 2011). Finally, an open porosity is required for the *in vivo* vascularization of the constructs (Loh and Choong, 2013). A much-debated question regards the optimal pore size for a scaffold for bone regeneration, as in literature a wide range of values has been investigated from 50 μm to 2 mm, without reaching a unanimous answer (Hollister, 2005; Gao *et al.*, 2017). Overall, constructs with a mean porosity higher than 300 μm have shown to favour osteogenesis and vascularization, as they facilitate cell migration. However, the presence of small size pores (i.e. < 100 μm) is important for cell attachment, as the decrease of the pore dimension increases the surface area of the material, favouring protein adsorption and a higher cell attachment (Murphy and O'Brien, 2010; Karageorgiou and Kaplan, 2005). At the same time constructs based only on small pores have shown to hamper cell migration,

leading to possible necrosis (Petrochenko and Narayan, 2010). Therefore, there is a general consensus on the need of both micro and macro pores in an ideal scaffold for bone regeneration (Turnbull *et al.*, 2018). An upper limit of porosity has also not been identified. Many studies involving the use of traditional processing techniques (e.g. freeze drying and solvent casting/particulate leaching) suggested an overall porosity up to 600 µm as optimal. However, with the introduction of additive manufacturing a range of constructs based on different material (e.g. PLGA and HA) have been obtained with dimension of pores up to 2 mm, showing no statistically significant differences in bone growth between the pore sizes (Simon *et al.*, 2003; Hollister, 2005). Large pore sizes and high porosity usually have a detrimental effect on the mechanical properties of the material, compromising the scaffold structural integrity. The scaffold degradation can also be affected, as a higher porosity leads to higher permeabilization and usually a faster degradability rate (Karageorgiou and Kaplan, 2005; Zhang *et al.*, 2018). Therefore, the degree of porosity and the pore size dimension need to be rationally designed and investigated when developing a construct for bone regeneration.

Alongside the described biological, mechanical and structural characteristics, the introduction of antibacterial features in the scaffold has recently attracted increasing interest (Johnson and García, 2015; Dorati *et al.*, 2017). Bone implants have a risk of infection of 2-5%, which increases to 30% in the case of open fractures (Darouiche, 2004; Trampuz and Widmer, 2006). In the presence of osteomyelitis (i.e. bacterial bone infection) the regeneration of the tissue is impaired and, if not treated, can result in chronic infection, characterized by bone necrosis and spreading to adjacent soft tissues. Moreover, resections due to infections are one of the major causes of large bone size defects, as described in the previous section. The most common pathogen involved is *S. aureus*, but other microorganisms have also been associated with such pathology including *S. epidermidis*, *Streptococci sp*., *Pseudomonas sp.* and *E. coli* (Kavanagh *et al.*, 2017; Boyce *et al.*, 2011). The rise of antibiotic resistance, already discussed at the begging of this chapter, has exacerbated such situation, making antibacterial properties an important requirement for bone regeneration. A variety of antimicrobial scaffolds have been investigated using the strategy described in section 1.2 based on the exploitation of either antibacterial materials (inherently or functionalized) or by incorporation of bioactive molecules (Johnson and García, 2015; Dorati *et al.*, 2017). Such constructs find application as materials to prevent the rise of infection or to combat existing ones. Moreover, an antimicrobial construct could

be beneficial in limiting the number of surgeries required in the case of bone infection, reducing patient distress and the costs involved. A revision plan in case of infection requires two or multiple surgeries, involving usually the implantation of a bone cement loaded with antibiotic used as a spacer, followed by insertion of a new graft. In such cases, a material capable of inducing adequate bone regeneration combined with antibacterial features would be highly beneficial, requiring only a one-surgery approach (Winkler *et al.*, 2018).

To date, none of the materials investigated possess all the requirements for bone regeneration, showing the need for further investiagtion in this area (Haugen *et al.*, 2019; Kashirina *et al.*, 2019).

1.4.2. Polyhydroxyalkanoates in Bone Tissue Engineering

Bone regeneration is one of the main areas of investigation of PHAs in the medical filed. As polymeric materials, they are candidates for such application due to their biodegradability, easy processability and versatile and tuneable physical and mechanical properties. As already mentioned, the fact that they can be obtained from natural and renewable resources makes them a good alternative to their synthetic counterparts. Moreover, PHAs have shown to possess less acid degradation products than other synthetic polymers such as PLA, PLGA and PGA, limiting the possibility of developing a late or chronic inflammation (Manavitehrani *et al.*, 2016; Bonartsev *et al.*, 2019). Compared to other natural-derived materials (e.g. collagen and chitosan), PHAs show better mechanical features and higher reproducibility as their production can be strictly controlled through fermentation processes(Koller and Braunegg, 2015). Moreover, they show higher thermal stability making them suitable for a wider range of processing techniques (Puppi *et al.*, 2019).

Scl-PHAs (i.e. P(3HB) and P(3HB-co-3HV)) are the main polyesters employed for this application due to their high crystallinity and mechanical properties (i.e. Young's modulus and ultimate tensile strength), closer to those of native bone (Karageorgiou and Kaplan, 2005). However, recently mcl-PHAs have also been investigated for non-load bearing applications (Ansari *et al.*, 2016).

PHAs are not inherently osteoconductive, therefore many studies have investigated the development of composite materials, coupling the polymers with ceramics. Synthetic hydroxyapatite is the main filler investigated due to its similarity to the inorganic component of bone and its biocompatibility and bioactivity (Zhou and Lee, 2011). Alternatively,

incorporation of bioactive glasses (BG) into the polymeric matrix has also been evaluated. BG are degradable silicate-based glasses that are able to create a strong bond with native bone through the formation of a carbonate layer on their surface upon contact with biological fluids (El-Rashidy *et al.*, 2017; Jones, 2015).

Several techniques have been employed for the development of 3D constructs. Simple solvent casting of scl and mcl-PHAs has been applied to evaluate the *in vitro* biocompatibility of the materials, which showed to be able to favour the attachment and proliferation of several bone cells, including MC3T3-E1 cell line and human derived bone marrow mesenchymal stem cells (Hu *et al.*, 2009; Li *et al.*, 2005; Ansari *et al.*, 2016).

Solvent casting/particulate leaching and electrospinning are the two main techniques investigated for the development of porous constructs. The former is based on the production of a suspension by mixing the polymer with a porogen (e.g. salt or sugar) in suitable solvent (e.g. chloroform). After casting the suspension in an appropriate mould, the scaffold is dried and then placed in water to allow the release of the porogen. The porogen dimensions and the porogen/polymer ratio are the key parameters to control the percentage of porosity and the pore size (Prasad *et al.*, 2017). In all the studies conducted to develop porous PHA scaffolds, crystal dimensions ranging from 100-300 μm were found to be optimal for the formation of interconnected pores of similar dimensions (Hajiali *et al.*, 2010; Saadat *et al.*, 2015; Lu *et al.*, 2016; Wang *et al.*, 2005; Hayati *et al.*, 2012; Torun-Köse *et al.*, 2003; Saadat *et al.*, 2013). Moreover, a high ratio of porogen over polymer ((80-90):(20-10), porogen:polymer) was also necessary to achieve a high porosity (average values >75%) (Ansari *et al.*, 2016; Hajiali *et al.*, 2010; Hayati *et al.*, 2012; Saadat *et al.*, 2015, 2013). Composite porous scaffold can be obtained using the solvent casting/particulate leaching technique by mixing the ceramic (e.g. HA and BG) in the polymer/porogen solution. A range of both scl and mcl PHAs (P(3HB), P(3HB-co-3HV), P(3HB-co-3HHx), P(3HHx-co-3HO)) have been investigated using such methods. The maximum quantity of HA or BG incorporated was 30% as higher percentages led to agglomeration of the ceramic and non-uniform distribution inside the scaffold (Ansari *et al.*, 2016; Saadat *et al.*, 2015; Wang *et al.*, 2005; Hayati *et al.*, 2012; Noohom *et al.*, 2009; Misra *et al.*, 2008; Sadat-Shojai *et al.*, 2013). The introduction of the filler inside the porous scaffold showed a positive effect on the mechanical properties of the constructs, increasing compressive strength and modulus compared to neat P(3HB), P(3HB-co-3HV) and P(3HB-co-3HHx) scaffolds, with an increase

of compressive strength and modulus, obtaining values more similar to the mechanical properties of natural bone (Hayati *et al.*, 2012; Wang *et al.*, 2005; Rai *et al.*, 2008; Misra *et al.*, 2008; Sadat-Shojai *et al.*, 2013; Noohom *et al.*, 2009). Moreover, the incorporation of the ceramic induced an improvement of the *in vitro* biological performance of the composite materials compare to the neat ones in terms of bioactivity and biocompatibility of a range of bone cells, including MG63, MC3T3-E1, rabbit-derived bone marrow cells and human osteoblast cells (hFOB 1.19) (Misra *et al.*, 2008; Saadat *et al.*, 2013; Hayati *et al.*, 2012; Sadat-Shojai *et al.*, 2013; Ansari *et al.*, 2016; Wang *et al.*, 2005). In particular, the biocompatibility of the scaffolds was characterized by an increase of cell attachment, proliferation and differentiation into bone cell lineage, combined with high levels of alkaline phosphatase activity (ALP). ALP is an enzyme produced by osteoblasts that is believed to be involved in the bone mineralization process, and is therefore used as a marker for the activity of osteoblasts (Sabokbar *et al.*, 1994).

Electrospinning is the other technique employed to produce porous scaffolds in the form of micro and nano-fibrous mats. Such method is based on the application of a high electric potential to a polymer solution to generate a charge imbalance that leads to the generation and deposition of fibres onto a collector (Jun *et al.*, 2018). Sombatmankhong *et al.* produced micro fibrous matrices with an average fibre diameter between 2-4 μm from P(3HB), P(3HB-3HV) and 50/50 blends of these materials. All the three scaffolds showed ability to induce attachment and proliferation of human osteoblasts (Saos-2) (Sombatmankhong *et al.*, 2007). In another study, P(3HB) electrospun scaffolds favoured osteogenic differentiation of human bone marrow-derived mesenchymal stem cells when cultured in osteogenic media (Köse *et al.*, 2016). Composite fibres have also been produced by mixing HA or BGs in the polymer solution in concentration up to 15 wt% and electrospinning such mixtures (Khoshraftar *et al.*, 2018; Ramier *et al.*, 2014; Iron *et al.*, 2019; Kouhi *et al.*, 2015). A novel approach was evaluated by Ramier *et al.* for the incorporation of HA in fibrous matrices by simultaneously electrospinning of a P(3HB) solution and electrospraying of an HA dispersion. In this way, the composite scaffolds produced showed the presence of HA on the surface of the fibres, compared to HA being entrapped within the fibres in the case of electrospinning of a mixture of P(3HB)/HA (Ramier *et al.*, 2014). The presence of the nano-HA on the surface induced a better cell interaction leading to higher cell proliferation. However, such structures showed lower mechanical properties compared to both neat P(3HB) and HA-entrapped P(3HB) mats. This result was ascribed to a lower cohesion of the fibrous material due to the presence of

nanoparticle aggregates between the fibres, leading to weaker interactions. On the contrary, the scaffold produced with the traditional method (i.e. direct electrospinning of polymer/HA solution) showed an enhancement of the mechanical properties with a 67% increase of the elastic modulus and 51% increase of the tensile strength at break compared to P(3HB) fibres (Ramier *et al.*, 2014).

A few studies have also been conducted on the use of 3D printing technology with PHAs for the development of bone substitutes to obtain structures with controlled and repetitive geometries. In particular, laser and extrusion-based technologies have been employed to developed PHA-based 3D structures. Selective Laser Sintering (SLS) was applied to produce porous structures of cubical form using P(3HB) (Pereira *et al.*, 2012). This technique uses a laser beam on a layer of powder material, inducing sintering of the particles. Once a layer has been sintered, the printer platform is lowered, and another level of powder is added on top and scanned again with the laser. The process is repeated until the desired 3D printed structure is obtained as schematized in Figure 1.12 a (Ji *et al.*, 2018). In the study by Pereira *et al.*, the structure obtained closely mimicked the virtual model and the thermal and chemical properties of P(3HB) remained stable after the process, without degradation (Pereira *et al.*, 2012). A similar scaffold was produced in a study by Saska *et al.*, and the surface of the material was coated with osteogenic growth factors by simple physical absorption to improve the bioactivity of the obtained 3D P(3HB) constructs (Saska *et al.*, 2018). An alternative technique was investigated to produce composite materials based on P(3HB-co-3HV) using SLS. In the study, microspheres of the polymer loaded with calcium phosphate were produced by an oil-in-water emulsion technique, and such microparticles were used as the starting powder material for the construction of the 3D printed scaffolds (Duan *et al.*, 2011). The other 3D printing techniques investigated with PHAs are based on extrusion. Such processes are characterized by the application of a mechanical or pneumatic pressure on a molten or viscous (i.e. polymer solution) polyester to obtain a continuous flow of material, as schematized in Figure 1.12 b (Jammalamadaka and Tappa, 2018). A 3D printed composite scaffold was produced through solution-based technology by applying compressed air on a mixture of P(3HB-co-3HHx) and BG dissolved in organic solvents. The 3D constructs were tested *in vivo* for the repair of bone defects in a rat model and showed ability to stimulate bone repair after 8 weeks of implantation (Zhao *et al.*, 2014). Alternatively, Yang *et al.* produced composite scaffolds by melt 3D printing of P(3HB-co-3HHx) followed by

immersion in solution containing BG to obtain surface functionalization. Such material showed enhanced cell proliferation and ALP activity of human mesenchymal stem cells compared to non-loaded P(3HB-co-3HHx) (Yang *et al.*, 2014).

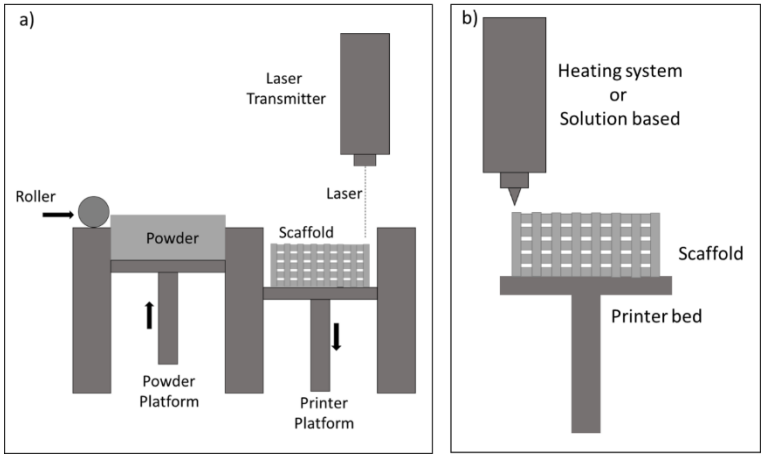

Figure 1.12 Schematic representation of two 3D printing techniques used for PHAs a) Selective Laser Sintering and b) Extrusion (solution or melting) based systems.

1.5. Aims and objectives of the project

The main aim of this project was the production of Polyhydroxyalkanoates with antibacterial properties and their modification to allow their use in bone tissue engineering applications. This was achieved by producing inherently antibacterial PHAs as well as by developing composite materials through the combination of PHAs with a novel antimicrobial hydroxyapatite.

This main aim was achieved by fulfilling the following objectives:

1. The first objective was to produce and characterize a range of Polyhydroxyalkanoates. A short chain length PHA, P(3HB) was produced by *B. subtilis* OK2 using glucose as the carbon source. Two novel medium chain length PHAs were produced by *P. mendocina* CH50 using coconut oil and glucose as the carbon source. The polymers were completely characterized in terms of chemical, physical, thermal, mechanical and biological properties.

2. The second objective was to produce inherently antibacterial PHAs through bacterial fermentation. Thioester-PHAs were produced by *P. putida* KT2442 using decanoic acid and 6-acethylthiohexanoic acid as the carbon sources. The material was completely characterized in terms of chemical, physical, thermal, mechanical, biological and antibacterial properties. Moreover, novel 2D inherently antibacterial films were developed by blending the thioester-PHA produced with the polymer obtained using the control conditions (P(3HHx-co-3HO-co-3HD)). The materials were characterized in terms of thermal, mechanical, biological and antibacterial properties.

3. The third objective was the development of novel antibacterial composite 2D films through the combination of P(3HO-co-3HD-co-3HDD) and P(3HB) with an antibacterial hydroxyapatite obtained by co-substitution of selenium and strontium ions (Se-Sr-HA). Se-Sr-HA was developed by Dr. Muhammad Maqbool, an early stage researcher involved in the same European Doctorate Programme (University of Erlangen, Lucideon Ltd). Novel 2D composite films with different filler percentages were developed and characterized in terms of physical, thermal and antibacterial properties.

4. The fourth objective was the optimization of the melt 3D printing of medium chain length PHAs. Investigation of the degradability of the 3D constructs was performed through an *in vitro* degradation study in PBS. The *in vitro* compatibility of the constructs was also analysed through the evaluation of the viability and differentiation of MC3T3-E1 cells seeded on the scaffolds Finally, the possibility of producing scaffolds with dual porosity was also evaluated through the combination of melt printing and salt leaching.

5. The fifth objective was the development of novel 3D PHA-based antibacterial synthetic bone substitutes. The novel 3D constructs were developed in collaboration with the Orthopaedic Surgery and Traumatology and Cell Therapy Department of the University of Navarra (Pamplona, Spain).

   Two strategies were investigated to achieve this objective:

   a. Development of novel 3D antibacterial composite scaffolds. The structures were obtained using the 2D composite films based on the combination of P(3HO-co-3HD-co-3HDD) and Se-Sr-HA (obtained in Chapter 5) as starting materials for the 3D melt printing. The structures were characterized in terms of physical, biological and antibacterial properties.
   b. Development of novel inherently 3D antibacterial scaffolds. The structures were produced using the 2D inherently antibacterial films obtained through the blending of thioester-PHA with P(3HHx-co-3HO-co-3HD) (obtained in Chapter 4) as the starting materials for the 3D melt printing. The scaffolds obtained were characterized in terms of physical, biological and antibacterial properties.

Chapter 2

Materials and Methods

2.1. Chemicals

All the chemicals were purchased from Sigma-Aldrich (Dorset, UK), VWR (Poole, UK), Thermo Fisher Scientific (Dartford, UK) and Lonza (Slough, UK).

2.2. Bacterial strains and maintenance

Pseudomonas putida KT2442 was obtained from Professor María Auxiliadora Prieto from the Environmental Biology Department, Centro de Investigaciones Biológicas, CSIC, Madrid, Spain. *Pseudomonas mendocina* CH50 was obtained from the National Collection of the Industrial and Marine Bacteria (NCIMB). *Bacillus subtilis* OK2 was obtained from the University of Westminster culture collection. These strains were used for PHAs production and were stored in cryovials at -80º C in a 20% glycerol solution. The bacterial strains were routinely cultured in sterile nutrient broth at 30°C and 200rpm for 16 hours in a shaking incubator. For the antibacterial characterization, *Staphylococcus aureus* 6538P and *Escherichia coli* 8739 were bought from the American Type Culture Collection (ATCC). They were cultured in sterile nutrient broth at 37°C and 200rpm for 16 hours in a shaking incubator and stored in cryovials at -80º C in a 20% glycerol solution.

2.3. Cell lines and maintenance

For *in vitro* studies, MC3T3-E1 subclone 4 (ATCC CRL-2593) mouse cell line was bought from ATCC. MC3T3-E1 mouse cell line was cultured in Alpha Minimum Essential Medium (α-MEM) with 10% (w/v) of foetal bovine serum (FBS) and 1% (w/v) of penicillin/streptomycin solution. The cells were cultured in T75 flasks at 37 °C in 5% CO_2 atmosphere and the media was changed every two days. The cells were passaged upon reaching 70-80% confluence using 3 mL of 0.25% trypsin/EDTA and incubating the cells for 5 minutes. After incubation, 10 mL of media were added, and the cells suspension was centrifuged at 1500 rpm for 5 minutes. The pellet was suspended in fresh media and transferred to a new T75 flask. A sub-cultivation ratio of 1:4 to 1:6 was used.

For long term storage the cell line was preserved in liquid nitrogen. The cells were stored in a freezing medium (95% complete growth medium, 5% dimethyl sulfoxide) at a concentration of approximately 1-2 x 10^6 cells/ mL.

2.4. Polymer production

2.4.1. P(3HB) production

P(3HB) was produced by the controlled fermentation of *B. subtilis* OK2 using glucose as the carbon source (Lukasiewicz *et al.*, 2018). A scheme of the production phases is presented in Figure 2.1. The media composition is shown in Table 2.1. A single colony was used to inoculate sterile nutrient broth (10% of the final volume) which was incubated for 16 hours at 30 °C. The culture was then used for inoculating the production stage which was conducted in a 10 L fermenter for 48 hours with air flow of 1 vvm, agitation speed of 200 rpm and temperature of 30 °C.

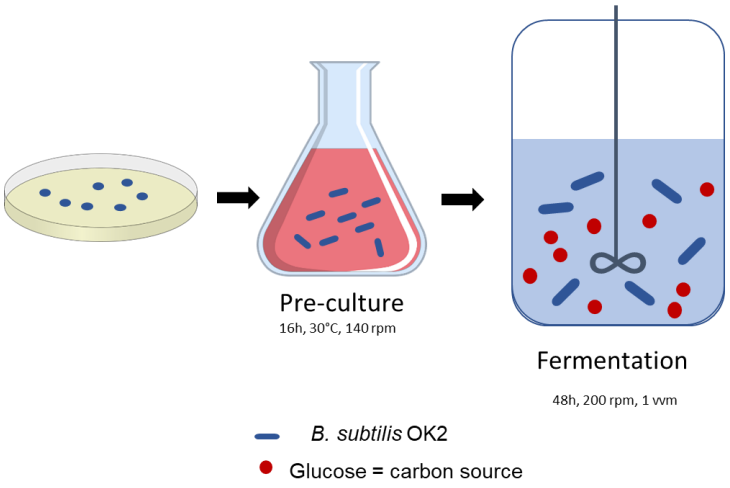

Figure 2.1 Scheme of the production of P(3HB) by *B. subtilis* OK2 using glucose as the carbon source.

Table 2.1 Media composition for P(3HB) production

Method	**Concentration (g/L)**
Yeast extract	2.5
$(NH_4)_2SO_4$	5
KCl	3
Glucose	35
Trace elements solution	1 mL/L

2.4.2. P(3HO-co-3HD) production

P(3HO-co-3HD) was produced via a two-stage fermentation process by *P. mendocina* CH50 using glucose as the carbon source. The scheme of the production of P(3HO-co-3HD) is shown in Figure 2.2. Firstly, a single colony was used to inoculate the nutrient broth, which was incubated for 16 hours at 30 °C at 140 rpm. This media was used to inoculate the second stage mineral salt (MSM) media (Rai *et al.*, 2011b). The cells were cultured for 24 hours at 30 °C at 140 rev/minute in 5 L shaken flasks. Finally, the second stage was used to inoculate the production media (MSM). This final stage was carried out in a 14 L fermenter for 48 hours with air flow of 1 vvm, agitation speed of 200 rpm and temperature of 30 °C. The media compositions are shown in Table 2.2.

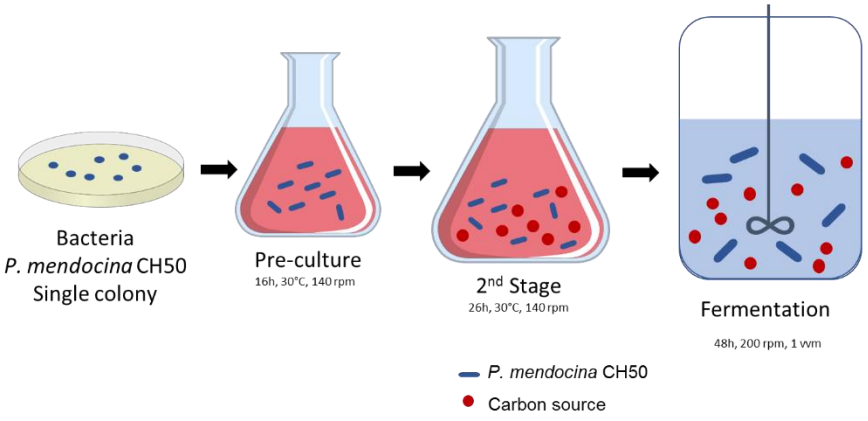

Figure 2.2 Scheme of the production of P(3HO-co-3HD) and P(3HO-co-3HD-co-3HDD) by *P.mendocina* CH50 using either glucose or coconut oil as the carbon sources.

Table 2.2 Media composition for P(3HO-co-3HD) production

Method	**Second stage (g/L)**	**Production stage (g/L)**
KH_2PO_4	0.45	0.5
$(NH_4)_2SO_4$	2.38	2.65
Na_2HPO_4	3.42	3.8
Glucose	20	20
$MgSO_4$	0.8	0.8
Trace elements solution	1 mL/L	1 mL/L

2.4.3. P(3HO-co-3HD-co-3HDD) production

P(3HO-co-3HD-co-3HDD) was produced via a two-stage fermentation process by *P. mendocina* CH50 using coconut oil as the carbon source. The scheme of the production of P(3HO-co-3HD-co-3HDD) is shown in Figure 2.2. Firstly, a single colony was used to inoculate the nutrient broth, which was incubated for 16 hours at 30 °C at 140 rev/minute. This media was used to inoculate the second stage mineral salt media (MSM) (Rai *et al.*, 2011b). The cells were cultured for 24 h at 30 °C at 140 rev/minute in 5 L shaken flasks. Finally, the second stage was used to inoculate the production media (MSM). This final stage was carried out in a 14 L fermenter for 48 hours with air flow of 1 vvm, agitation speed of 200 rpm and temperature of 30 °C. The media compositions are shown in Table 2.3.

Table 2.3 Media composition for P(3HO-co-3HD-co-3HDD) production

Method	**Second stage (g/L)**	**Production stage (g/L)**
KH_2PO_4	0.45	0.5
$(NH_4)_2SO_4$	2.38	2.65
Na_2HPO_4	3.42	3.8
Glucose	20	20
$MgSO_4$	0.8	0.8
Trace elements solution	1 mL/L	1 mL/L

2.4.4. Production of thioester-PHAs

Thioester containing PHAs were produced by *P. putida* KT2442 as described by Escapa *et al.*, 2011. A one-stage fermentation process was employed using the media composition as shown in Table 3. The scheme of the production of thioester-PHAs is shown in Figure 2.3. Firstly, a single colony was used to inoculate the lysogeny broth (LB) medium which was incubated at 30°C for 16 hours. The cells were collected and washed in 0.85% w/v saline solution and adjusted to an optical density at 630 nm (OD_{630}) of 0.15 in the production media. This stage was carried out in 1L shaken flasks (200 mL working volume) at 30 °C and 140 rpm for 24 hours.

Media containing 12 mM decanoic acid, as the sole carbon source, was used as the control condition. The media compositions are shown in Table 2.4.

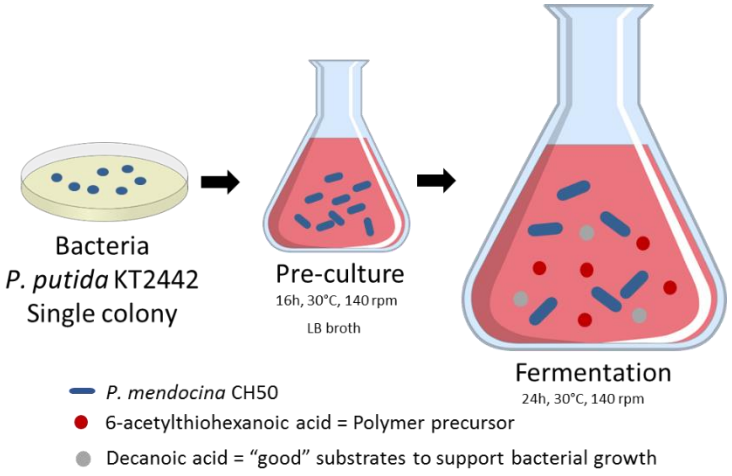

Figure 2.3 Scheme of the production of thioester-PHAs.

Table 2.4 Media composition for thioester- PHA production by *P. putida* KT2442

Chemical	**Second stage (g/L)**
KH_2PO_4	13.6
$(NH_4)_2SO_4$	0.2
$MgSO_4$	0.25
Decanoic acid	2.4 mM
6-acethylthiohexanoic acid	12 mM
Trace elements solution	1 mL/L

2.5. Analytical studies

For P(3HB), P(3HO-co-3HD) and P(3HO-co-3HD-co-3HDD) a temporal profiling of the production was conducted by monitoring optical density, biomass, nitrogen and glucose concentrations, polymer yield, pH and dissolved oxygen tension (DOT) at regular intervals during the course of the fermentation.

Bacterial growth was measured by monitoring the optical density (OD) at 450 nm for *P. mendocina* CH50 and at 600 nm for *B. subtilis* OK2. For biomass and pH measurements, 1 mL of culture was collected and centrifuged at 12,000 rpm for 10 minutes (Heraeus Pico 17 Centrifuge, Thermofisher Scientific, MA, US) in pre-weighted falcon tubes. The pellet was freeze-dried and weighted for biomass content. The pH of the supernatant was measured using the Seven Compact pH meter (Mettler Toledo Ltd., Leicester).

For polymer yield content, 30 mL of culture were collected, centrifuged and the pellet was freeze-dried. The obtained biomass was subjected to extraction by solvent dispersion method (Section 2.6).

The polymer yield was calculated as:

$$Yield\ (\%) = \frac{Wp}{Wb} x\ 100$$

Where W_p is the weight of the polymer after extraction and W_b is the weight of the lyophilized biomass.

The nitrogen content in terms of ammonium ions was estimated by phenol-hypochlorite method following the procedure described in Rai *et al.*, 2011b. 250 µL of the supernatant were incubated with 100µL of nitroprusside reagent and 150µL of alkaline reagent for 45 minutes at room temperature in the dark. The reagents compositions are described in Table 2.5. After the time of incubation, the absorbance was read at 635nm. The amount of ammonium ions was calculated through a calibration curve obtained using ammonium sulphate at known concentrations.

The concentration of glucose in the supernatant was determined using the dinitrosalicylic acid assay (DNS) following the procedure described by Miller, 1959. 1mL of diluted supernatant was incubated with 1mL of the DNS reagent at 90°C for 10 minutes in reaction

tubes. The reagent compositions are described in Table 2.5. At the end of the incubation time, 330µL of 40% sodium potassium tartrate solution were added to each test tubes to stop the reaction. The absorbance was read at 575nm and the concentration of glucose was calculated from the calibration curve.

Table 2.5 Composition of reagents for glucose and nitrogen estimation.

Reagent	**Compound**	**Quantity (g/L)**
DNS reagent	Sodium hydroxide	10.0
	Sodium sulphite	0.5
	Dinitrosalicylic acid	10.0
	Phenol	2.0
Phenol-nitroprusside buffer	Trisodium Phosphate Dodecahydrate	30
	Monosodium citrate	30
	EDTA	60
	Sodium nitroprusside dihydrate	0.2
Alkaline Hypochloride reagent	Sodium hypochlorite	2.5
	Sodium hydroxide	16

2.6. Extraction of PHAs

For all the PHAs produced, the biomass was obtained by centrifugation at 4600 rpm for 30 minutes and then lyophilized and milled into fine powder. Such biomass was then treated with different methods in order to extract the polymer.

2.6.1. Chloroform/sodium hypochlorite dispersion method

For the chloroform/sodium hypochlorite dispersion methods, the biomass was incubated in a solution containing 80% of sodium hypochlorite and chloroform in 1:4 ratio at 30 °C, for two hours at 140 rpm (Rai *et al.*, 2011b; Lukasiewicz *et al.*, 2018). The biomass to sodium hypochlorite solution ratio was 1:16. After incubation, the obtained suspension was transferred to 50 mL Falcon tubes and was centrifuged for 20 minutes at 3900 rpm to allow the formation of three layers. The first two layers contained sodium hypochlorite and cellular debris and were therefore discarded. The bottom layer contained the polymer in solution in chloroform. This layer was precipitated in ice-cold methanol in the ratio 1:10 under continuous stirring at room temperature.

2.6.2. Soxhlet extraction

A two-stage method was employed for Soxhlet extraction (Lukasiewicz *et al.*, 2018). For this method, the biomass was treated with a homogenizer for 15 minutes before lyophilization to induce cell disruption. For the first stage, 20 g of biomass were placed in cellulose thimbles (Whatman 28mmx100mm, GE Healthcare Life Sciences) and extracted with 250 mL of methanol for 24 hours at 80 °C under reflux. For the second stage, the methanol solution was discarded, and the biomass was extracted with 250 mL of chloroform for 48 hours at 70 °C under reflux. The chloroform solution obtained was concentrated using Rotary Evaporator (R-215, Buchi Labortechnick AG, Switzerland) and the polymer was precipitated in cold methanol in the ratio 1:10 under continuous stirring at room temperature.

2.7. Polymer characterization

2.7.1. Fourier Transform Infrared Spectroscopy (FT-IR)

Preliminary characterization of the polymer was carried out using by attenuated total reflectance Fourier transform infrared (ATR-FT-IR) spectroscopy. The analyses were performed in a spectral range of 4000 to 400 cm^{-1} with a resolution 4 cm^{-1} using PerkinElmer FT-IR spectrometer Spectrum Two (PerkinElmer Inc, USA).

2.7.2. Nuclear Magnetic Resonance (NMR)

Structural characterization of the polymer was carried out using ^{13}C-NMR, ^{1}H- NMR and HSQC (Varian NMR System 400MHz Spectrometer) at the University College London. For this analysis, 20 mg of polymer was dissolved in 1 mL of deuterated chloroform.

2.7.3. Gas Chromatography Mass Spectrometry (GC-MS)

Evaluation of the monomeric composition of the produced polymers was conducted through GC-MS analysis. For this analysis, acidic methanolysis was carried out on 20 mg of sample. The sample was dissolved in 2 mL of chloroform and 2mL of 15% of sulphuric acid solution in methanol. 20µL of methyl benzoate was used as the internal standard. The reaction mixture was refluxed for 16hours in the case of mcl-PHAs and for 4h in the case of scl-PHAs. At the end of the reaction period, 2mL of water were added to the mixture. The organic layer was collected and dried over 10mg of sodium sulphate and 10 mg sodium bicarbonate, filtered using Whatmann Grade 1 filter paper and then stored in GC vials (Agilent) at -20°C for further analysis. GC-MS analysis was carried out using Chrompack CP-3800 (Varian Inc, California, USA) and a Saturn 2000 MS/MS workstation. The CP-3800 gas chromatograph was equipped with Elite-5MS capillary column (PerkinElmer, Massachusetts, USA).

2.7.4. Gel Permeation Chromatography (GPC)

The molecular weight of the polymer was determined by Gel Permeation Chromatography analysis (GPC) using PLgel 5µm MIXED-C (300x7.5 mm) column (Agilent). For the analysis 2 mg/mL polymer solution in chloroform was used. The data was analysed using Agilent GPC/SEC software.

2.8. Fabrication of 2D antibacterial solvent casted films

2.8.1. Fabrication of 2D inherently antibacterial films

To develop inherently antibacterial films, blending of thioester-PHA and P(3HHx-co-3HO-co-3HD) was investigated. Control films were obtained by dissolving 0.5 g of P(3HHx-co-3HO-co-3HD) in 10 ml of chloroform (5% w/v) and casting the solution into 60 mm diameter glass Petri dishes. For the blend films, the same polymer weight percentage was maintained with the following ratios: 100:0, 90:10, 80:20 (P(3HHx-co-3HO-co-3HD): thioester-PHA). The films were air dried for 5 weeks at room temperature to allow complete crystallization of the samples (Lizarraga Valderrama *et al.*, 2020).

2.8.2. Fabrication of 2D composite antibacterial scaffolds

For the development of 2D composite antibacterial scaffolds, an antibacterial hydroxyapatite obtained by co-substitution of selenium and strontium ions (Se-Sr-HA) was used. This material was developed by Dr. Muhammad Maqbool, an early stage researcher involved in the same European Doctorate Programme (University of Erlangen, Lucideon Ltd). Se-Sr-HA was synthesized by Dr. Maqbool through a wet-precipitation method, following a similar methodology to the one described by Gritsch *et al.*

For the preparation of composite films, P(3HO-co-3HD-co-3HDD) and P(3HB) were selected. The polymer (5% w/v) was first dissolved in chloroform at room temperature and stirred for 24 hours. The desired amount of filler was added in the polymer solution and the mixture was then sonicated in an ultrasonic water bath (XUBA3 Ultrasonic Bath, Grant Instruments) for 15 minutes. The obtained suspension was then poured in petri-dishes and left to evaporate at room temperature. Composite antibacterial films containing 10, 20 and 30 wt% of Se-Sr-HA were prepared. The films were air dried for 5 weeks at room temperature to allow complete crystallization of the samples (Lizarraga-Valderrama *et al.*, 2020; Lukasiewicz *et al.*, 2018).

2.9. Fabrication of scaffolds by melt 3D printing

3D printed scaffolds for bone regeneration were developed using Cellink's Inkredible+ 3D Bio-printer (Cellink, Goteborg Sweden). P(3HO-co-3HD-co-3HDD) was chosen as the material for the optimization of the parameters for the melt printing of MCL-PHAs. The 3D general printing process is described in Figure 2.4. The polymer was inserted in an aluminium cartridge, heated for 15 minutes before printing and extruded using compressed air. An aluminium cartridge and a stainless-steel nozzle with an inner diameter 0.600 mm were used. Slic3r software was used to define the printing parameters and to generate the G-codes.

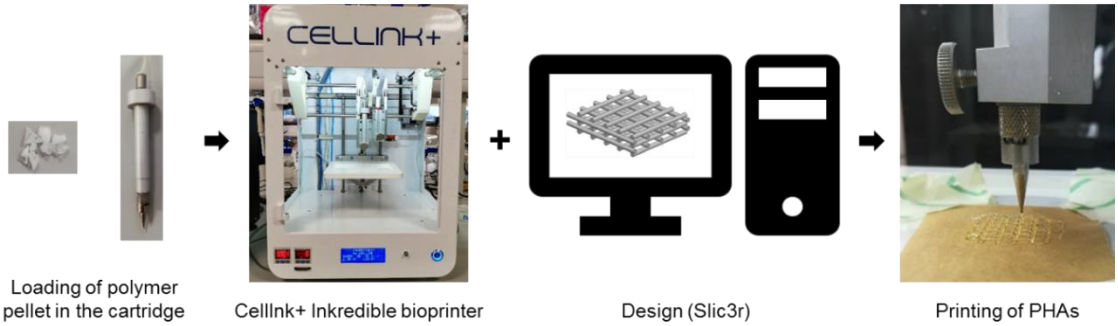

Figure 2.4 Cellink Inkredible+ 3D Bioprinter (on the left) and close up of the aluminium cartridge and stainless-steel nozzle used while printing P(3HO-co-3HD-co-3HDD).

In order to optimize the melt printing of P(3HO-co-3HD-co-3HDD), the following parameters were considered: the writing speed (i.e. movement of the printer head), the melting temperature and the pressure of extrusion. The range of the parameters evaluated are reported in Table 2.6 and were chosen based on literature studies and the intrinsic limitation of the 3D printer used (Domingos *et al.*, 2012; Sheshadri and Shirwaiker, 2015; Hoque *et al.*, 2009). Structures with a rectilinear pattern (0/90° lay down pattern) with a 1.5 mm distance between the filaments (i.e. pore size) and the deposition of 2 layers of materials were used as a template for the optimization, as shown in Figure 2.5 a. The parameters were varied one at the time and the scaffolds obtained were analysed through ImageJ software to determine the filament width. A combination of parameters was considered feasible if a well-defined structure could be obtained, matching that of the implemented design.

Table 2.6 Summary of the parameters investigated in the screening experiment to optimize the melt 3D printing of P(3HO-co-3HD-co-3HDD).

Parameter	Values considered			
Temperature (°C)	80	90	100	110
Velocity (mm/s)	0.5	1	2	4
Pressure (kPa)	50	100	200	-

Using the optimized parameters, scaffolds with different porosities were obtained by changing the filament distances from 1.5 to 0.5 mm. To further investigate the printability of the material, structures using a honeycomb pattern were also printed as shown in Figure 2.5 b.

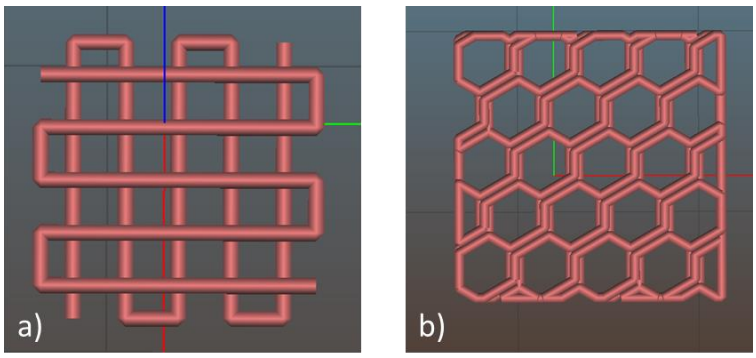

Figure 2.5 2D model obtained using Slic3r software of a) the template used for optimization with a 1.5x1.5 pore size using a rectilinear patter (0/90° lay down patter) and b) the honey-comb pattern used to evaluate the materials printability.

2.9.1. Fabrication of 3D printed scaffolds with dual porosity

To develop scaffolds with dual porosity, 3D printing and salt leaching were combined. Firstly, P(3HO-co-3HD-co-3HDD) was mixed with salt particles of two different sizes and in three different ratios, as described in Table 2.7. The salt particle sizes considered were <100 µm and between 100 and 300 µm, and the ratios of P(3HO-co-3HD-co-3HDD)/NaCl were 50:50, 35:65 and 25:75. The different salt particle sizes were obtained using sieves with a pore size of 100 and 300 µm (Endecotts, London UK). In particular, the salt was firstly sieved using the 300 µm sieve and then sieved again using the 100 µm sieve. The particles obtained after both sieving processes were identified as NaCl size <100 µm. The particles

obtained after the first sieving process (300 µm sieve), that could not pass through the 100 µm sieve were identified as NaCl of size between 100 and 300 µm. Slurry solutions of each composition were obtained by mixing the polymer with NaCl in chloroform and they poured in glass petri dishes to obtain films with a homogeneous distribution of salt. Such films were then used as the starting materials to load in the printer cartridge and printed as described in section 2.9.

The obtained scaffolds were then leached in distilled water for two weeks to remove the porogen.

Table 2.7 Composition of 3D printed scaffolds with dual porosity.

Sample	***Polymer Content (%w/w)***	***NaCl Content (% w/w)***	***NaCl Size (µm)***
50:50 P(3HO-co-3HD-co-3HDD)/$NaCl_{100um}$	50	50	<100
35:65 P(3HO-co-3HD-co-3HDD)/$NaCl_{100um}$	35	65	<100
25:75 P(3HO-co-3HD-co-3HDD)/$NaCl_{100um}$	25	75	<100
50:50 P(3HO-co-3HD-co-3HDD)/$NaCl_{300um}$	50	50	100-300
35:65 P(3HO-co-3HD-co-3HDD)/$NaCl_{300um}$	35	65	100-300
25:75 P(3HO-co-3HD-co-3HDD)/$NaCl_{300um}$	25	75	100-300

2.10. Fabrication of 3D antibacterial scaffolds for bone regeneration

2.10.1. Fabrication of 3D composite structures

Composite melt printed scaffolds were obtained using P(3HO-co-3HD-co-3HDD) and Se-Sr-HA. Firstly, composite films containing 10, 20 and 30 wt% of Se-Sr-HA were obtained as described in section 2.8.2. These films were cut into small pieces (< 5 mm) and then used as the starting material to load in the printer cartridge. The materials were printed using the same process as described in section 2.9.

2.10.2. Fabrication of 3D inherently antibacterial structures

Inherently antibacterial melt printed structured were obtained using P(3HHx-co-3HO-co-3HD) and thioester-PHA. Firstly, films in a ratio 80:20 (P(3HHx-co-3HO-co-3HD): thioester-PHA) were prepared as described in 2.8.1 These films were cut into small pieces (< 5 mm) and then used as the starting material to load in the printer cartridge. The materials were printed using the same process as described in section 2.9

2.11. Characterization of the developed scaffolds

2.11.1. Scanning electron microscopy (SEM)

Scanning electron microscopy analysis was performed to evaluate the surface topography of the samples. The SEM images were taken using a beam of 5keV at 10 cm working distance (JOEL 5610LV-SEM). For the analysis, all the samples were coated with gold for 2 minutes using a EMITECH-K550 gold spluttering device. This analysis was carried out at the Eastman Dental Hospital, University College London.

For 3D printed scaffolds with dual porosity, SEM images were analysed with ImageJ software to evaluate the dimension of the pore created on the surface. For the analyses, three images at the same magnification (200x) were selected for each composition. The built in plugin "Analyse particles" was applied to each image after thresholding it to obtain a black and white image containing only the pores, as shown in Figure 2.6 (Zhou *et al.*, 2015).

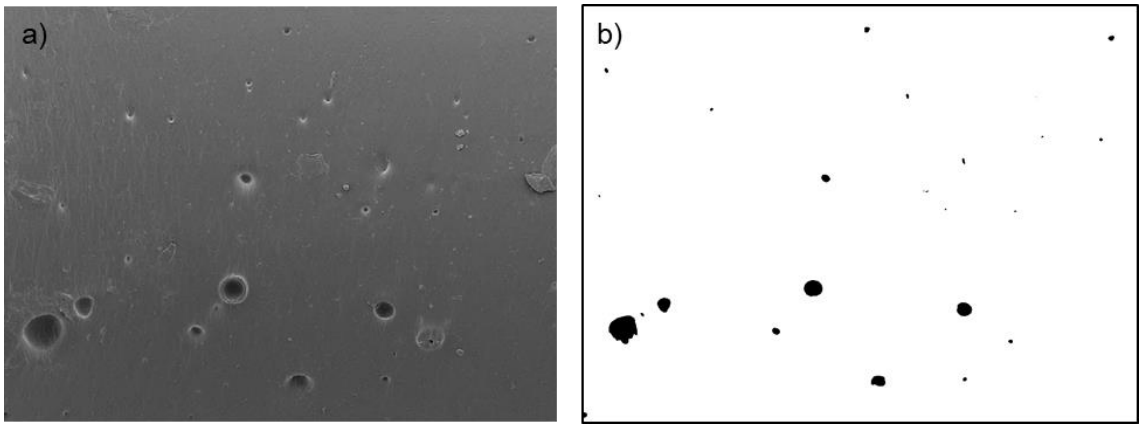

Figure 2.6 SEM image of the surface of 50:50 P(3HO-co-3HD-co-3HDD)/$NaCl_{100um}$ a) before the analyses and b) after analysis using the plugin "Analyse particles" of ImageJ software, highlighting only the pores present on the surface of the material.

2.11.2. Energy-dispersive X-ray spectroscopy (EDX)

Energy-dispersive X-ray spectroscopy was used to perform a qualitative elemental analysis of the materials developed. The samples were prepared as described in section 2.11.1 (SEM analysis). The EDX spectra were taken using a beam of 20 keV at 10 cm working distance (JOEL 5610LV-SEM). The data were analysed using the software IncaEDX Energy System. This analysis was carried out at the Eastman Dental Hospital, University College London.

2.11.3. X-ray microtomography (MicroCT)

MicroCT analysis of 3D composite scaffolds of P(3HO-co-3HD-co-3HDD) containing 10 wt% of Se-Sr-HA was performed to investigate the distribution of the filler inside the constructs. Samples of 2-4mm length and 1 mm width were cut using a surgical blade. A series of X-Ray images were collected by rotating the samples of 180° at a rotational step of 1° (JOEL 5610LV-SEM) and were analysed using the Bruker Micro-CT CTan and CTVox software. This analysis was carried out at the Eastman Dental Hospital, University College London.

2.11.4. Differential Scanning Calorimetry (DSC)

The thermal properties of the 2D neat, composite and blend films aged for 5 weeks were analysed using DSC Polyma (Netzsch, Germany), equipped with Intracooler IC70 cooling system. Two cycles were performed on each specimen under the flow of nitrogen at 60 mL/minute. The first heating ramp was set at 20 °C /minute between -70 °C and 200 °C for scl-PHAs and -70 °C and 130 °C for mcl-PHAs. The second ramp was set at the rate of 10 °C/minute between -70 °C and 210 °C for scl-PHAs and -70 °C and 130 °C for mcl-PHAs (Lizarraga-Valderrama *et al.*, 2015; Lukasiewicz *et al.*, 2018). The melting temperature (T_m), glass transition temperature (T_g) and the enthalpy of fusion (ΔH_m) the samples were calculated using the Proteus 7.0 Analysis Software (Netzsch, Germany).

For composite and blend materials, the enthalpy of fusion was normalized to take into account the weight fraction of the filler (or blend polymer)(w_f) (Suchitra, 2004):

$$\Delta H_{\mathrm{m}}^{n} = \frac{\Delta H\mathrm{m}}{(1 - w_f)}$$

Where $\Delta H_{\mathrm{m}}^{n}$ is the normalized enthalpy of fusion of the material, ΔH_{m} is the enthalpy of fusion of the material and w_f is the weight fraction of the filler (or blend polymer).

For P(3HB)-based samples, the percentage crystallinity of the materials (X_c%) was calculated according to the following formula:

$$X_c\% = \frac{\Delta H\mathrm{m}}{\Delta H^{\circ}} * 100$$

Where ΔH_{m} is the enthalpy of fusion of the material, ΔH° is the enthalpy of fusion for the material with 100% crystallinity, which for P(3HB) is 146 J/g (Ho *et al.*, 2014). In case of composite films, ΔH_{m} was replaced with $\Delta H_{\mathrm{m}}^{n}$.

2.11.5. Mechanical characterization - Tensile Testing

Tensile testing was performed on 2D composite and blend films using Instron 5940 testing system equipped with 500N load cell. 4-5 mm wide and 35 mm long stripes were cut from 5% w/v PHAs films which were obtained through the solvent casting technique (as described in section 2.8.1 and 2.8.2). Before the test, the thickness and the width of each specimen were measured in different areas using a stainless steel digital caliper for the determination of the cross-sectional area. The gauge length of the sample holder was 23 mm. A deformation rate of 10 mm/minute was applied for mcl-PHAs, while 5 mm/minute was used for scl-PHAs (Lukasiewicz *et al.*, 2018; Lizarraga-Valderrama *et al.*, 2020). The data were acquired and analysed using a BlueHill 3 software. The elastic modulus (E), ultimate tensile stress (σ_u) and elongation at break (ε_b) were calculated for each sample.

2.11.6. *In vitro* Degradation Studies

Degradation studies were conducted on 3D P(3HO-co-3HD-co-3HDD) scaffolds by incubating the samples in 3 mL of PBS at 37°C for 1,2,3,4, 5 and 6 months. 1x 1 cm samples were cut using a surgical blade and their weight was recorded. After each time point, the samples were weighted after being passed on blotting paper to remove the excess of water. The samples were then dried out at room temperature until no variation of weight was evidenced.

Two parameters were evaluated:

- The percentage water uptake (%WU), connected to the capacity of swelling:

$$\%WU = \frac{Wf}{Wi} * 100$$

Wi: initial hydrated weight, Wf: final hydrated weight

- The percentage dried weight variation (%DWV), connected to the solid part loss:

$$\%DWV = \frac{DWf}{DWi} * 100$$

DWi: initial dried weight, DWf: final dried weight

The dried samples were also analysed with respect to their thermal properties (DSC) and molecular weight variation (GPC).

2.11.7. Porosity studies

The porosity of the 3D printed scaffolds with dual porosity was measured using the gravimetric method, following an adapted method described by Kim *et al.*, 2017. For the test, 5x5 mm scaffolds with a pore size of 1.5x1.5 mm were cut using a surgical blade. The % porosity of the scaffolds struts was calculated using the following formula:

$$\%\mathrm{P} = \left(1 - \frac{\rho_s}{\rho_c}\right) * 100$$

Where ρ_s represents the apparent density of the dual porosity scaffolds and ρc is the density of the neat scaffolds (3D P(3HO-co-3HD-co-3HDD)), calculated as follow

$$\rho = \frac{W}{V}$$

Where W is the weight of the scaffolds and V the volume. The volume was calculated by measuring both external and internal dimensions of each sample. In this way only the porosity of the filament struts was obtained, without considering the macro porosity obtained with the 3D printing design used (i.e.40% due to 4 pores of 1.5 x 1.5 mm pore size).

2.12. Biological characterization

2.12.1. Sample sterilization

For both antibacterial and *in vitro* cell compatibility studies the samples were sterilized prior to the test. Each sample was transferred in a 96 or 24 multiwell plate (accordingly to the size) and covered with 70% ethanol solution for 30 minutes. The ethanol solution was removed and the samples were left to dry for 24 hours. The samples were then subjected to UV sterilization at 254 nm for 15 minutes on each side.

2.12.2. Antibacterial characterization

2.12.2.1. Direct contact test - ISO 22196

The antibacterial properties of the materials produced were evaluated following the ISO 22196.

For thioester PHAs, polyethylene terephthalate (PET) discs of 6 mm of diameter were coated with 2% w/v) chloroform solutions of thioester-PHA or P(3HHx-co-3HO-co-3HD) by solvent casting. 20 µL of the polymer solution were applied over the PET disk and allowed to dry for 72 h at room temperature (Dinjaski *et al.*, 2014). For 2D inherently antibacterial and composite antibacterial films, samples 6 mm in diameter were cut out using a puncher. For 3D composite and blend samples, samples of 4 x 4 mm were cut using a surgical blade. All the samples were sterilized by UV light for 15 minutes and placed onto agar plates. *S. aureus* 6538P or *E. coli* 8739 were incubated in sterile Mueller Hinton Broth at 37 °C for 16 hours. After the incubation time the inoculum was adjusted to a concentration of 3-10 $x10^5$ CFU/mL in 1/500 Nutrient Broth. 10 µL (for 2D samples) or 20 µL (for the 3D samples) of *S. aureus* 6538P or *E. coli* 8739 inoculum were pipetted directly on the surface of each sample. The samples were incubated in static conditions at 37 °C for 24 hours. For the thioester PHAs, PET discs without polymer coating were used as controls, while for the 2D inherently antibacterial samples and 3D and 2D antibacterial composites, 3D and 2D neat samples were used. After the incubation time, each sample was collected in an Eppendorf tube using 90 µL sterile phosphate buffer saline (PBS) and vortexed three times for one minute. Several 10-fold dilutions were performed using PBS and 10 µL of each dilution were plated in triplicate on nutrient agar plates using the drop plate technique (Herigstad *et al.*,

2001). When the drops where completely dried, the plates were inverted and incubated at 37 °C in static conditions for 16 hours. The number of viable cells was evaluated by colony counting considering the dilution factor and normalised to the surface area. The antibacterial activity (R) was expressed using the following formula, according to the ISO 22196 standard:

$$R = \log(U) - \log(T)$$

Where *U* is the number of viable bacteria, in CFU/cm^2, recovered from the control specimens after 24 h, *T* is the number of viable bacteria, in CFU/cm^2, recovered from the treated test specimens after 24 hours.

The results were also expressed as the % reduction of the number of cells, which was calculated using the formula:

$$R(\%) = \frac{U - T}{U} * 100$$

2.12.2.2. Minimal inhibitory concentration (MIC) and Minimal Bactericidal Concentration (MBC)

Se-Sr-Ha antibacterial activity was investigated using the ISO 20776 against *Staphylococcus aureus* 6538P and *Escherichia coli* 8739. A range of concentration of the material in powder form (5-100 mg/mL) prepared in MH broth was incubated with a microbial suspension adjusted to achieve a final concentration of 5 x 10^5 CFU/ml and incubated at 37ºC for 24 hours at 100 rpm in 96 multi-well plates (final volume 100 µL). After the incubation time, the OD_{600} of the wells was measured to determine the concentration of the Se-Sr-HA able to inhibit the growth (minimal inhibitory concentration – MIC) of each bacteria strain. The OD was measured using the Spectrostar Nano Microplate Reader (Bmg Labtech, Germany). Following the MIC test, the entire volume (100 µL) of the well containing the concentration of Se-Sr-HA identified as the MIC and of the wells with a concentration higher than the MIC were spread evenly onto agar plates. The plates were incubated 37ºC for 16-20 hours. To quantify the reduction in the number of bacteria for the highest concentration of Se-Sr-HA investigated (i.e. 100 mg/mL), several 10-fold dilutions were performed using PBS and 10 µL of each dilution were plated in triplicate on nutrient agar plates using the drop plate technique (Herigstad *et al.*, 2001). When the drops where completely dried, the plates were inverted and incubated at 37 °C in static conditions for 16 hours. After the incubation time,

the colony forming units were counted and compared to the CFU/mL of the initial inoculum. The MBC was determined as the lowest concentration of compound that induced 99.9% killing of the bacteria.

2.12.2.3. Antibacterial ion release studies

Antibacterial ion release studies were performed on all the samples containing Se-Sr-HA, following an adapted method described by Cao *et al.*,2017. For 2D inherently antibacterial and composite antibacterial films, samples of 6 mm of diameter were cut out using a puncher. For 3D composite and blend samples, samples of 5 x 5 mm were cut using a surgical blade. All the samples were sterilized by UV light for 15 minutes. The 2D film samples were incubated in 1 mL of Mueller Hinton broth at 37 °C for 1, 3, 6 and 24 hours, while the 3D samples for incubated for 1, 3 and 7 days. After each time point, the media with the eluted agent/ion was collected and replaced with fresh media.

S. aureus 6538P or *E. coli* 8739 were incubated in sterile Mueller Hinton broth at 37 °C for 16 hours. 180 µL of the eluates obtained from the materials were incubated with 20 µL of the microbial suspension adjusted to 10 x 0.5 McFarland and incubated for 24h at 37°C. After 24h, the absorbance at 600 nm was measured using Spectrostar Nano Microplate Reader (Bmg Labtech, Germany). The control consists of MH broth incubated for the same time period with 2D or 3D neat samples.

The antibacterial activity was calculated as the % reduction of the OD at 600 nm compared to the positive control (% bacterial cells killed) using the following formula:

$$\%\ OD_{600}\ reduction = \frac{(OD_c - OD_s)}{OD_c} * 100$$

OD_c is the optical density at 600 nm of the control samples and OD_s is the optical density at 600 nm of the sample.

2.12.3. *In vitro* cell compatibility studies

2.12.3.1. Indirect cytotoxicity

Material indirect cytotoxicity of all the produced materials was investigated following an adapted ISO 10993-5 procedure for the biological evaluation of medical devices. All the samples were incubated with 200 µl of α-MEM for 24 hours at 37° C in an atmosphere of

5% CO_2. For PHAs films, samples of 6 mm diameter were cut out using a puncher. For 3D composite and blend samples, samples of 5 x 5 mm were cut using a surgical blade. For thioester-PHAs, PET disks of 6 mm diameter were coated with 2% (w/v) chloroform solutions of thioester-PHA or P(3HHx-co-3HO-co-3HD) (as described in section 2.12.2.1). 30000 cells/well were seeded in a 96-well plate and incubated overnight. The following day, the media was removed and replaced with the eluates obtained from the materials. The cells were cultured at 37° C in an atmosphere of 5% CO_2. The control consists of cells cultivated in the same conditions with non-conditioned medium. After 24 hours the media was replaced with 150 µL 10% (w/v) Alamar blue solution, incubated for 3 hours and the absorbance was read at 570 nm and 600 nm (FluoStar Optima plate reader, SMG Labtech). The cell viability of the samples was compared to that of the control using the following equation:

$$\%\ cell\ viability = \frac{(O_2 * A_1) - (O_1 * A_2)}{(O_2 * P_1) - (O_1 * P_2)} * 100$$

Where O_1 is the molar extinction coefficient of oxidized Alamar Blue at 570 nm, O_2 is the molar extinction coefficient of oxidized Alamar Blue at 600 nm, A_1 is the absorbance of the samples at 570 nm, A_2 is the absorbance of the samples at 600 nm, P_1 is the absorbance of the positive control (cells cultured on tissue culture plastic) at 570 nm and P_2 is the absorbance the positive control (cells cultured on tissue culture plastic) at 600 nm.

2.12.3.2. Direct cytocompatibility

Quantitative evaluation of the cell viability after direct contact with the materials was conducted following an adapted protocol described by Basnett *et al*, 2017b. The samples were prepared as described in the previous section. The materials were incubated in 200 µL of media for 24 hours. After the incubation time, each sample was seeded with a cell seeding density of 70000 cells/cm^2. The samples were incubated for 1, 3 and 7 days at 37 °C in an atmosphere of 5% CO_2. After each time point Alamar blue assay was performed to evaluate cell viability. The media was removed, replaced with 150 µl 10% (w/v) of Alamar blue solution and incubated for 3 h and the absorbance was read at 570 nm and 600 nm (Spectrostar Nano microplate reader, BmgLabtech). The data were analysed as described in the previous section. The controls consist of cell cultivated on tissue culture plastic for the same time points.

2.12.3.3. SEM analysis

After the direct compatibility tests, the samples were analysed using SEM (section 2.11.1) to evaluate the cell morphology and proliferation on the materials. To prepare the samples for the analysis, after the Alamar Blue assay the supernatant was removed and replaced with 4% w/v % formaldehyde solution to fix the cells on the materials and stored at 4°C. A day before the SEM, the samples were dehydrated using a series of ethanol concentrations in distilled water (50%, 60%, 70%, 80%, 90% and 100% ethanol) and let to dry overnight under a fume cupboard.

2.12.4. Live and dead analysis

Live/dead viability assay was done using fluorescence dyes, such as: Calcein AM and Ethidium homodimer-1. Calcein-AM is used to determine viable cells, by conversion of non-fluorescent form of Calcein, present in live cells to green fluorescent form by an intracellular esterase. Ethidium homodimer-1 emits red fluorescence while intercalated within the DNA of dead cells. After growing the cells for 7 days on the polymer scaffolds, the culture medium was removed and cells rinsed with Dulbecco's Phosphate Buffered Saline (DPBS). Then 300 µL of working solution, which contains 2 µM Calcein AM and 4 µM Ethidium homodimer-1 in DPBS were added directly to cells and incubated for 30-45 minutes in the absence of light at room temperature (ThermoFisher Scientific LIVE/DEAD™ Viability/Cytotoxicity Kit Protocol). Following incubation, about 2mL of the DPBS was added to a 6 well plate. The samples were imaged using 40x objective under the confocal microscope (Leica TCS SP2).

2.12.5. *In vitro* cell differentiation studies

Differentiation studies of MC3T3-E1 cells were conducted on 3D P(3HO-co-3HD-co-3HDD) scaffolds. Samples of 5x5 mm were cut using a surgical blade and incubated in α-MEM with 10% (w/v) of foetal bovine serum (FBS) and 1% (w/v) of penicillin/streptomycin solution (complete medium) for 24 hours. After the incubation time, each scaffold was seeded with cell seeding density of 70000 cells/cm^2 and incubated with 200 µL of complete medium for 24 hours. The media was then removed and replaced with 200 µL of osteogenic media (α-MEM complete medium supplemented with 50 µg/mL of ascorbic acid and 10 mM of β-glycerophosphate) (Hwang and Horton, 2019). The samples

were then incubated for 1, 7, 14 and 21 days. At each time point cell viability was tested using Alamar Blue solution as described in section 2.12.3.1. The tests described in the following sections were also performed to evaluate the ability of the materials to favour the differentiation of MC3T3-E1 cells into osteoblasts.

2.12.5.1. Alkaline phosphatase and DNA quantification – Sample preparation

The samples were prepared following an adapted protocol by Yu *et al*., 2017 and Gothard *et al.*, 2015. At each time point the media was removed and the scaffolds were washed twice in PBS. The samples were fixed using 200 µL of 4% formaldehydes solution for 30 minutes. The fixing solution was removed, and the materials were washed twice with PBS and air dried for 30 minutes. 150 µL of 0.05% Triton X solution was added to each well and the plate was incubated at -20 °C overnight. In order to lyse the cells, the freeze-thaw lysis method was employed. The plate was thawed at 37°C for 30 minutes and subsequently frozen at -20°C for 30 minutes. This process was repeated 3 times. At each thawing stage the obtained suspension was mixed 3 times. The supernatant was then used for alkaline phosphatase and DNA quantification as described in the two sections below.

2.12.5.2. DNA quantification

The quantification of double stranded DNA (dsDNA) was performed using the PicoGreen Assay (ThermoFisher Scientific). 10 µL of the cell lysate obtained as described in previous section were mixed with 90 µL of 1X Tris/EDTA buffer. 100 µL of PicoGreen working solution were added in each well and incubated for 5 minutes in the dark. The fluorescence emission was read using an excitation wavelength of 480 nm and an emission of 520 nm (FluoStar Optima plate reader, SMG Labtech). The quantity of DNA was obtained using a calibration curve of the DNA standard provided in the kit at a concentration 0-1 mg/mL.

2.12.5.3. Alkaline phosphatase (ALP) quantification

The ALP activity of MC3T3-E1 cells seed on the scaffolds was determined as described by Yu *et al*., 2017 and Gothard *et al.*, 2015. 10 µL of the cell lysate obtained as described in section 2.12.5.1 were mixed with 90 µL of 3.6 mM *p*-Nitrophenyl phosphate (*p*NPP) substrate solution in 0.5 Alkaline buffer solution. The samples were incubated for 1 hour at 37°C. After the incubation time, 100 µL of 1M NaOH were added in each well to terminate

the reaction. The absorbance of the solution was read at 410 nm using the Spectrostar Nano Microplate Reader (Bmg Labtech, Germany). The ALP activity of each sample was calculated using a calibration curve obtained with p-nitrophenol standards. The final ALP activity of cells in nmol was normalized to the total content of DNA (ng) present in each sample.

2.12.5.4. Mineralization – Alizarin red S (ARS)

The deposition of calcium was evaluated through Alizarin red S (ARS) staining of scaffolds seeded with MC3T3-E1 cells following an adapted protocol by Stanford *et al.*,1995 and Lu *et al.*, 2013. At each time point, the media from each sample was removed and the materials were washed twice in ultra-pure water. The samples were fixed using 200 µL of 4% formaldehydes solution for 30 minutes. The fixing solution was removed and the materials were washed twice with PBS. 150 µL of 50 mM ARS solution were added on each scaffold for 20 minutes at 37 C. After the incubation time, the solution was removed and the samples were washed five times in ultra-pure water. In order to quantify the calcium deposition, 150 µL of 10% w/v cetylpyridinium chloride in 10 mM sodium phosphate solution were added to each sample and incubated for 1 hour at 37 °C. The absorbance was read at 540 nm using Spectrostar Nano Microplate Reader (Bmg Labtech, Germany).

2.13. Statistical analysis

All measurements were made in triplicate, and data are presented as mean values ± standard deviation. One-way Anova and Student's t-test were performed with GraphPad Prism 7 software and differences were considered statistically significant when the *p*-values resulted lower than 0.05. Tukey post-hoc test was conducted between two or more groups to determine if there were statistically significant differences between populations In particular, *p*-value<0.05 (*), *p*-value <0.01 (**), *p*-value <0.001 (***) and *p*-value <0.0001 (****).

Chapter 3

Production of scl and mcl- PHAs

3.1. Introduction

Polyhydroxyalkanoates are a family of polyesters produced by bacterial fermentation that have attracted attention in recent years as possible alternative to synthetic petroleum-derived polymers.

PHAs are usually produced under unbalanced growth conditions, i.e. excess of carbon source and limitation of nutrients (e.g. nitrogen), and they are stored as granules inside the cells as carbon reserves. Based on the type of carbon source and the species of bacteria utilized for the production, two classes of PHAs can be obtained, scl-PHAs and mcl-PHAs. The former contains 3-5 carbon atoms in their monomeric units, while the latter is characterized by 6-14 carbon atoms (Sudesh *et al.*, 2000). Scl-PHAs can be produced by both Gram negative (e.g. *C. necator*) or Gram positive (e.g. *Bacillus* species) bacteria. The latter have the advantage of lacking the outer layer composed of proteins and lipopolysaccharides that are known pyrogen and immunogens (Chen and Wu, 2005). Moreover, the FDA identified most *Bacillus* sp. as safe, including the one used in this study *B. subtilis* OK2 which is a GRAS organism (Generally Recognized As Safe) (Sewalt *et al.*, 2016). *Bacillus* sp. are able to accumulate scl-PHAs from unrelated carbon sources, using both simple (e.g. glucose) and complex (e.g. molasses) carbohydrates (Mohapatra *et al.*, 2017). *Pseudomonas* species are the main producer of mcl-PHAs (Tortajada *et al.*, 2013). Such bacteria are able to utilize both structurally related (e.g. fatty acid) and unrelated carbon sources (e.g. carbohydrates) for the production of PHAs (Zinn and Hany, 2005; Sun *et al.*, 2007; Rai *et al.*, 2011a). PHAs have recently attracted interest in the medical field for their biocompatibility and biodegradability (Chen and Zhang, 2018; Koller, 2018; Valappil *et al.*, 2006; Ali and Jamil, 2016). They have been used for a variety of applications as medical devices, e.g. drug delivery systems, vascular grafts, wound dressings and nerve conduits. Among the PHAs produced P(4HB),

Poly-4-hydroxybutyrate obtained FDA approval in 2007 for its use as a suturing material and has been applied for the fabrication of meshes for the repair of ligament, tendon and hernia (Williams *et al.*, 2013). Bacterial polyesters have shown to be able to favour the attachment, growth and proliferations of cells for regeneration of a range of tissues both *in vitro* and *in vivo*, including bone, cartilage, nerve and skin (Chen and Wu, 2005; Valappil *et al.*, 2006; Brigham and Sinskey, 2012; Lim *et al.*, 2017).

PHAs have shown advantages in comparison with conventional plastics. Firstly, they are biobased polymers that are obtained from renewable resources, hence representing a valid alternative to petroleum-based plastic. Upon degradation, these polymers result in less acidic products compared to other biobased synthetic polyesters (e.g. PLA), reducing the risk of lowering the pH of the tissue and the subsequent possibility of evoking a late inflammatory response (Kim *et al.*, 2007; Lee *et al.*, 2012; Wu *et al.*, 2015b; Ali and Jamil, 2016). However, one of the main disadvantages of the use of PHAs is associated with their production costs, not yet comparable to the synthetic materials (Sun *et al.*, 2007). Two aspects affect mainly the total price of such polymers, the carbon source and the down streaming process. In particular, the former accounts for 50% of the total price of the PHA production (Kumar and Kim, 2018). For this reason, recent research has been focusing on the use of cheap carbon feedstocks. The production of PHAs has been investigated using a range of inexpensive carbon substrates, including biodiesel waste and molasses (Tsuge, 2002; Favaro *et al.*, 2019). Among the alternatives, plants oils are suitable for mcl-PHA production as they are characterized by a mixture of fatty acids (Ciesielski *et al.*, 2015). Higher polymer yields using such oils should be achieved compared to the use of sugars, as plants oils are characterized by a higher carbon to weight ratio. Moreover, such materials are also usually less expensive than common carbohydrates (Chee *et al.*, 2010; Ciesielski *et al.*, 2015).

In this chapter, the production of three PHAs was investigated. Two mcl-PHAs were produced by *P. mendocina* CH 50 using two carbon sources glucose and coconut oil and one scl-PHA was produced by *B. subtilis* OK2 using glucose as the carbon source. The production process was monitored and controlled throughout the course of the fermentation. The polymers produced were characterized in terms of chemical, physical, thermal and mechanical properties. Finally, as the main aim of this project is the development of scaffold for bone tissue engineering, the *in vitro* cytocompatibility of the produced materials was investigated using a pre-osteoblast cell line.

3.2. Results

3.2.1. Production of PHAs by *P. mendocina* CH50 using glucose as the carbon source

The temporal profiling of the production by *P. mendocina* CH50 using glucose as the carbon source carried out in 10 L fermenters is shown in Figure 3.1.

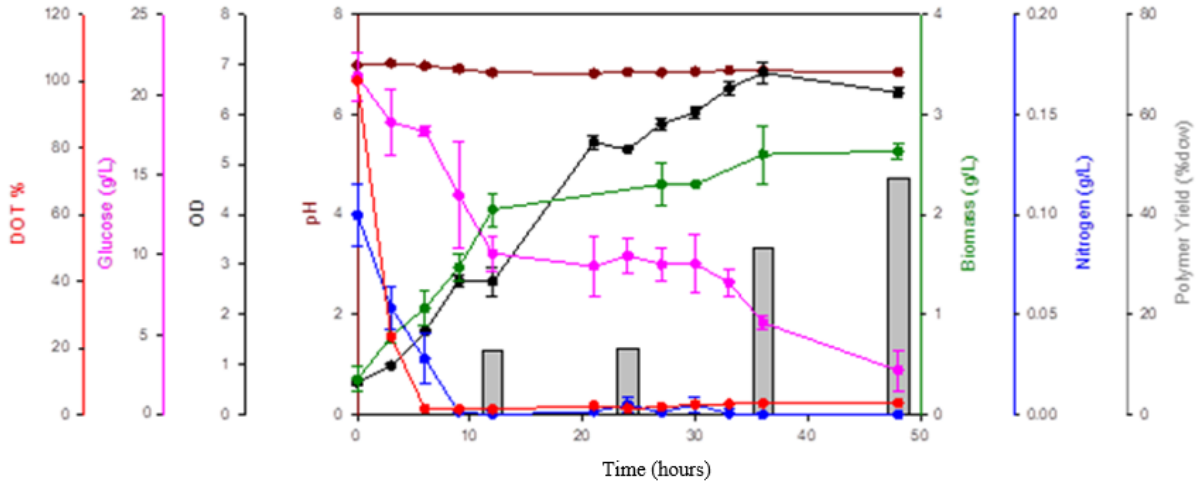

Figure 3.1 Temporal profile of PHA production by *P. mendocina* CH50 using 20 g/L of glucose as the carbon source conducted in a 10 L fermenter for 48 hours. Polymer yield (%dcw, grey bars), OD_{450}(black line), pH (dark red line), glucose concentration (g/L, pink line), nitrogen concentration (g/L, blue line), biomass concentration (g/L, green line), dissolved oxygen tension (DOT %, red line).

The OD_{450} increased constantly during the course of the fermentation reaching a maximum value of 6.8 at 36 hours. The biomass concentration increased gradually during the course of fermentation reaching a maximum value of 2.7 g/L after 48 hours. Nitrogen was completely utilized after 9 hours indicating that nitrogen limiting conditions were achieved during the fermentation, necessary for polymer accumulation. The dissolved oxygen tension (DOT%) decreased during the first hours of the fermentation process reaching 0% after 9 hours. Glucose was consumed over the course of the process, starting from 20 g/L and reaching a final value of 4 g/L. Finally, the polymer yield increased during the process, reaching a final value of 47 % dcw.

3.2.2. Production of PHAs by *P. mendocina* CH50 using coconut oil as the carbon source

The temporal profiling of the production by *P. mendocina* CH50 using coconut oil as the carbon source in a 10L fermenter is shown in Figure 3.2.

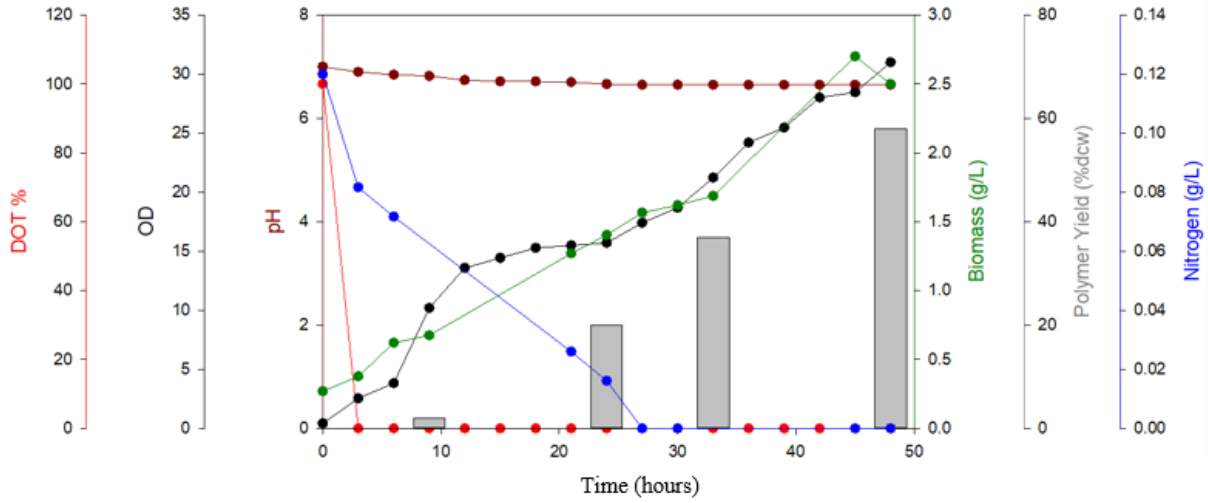

Figure 3.2 Temporal profile of PHA production by *P. mendocina* CH50 using 20 g/L of coconut oil as the carbon source conducted in a 10 L fermenter for 48 hours. Polymer yield (%dcw, grey bars), OD_{450}(black line), pH (dark red line), nitrogen concentration (g/L, blue line), biomass concentration (g/L, green line), dissolved oxygen tension (DOT %, red line).

A gradual increase of the optical density (OD_{450}) could be noticed throughout the course of the fermentation, reaching a maximum value of 31.0 at 48 hours. A similar trend could be detected for the biomass concentration up to 45 hours, reaching a maximum value of 2.7g/L; then the concentration decreased to 2.5g/L at 48 hours. The pH of the production slightly decreased during the fermentation, from 7 to 6.6. Nitrogen was completed depleted during the first 27 hours of the fermentation, starting from a concentration of 0.12 g/L. This data showed that the fermentation after 27 hours was carried out under nitrogen limiting conditions. The dissolved oxygen tension (DOT%) decreased drastically during the first hour of the process from 100% to 0%. Finally, the polymer content increased gradually from 1.5 % dcw at 9 hours to maximum of 58 % dcw after 48 hours.

3.2.3. Production of PHA by *B. subtilis* OK2 using glucose as the carbon source

The temporal profiling of *B. subtilis* OK2 using glucose as the carbon source is shown in Figure 3.3.

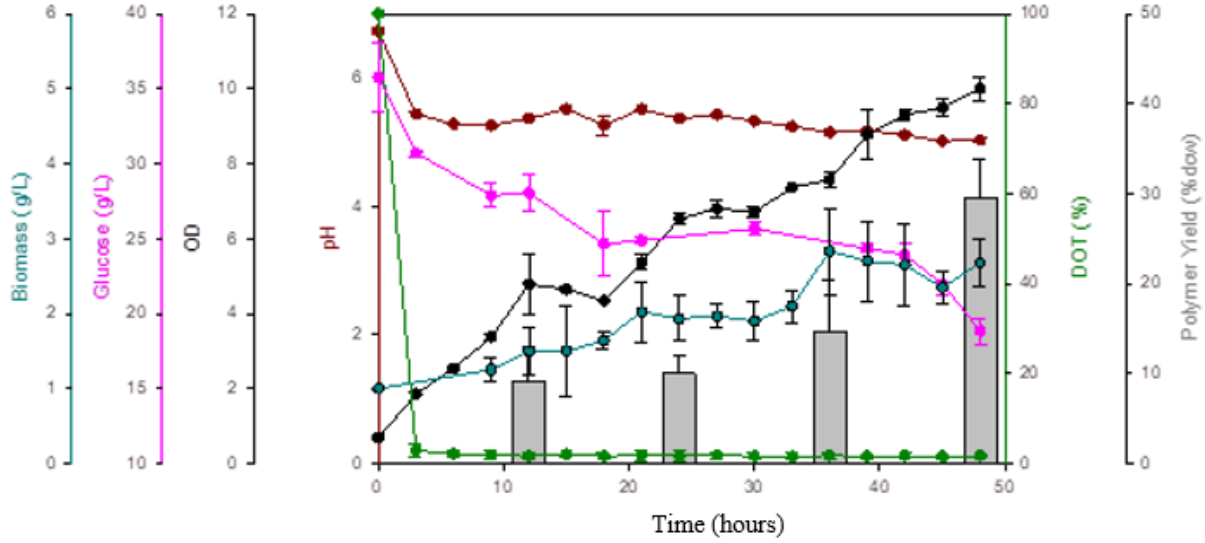

Figure 3.3 Temporal profile of PHA production by *B. subtilis* OK2 using 35 g/L of glucose as the carbon source in a 10 L fermenter for 48 hours. Polymer yield (%dcw, grey bars), OD_{600}(black line), pH (dark red line), glucose concentration (g/L, pink line), biomass concentration (g/L, blue line), dissolved oxygen tension (DOT %, green line).

The OD_{600} increased steadily during the course of the fermentation reaching a final value of 10 after 48 hours. The biomass increased as well reaching a maximum value of 3 g/L at 36 hoursand then remained constant. The DOT% decreased drastically the first three hours of fermentation from 100% to 0%. Glucose was consumed throughout the fermentation process reaching a final value of 19 g/L. The pH of the media decreased as well from 6.8 to 5.2. Finally, the polymer yield was maximum at 48 hours with a value of 30% dcw.

3.2.4. Polymer characterization

3.2.4.1. Chemical characterization

Preliminary characterization of the polymers produced was carried out using FT-IR and are reported in Figure 3.4. In all the spectra the characteristic peak related to the stretching of the carbonyl group (1720-1740 cm^{-1}) in the ester bond was present, confirming that the polymers

produced are polyesters (Randriamahefa *et al.*, 2003). In particular for the polymers produced by *P. mendocina* CH50 the peak were at 1727 cm^{-1}, while for *B. subtilis* OK2 at 1720 cm^{-1}. The shift of this peak is a first indication of the different nature of the two PHAs. Higher values are due to an higher amorphous composition of the material and are associated with mcl-PHAs, while a lower value of the wavenumber is an indication of higher crystallinity related to scl-PHA (Kann *et al.*, 2014). The area around 2900 cm^{-1}, is related to the stretching of carbon-hydrogen bond of methyl and methylene group (CH_3, CH_2). Such an area is more prominent for mcl-PHAs than scl-PHAs, confirming the hypothesis that *P. mendocina* CH50 and *B. subtilis* OK2 produced two mcl-PHAs and a scl-PHA respectively (Kann *et al.*, 2014; Randriamahefa *et al.*, 2003).

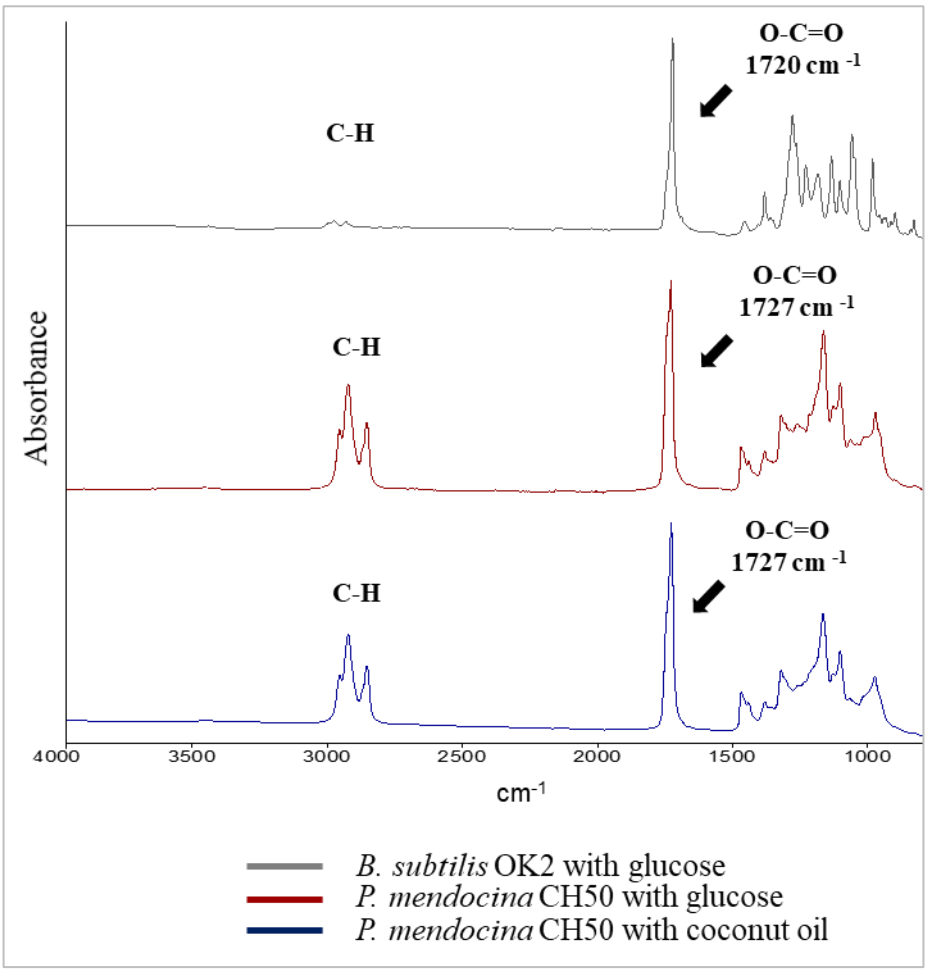

Figure 3.4 FT-IR spectra of the PHA produced by *B. subtilis* OK2 using glucose as the carbon source (grey), *P. mendocina* CH50 using glucose as the carbon source (red) and *P. mendocina* CH50 using coconut oil as the carbon source (blue).

The monomeric composition of the polymers produced was investigated using GC-MS. For *P. mendocina* CH50 cultured using glucose, the spectra shown in Figure 3.5a shows the presence of two peaks at 7.655 minutes and 9.199 minutes. Using NIST the peaks were identified as the methyl esters of 3-hydroxyoctanoic acid and 3-hydroxydecanoic acid. Thus, the polymer produced by *P. mendocina* CH50 using glucose as the carbon source was identified as the copolymer of 3-hydroxyoctanoate and 3-hydroxydecanoate, Poly(3-hydroxydecanoate-co-3-hydroxydodecanoate) or P(3HO-co-3HD). For the polymer produced using coconut oil, three peaks were detected at 6.745, 9.204 and 10.622 minutes (Figure 3.5b). These peaks were identified MS (NIST) library as methyl ester of 3-hydroxyoctanoic acid, 3-hydroxydecanoic acid and 3-hydroxydodecanoic acid. Thus, the polymer produced by *P. mendocina* CH50 using coconut oil as carbon source was identified as the terpolymer of 3-hydroxyoctanoate, 3-hydroxydecanoate and 3-hydroxydodecanoate, Poly(3-hydroxyactanoate-co-3-hydroxydecanoate-co-3-hydroxydodecanoate) or P(3HO-co-3HD-co-3HDD).

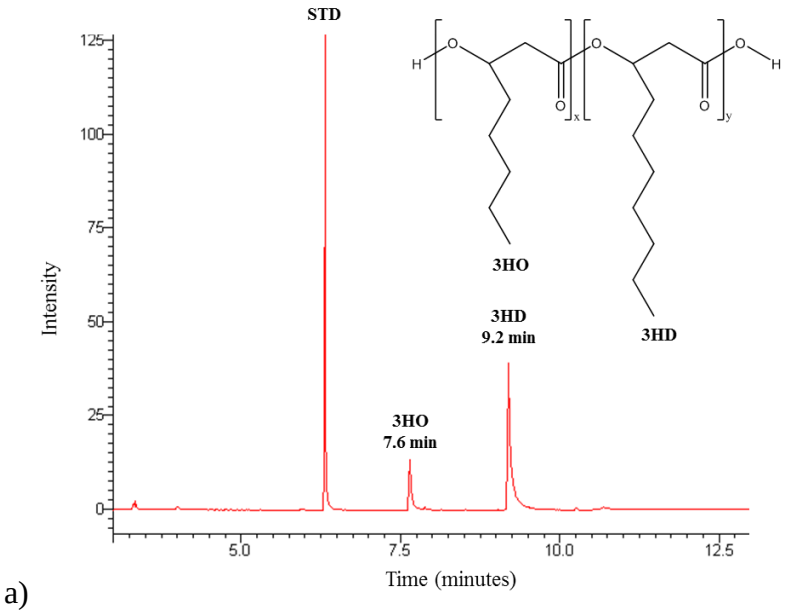

a)

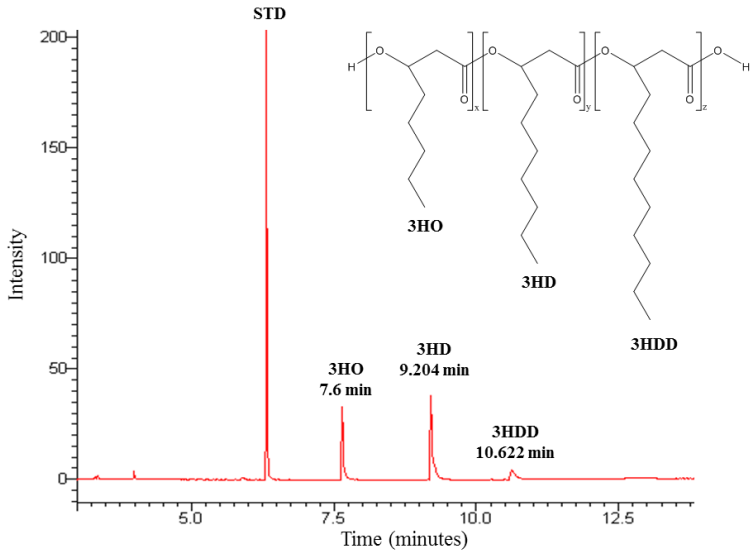

b)

Figure 3.5 Gas chromatogram of a) P(3HO-co-3HD) and b) P(3HO-co-3HD-co-3HDD). In both graphs the peaks at R_t = 7.6 and 9.2 minutes were identified using NIST library as the methyl esters of 3-hydroxyoctanoic acid (3HO) and 3-hydroxydecanoic acid (3HD) respectively. In graph b) the peak at R_t= 10.6 minutes was identified as the methyl esters of 3-hydroxydodecanoic acid (3HDD) Methyl benzoate was used as the internal standard (STD).

Gas chromatogram of reference standards of methyl esters of 3- hydroxyalkanaotes: 3-hydroxybutyrate (3HB), 3-hydroxyhexanoate, 3- hydroxyoctanoate (3HO), 3-hydroxydecanoate (3HD), 3-hydroxydodecanoate (3HDD). Methyl benzoate (MB) was used as an internal standard.

GC-MS was used to determine the monomeric composition of the polymer, which is reported in Table 3.1. P(3HO-co-3HD) is characterized by 76 mol% of 3-hydroxydecanoate and 24 mol% of 3-hydroxyoctanoate. P(3HO-co-3HD-co-3HDD) is characterized by 32 mol% of 3-hydroxyoctanoate, 52 mol% of 3-hydroxydecanoate and 16 mol% of 3-hydroxydodecanoate.

Table 3.1 Monomeric composition of P(3HO-co-3HD) and P(3HO-co-3HD-co3HDD) calculated from GC-MS. The results are expressed as average ± standard deviation (n=6).

Polymer	**3HO (mol%)**	**3HD (mol%)**	**3HDD (mol%)**
P(3HO-co-3HD)	24 ± 6.5	76 ± 6.5	-
P(3HO-co-3HD-co-3HDD)	32 ± 4	52 ± 2	16 ± 3

For the polymer produced from *B. subtilis* OK2 (Figure 3.6), one peak was observed at 4.072 minutes and identified as the methyl ester of 3-hydroxybutyric acid. Thus, the polymer produced by *B. subtilis* OK2 using glucose as the carbon source is the homopolymer of 3-hydroxybutyrate, Poly(3-hydroxybutyrate) or P(3HB).

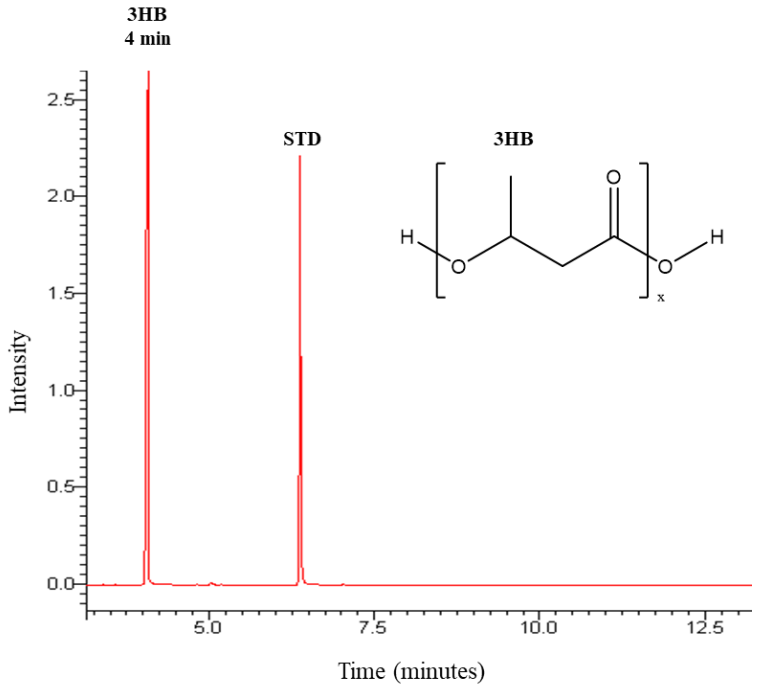

Figure 3.6 Gas chromatogram of P(3HB).). The peak at R_t = 4 minutes was identified using NIST library as the methyl esters of 3-hydroxybutyric acid (3HB). Methyl benzoate was used as the internal standard (STD).

The polymeric structures were further confirmed by ^{1}H-NMR and ^{13}C-NMR.

The ^{1}H-NMR spectra of P(3HO-co-3HD) and P(3HO-co-3HD-co-3HDD) showed 5 peaks typical of an mcl PHAs and assigned as in Figure 3.7 a and b respectively. ^{13}C NMR of P(3HO-co-3HD) revealed the presence of 18 peaks corresponding to the two monomeric units present in the copolymer (Figure 3.8 a). The peaks are assigned in Table 3.2. For P(3HO-co-3HD-co-3HDD) ^{13}C NMR showed the presence of 30 peaks (Figure 3.8 b), assigned in Table 3.2.

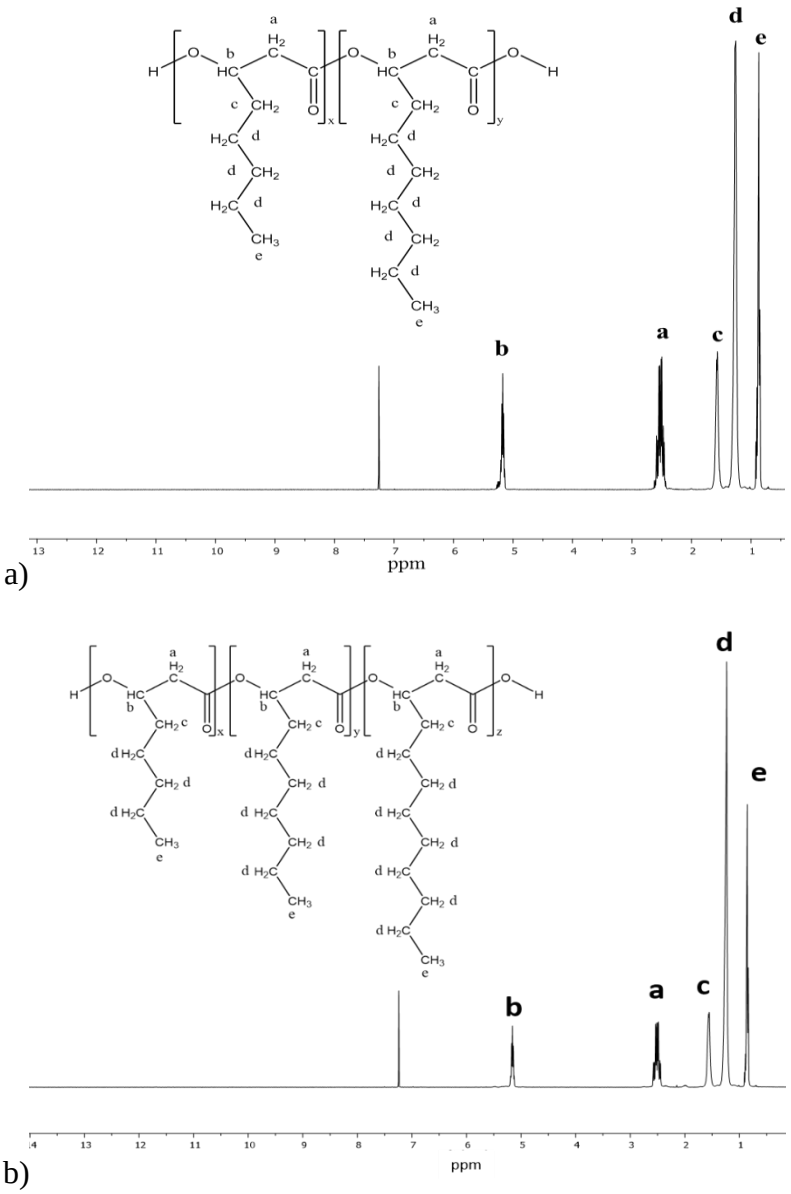

Figure 3.7 ^{1}H-NMR spectra of a) P(3HO-co-3HD) and b) P(3HO-co-3HD-co-3HDD). The chemical structure of the both polymers is shown in each figure, indicating the assignment of each peak to the corresponding proton atom in the molecule.

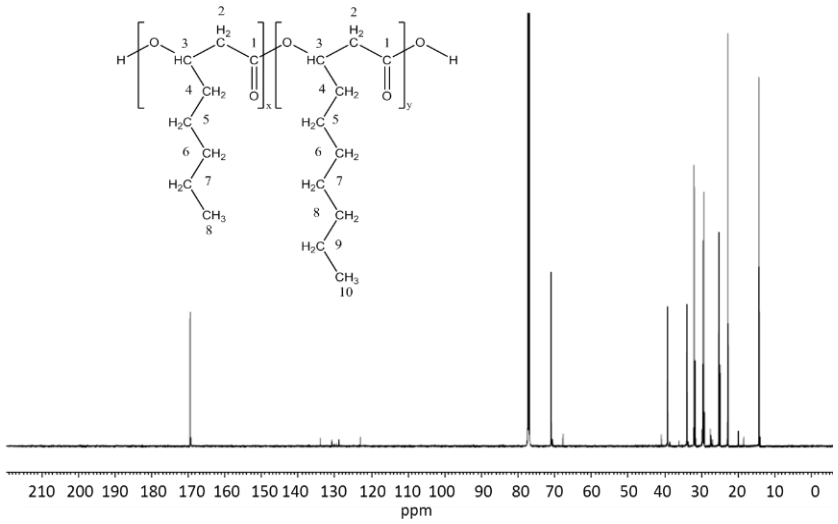

a)

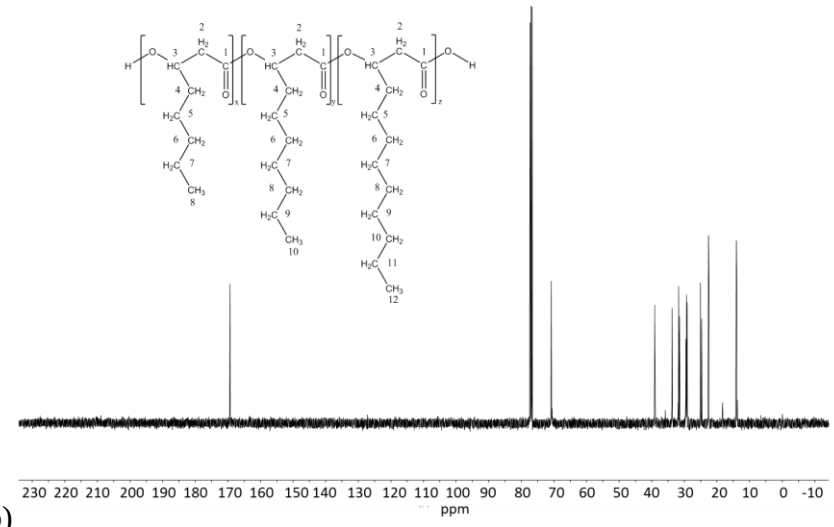

b)

Figure 3.8 ^{13}C-NMR spectra of a) P(3HO-co-3HD) and b) P(3HO-co-3HD-co-3HDD). The chemical structure of the both polymers is shown in each figure, indicating the assignment of each peak to the corresponding carbon atom in the molecule.

Table 3.2 List of the ^{13}C NMR peaks assigned for P(3HO-co-3HD)

Carbon atoms	P(3HO-co-3HD)		P(3HO-co-3HD-co-3HDD)		
	3HO (δ, ppm)	3HD (δ, ppm)	3HO (δ, ppm)	3HD (δ, ppm)	3HDD (δ, ppm)
C1	169.37	169.37	169.53	169.53	169.53
C2	39.09	39.09	39.20	39.20	39.20
C3	70.83	70.83	70.95	70.95	70.95
C4	33.73	33.80	33.86	33.92	33.92
C5	24.70	25.07	24.84	25.2	25.2
C6	22.63	31.91	31.64	29.48	29.48
C7	22.48	29.34	22.63	29.32	29.69
C8	13.96	29.17	14.12	31.91	29.48
C9	-	22.61	-	22.76	29.32
C10	-	14.05	-	14.05	14.22
C11	-	-	-	-	22.81
C12	-	-	-	-	14.25

The ^{1}H NMR of P(3HB) showed the presence of three peaks as reported in literature (Doi *et al.*, 1995) and assigned as in Figure 3.9 a. 4 peaks were detected in ^{13}C NMR confirming the presence of one single monomeric unit and are assigned in Figure 3.9 b.

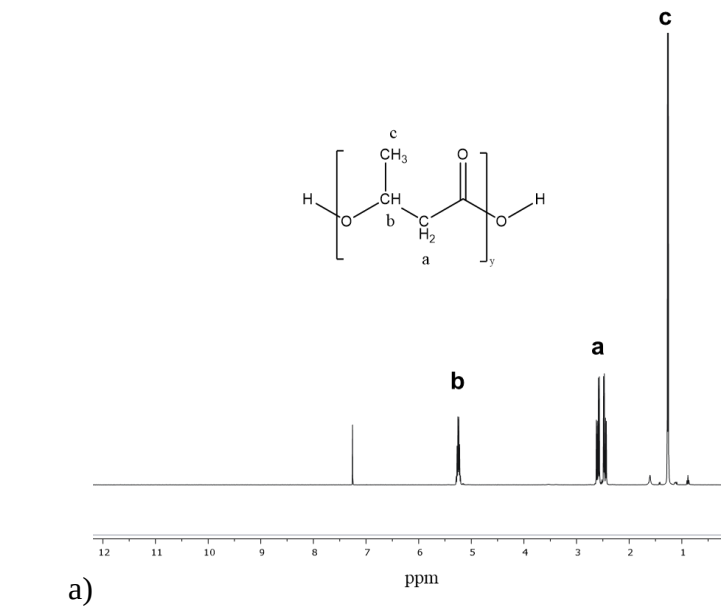

a)

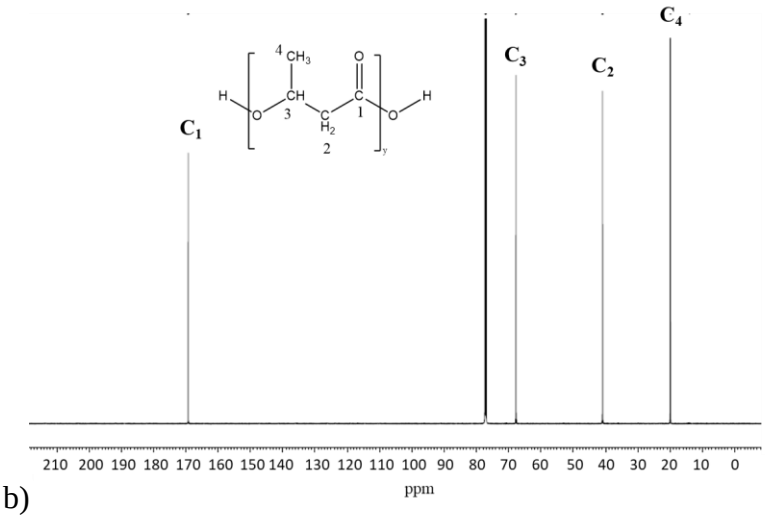

b)

Figure 3.9 a) ^{1}H-NMR spectra and b) ^{13}C-NMR spectra of P(3HB). The chemical structure of the polymer is shown in each figure, indicating the assignment of each peak to the corresponding proton or carbon atoms in the molecule.

The molecular weight of the three polymers produced was investigated using GPC and is shown in Table 3.3. All the three PHAs showed high molecular weight. P(3HB) showed the highest average molecular weight of 470 kDa. As regards the mcl-PHAs, P(3HO-co-3HD) showed an average molecular weight of 364 kDa, while P(3HO-co-3HD-co-3HDD) showed an average M_w of 306 kDa) (p-value< 0.01). The polydispersity index of the three materials was comparable. The PDI represents the uniformity in the distribution of the polymer chains of a polymer. If the PDI equals 1, the polymer chains have a uniform chain length.

Table 3.3 Molecular weight of P(3HO-co-3HD), b) P(3HO-co-3HD-co-3HDD) and c) P(3HB). The results are expressed as average ± standard deviation (n=3).

Polymer	M_w (kDa)	M_n(kDa)	PDI
P(3HO-co-3HD)	364 ± 40	91 ± 12	3.8 ± 0.5
P(3HO-co-3HD-co-3HDD)	306 ± 32	61 ± 20	4.5 ± 0.7
P(3HB)	470±40	126±7	3.7±0.2

3.2.4.2. Thermal characterisation

Solvent cast films were prepared from the three polymers produced and were used to assess the thermal and mechanical properties of the materials.

The thermal properties of the three PHAs were investigated through DSC analysis. Figure 3.10 shows the representative DSC thermograms for the three PHAs, while their properties are reported in Table 3.4.

Both mcl-PHAs showed similar properties, without any statistically significant differences for the parameters evaluated. Both materials were characterized by similar glass transition temperatures, -45°C for P(3HO-co-3HD) and -44°C for P(3HO-co-3HD-co-3HDD), indicating that the polymers were in a rubbery state at room temperature. The mcl-PHAs showed the same melt range from 40°C to 60°C and similar enthalpy of fusion (20 J/g for P(3HO-co-3HD) and 24 J/g for P(3HO-co-3HD-co-3HDD)). For the two mcl-PHAs, the value of crystallinity could not be calculated from the enthalpy of fusion of the material as the enthalpy of fusion for a 100% crystalline material was not known (Suchitra, 2004). As shown in Figure 3.10a, during the second heating cycle, no melting peak could be detected for the two polyesters. These results indicated that cooling rate of 20 °C/minute did not allow crystallization for both mcl-PHAs. Such behaviour is typical of mcl-PHAs and indicates the slow rate of crystallization observed for such polyesters (Nerkar *et al.*, 2015; Puppi *et al.*, 2019).

P(3HB) showed an average glass transition of 2°C, a melting temperature range between 155-175°C and an average enthalpy of fusion of 82 J/g. As shown in Figure 3.10 b, the scl-PHA showed a cold crystallization peak (exothermic peak) during the second heating scan, with

an average cold crystallization temperature of 47°C. Moreover, during the first heating scan no glass transition was detected, indicating the transformation of the amorphous fraction of the polymer into a rigid amorphous phase due to vitrification during storage of the films at room temperature for five weeks (Crétois *et al.*, 2016; dos Santos *et al.*, 2017). For P(3HB), the crystallinity of the material was also calculated as described in the materials and methods section 2.11.4. This was obtained by comparing the observed enthalpy of fusion of the material to that of a 100 % crystalline sample of the same polymer, which for P(3HB) is 146 J/g (Ho *et al.*, 2014). The P(3HB) produced showed an average crystallinity of 56%.

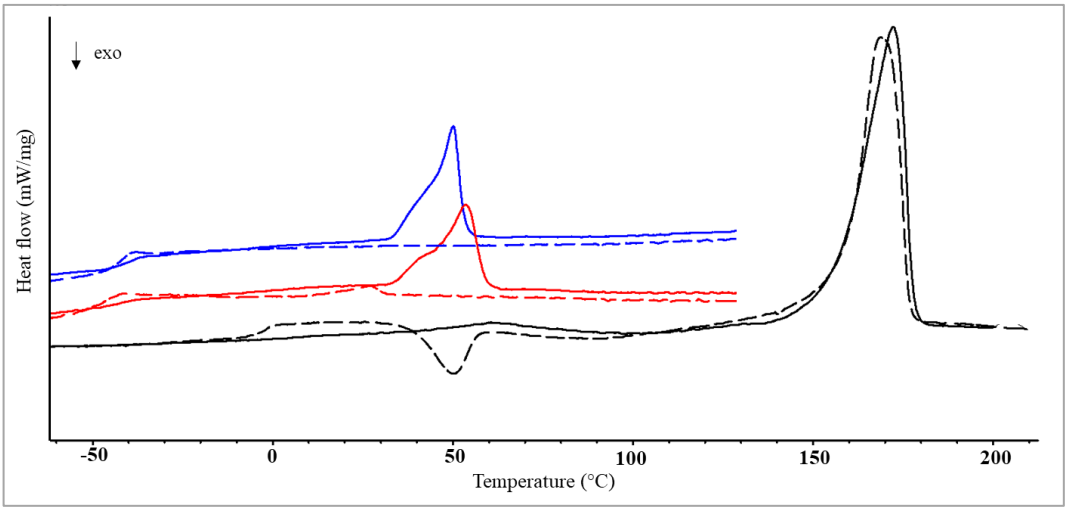

Figure 3.10 Representative DSC thermograms of P(3HO-co-HD) (red), P(3HO-co-3HD-co-3HDD (blue) and P(3HB) (black). Solid lines represent first heating (–), while dashed lines (- -) represent second heating. Thermograms were shifted vertically for better visibility.

Table 3.4 Thermal properties of P(3HO-co-HD), P(3HO-co-3HD-co-3HDD) and P(3HB).T_m is the melting peak, T_g is the glass transition, ΔH_m is the enthalpy of fusion and X_c is the % polymer crystallinity. The results are expressed as average ± standard deviation (n=3).

Polymer	Melting range (°C)	T_m (°C)	T_g (°C)	ΔH_m (J/g)	X_c (%)
P(3HO-co-3HD)	40-60	53 ± 3	-45 ± 3	20 ± 5	-
P(3HO-co-3HD-co-3HDD)	40-60	53 ± 5	-44 ± 2	24 ± 2	-
P(3HB)	155-175	169 ± 2	2 ± 3	82 ± 4	56 ± 4

3.2.4.3. Mechanical characterisation

The mechanical properties of the solvent-cast films were assessed through tensile testing. Figure 3.11 shows the representative stress-strain curves for the three polyesters. The three materials exhibited different properties as can be seen in Table 3.5. P(3HB) showed a high elastic modulus of 0.9 GPa and a low elongation at break of 16%. On the other hand, the two mcl-materials showed a typical elastomeric behaviour of mcl-PHAs. P(3HO-co-3HD) showed an average elastic modulus of 5.7 MPa, an average ultimate tensile strength of 8.6 MPa and an average elongation at break of 536%. P(3HO-co-3HD-co-3HDD) showed an elastic modulus of 5.3 MPa, an average ultimate tensile strength of 6.6 MPa and an average elongation at break of 414%. No statically significant difference was detected between the elastic modulus of the two mcl-PHAs. P(3HO-co-3HD) showed statistically significant higher values compared to P(3HO-co-3HD-co-3HDD) for the elongation at break (*p*-value <0.0001) and ultimate tensile strength (*p*-value <0.05).

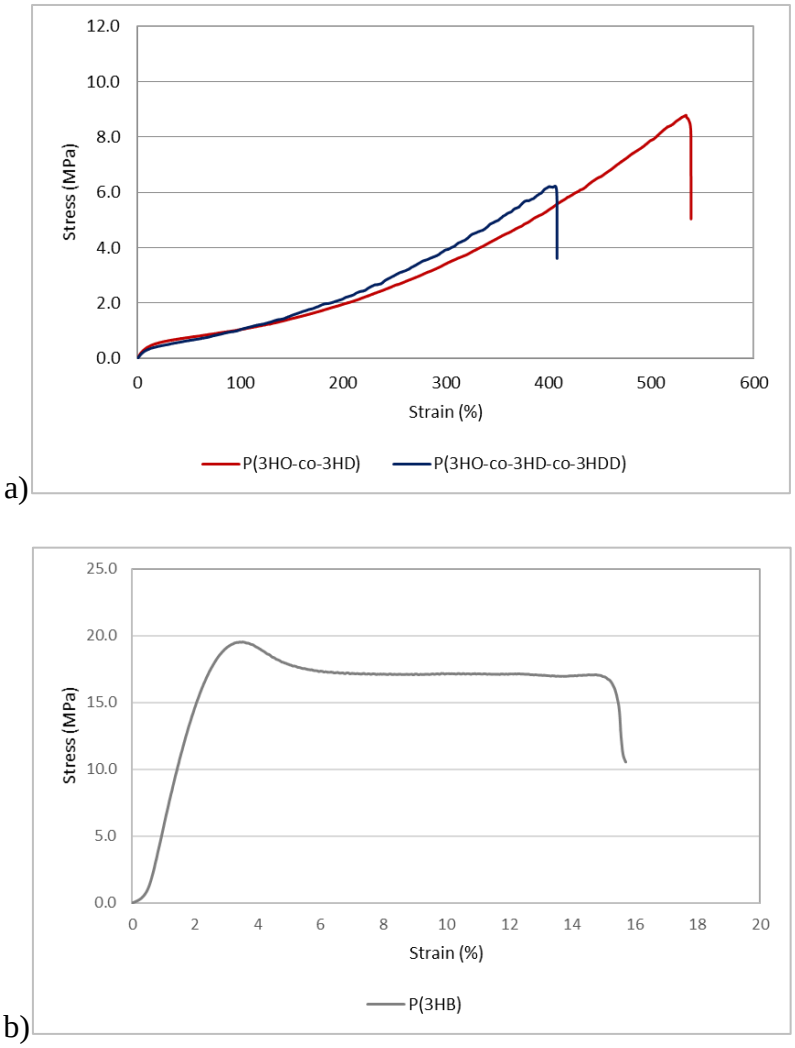

Figure 3.11 Representative stress-strain curves for a) P(3HO-co-HD) (red), P(3HO-co-3HD-co-3HDD) (blue) and b) P(3HB) (grey).

Table 3.5 Mechanical properties of P(3HO-co-HD), P(3HO-co-3HD-co-3HDD) and P(3HB). E is the Young's modulus, σ_U is the ultimate tensile strength and ε_U is the elongation at break. The results are expressed as average ± standard deviation (n=9)

PHA	E [MPa]	σ_U [MPa]	ε_U [%]
P(3HO-co-3HD)	5.7±0.2	8.6±2	536±20
P(3HO-co-3HD-co-3HDD)	5.3±2	6.6±1	414±32
P(3HB)	900 ± 120	19 ± 1.5	16 ± 8

3.2.4.4. Biological characterization

The final aim of this project was to develop a range of antibacterial scaffolds for bone tissue engineering using a combination of the materials produced. For this reason, preliminary *in vitro* cell compatibility of the three polymers was conducted using the osteogenic cell line MC3T3-E1.

Indirect cytotoxicity was carried out to investigate the potential release of toxic products from the P(3HO-co-3HD), P(3HO-co-3HD-co-3HDD) and P(3HB) film samples. As shown in Figure 3.12, all the materials showed a cell viability comparable to the positive control (tissue culture plastic, TCP) without statistically significant differences.

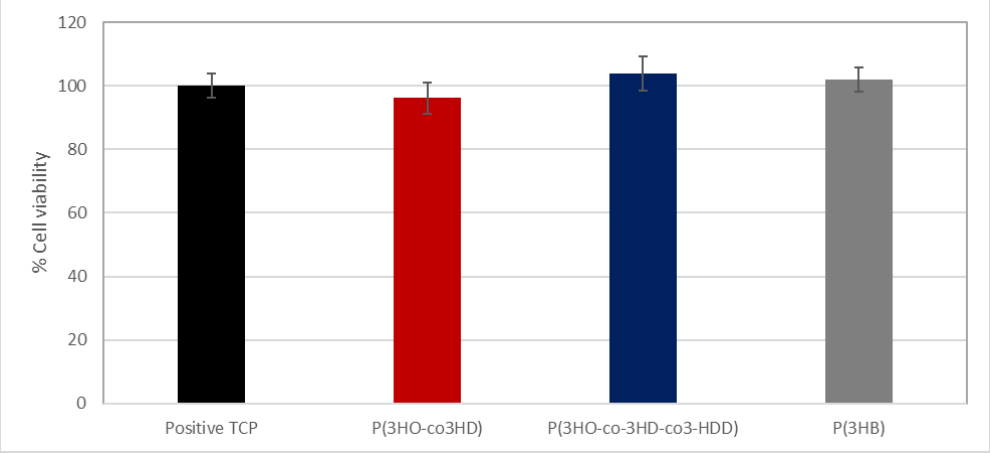

Figure 3.12 Indirect cytotoxicity studies using MC3T3-E1 of P(3HO-co-3HD) (red), P(3HO-co-3HD-co-3HDD) (blue) and P(3HB) (grey) film samples (n=3). The positive control was Tissue Culture Plastic (TCP). There was no statistically significant difference between the samples (*p*-value > 0.5).

Cell viability studies were conducted by seeding MC3T3-E1 on the produced materials for 1, 3 and 7 days.

As regards the two mcl-PHAs, the cell viability was comparable to the positive control (TCP) for all the time points evaluated, as shown in Figure 3.13.

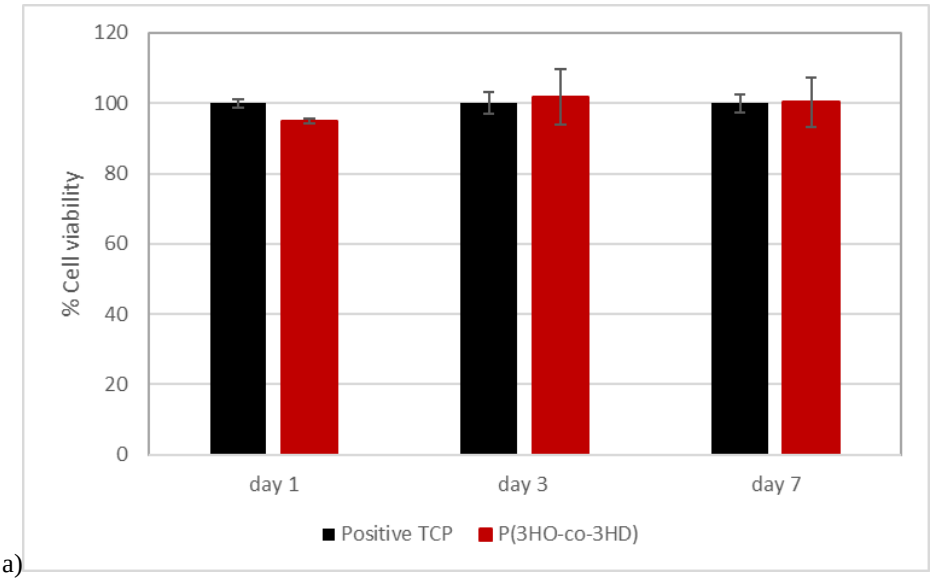

a)

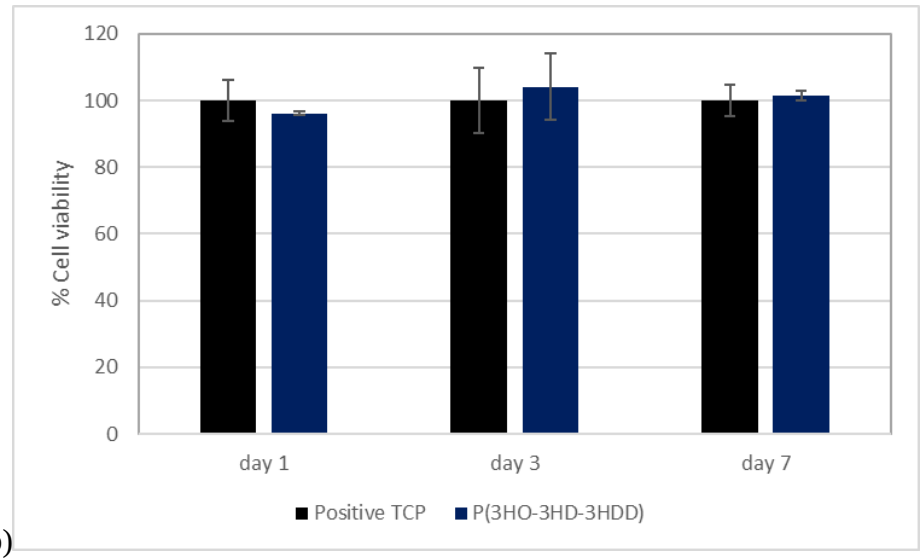

b)

Figure 3.13 Cell viability studies of MC3T3-E1 cells cultured directly on a) P(3HO-co-3HD) (red) and b) P(3HO-co-3HD-co-3HDD) (blue) at day 1, 3 and 7 (n = 3). The positive control was Tissue Culture Plastic (TCP). There was no statistically significant difference between the samples (*p*-value > 0.5).

For P(3HB), at day 1 and day 3 the cell viability was comparable with the positive control, without statistically significant differences (Figure 3.14). At day 7 the material showed a significantly increased cell viability compared to the positive control, with an average cell viability of 139% ± 6 and 100% ± 7 respectively (p-value<0.001). Moreover, the cell viability at day 7 on the P(3HB) polymeric samples was significantly higher than the cell viability at day 3 (p-value<0.01).

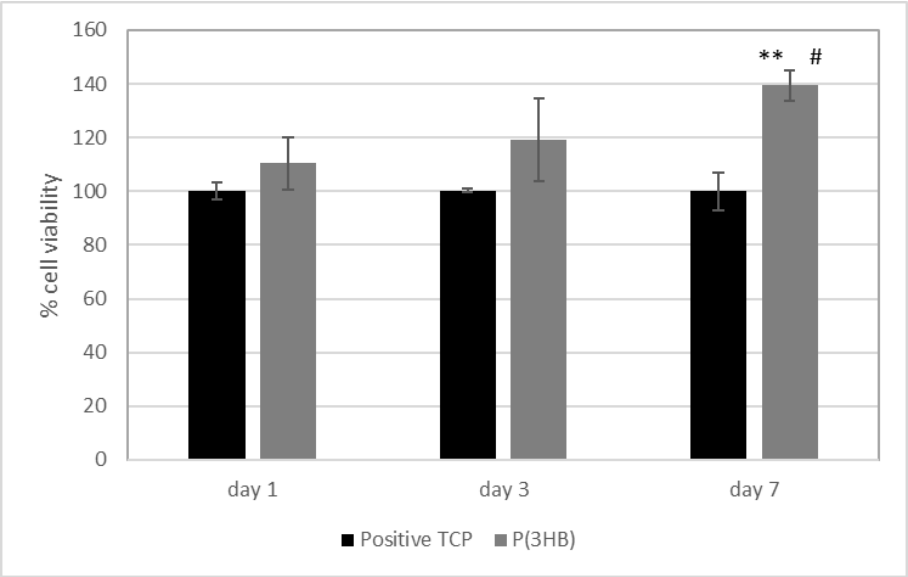

Figure 3.14 Cell viability studies of MC3T3-E1 cells cultured directly on P(3HB) (grey) at day 1, 3 and 7 (n = 3). The positive control was Tissue Culture Plastic (TCP). ** indicates significant difference between P(3HB) samples and the control at day 7 (*p*-value<0.01). # indicates significant difference between P(3HB) sample at day 7 and P(3HB) sample at day 1 (*p*-value<0.001).

3.3. Discussion

In this chapter the production of scl and mcl-PHAs by *B. subtilis* OK2 and *P. mendocina* CH50 was reported.

Pseudomonas species are well known producers of mcl-PHAs when cultured using both structurally related (e.g. fatty acid) and unrelated carbon sources (e.g. carbohydrates) through two different metabolic pathways. Intermediates of the β-oxidation pathway are converted into the PHAs precursor, (R)-3-hydroxyacyl-CoA, when alkanoic acid are utilized (Sudesh *et al.*, 2000). While *de novo* fatty acid biosynthesis pathway is involved in the production of mcl-PHAs from unrelated carbon sources. In this work, *P. mendocina* CH50 was cultured using both glucose and coconut oil. When cultured on glucose, a biomass concertation of 2.8 g/L with a polymer content of 47% dcw was achieved after 48 hours of fermentation. In literature a range of polymer yields from 14.7 to 52% dcw has been obtained when culturing wild type *Pseudomonas* species using glucose (Phukon *et al.*, 2013; Blunt *et al.*, 2019; Zhang *et al.*, 2006; Poblete-Castro *et al.*, 2014; Huijberts *et al.*, 1992; Wang *et al.*, 2016c). This is due to the fact that the PHA yield is affected by several parameters including type of strain, amount of carbon source used and type and duration of fermentation process (e.g.

fermentation using shaken flask or fermenter). A higher final polymer yield of 58% dcw was obtained using coconut oil as the carbon source. In literature it is known that a higher efficiency can be obtained using structurally related carbon sources compared to unrelated ones (Sun *et al.*, 2007; Poblete-Castro *et al.*, 2014; Chanasit *et al.*, 2016). In case of glucose, lower yields are usually attributed to the production of extracellular products like alginate by *Pseudomonas mendocina* strains (Müller and Alegre, 2007; Wang *et al.*, 2016c; Kumar and Kim, 2018). This competitive mechanism of production was proven by Guo *et al.*. In their study, they showed an enhanced production of alginate after suppression of the pathway for PHA production by deletion of the gene encoding for PHA synthase in *P. mendocina* NK-01(Guo *et al.*, 2011). A few *Pseudomonas* species have been shown to be able to produce PHAs when cultured using coconut oil. The yields obtained were lower than the one in this study. A value of 51.8% dcw was obtained using *P. corrugata* 388 for 72h (Solaiman *et al.*, 2002), while after 48 h of fermentation *P. aeruginosa* 7925 resulted in an yield of 25.3% dcw (Singh and Mallick, 2009) and 51 %dcw for *P. resinovorans* B-2649 (Ashby and Foglia, 1998). A possible explanation might be related to the fact that in all the three studies the bacterial fermentation was conducted in shake flasks, while in this work a 10L fermenter was used. It has in fact been shown that a higher yield can usually obtained when using a bioreactor as compared to shake flasks as certain production parameters such as oxygen rate can be controlled more efficiently (Raza *et al.*, 2019).

Chemical characterization of the two polymers confirmed that mcl-PHAs were produced by *P. mendocina* CH50 using glucose and coconut oil as the carbon source. In the presence of the unrelated carbon substrate, the polymer obtained was P(3HO-co-3HD) and was characterized by a monomeric composition of 76 mol% of 3-hydroxydecanoate and 24 mol% of 3-hydroxyoctanoate. Several studies in literature showed that *Pseudomonas* species accumulate PHAs with a high content of 3-hydroxydecanoate when cultured using unrelated carbon sources (e.g. glucose, glycerol) (Sudesh *et al.*, 2000; Wang and Nomura, 2010; Poblete-Castro *et al.*, 2014). Such results are linked to the activity of the enzyme 3-hydroxydecanoyl-ACP-CoA transacylase involved in the conversion of the products of de novo fatty acid pathway to PHA precursors (i.e. (R)-3-hydroxyacyl-CoA). This enzyme has a high affinity to substrate containing 10 carbon atoms (Poblete-Castro *et al.*, 2014; Mozejko-Ciesielska *et al.*, 2019). The same strain as the one used in this study produced a polymer

with 3HD as the dominant monomeric unit when cultured with biodiesel waste (high content of glycerol) (Basnett *et al.*, 2017b).

In the presence of coconut oil, the polymer produced was P(3HO-co-3HD-co-3HDD) and was characterized by a monomeric composition of 32 mol% of 3-hydroxyoctanoate, 52 mol% of 3-hydroxydecanoate and 16 mol% of 3-hydroxydodecanoate. When the β-oxidation pathway is involved in the polymer production, the structure of the mcl PHA produced is strictly correlated with the one of the carbon sources utilized. The polymer produced contains only monomer with an even (or odd) number when the substrate used has an even (or odd) number of carbon atom, as the fatty acids are shortened by 2 (or multiple of 2) carbon atoms each cycle of the β-oxidation (Sudesh *et al.*, 2000; Madison and Huisman, 1999; Ciesielski *et al.*, 2015). This behaviour was evidenced in this study, as coconut oil contained an even number of carbon atoms and therefore the PHA produced had three even monomer units (C8, C_{10} and C_{12}) (Appaiah *et al.*, 2014). Moreover, the enzyme involved in the PHA polymerization (i.e. PHA synthase) has a higher specificity for 3-hydroxyanoyl-CoA precursor containing eight or ten carbon atoms (i.e. 3-hydroxyoctanoyl-CoA and 3-hydroxydecanoyl-CoA 3-hydroxyoctanoate), leading to polyesters with a high content of C_8 and C_{10} monomers (Ashby and Foglia, 1998). Such mechanism was also observed in this study as 3-HO and 3-HD accounted for 32 mol% and 52 mol% of the total monomeric composition. Similar considerations were evidenced in literature culturing *Pseudomonas* species using coconut oil, even though the final monomeric compositions of the PHAs produced were different to the one described in this study. Solaiman *et al.* showed that *P. saccharophila* NRRL B-628 produced a polymer containing 30 mol% of 3-HO and 40 mol% of 3-HD as the main monomers, and 6 mol% of 3-HHx, 17 mol% of 3-HDD and 7 mol% of monomers with C>14 as minor constituents (Solaiman *et al.*, 1999). In another study by the same group, *P. corrugata* 388 produced an mcl-PHAs containing 42 mol% of 3-HO and 35 mol% of 3-HD as the main monomers, and 3 mol% of 3-HHx, 17 mol% of 3-HDD and 4 mol% of monomers with C>14 as minor consituents (Solaiman *et al.*, 2002). Finally, Ashby *et al.* cultured *P. resinovorans* NRRL B-2649 using coconut oil and obtained an mcl-PHA composed mainly of 3-HO (28 mol%) and 3-HD (44 mol%), and with 3-HHx (3 mol%), 3-HDD (20 mol%) and monomers with C>14 (5 mol%) (Ashby *et al.*, 2001).

Bacillus sp. are among the most investigated bacteria for the production of P(3HB) (Mohapatra *et al.*, 2017). They have the advantages over Gram negative bacteria of lacking

the outer layer composed of lipopolysaccharides, known pyrogens/immunogens, making the polymer produced safer for medical applications. In this study *B. subitlis* OK2 was cultured using glucose as the carbon source following optimized conditions described by Lukasiewicz *et al.* A final polymer yield of 30% dcw was obtained after 48h of production, comparable with literature results (30.8% dcw) (Lukasiewicz *et al.*, 2018). The same strain showed a higher productivity (41% dcw) when grown using orange peel as the carbon source (Sukan *et al.*, 2017). The higher value could also be due to the presence of citrate in the media. Citrate has in fact been shown to increase PHA production by blocking the citric acid cycle (TCA), which competes with the PHA biosynthic pathway for the use of acetyl-CoA (Kessler and Witholt, 2001; Aldor and Keasling, 2003; Sukan *et al.*, 2014). The polymer produced was analysed for chemical composition and the results confirmed that the homopolymer P(3HB) was obtained as described in literature (Lukasiewicz *et al.*, 2018).

The molecular weight of the three polymers produced was investigated using GPC as this is an important parameter that significantly effects the materials properties. Generally, PHAs are considered high molecular weight polymers, but a wide range of average molecular weight has been described in literature for such materials. The molecular weight is in fact effected by several parameters including the type of bacteria, the carbon source, the process parameters and the extraction method utilized (Zinn *et al.*, 2001; Tsuge, 2016; Keshavarz and Roy, 2010). In this study, *P. mendocina* CH50 produced polymers with an average molecular weight of 340 kDa and of 306 kDa when cultured respectively using glucose and coconut oil, while *B. subtilis* OK2 produced P(3HB) of 470 kDa. For mcl-PHAs an average molecular weight between 60-410 kDa has been described by Valappil *et al.*, while scl-PHAs with a molecular weight up to 1000 kDa have been obtained (Zinn *et al.*, 2001; Sudesh *et al.*, 2000). Therefore, the values obtained in this study were in agreement with literature.

Thermal and mechanical properties of polymers are strictly depended on the monomeric composition of the material. For this reason, such features are significantly different between scl and mcl-PHAs (Sudesh *et al.*, 2000; Gopi *et al.*, 2018). P(3HB) is described in literature as a highly crystalline material (crystallinity > 50%), possessing a high melting temperature between 165 and 178 °C and a glass transition around 0-4 °C (Bugnicourt *et al.*, 2014; Tan *et al.*, 2014; Sudesh *et al.*, 2000). The polymer produced in this study possessed properties in agreement with such values. Moreover, the thermal analysis of the solvent cast films obtained after five-weeks storage period at room temperature indicated the presence of a rigid

amorphous phase in P(3HB). Such behaviour is known in literature and has been attributed to two mechanisms, physical ageing and secondary crystallization of the material (Crétois *et al.*, 2016; dos Santos *et al.*, 2017). The former is related to the vitrification of the amorphous phase of the material during storage (Di Lorenzo and Righetti, 2013). The latter has been described as the formation of new small crystallites during the storage of the materials at room temperature. Such mechanism occurs as the glass transition temperature of P(3HB) is below room temperature, allowing sufficient mobility to the polymeric chains to form crystals (Crétois *et al.*, 2016; Righetti *et al.*, 2019).

Mcl- PHAs have been reported to show lower values of melting temperature (40-70°C) and glass transition (-25 to -50 °C) compared to scl-PHAs (Rai *et al.*, 2011a; Zinn and Hany, 2005). The two mcl-PHAs produced in this study showed properties in agreement with such values. For mcl-PHAs, the length of the side chains effects the thermal features of such materials. In particular, several studies reported that the glass transition (T_g) of the polymer decreases with the increase of the length of the side chain from C_6 to C^{10} due to a higher increase in chain mobility, and the values remain constant for polymers with longer monomeric units (C>10) (Rai *et al.*, 2011a; Gopi *et al.*, 2018; Ouyang *et al.*, 2007; Abe *et al.*, 2012). For instance, Abe *et al.* showed a T_g of -20°C for P(3HHx) (C_6) and -53°C for P(3HD) (C_{10}). The results obtained in this study were in agreement with these observations as the two mcl-PHAs produced exhibited similar glass transition temperatures as they are characterized by long monomeric units (C>10). As regards the melting temperature (T_m) and the enthalpy of fusion of mcl-PHAs, literature studies have shown that the correlation between the variation of these values and the length of the alkyl side chain is influenced by the monomeric composition and the regularity in monomer distribution (Barbuzzi *et al.*, 2004; Gopi *et al.*, 2018; Rai *et al.*, 2011a; Abe *et al.*, 2012). In the case of mcl-PHAs homopolymers or near-homopolymers (i.e. main monomer molar composition > 96 mol%), the T_m and the enthalpy of fusion have been shown to increase with increasing chain length (Abe *et al.*, 2012; Rai *et al.*, 2011a; Gopi *et al.*, 2018). On the contrary, Barbuzzi *et al.* showed that in the case of copolymers, the uniformity of the repeating units also influences the final values of melting temperature (T_m) and the enthalpy of fusion. In their study, the T_m and the enthalpy of fusion did not increase but remained constant with an increase of the average side chains as the number of different monomeric units also increases, inducing a counterbalance effect (Barbuzzi *et al.*, 2004). Such behaviour was also confirmed by this study. Even though P(3HO-co-3HD-co-3HDD) contained monomer units with a longer chain length (C_{12})

compared to P(3HO-co-3HD) (C_{10}), the T_m and the enthalpy of fusion were comparable between the polymers.

The differences in the thermal characteristics of the two types of PHAs reflected the variation in their mechanical properties. The P(3HB) produced showed high crystallinity with a rigid amorphous phase, leading to a stiff and strong (average Young's modulus of 0.9 GPa and tensile strength of 19 MPa) but brittle (average elongation at break of 16%) material. Moreover, the results obtained were in line with the reported mechanical properties of P(3HB). P(3HB) usually exhibits a Young's modulus between 0.5 and 3.5 GPa and a tensile strength between 15 and 50 MPa and an average extension at break between 5-20% (El-Hadi *et al.*, 2002; Możejko-Ciesielska and Kiewisz, 2016; Chanprateep, 2010; Singh *et al.*, 2015; Zinn and Hany, 2005).

The two mcl-PHAs produced were able to withstand large deformations with a high elongation at break (536% for P(3HO-co-3HD) and 414% for P(3HO-co-3HD-co-3HDD)), thanks to the rubbery state of their amorphous phases. Both materials were relatively soft polymers; with an average modulus of elasticity of 5.7 MPa for P(3HO-co-3HD) and of 5.3 MPa for P(3HO-co-3HD-co-3HDD). Such values were in agreement with the range of mechanical properties reported in literature for mcl-PHAs. Such polyesters are usually characterized by an elastomeric behaviour with a relatively low Young's modulus (4-50 MPa) and high elongation at break in tensile ranging from 200-500% (Rai *et al.*, 2011b; Zinn and Hany, 2005; Jiang *et al.*, 2012; Larrañaga *et al.*, 2014).

Finally, as the final aim of this thesis was to produce PHA-based antibacterial materials for bone tissue engineering, preliminary *in vitro* compatibility of the three polymers produced was conducted using MC3T3-E1 cell line, a preosteoblastic mouse line extensively used in literature for materials characterisation (Czekanska *et al.*, 2012; Hwang and Horton, 2019). Firstly, the indirect cytotoxicity was performed to evaluate if toxic leachable compound were present in the polymeric samples. All the three polymers did not show any toxic effect after 24 h of incubation. Direct cell compatibility studies were conducted by culturing the cells directly on the surface of the polymeric samples for 1, 3 and 7 days. All the three PHAs produced exhibiting high level of cytocompatibility for all the time points tested, showing the potential materials for the development of scaffolds for bone regeneration.

3.4. Conclusions

In this chapter, the production of PHAs through bacterial fermentation was studied. Three PHAs were produced and completely characterized in terms of chemical, physical, thermal, mechanical and biological properties. A short chain length PHA, P(3HB) was produced by *B. subtilis* OK2 using glucose as the carbon source. Two novel medium chain length PHAs, P(3HO-co-3HD) and P(3HO-co-3HD-co-3HDD), were produced by *P. mendocina* CH50 using glucose and coconut oil as the carbon sources respectively. Preliminary *in vitro* studies showed that the three polyester possessed good cytocompatibility towards a pre-osteoblastic cell line, MC3T3-E1, showing potential for their use in bone tissue regeneration.

Based on the results of this chapter, P(3HO-co-3HD-co-3HDD) was selected over P(3HO-co-HD) as the mcl-PHAs to be used as the bulk material for the development of scaffolds. The two mcl-PHAs showed in fact comparable physical, mechanical and biocompatibility properties, but a higher polymer yield was obtained using coconut oil compared to glucose (58% vs 47% dcw). As mentioned in the Introduction chapter, one of the major deterrents for PHAs utilisation over synthetic polymer is their higher production cost. Therefore, the higher productivity combined with the cheaper cost of the carbon source compared to glucose makes P(3HO-co-3HD-co-3HDD) a more promising candidate for the application of PHAs in the medical field.

Chapter 4

Production of thioester- PHAs and 2D inherently antibacterial films

4.1. Introduction

Bacterial infections represent one of the major threats to the successful functioning of medical implants. The introduction of a device inside the human body is inherently associated with the risk of infection (Vinh and Embil, 2005; Darouiche, 2001; Percival *et al.*, 2015). Moreover, the widespread use and abuse of antibiotics over the last decades as a treatment of microbial infections has led to the rapid development of multi-drug resistant bacteria (Watson *et al.*, 2017; Levy and Bonnie, 2004; Munita and Arias, 2016). For these reasons, researchers have been focusing on the development of new therapeutics to prevent bacterial attachment and proliferation. One of the main strategies investigated is to develop inherently active antibacterial materials (Darouiche, 2003; Muñoz-Bonilla and Fernández-García, 2012; Siedenbiedel and Tiller, 2012; Santos *et al.*, 2016). This goal can be achieved by either the use of polymers possessing bactericidal effect (e.g. chitosan) or through the introduction of antibacterial groups (e.g. quaternary ammonium groups) in the polymer structure or on the surface of the materials by chemical modification. Inherently antibacterial polymers offer the advantages of possessing long-term activity and durability due to their chemical stability (Xue *et al.*, 2015).

Polyhydroxyalkanoates are generally not inherently antibacterial. A few studies have been conducted to introduce antimicrobial moieties through chemical modification. Overall the chemical modification of PHAs can be challenging due to lack of active functional groups and the limited solubility in organic solvents, especially of scl-PHAs (Jiang *et al.*, 2006). For these reasons, modifications have been limited mainly to the surface of PHA films or membranes through the introduction of known bactericidal groups such as quaternary

ammonium groups by UV grafting, chemical grafting or ozone treatment (Babinot *et al.*, 2010; Versace *et al.*, 2013; Chung *et al.*, 2012). Alternatively, PHA oligomers were obtained by the hydrolysis of the polymer to achieve a higher number of chemical groups that are able to be functionalized (i.e. carboxylic groups or hydroxyl groups), and the oligomers were modified through the introduction of antimicrobial moieties (Abdelwahab *et al.*, 2019; Snoch *et al.*, 2019).

PHAs containing functional moieties in their side chains can also be produced directly by bacterial fermentation through the exploitation of their intrinsic metabolic pathways of production (Tortajada *et al.*, 2013; Zinn and Hany, 2005; Tan *et al.*, 2014). In the case of *Pseudomonas* species, incorporation of specific groups can be obtained through the use of the β-oxidation pathway and structurally related carbon sources by selecting the substrates containing the desired functional group that can be metabolized by the bacteria. In this way a wide variety of tailored bacterial polyesters has been produced, containing for example unsaturated, aromatic and halogenated groups (Tortajada *et al.*, 2013; Ishii-Hyakutake *et al.*, 2018). Recently, Escapa *et al.* discovered a new class of PHAs containing thioester groups in their side chains (i.e. thioester-PHAs). This polymer was obtained using *P. putida* KT2442 using a co-feeding experiment with fatty acids (i.e. decanoic acid) as the "good" substrates to support bacterial growth and polymer accumulation and carbon sources containing thioester groups as the polymer precursor (i.e. 6-acetylthiohexanoic acid) (Escapa *et al.*, 2011;Escapa *et al.*, 2013). These materials were demonstrated to be inherently antibacterial as they showed activity against methicillin-resistant *Staphylococcus aureus* (MRSA) both *in vitro* and *in vivo*, even though their mechanism of action has still not been discovered (Dinjaski *et al.*, 2014). Moreover, the polymer was able to support the attachment and proliferation of fibroblasts, showing potential for tissue engineering applications (Dinjaski *et al.*, 2014).

In this chapter, the production of thioester–PHAs through bacterial fermentation was investigated as described by Escapa *et al*, 2011. The polymer was completely characterized in terms of physical, chemical and thermal properties and compared to the polymer obtained using control conditions (i.e. only decanoic acid). The antibacterial activity of the material was investigated using the ISO 22196. *In vitro* biocompatibility studies were also conducted using MC3T3- E1 preosteoblastic cell line. Finally, the thioester-PHAs were blended with the mcl-PHA obtained with the control conditions to investigate the potential of this material

for the development of 2D inherently antibacterial scaffolds for bone regeneration. The blend films obtained were characterized in terms of thermal, mechanical, antibacterial properties and their biocompatibility.

4.2. Results

In this study, the production of inherently antibacterial PHAs was investigated through the fermentation of *P. putida* KT2442 using a co-feeding experiment (i.e. decanoic acid and 6-acetylthiohexanoic acid) as described by Escapa *et al.*, 2011. The polymer produced was characterized and compared to the one obtained from control condition (i.e. decanoic acid as the sole carbon source).

For both conditions, the polymers obtained were extracted using the chloroform/sodium hypochlorite dispersion method. As shown in Table 4.1, the yield after 24 hours for thioester PHAs was 0.12 g/L in agreement with published data (Escapa *et al.*, 2011).

Table 4.1 Comparison of biomass and polymer yield values obtained by culturing *P. putida* KT2442 in different conditions

Condition	***Biomass [g/L]***	***Polymer yield***	
		[g/L]	***%DCW***
2.4 mM decanoic acid + 12 mM 6-ATH	0.50	0.12	24
12 mM Decanoic acid (Control condition)	2.5	0.69	28
Published data (Escapa *et al.*, 2011) (2.4 mM decanoic acid+ 12 mM 6-ATH)	0.59	0.09	16

4.2.1. Polymer characterization

4.2.1.1. Chemical characterization

Preliminary FT-IR analyses of the two PHAs produced are shown in Figure 4.1 a and b. Both spectra showed peaks around 1730 cm^{-1} related to the stretching of the carbonyl group of the ester bond, confirming that the polymers produced are polyesters (Randriamahefa *et al.*, 2003). Moreover, both spectra showed the presence of peaks around 2930 cm^{-1}, related to the stretching of carbon-hydrogen bond of methyl and methylene group (CH_3, CH_2). Compared to the control condition (Figure 4.1b), the polymer obtained from the co-feeding experiment showed the presence of an extra peak at 1690 cm^{-1} which is associated to the stretching of the carbonyl group present in thioester groups (Lütke-Eversloh *et al.*, 2001). Therefore, the analysis confirmed the production of a PHA containing thioester groups.

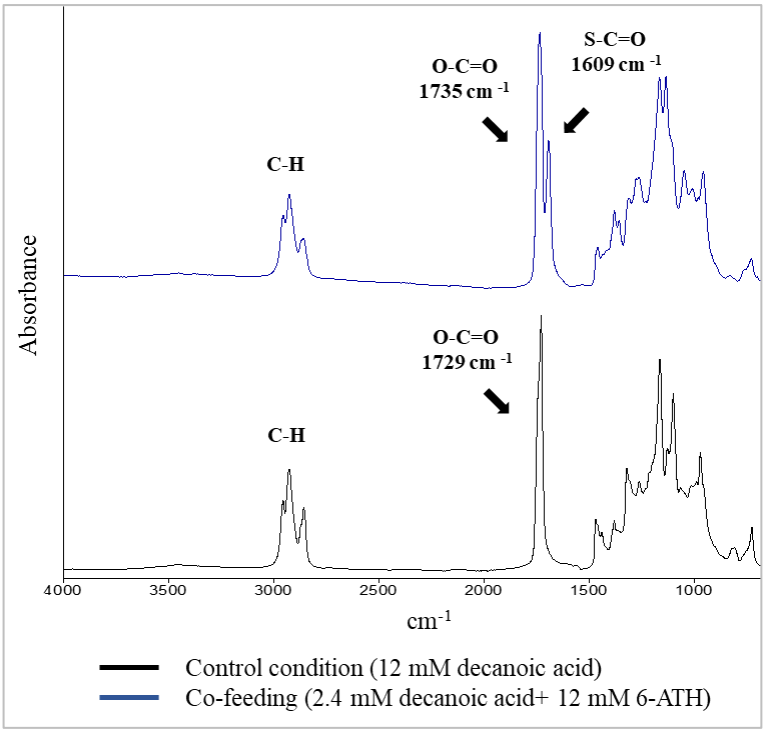

Figure 4.1 FT-IR spectra of the polymer produced by *P. putida* KT2442 using decanoic acid (12 mM) as the carbon source (black) and 6-ATH (12 mM) and decanoic acid (2.4 mM) as the carbon sources (i.e. co-feeding experiment) (blue).

The characterization of the monomeric composition of the polymers obtained from both conditions was performed using GC-MS (Figure 4.2). The polymer produced using the control condition showed three peaks at the retention times of 5.875, 7.633 and 9.176 minutes (Figure 4.2a). Using the NIST library these peaks were identified as the methyl esters of 3-hydroxyhexanoate, 3-hydroxyoctanoate and 3-hydroxydecanoate, P(3HHx-co-3HO-co-3HD). The spectra of the polymer obtained using the co-feeding experiment (Figure 4.2b) showed two extra peaks at 6.85 and 8.701 minutes. Using the MS spectra, the peaks were identified as methyl esters of 3-hydroxy-6-acetylthiohexanoic acid, 3-hydroxy-4-acetylthiobutanoic acids. The polymer produced was identified as the copolymer of 3-hydroxyhexanoate, 3-hydroxyoctanoate, 3-hydroxydecanoate, 3-hydroxy-4-acetylthiobutanoate and 3-hydroxy-6-acetythiolhexanoate, P(3HHx-co-3HO-co-3HD-co-3H4ATB-co-3H6ATH), also referred as thioester-PHA.

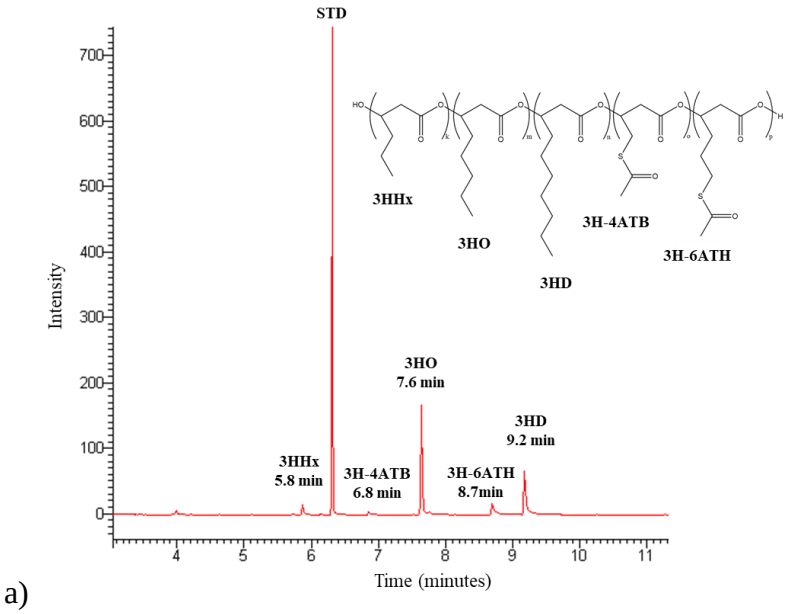

a)

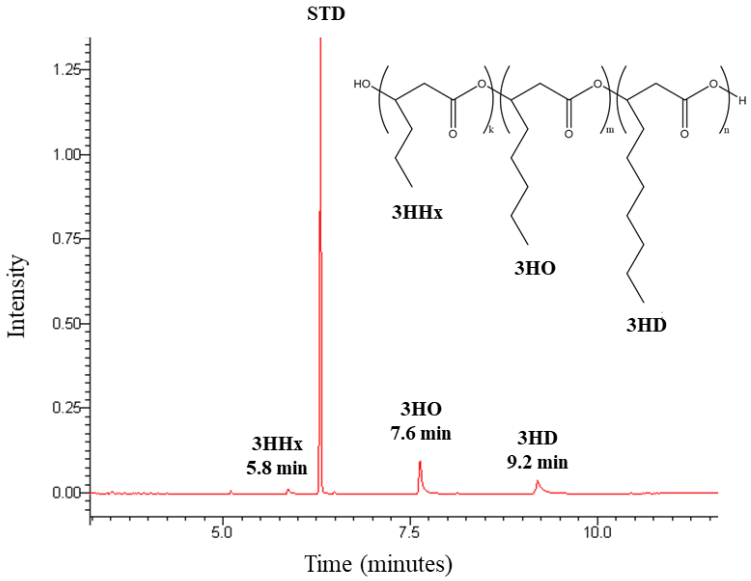

b)

Figure 4.2 Gas chromatogram of a) P(3HHx-co-3HO-co-3HD-co-3H4ATB-co-3H6ATH) and b) P(3HHx-co-3HO-co-3HD). In both graphs the peaks at R_t = 5.8, 7.6 and 9.2 minutes were identified as the methyl esters of 3-hydroxyhexanoic acid (3HHx), 3-hydroxyoctanoic acid (3HO) and 3-hydroxydecanoic acid (3HD) respectively. In graph a) the peaks at R_t= 6.8 and 8.7 minutes were identified as the methyl esters of 3-hydroxy-4-acetylthiobutanoic acid (3H-4ATB) and 3-hydroxy-6-acetylthiohexanoic acid (3H-6ATH). Methyl benzoate was used as the internal standard (STD).

GC-MS and ^{1}H-NMR were used to calculate the mol% of the produced polyester, which is presented in Table 4.2. P(3HHx-co-3HO-co-3HD) was characterized by 7 mol% of 3-hydroxyhexanoate, 64 mol% of 3-hydroxydecanoate and 29 mol% of 3-hydroxyoctanoate. P(3HHx-co-3HO-co-3HD-co-3H4ATB-co-3H6ATH) was characterized by 5 mol% of 3-

hydroxyhexanoate, 31 mol% of 3-hydroxyoctanoate, 13 mol% of 3-hydroxy-4-acetylthiobutanoate, 18.5 mol% of 3-hydroxydecanoate and 32.5 mol% of 3-hydroxy-6-acetythiolhexanoate.

Table 4.2 Monomeric composition of P(3HHx-co-3HO-co-3HD) and P(3HHx-co-3HO-co-3HD-co-3H4ATB-co-3H6ATH) calculated through GC-MS and ^{1}H-NMR. The results are expressed as average standard deviation (n=3).

Polymer	3HHx (mol%)	3HO (mol%)	3HD (mol%)	3H4ATB (mol%)	3H6ATH (mol%)
P(3HHx-co-3HO-co-3HD)	7 ± 1	64 ± 7.5	29 ± 8	-	-
Thioester-PHA	5 ± 1	31 ± 1	18.5 ± 1	13 ± 2	32.5 ± 1

The chemical structure of the polymers was also confirmed through ^{1}H-NMR, ^{13}C NMR and HSQC. For the control condition, ^{1}H NMR showed the presence of 5 peaks (Figure 4.3 b), typical of an mcl-PHA (de Rijk *et al.*, 2005). The multiplet at δ=2.5 ppm and the signal at around δ =5.2 ppm originated from hydrogens bound to carbon atoms in the polymer backbone, namely C_2 and C_3, respectively. The peak at δ =0.88 ppm was assigned to the hydrogen of the end methyl group (C_6 for 3-hydroxyhexanoate, C_8 for 3-hydroxyoctanoate and C_{10} for 3-hydroxydecanoate). The peak at δ =1.58ppm was assigned to two hydrogens bound to C_4. The peak at δ =1.27 ppm was assigned to the hydrogen atoms bound to C_5 carbon of 3-hydroxyhexanoate, C_5-C_7 of 3-hydroxyoctanoate and C_5-C_9 of 3-hydroxydecanoate. The ^{1}H NMR is not capable of discriminating methylene hydrogen atoms in pendant alkyl chains. To identify the presence of the three monomeric units ^{13}C NMR was used in combination with HSQC (Figure 4.4b, Figure 4.5b). 24 peaks were identified in the ^{13}C NMR corresponding to the three monomers and classified as shown in Table 4.3.

For the polymer containing thioester groups, ^{1}H NMR showed the presence of 12 peaks related to the presence of the two new monomeric structures, which were assigned as shown in Figure 4.3 a. The use of ^{13}C NMR in combination with HSQC allowed the identification of the 36 peaks present in the ^{13}C NMR related to the presence of the four monomers (listed in Table 4.4, Figure 4.4a and Figure 4.5a).

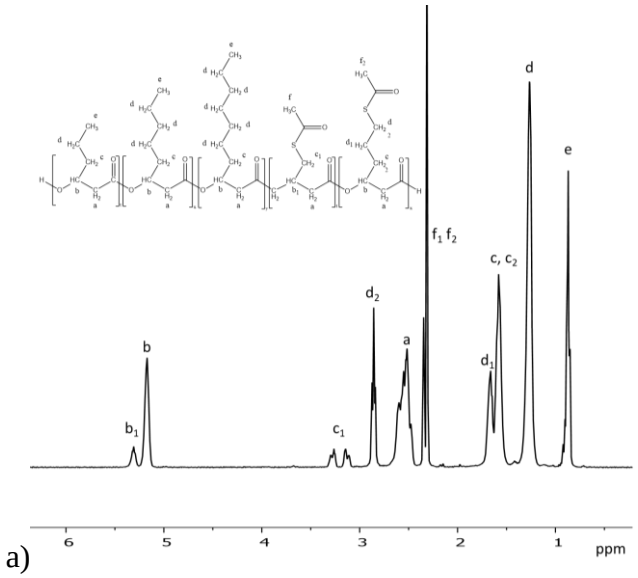

a)

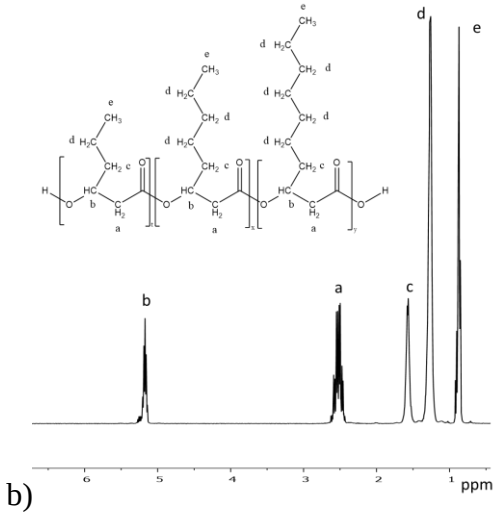

b)

Figure 4.3 ^{1}H-NMR spectra of a) P(3HHx-co-3HO-co-3HD-co-3H4ATB-co-3H6ATH) and b) P(3HHx-co-3HO-co-3HD). The chemical structure of the both polymers is shown in each figure, indicating the assignment of each peak to the corresponding proton atom in the molecule.

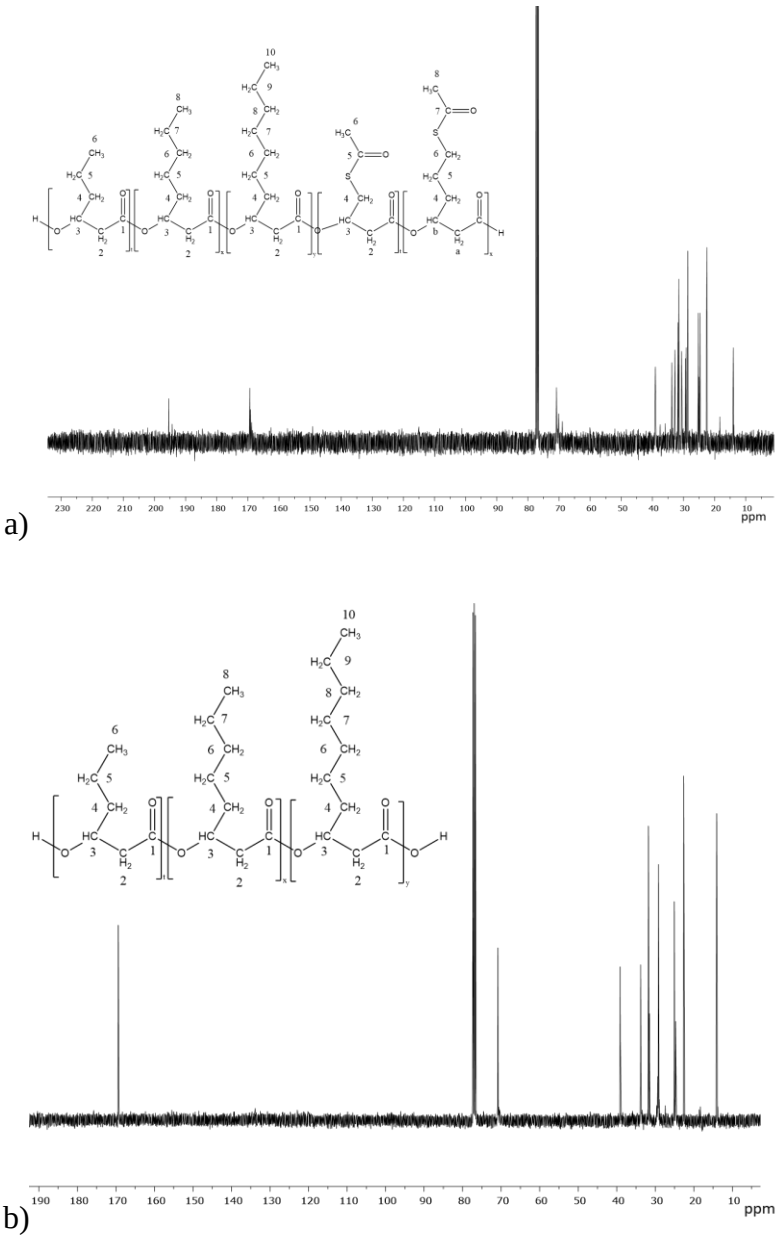

Figure 4.4 ^{13}C-NMR spectra of a) P(3HHx-co-3HO-co-3HD-co-3H4ATB-co-3H6ATH) and b) P(3HHx-co-3HO-co-3HD). The chemical structure of the both polymers is shown in each figure, indicating the assignment of each peak to the corresponding carbon atom in the molecule.

Table 4.3 List of the ^{13}C NMR peaks assigned for P(3HHx-co-3HO-co-3HD)

Carbon atoms	3HHx (δ, ppm)	3HO (δ, ppm)	3HD (δ, ppm)
C1	169.37	169.37	169.37
C2	39.09	39.09	39.09
C3	70.83	70.83	70.83
C4	35.8	33.73	33.80
C5	18.27	24.70	25.07
C6	13.78	22.63	31.91
C7		22.48	29.34
C8		13.96	29.17
C9			22.61
C10			14.05

Table 4.4 List of the ^{13}C NMR peaks assigned for P(3HHx-co-3HO-co-3HD-co-3H4ATB-co-3H6ATH)

Carbon atoms	3HHX (δ, ppm)	3HO (δ, ppm)	3HD (δ, ppm)	3H4ATB (δ, ppm)	3H6ATH (δ, ppm)
C1	169.37	169.37	169.37	169.17	169.37
C2	38.98	38.98	38.98	37.48	38.98
C3	70.77	70.77	70.77	68.97	70.77
C4	35.87	33.76	33.76	31.83	25.23
C5	18.30	24.70	25.07	30.44	32.76
C6	13.78	22.63	31.91		28.58
C7		22.48	29.34		30.60
C8		13.96	29.17		
C9			22.61		
C10			14.05		

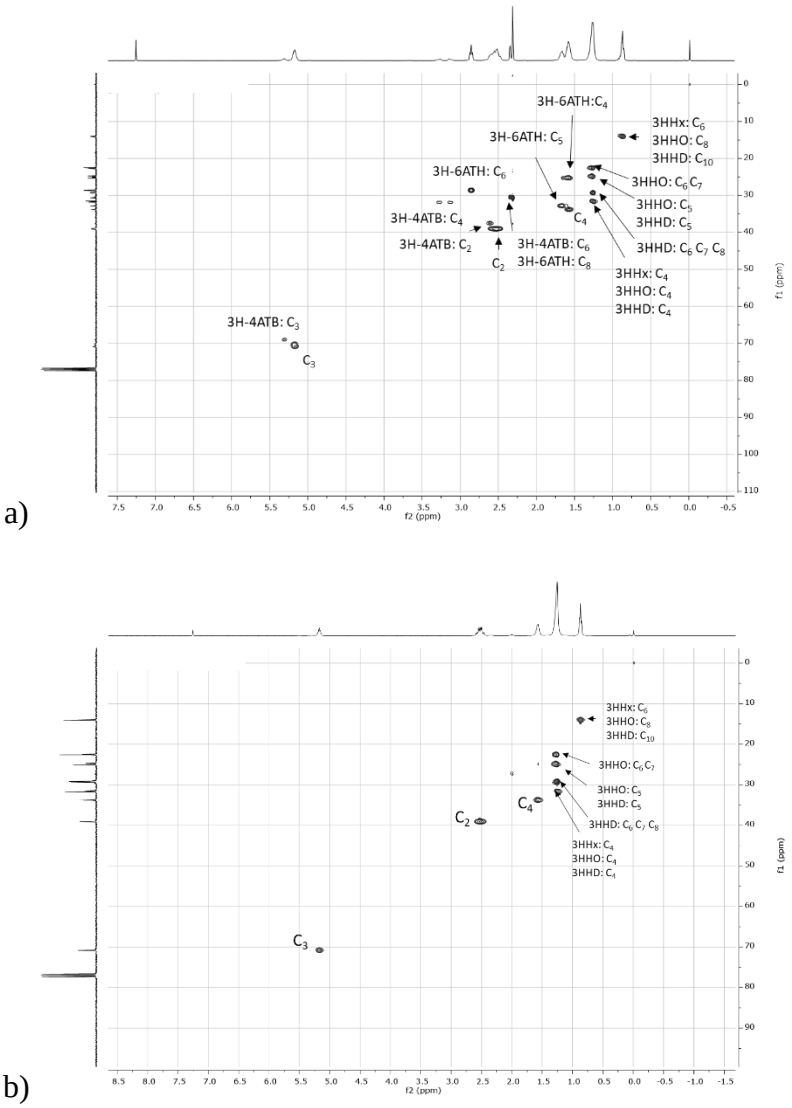

Figure 4.5 2D ^{1}H-^{13}C HSQC spectra of a) P(3HHx-co-3HO-co-3HD-co-3H4ATB-co-3H6ATH) and b) P(3HHx-co-3HO-co-3HD). In each spectrum, the cross-peaks were identified and labelled with the specific monomeric unit and the carbon atom involved in the single bond correlation (following the carbon atom assignments of Figure 4.4).

4.2.1.2. Thermal characterization

The thermal properties of the two polymers were investigated by DSC analysis and are shown in Table 4.5 and Figure 4.6.

The two materials showed different behaviour. P (3HHx-co-3HO-co-3HD) is a semi-crystalline material with a glass transition temperature of -41°C and a melting temperature peak of 51 °C and a melting range between 40-60 °C, properties typical of mcl-PHAs (Sudesh *et al.*, 2000). No melting temperature peak was detected for thioester-PHA (P(3HHx-co-3HO-co-3HD-co-3H4ATB-co-3H6ATH), indicating that the material was completely amorphous. The material showed only a glass transition of -32°C and was therefore in a rubbery state at room temperature.

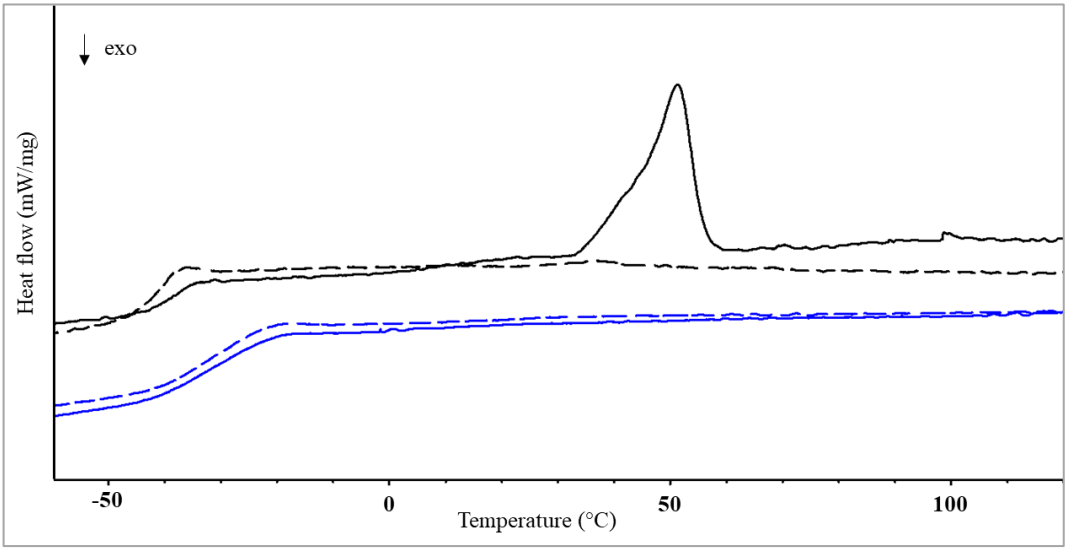

Figure 4.6 Representative DSC spectra of thioester-PHA (blue) and P(3HHx-co-3HO-co-3HD) (black). Solid lines represent first heating (–), while dashed lines (- -) represent second heating. Thermograms were shifted vertically for better visibility.

Table 4.5 Thermal properties of thioester-PHA and P(3HHx-co-3HO-co-3HD). T_m is the melting peak, T_g is the glass transition temperature, ΔH_m is the enthalpy of fusion and X_c is the % polymer crystallinity. The results are expressed as average ± standard deviation (n=3).

Polymer	Melting range (°C)	T_m (°C)	T_g (°C)	ΔH_m (J/g)
P (3HHX-co-3HO-co-3HD)	40-60	51 ± 2	-41 ± 1	15 ± 2
Thioester-PHA	n.d.	n.d.	-32 ± 1	n.d.

4.2.1.3. Biological characterization

4.2.1.3.1. Antibacterial properties

Preliminary investigation of the antibacterial activity of the thioester containing PHAs was evaluated using the ISO 22196 against *S. aureus* 6538P and *E. coli* 8739. As described in the materials and methods, polyethylene terephthalate (PET) discs of 6 mm of diameter were coated with 2% (w/v) solutions of thioester-PHA and P(3HHx-co-3HO-co-3HD) for the test. PET discs without polymer coating were used as controls. The standard test is used to evaluate and quantify the antibacterial activity of polymeric surfaces by seeding a known amount of bacterial inoculum directly on the surface of the materials. After 24 hours of incubation, the number of viable cells were counted using a colony forming assay and normalised to the surface area of the material. As described in the standard procedure, the antibacterial activity (R) was expressed as the difference between the logarithm of the number of colony forming units present on the samples and the logarithm of the number of colony forming units present on the control (i.e. PET). The percentage antibacterial activity (R%) was also calculated as a % reduction of the number of microorganisms on the samples compared to the control.

As shown in Figure 4.7, thioester–PHAs were active against *S. aureus* 6538P as a significant decrease in the number of cells present on the surface of the material could be detected (p-value<0.0001). Thioester-PHAs induced a 92% reduction of the bacterial cell count, corresponding to an average antibacterial activity R of 1.15.

P(3HHx-co-3HO-co-3HD) did not show any antibacterial effect against the Gram positive bacteria. The negative average values of both R and R% for this material indicates that there

was a slightly increase in the number of viable cells present of this surface compared to the PET discs.

In the case of *E. coli* 8739, both the thioester-PHAs and P(3HHx-co-3HO-co-3HD) were not active against the Gram negative bacteria. P(3HHx-co-3HO-co-3HD) exhibited average values of R and R% of 0. For the thioester PHAs, a slight reduction of the bacterial cell count was observed (R% of 10%, R of 0.05), but no significant difference was detected between the thioester-PHA and P(3HHx-co-3HO-co-3HD).

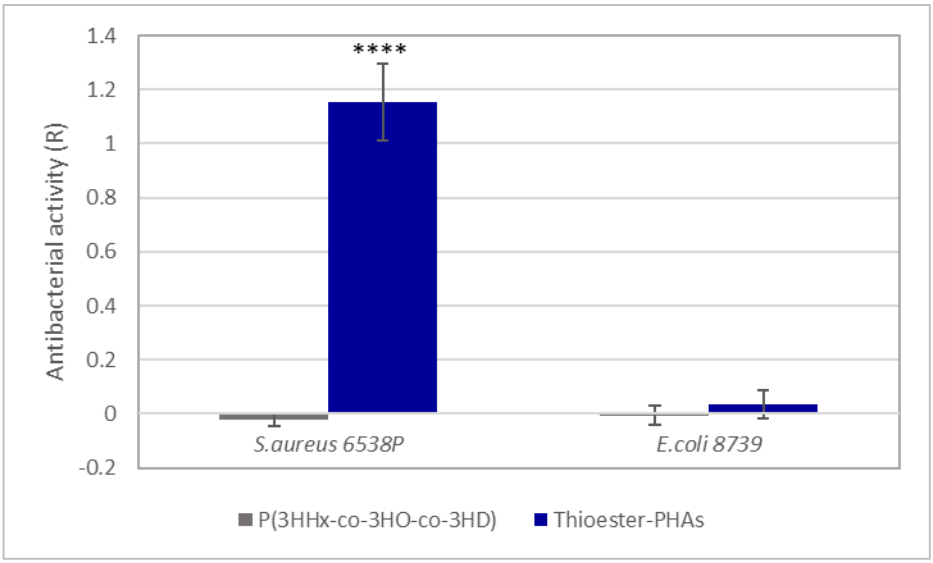

Figure 4.7 Antibacterial activity (R) (ISO 22196) of P(3HHx-co-3HO-co-3HD) (grey) and thioester-PHA (blue) against *S. aureus* 6538P and *E. coli* 8739. ** indicates statistically significant difference between thioester-PHA and P(3HHx-co-3HO-co-3HD) against *S. aureus* 6538P (*p*-value <0.0001). There was no statistically significant difference between the samples against *E. coli* 8739.**

Table 4.6 Percentage antibacterial activity (R%) and Antibacterial activity (R) values of thioester- PHA and P(3HHx-co-3HO-co-3HD) against *S. aureus* 6538P and *E. coli* 8739.

Sample	***S. aureus* 6538P**		***E.coli* 8739**	
	R	***R(%)***	***R***	***R(%)***
P(3HHx-co-3HO-co-3HD)	-0.02 ± 0.03	-5 ± 6	0 ± 0.04	0 ± 8
Thioester-PHA	1.15 ± 0.15	92 ± 4	0.05 ± 0.1	9 ± 11

4.2.1.3.2. In vitro cell compatibility studies

Preliminary cell viability studies were conducted culturing MC3T3-E1 cells on the surface of the materials for 1, 3 and 7 days. Figure 4.8 shows the cell viability of P(3HHx-co-3HO-co-3HD) and P(3HHx-co-3HO-co-3HD-co-3H4ATB-co-3H6ATH) compared with the positive control (i.e. cell cultured on TCP). For all the time points, the cell growth on both materials was comparable to that of the positive control without statistically significant differences.

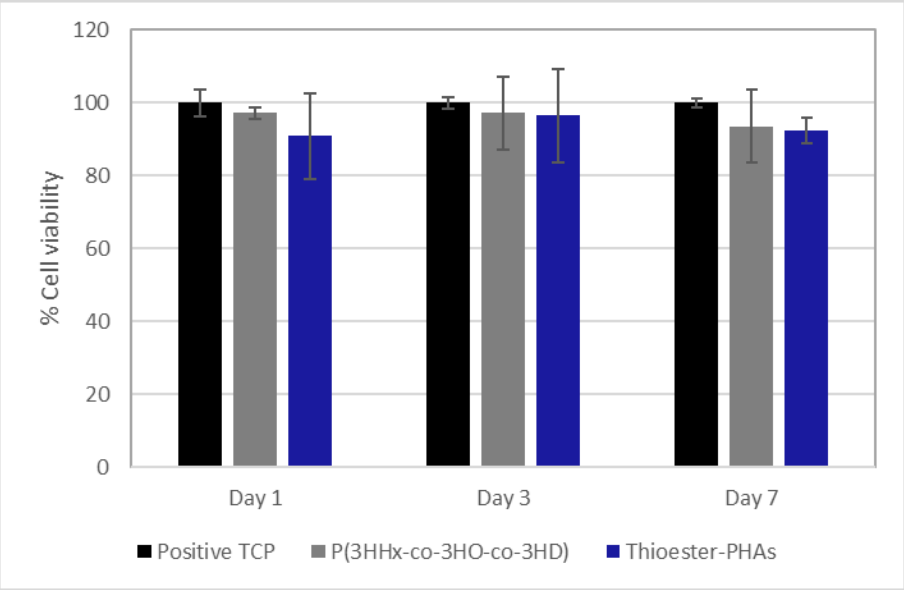

Figure 4.8 Cell viability study of MC3T3-E1 cells on thioester-PHA (blue) and P(3HHx-co-3HO-co-3HD) (grey) at day 1, 3 and 7 (n = 3). The positive control was Tissue Culture Plastic (TCP) (black). There was no statistically significant difference between the samples (*p*-value > 0.5).

4.2.2. Development of 2D antibacterial blend films

Due to the amorphous properties of thioester-PHAs, these materials were not suitable as bulk materials for the production of scaffolds. For this reason, physical blending with P(3HHx-co-3HO-co-3HD) was evaluated. Solvent cast films of 5% w/v polymer solutions were obtained with the following ratios: 100:0, 90:10, 80:20 (P(3HHx-co-3HO-co-3HD): thioester-PHA). Samples with a concentration of thioester PHA higher than 20 were not processable, as the films obtained were sticky and could not be removed from the glass petri dish.

The blend films obtained were characterized in terms of thermal, mechanical, antibacterial and biocompatibility properties.

4.2.2.1. Thermal characterization

The thermal properties of the blend films were investigated using DSC analysis and are reported in Table 4.7. Representative thermograms of the blend films are shown in Figure 4.9.

The blend films containing 10 and 20% of thioester-PHA showed properties comparable with the neat P(3HHx-co-3HO-co-3HD) films without any statistically significant differences. In particular their properties were typical of mcl-PHAs showing a melting range between 40 and 60 °C and a glass transition of -44°C, indicating that the materials are in a rubbery state at room temperature. As described in the materials and methods section 2.11.4, the enthalpy of fusion of the blend films was normalized to mass fraction of the P(3HHx-co-3HO-co-3HD) (i.e. 1, 0.9 and 0.8 for 100:0, 90:10 and 80:20 blends). No statistically significant differences in the normalized enthalpy of fusion could be detected between the blend samples and P(3HHx-co-3HO-co-3HD) films.

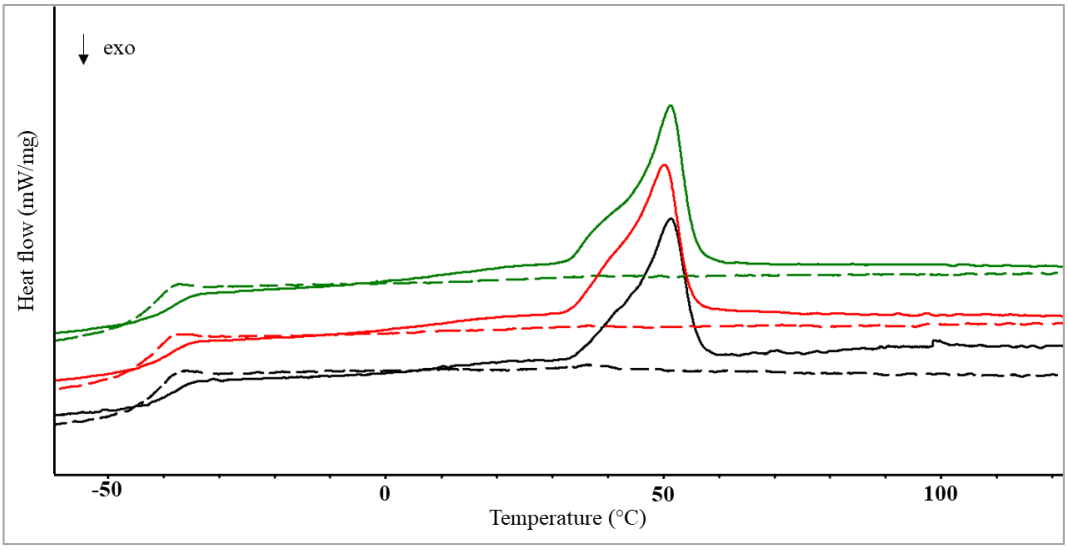

Figure 4.9 Representative DSC thermograms of P(3HHx-co-3HO-co-3HD): thioester-PHA) blends, 100:0 (black), 90:10 (red), 80:20 (green), 0:100 (P(3HHx-co-3HO-co-3HD): thioester-PHA). Solid lines represent first heating (–), while dashed lines (- -) represent second heating. Thermograms were shifted vertically for better visibility.

Table 4.7 Thermal properties of 100:0, 90:10, 80:20, 0:100 (P(3HHx-co-3HO-co-3HD): thioester-PHA) P(3HHx-co-3HO-co-3HD) and thioester-PHA blends. T_m is the melting peak, T_g is the glass transition temperature, ΔH^n_m is the enthalpy of fusion normalized to the mass fraction of P(3HHx-co-3HO-co-3HD). The results are expressed as average ± standard deviation (n=3).

Polymer	Melting range (°C)	T_m (°C)	T_g (°C)	ΔH (J/g)
P(3HHx-co-3HO-co-3HD)	40-60	51 ± 2	-41 ± 1	15 ± 2
90:10	40-60	53 ± 1	-45 ± 1	17 ± 2
80:20	40-60	53 ± 3	-44 ± 3	18 ± 1
Thioester - PHA	n.d.	n.d.	-32 ± 1	n.d.

4.2.2.2. Mechanical characterization

The mechanical properties of the blend films were assessed by tensile testing of the films and are reported in Table 4.8.

The control samples P(3HHx-co-3HO-co-3HD) (100:0) showed a typical elastomeric behaviour of mcl-PHAs, with an average elastic modulus of 2.8 MPa, ultimate tensile strength of 3.1 MPa and an elongation at break of 325%.

Both blend films 90:10 and 80:20 still showed an elastomeric behaviour, as expected. In particular, the samples containing 10% w/w of thioester PHAs did not show significantly different properties compared to the control material for all the parameters evaluated (*p*-value>0.05). On the contrary, blend films containing 20% w/w of thioester PHAs induced a significant increase of the elongation at break (average value of 392%, *p*-value < 0.05).

Table 4.8 Mechanical properties of 100:0, 90:10, 80:20 (P(3HHx-co-3HO-co-3HD): thioester-PHA) P(3HHx-co-3HO-co-3HD) and thioester-PHA blends E is the Young's modulus, ε_u is the ultimate tensile strength and σ_u is the elongation at break. The results are expressed as average ± standard deviation (n=3)

PHA	E [MPa]	σ_U [MPa]	ε_U [%]
P(3HHx-co-3HO-co-3HD)	2.8 ± 1	3.1 ± 0.5	325 ± 40
90:10	2.5 ± 0.5	3.5 ± 2	345 ±25
80:20	3.1 ± 1.5	3 ± 2	392 ± 16

4.2.2.3. Biological characterization

4.2.2.3.1. Antibacterial properties

The antibacterial properties of the blend films against *S. aureus* 6538P were investigated using the ISO 22196 as described in the previous section and the results are shown in Figure 4.10 and Table 4.9. The control was neat P(3HHx-co-3HO-co-3HD) (i.e. 100:0 blend).

Blends with 10% of the thioester-PHA showed a low average reduction of the bacterial cell count (R%) of 13%, corresponding to an average R value lower than 0.1. However, no statistically significant differences were detected between the 100:0 blends and 90:10 blends. A higher activity was detected for blends with 20% of thioester-PHA, inducing an average 71% reduction of the number of cells growing on the surface of the material (average R value of 0.56). This value was statistically higher than both 100:0 (p-value<0.01) and 90:10 (p-value<0.05) blends.

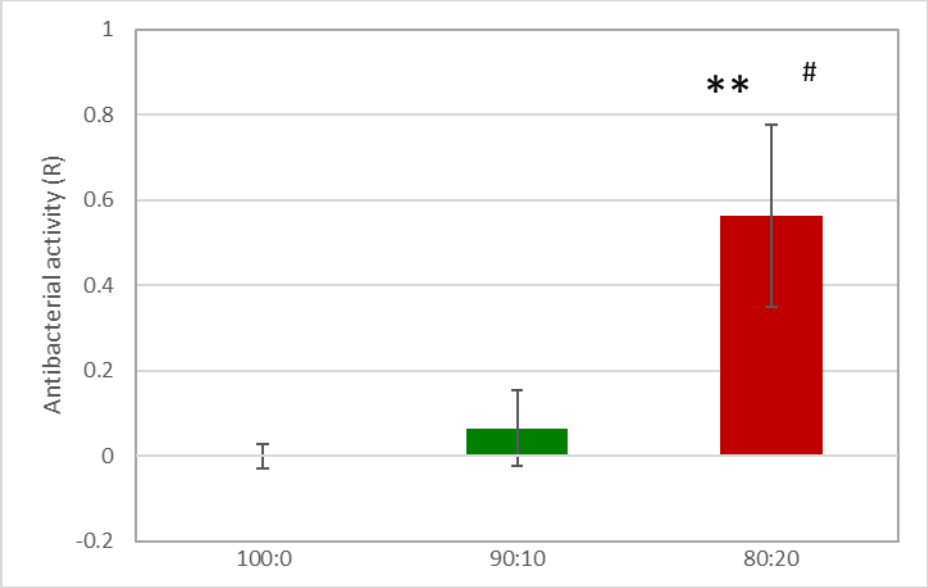

Figure 4.10 Antibacterial activity (R) (ISO 22196) of 100:0 (grey), 90:10 (green), 80:20 (red) (P(3HHx-co-3HO-co-3HD): thioester-PHA) P(3HHx-co-3HO-co-3HD) and thioester-PHA blend films against *S. aureus* 6538P (n=3). **indicates significant difference between of 80:20 P(3HHx-co-3HO-co-3HD)/Thioester-PHA and 100:0 P(3HHx-co-3HO-co-3HD)/Thioester-PHA samples (p-value<0.01). # indicates statistically significant difference between of 80:20 P(3HHx-co-3HO-co-3HD)/Thioester-PHA and 90:10 P(3HHx-co-3HO-co-3HD)/Thioester-PHA samples (p-value<0.05).

Table 4.9 Percentage antibacterial activity (R%) and Antibacterial activity (R) values of 100:0, 90:10, 80:20 (P(3HHx-co-3HO-co-3HD): thioester-PHA) P(3HHx-co-3HO-co-3HD) and thioester-PHA blends against *S. aureus* 6538P.

Sample	*S. aureus* 6538P	
	R	***R (%)***
100:0	0 ± 0.03	0 ± 6
90:10	0.07 ± 0.1	13 ± 16
80:20	0.56 ± 0.2	71 ± 14

4.2.2.3.2. In vitro cell compatibility studies

The direct biocompatibility of the 2D antibacterial blend films of thioester-PHA and were investigated using MC3T3-E1 cell line (Figure 4.11). The cells were seeded on top of the samples for 1,3, and 7 days and the cell viability was compared with the positive control (Tissue culture plate, TCP).

In the case of the blend film with 10% of thioester-PHA, no statistically significant difference was evidenced between the samples and the positive control for all the time points evaluated.

At day 1, the blend with 20% of thioester showed a lower cell viability compared to the positive control, showing an average cell viability of 81% (p-value<0.001). The compatibility of the blend samples increased over time. At day 1 and day 7 no significance difference was detected between the blend film and the positive control (average cell viability of 94% and 103% respectively). Moreover, the cell viability of the samples at day 1 was significantly higher than at day 3 (p-value<0.001) and the cell viability at day 7 was significantly higher than at day 3 (p-value<0.01).

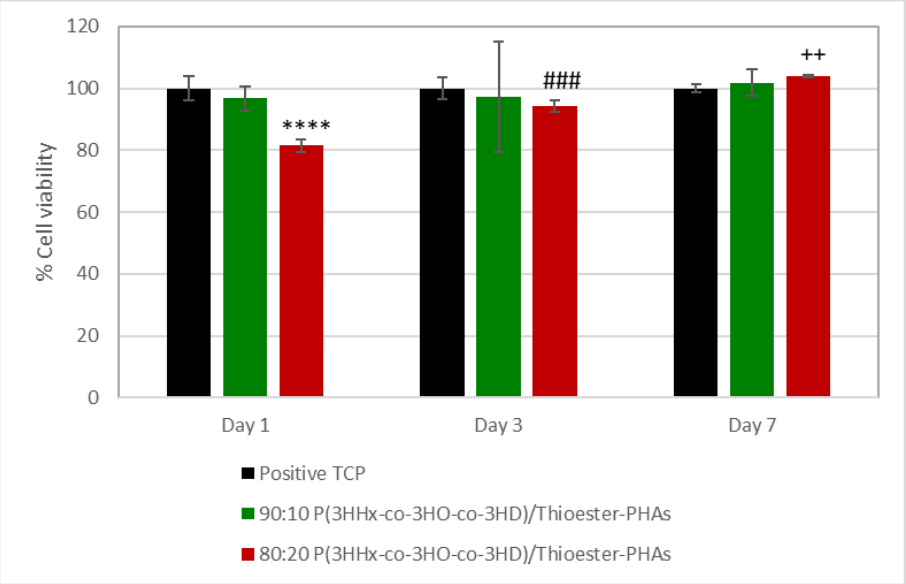

Figure 4.11 Cell viability studies of MC3T3-E1 cells seeded on 90:10 (green) and 80:20 (red) (P(3HHx-co-3HO-co-3HD): thioester-PHA) blend films at day 1,3 and 7 (n = 3). The positive control was Tissue Culture Plastic (TCP) (black). **** indicates statistically significant difference between 80:20 P(3HHx-co-3HO-co-3HD)/Thioester-PHA and the positive control (*p*-value<0.0001) at day 1. $^{###}$ indicates statistically significant difference of 80:20 P(3HHx-co-3HO-co-3HD):thioester-PHA between day 1 and day3 (*p*-value<0.001). $^{++}$ indicates statistically significant difference of 80:20 P(3HHx-co-3HO-co-3HD)/Thioester-PHA between day 3 and day 7 (*p*-value<0.01).

The morphology, adhesion and proliferation of the MC3TC-E1 cells on the blend samples at day 1 and day 3 was investigated using SEM imaging.

Figure 4.12 shows that at day 1 the cells were able to attach on the surface of both 90:10 and 80:20 (P(3HHx-co-3HO-co-3HD): thioester-PHA) blend films. The cells showed a triangular and elongated shape with filopodia typical of the MC3T3-E1 cell line (Gong *et al.*, 2013). At day 7, a continuous monolayer could be detected, showing that the cells were able to grow and proliferate on the surface of both materials. These qualitative results were also a confirmation of the cell viability data.

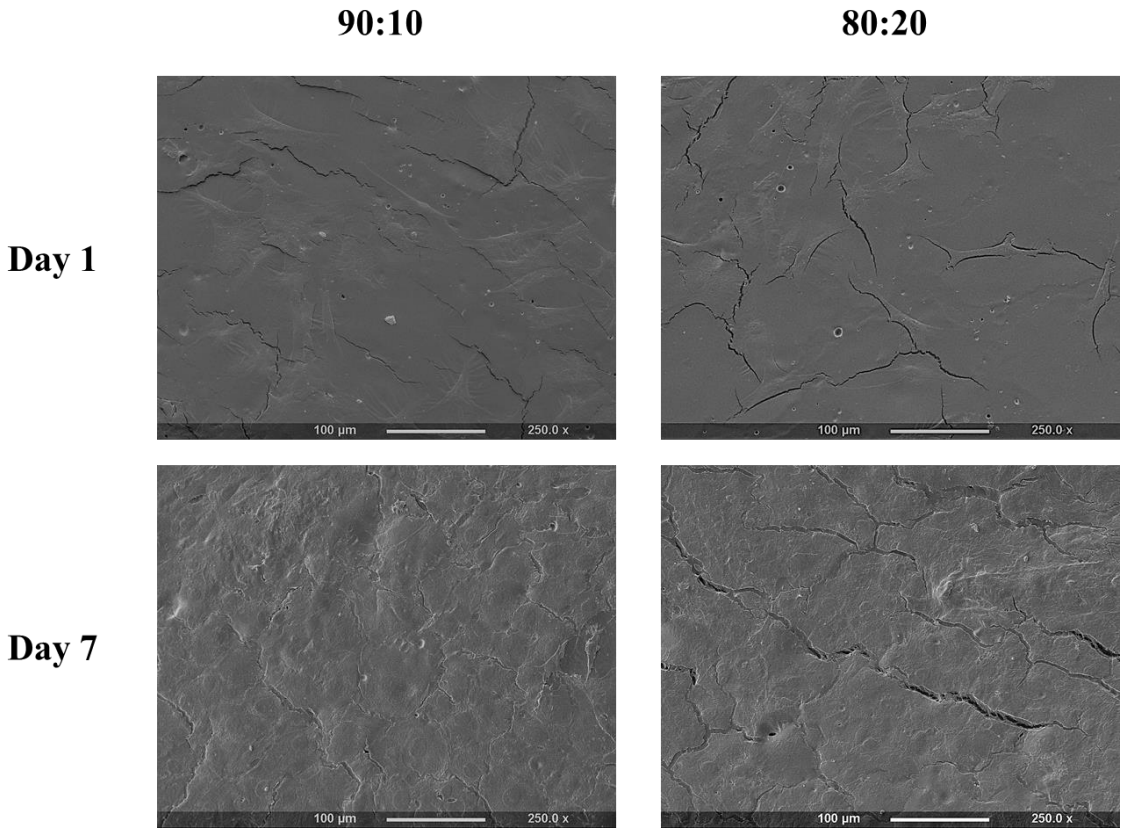

Figure 4.12 SEM images of MC3T3-E1 cells seeded on 90:10 and 80:20 (P(3HHx-co-3HO-co-3HD): thioester-PHA)blend films at day 1 and day 7.

4.3. Discussion

In this chapter the production of inherently active antibacterial polyhydroxyalkanoates was investigated and the polymers obtained were completely characterized in terms of physical, chemical and thermal properties.

Co-metabolism strategies have been employed to obtained PHAs with tailored functional groups. Cofeeding strategies are required as the carbon sources utilized can be divided into two categories. The "good" substrates are able to favour both growth of the bacteria and polymer accumulation, "poor" substrates are able to support growth but not PHAs accumulation or cannot support both growth and polymer accumulation (Lenz *et al.*, 1992; Scholz *et al.*, 1994; Kim *et al.*, 2000). Therefore, when a "poor" substrate is required to obtain a polyester with a specific composition, mixtures with "good" substrates have to be employed. For example, in order to produce copolymers of poly(3-hydroxybutyrate- co-hydroxyvalerate), P(3HB-co-3HV), propionic acid or alternative propionogenic compounds

are required, which however significantly hinder bacterial growth at low concentrations. For this reason cofeeding with for instance glucose has been investigated to obtain such PHAs (Hazer and Steinbüchel, 2007; Ramsay *et al.*, 1990). For mcl-PHAs, *P. oleovorans* 2937 has been investigated for the production of PHAs incorporating several functional groups, such as aromatic groups or methyl branched or phenoxy groups, through the use of cofeeding strategies with fatty acid (i.e. nonanoic or octanoic acid) to support and enhance bacterial growth (Scholz *et al.*, 1994; Curley *et al.*, 1996; Kim *et al.*, 1996).

In this chapter, a cofeeding strategy was employed to obtain PHAs containing thioester groups in the side chains, following an optimized protocol by Escapa *et al.*, 2011. The compound selected possessing the desired functional groups, 6 acetylthiohexanoic acid, can be in fact categorized as a poor substrate as it cannot support bacterial growth. By mixing it with decanoic acid, P. *putida* KT2442 was able to grow and accumulate PHAs with a final polymer yield of 24% dcw and a biomass concentration of 0.5 g/L.

Even though cofeeding approaches have been greatly investigated to obtain mcl-PHAs with novel functional groups, the molecular mechanism behind the use of such strategies has not been fully elucidated. Recently the use of fatty acids as the good substrates for co-metabolism strategies in *P. putida* strains has been attributed to the role of PhaD protein, which acts as a transcription factor for the expression of phasins, proteins that are involved in the formation of PHA inclusions (Sandoval *et al.*, 2007; Sudesh *et al.*, 2000). The PhaD protein has been shown to regulate the *pha* cluster (i.e. the group of genes involved in the expression of proteins involved in PHA metabolism) and its activation has been described to be induced by the presence of intermediates of the β-oxidation pathway (pathway used in the presence of fatty acid) (De Eugenio *et al.*, 2010; Tortajada *et al.*, 2013). De Eugenio *et al.* showed in fact a significant decrease of PHAs accumulation when a mutant strain of *P. putida* lacking the gene *phaD* (encoding for PhaD protein) was grown in the presence of octanoic acid compared to the wild type strain (18%dcw vs 70%dcw). Moreover, an increased transcription level of the genes encoding for crucial proteins for PHA accumulation were significantly higher in the presence of octanoic acid compared to glucose (i.e. structurally unrelated carbon source) (De Eugenio *et al.*, 2010). Thus, the role of the PhaD protein also supports the lower productivity of *Pseudomonas sp*. when cultured using structurally unrelated carbon sources (e.g. glucose) as in this case the *pha* cluster would be activated due to the basal activity of *pha* promoters (Tortajada *et al.*, 2013; De Eugenio *et al.*, 2010; Prieto *et al.*, 2016).

The polymer produced was characterized in terms of physical, chemical and thermal properties and compared to the PHAs obtained using control conditions (i.e. decanoic acid as the only carbon source with equimolar carbon concentration).

Preliminary characterization of the materials produced was conducted through FT-IR analysis. The polymer obtained with the co-feeding experiment showed an extra peak at 1690 cm^{-1} in addition to the two typical peaks of mcl-PHAs (1735 cm^{-1} for the carbonyl group and 2930 cm^{-1} for the aliphatic groups). This peak is associated with the stretching of the carbonyl group of the thioester bond and has been firstly identified by Lütke-Eversloh *et al.*. In their work they identified a new class of PHAs containing thioester bonds in the main chain in the form of 3-mercaptopropionate (3MP), 3-mercaptobutyrate (3MB) or 3-mercaptovalerate (3MV), which were incorporated as copolymers with 3-hydroxybutyrate (3HB). Therefore, the FT-IR confirmed that the polymer produced by P. *putida* KT2442 is a polyester containing thioester bonds.

The characterization of the monomeric composition of the materials produced was conducted through GC-MS and NMR analysis. When *P. putida* KT2442 was cultured in control conditions, using only decanoic acid as the carbon source, 3 monomeric units were detected, 3HHx (7 mol%), 3HO (64 mol%), 3HD (29 mol%). A similar composition was obtained by Ouyang *et al.* by culturing *P. putida* KT2440 in decanoic acid (3HHx 16 mol%, 3HO 54 mol% and 3HD 28 mol%). As described in the discussion session of Chapter 3, in the presence of structurally related carbon sources the β-oxidation pathway is involved in the polymer production and the structure of PHA produced is closely linked to the one of the carbon source employed. The longest monomer unit (in this case 3 -hydroxydecanoate) corresponds to the length of the carbon compound used as the substrate (decanoic acid, 10 carbon atoms). Moreover, the length of the other monomeric units present (3-hydrohyhexanoate, six carbons and 3-hydroxyoctanoate, eight carbons) are obtained by decreasing the number of carbon atoms of the substrate (ten carbon atoms) by 2 (or multiple of 2), as during each cycle of the β-oxidation pathway the fatty acids are shortened by 2 carbon atoms (Sudesh *et al.*, 2000; Madison and Huisman, 1999; Ciesielski *et al.*, 2015). Finally, the high content of 3HO and 3HD is due to the high specificity of the enzyme involved in the PHA polymerization (i.e. PHA synthase) for 3-hydroxyanoyl-CoA precursor containing eight or ten carbon atoms (i.e. 3-hydroxyoctanoyl-CoA and 3-hydroxydecanoyl-CoA) (Ashby and Foglia, 1998). The same considerations on the molecular composition apply to the polymer obtained using the co-feeding experiment. In particular, due to the

presence of 6-acetylthiohexanoic acid the polyester obtained was characterised by two extra monomeric units, 3-hydroxy-6-acetylthiohexanoate (32.5 mol%) and 3-hydroxy-4-acetylthiobutanoate (13 mol%). As expected the former showed the same chemical structure of the carbon source utilized and the latter was shortened by 2 carbon atoms due to the inherent mechanism of the β-oxidation pathway (Sudesh *et al.*, 2000; Ashby and Foglia, 1998).

As regards the thermal properties of the material, P(3HHx-co-3HO-co-3HD) showed typical features of an mcl-PHAs with a melting temperature range between 40-60 °C and a low glass transition of -41°C. On the contrary, the thioester PHAs did not show a melting peak and possessed a glass transition of -32 °C. These results indicate that the thioester copolymer produced was completely amorphous as the presence of thioester groups hindered the formation of crystalline regions in the polymer. This behaviour is known in literature and is usually found in PHAs containing a high amount of long polymeric chains or due to the presence of unusual functional groups in their side chains, such us phenoxy, methylphenoxy, nitrophenyl and thiophenoxy groups (Basnett, *et al.*, 2017b; Muangwong *et al.*, 2016; Takagi *et al.*, 1999; Aróstegui *et al.*, 1999; Kim *et al.*, 2000, 1996). In this case the presence of thioester groups hinders the arrangement of the polymer into organized structures.

The antibacterial properties of the produced polymers were investigated using a standard ISO test (ISO 22196), a direct contact method largely used for the quantification of the antimicrobial activity of materials (Molling *et al.*, 2014). The test evaluates the reduction in the number of viable bacterial cells after their incubation on the surface of the material for 24h. Among the bacteria suggested in the ISO, *S. aureus* 6538P and *E. coli* 8739 were chosen as examples of Gram positive and Gram negative bacteria. The thioester- PHAs showed an antibacterial effect against *S. aureus* 6538P, inducing a 91% reduction of the bacteria cell count. On the contrary, no significant efficacy could be detected against *E. coli* 8739. The activity of the polymer is most probably related to the presence of thioester groups in the polymer as P(3HHx-co-3HO-co-3HD) was inactive against *S. aureus* 6538P. These results confirmed that thioester-PHAs can be considered as inherently antibacterial polymers possessing a biocidal mode of action on contact. However, the mechanism behind the antimicrobial activity of thioester groups has not yet been determined. To date in literature no other polymers containing thioester groups have been studied for antibacterial properties. Recently, chitosan functionalized with thiol-alkyl chains showed higher antimicrobial

activity compared to normal chitosan. The higher efficiency was hypothesized to be related to hydrophobic interaction of the alkyl chains with the bacterial cell wall components and a reaction of the thiol-groups with cysteine residues (Croce *et al.*, 2016; Borsagli *et al.*, 2019; Dragostin *et al.*, 2016).

The higher selective towards Gram positive bacteria compared to Gram negative bacteria has been evidenced for many antimicrobial polymers that exert their activity through the interaction and disruption of the bacterial cell membrane (Muñoz-Bonilla and Fernández-García, 2012; Timofeeva and Kleshcheva, 2011). This is due to the fact that Gram negative bacteria possess a more complex cell membrane as they present an additional layer composed of lipopolysaccharides and phospholipids compared to Gram positive ones. This extra layer acts as a barrier against harmful molecules (Ghai and Ghai, 2018; Choi and Lee, 2019; Miller, 2016). The presence of long alkyl chains in the polyhydroxyalkanoates could also participate in the antibacterial activity of the material. Many antimicrobial polymers possess in fact cationic groups conjugated with hydrophobic alkyl chains or a random distribution of cationic side groups and hydrophobic chains (Palermo *et al.*, 2019; Timofeeva and Kleshcheva, 2011; Nigmatullin and Gao, 2012). Their mechanism of action is generally considered to be characterized by binding of the positive moieties to the bacterial cell membrane through electrostatic interactions causing disruption, followed by penetration of the hydrophobic alkyl chains inside the hydrophobic cell wall, inducing permeabilization and cellular death (Ergene *et al.*, 2018; Kuroda *et al.*, 2009; Palermo *et al.*, 2019). Nevertheless, in depth studies need to be conducted to gain insight into the mode of operation of the produced thioester-PHAs.

Limited work has been conducted in literature regarding the application of thioester-PHAs as materials in the medical field. Dinjaski *et al.* performed preliminary biocompatibility studies of the material applied in the form of coatings on PET disks using BALB 3T3 fibroblasts, showing that the polymer does not show any detrimental effect against these mammalian cell lines. The materials were also implanted *in vivo* subcutaneously in mice, inducing low inflammation and still possessing antibacterial activity (Dinjaski *et al.*, 2014).

In this study the possibility of applying thioester-PHAs in bone tissue engineering applications was evaluated. Preliminary direct biocompatibility studies were performed seeding MC3T3-E1 cells on the surface of PET samples coated with the inherently

antibacterial material. The results show that the thioester-PHAs possessed good cytocompatibility towards the MC3T3-E1 cell line.

To further expand the application of thioester-PHAs in tissue engineering, blending with P(3HHx-co-3HO-co-3HD) was carried out to develop materials that could be used as bulk components for the production of scaffolds. The amorphous nature of such inherently antibacterial polymer combined with the low glass transition (below zero degrees) limit its use to the production of antimicrobial coatings or adhesives. Physical blending is an easy and simple technique that has been extensively investigating in literature to combine materials properties, merging the advantages of each single components and overcoming their limitations. In this case, P(3HHx-co-3HO-co-3HD) conferred mechanical properties and processability to the final material while thioester-PHAs introduced antibacterial features.

Blend films with a ratio of 90:10 and 80:20 (P(3HHx-co-3HO-co-3HD): thioester-PHA) were obtained through solvent casting technique in chloroform and the samples were characterized in terms of thermal, mechanical and biological properties. Films with a higher content of thioester-PHA (70:30, P(3HHx-co-3HO-co-3HD): thioester-PHA) could not be processed as the resulting sample were difficult to handle.

When mixing two polymers, three different systems can be obtained: miscible, partially miscible or immiscible. Analysis of the glass transition of the final system is used as one of the main tools to determine the state achieved. If one single T_g with a value intermediate between the two components is obtained the system is considered miscible. If two T_gs are obtained each corresponding to the one of the components, the system is immiscible. When two T_gs are evidenced with intermediate values, the two material are considered partially miscible (Runt and Huang, 2002; Sarath *et al.*, 2014; Niaounakis, 2015). In this study, one T_g was detected in the blend films containing 10 and 20 % of thioester-PHA, indicating that a miscible system was obtained. Several studies have analysed the possibility of blending different types of PHAs. When mixing mcl and scl-PHAs an immiscible system was obtained. Dufresne and Vincendon, and Lizarraga-Valderrama *et al.* produced blends of P(3HB) and P(3HO) with a range from 100:0 (pure P(3HB)) to 0:100 (pure P(3HO)). Thermal analysis of all the samples showed the presence of two T_gs corresponding to the ones of the single polymers, confirming that a biphasic system was obtained (Dufresne and Vincendon, 2000; Lizarraga-Valderrama *et al.*, 2015). Conversely, miscible systems were obtained by combining P(3HB) with a hydrolysed low molecular weight amorphous mcl-PHA with a ratio of 80:20 (P(3HB): oligo mcl-PHA). The additive acted as a plasticiser

decreasing the crystallinity of the films and increasing their flexibility and ductility (Lukasiewicz *et al.*, 2018). Blending of two scl-PHAs has been shown to produce miscible systems (Chen and Luo, 2009). The miscibility of P(3HB) with P(3HB-co-3HV) depended on the monomeric content of 3-hydroxyvalerate. Copolymers containing a low amount of 3HV (<30%) showed compatibility with P(3HB) due to the similarity of their crystalline structure and crystallinity rate, inducing co-crystallization. Whilst a high content of 3HV led to immiscible systems and phase separation (Yoshie *et al.*, 1996; Saito *et al.*, 2001). Zheng *et al.* investigated blending of P(3HB) with P(3HB-co-3HHx) (with a 12 mol% of 3-hydroxyhexanoate) with a range of concentrations from 0 to 100%. All the compositions investigated resulted in miscible systems with a single T_g which decreased with increasing concentration of P(3HB-3HHx) (Zheng *et al.*, 2005). However, to date, no detailed investigations have been conducted on blends of mcl-PHAs. Therefore, further studies should be conducted to investigate the possible systems formed by such materials.

The influence of the incorporation of thioester-PHAs on the mechanical properties of the developed materials was investigated. The data obtained revealed that the blend films possessed an elastomeric behaviour comparable with the neat film (100:0 P(3HHx-co-3HO-co-3HD): thioester-PHA). In particular, the materials showed an average elastic modulus of 3 MPa and high elongation at break (>300%) which is typical of mcl-PHAs, with similar values to the one described in literature (Zinn and Hany, 2005; Jiang *et al.*, 2012). The presence of the thioester-PHAs did not significantly change the mechanical properties of the film. From literature it is known that the mechanical properties of blends are influenced by the ratio of the two polymers utilised (Utracki and Wilkie, 2014; Chen and Luo, 2009). For instance, Zhao *et al* showed that the mechanical properties of blend films of P(3HB) and P(3HB-co-3HHx) remained unchanged when 20% of P(3HB-co-3HHx) was used, while significant differences could be detected with higher concentrations (namely lower elastic modulus and higher elongation at break) (Zhao *et al.*, 2003). In this study, the materials with a higher concentration of thioester (i.e. 30%) were not handleable, while the two compositions developed could be processed and tested. On the contrary, other reports showed that the mechanical features of PHA-based blend films could be influenced with the use of low amounts of the minor constituent of the blend system (<30%). Lukasiewicz *et al.* evidenced higher elongation at break and lower elastic modulus for 90:10 and 80:20 P(3HB): oligo mcl-PHA blends compared to P(3HB). A similar behaviour was obtained by Lizarraga-Valderrama *et al.* when mixing P(3HB) with P(3HO) in a ratio of 75:25. In both studies

however, the changes in mechanical properties were correlated with a decreased in the enthalpy of fusion (and thereby of the degree of crystallinity) of the polymeric samples (Lizarraga-Valderrama *et al.*, 2015; Lukasiewicz *et al.*, 2018). In this study instead no significant change in the enthalpy of fusion of the samples could be detected.

To evaluate whether the blend films still preserved antibacterial properties, the quantitative standard ISO (ISO 22196) was performed. The study was conducted using *S. aureus* 6538P as the thioester-PHAs only showed a bactericidal activity against this bacterial strain. The antibacterial efficacy was dependent on the concentration of the inherently antibacterial material. Blend films with a low content of antimicrobial additive did not show a statistically significant activity. Blends with a higher content of thioester-PHAs (80:20) resulted in a 77% reduction in the number of bacteria.

Finally, *in vitro* biocompatibility studies were performed by seeding the MC3T3-E1 cells on the surface of blend materials for 1, 3 and 7 days. The sample with the lower content of thioester PHAs showed good cell viability for all the time points evaluated. The 80:20 blend films showed a reduction of the cell viability at day 1 compared to the positive control (tissue culture plastic). However, the average viability value for the samples was 81%, higher than 70%, the threshold value for a material to be considered biocompatible according to ISO 10993-5:2009 for the Biological Evaluation of Medical Devices. Moreover, at day 7 no statistically significant difference was detected between the sample and the control, indicating that the blend films were able to favour the attachment and growth of the preosteoblastic cells. In particular, SEM analysis confirmed such results, showing the formation of a continuous layer on the surfaces of the 2D inherently antibacterial blend films after 7 days.

In conclusion, these preliminary *in vitro* results show the potential of the 80:20 blend films of the thioester-PHAs and P(3HHx-co-3HO-co-3HD) as material for the development of biocompatible and inherently antibacterial scaffolds for bone regeneration.

4.4. Conclusions

In this chapter, inherently antibacterial PHAs, thioester-PHAs, were successfully produced through bacterial fermentation by *P. putida* KT2442 using decanoic acid and 6-acetylthiohexanoic acid as carbon sources. The material was completely characterized in terms of physical, chemical and thermal properties. The antibacterial properties of the produced polymer were evaluated using ISO 22196 against different bacterial strains. Thioester-PHAs exhibited antibacterial activity against *S. aureus* 6538P, showing a decrease in the number of cells growing on the surface of the material. This activity was most likely due to the presence of thioester groups in the polymer as the polymer obtained from the control condition was inactive against *S. aureus* 6532P. Moreover, the material exhibited good cytocompatibility towards MC3T3-E1 cells, showing potential for its use in bone tissue regeneration. Physical blending of thioester-PHAs and P(3HHx-co-3HO-co-3HD) (i.e. polymer obtained using control conditions) was investigated to broaden the medical applications of such amorphous inherently antibacterial materials. A composition of 80:20 (P(3HHx-co-3HO-co-3HD): thioester-PHA) was found to be optimal for the achievement of miscible, handleable and processable materials possessing antibacterial and biocompatibility properties.

Chapter 5

Development of novel 2D composite antibacterial structures

5.1. Introduction

Composite materials are being widely investigated in literature due to the possibility of obtaining novel structures with superior properties by combining the advantageous features of two or more compounds. The use of composite materials can be beneficial to improve the mechanical properties, the processability and the degradability of the final scaffold. Moreover, a combination of different compounds allows to create a structure that can better mimic the complex architecture of human tissues. This is particularly important in bone regeneration. Bone is indeed intrinsically a heterogeneous composite material composed of cells, an organic phase (the extra cellular matrix containing mainly collagen fibrils), an inorganic phase (mainly hydroxyapatite) and water (Chocholata *et al.*, 2019; Qu *et al.*, 2019; Clarke, 2008). Therefore, it is not surprising that in the last decades composite scaffolds have attracted great attention for bone tissue engineering applications (Rezwan *et al.*, 2006; Lei *et al.*, 2019). In particular, the most studied combination involves the use of polymers to provide elasticity and biodegradability, mimicking the role of the extracellular matrix, and ceramic to increase the mechanical strength and improve the interactions between the tissue and the final constructs (Kashirina *et al.*, 2019; Hajiali *et al.*, 2018).

Hydroxyapatite, $Ca_{10}(PO_4)_6(OH)_2$, is the main ceramic material used in the fabrication of composite scaffolds for bone regeneration as its chemical and crystal structure closely resembles that of natural hydroxyapatite (Kaur *et al.*, 2019a). This material has shown good biocompatibility, not-toxicity, osteoconductive properties, described as the ability to induce bone growth on the scaffold surface, and osteointegration, which refers to the formation of a stable anchorage between the bone and the constructs (García-Gareta *et al.*, 2015).

Moreover, the compressive strength of hydroxyapatite is similar to that of native bone, but the material possesses a brittle nature with low fracture toughness, limiting its use in load-bearing application and requiring its combination with polymeric materials (Rezwan *et al.*, 2006; Chocholata *et al.*, 2019). Another advantage of hydroxyapatite is that its crystalline structure can allow ion substitutions, meaning that the hydroxyl, phosphate and calcium ions can be substituted by ions of similar size and charge (Šupová, 2015; Li, 2017). Such ion exchange can be usually obtained either by co-precipitation methods, based on the addition of the metal ions before the hydroxyapatite formation, or by ion exchange mechanisms, where the ions are added after the hydroxyapatite has been produced (Li, 2017). The production of substituted hydroxyapatite has been studied to obtain a structure which resembles better the physiological composition of the bone, which is characterized by the presence of traces of several ions (K^+, Na^+, Cl^-, F^-, Fe^{2+}, Zn^{2+}, Sr^{2+}, Mg^{2+},SiO_4^{4-}, | CO_3^{2-}) (Ratnayake *et al.*, 2017; Kolmas *et al.*, 2014b). Moreover, the introduction of additional ions, defined as therapeutic ions (TIs), has emerged as an alternative to the use of bone morphogenetic proteins (BMPs) to introduce osteoinductive properties in the material. TIs offer the advantages of being less expensive and more stable than BMPs. Moreover, in addition to osteoinduction, the incorporation of TIs has been used to enhance the existing properties of the material (e.g. mechanical characteristics through the use of $Sr^{2+}$and Mg $^{2+}$) or introduce novel features (e.g. antibacterial properties with the use of Ag^+, Cu^{2+}) (Mouriño *et al.*, 2012; Hoppe *et al.*, 2013). In this study, a novel co-substituted hydroxyapatite was used, characterized by the introduction of strontium (Sr^{2+}) and selenite (SeO_3^{2-}) ions by a wet-coprecipitation method. The presence of such ions should confer to the material both osteoinductive and antibacterial properties. Strontium ions are one of the trace elements of the bone that has been studied due to its pivotal role in bone mineralization. Strontium has attracted attention in the latest years due to it is effect on bone cells. Strontium has been shown to elicit a bone remodelling effect through the increase of osteoblast activity inducing bone formation and the reduction of osteoblast proliferation and activity, therefore reducing bone reabsorption (Pors-Nielsen, 2004; Ratnayake *et al.*, 2017). For this reason, since 2004 a drug containing strontium, strontium ranelate, has been administered in Europe as a treatment for osteoporosis (Glenske *et al.*, 2018). The mechanism of action of this metal ion is related to its similarity with calcium which allows it to bind to calcium receptors present on the membrane of both osteoclasts and osteoblasts (Glenske *et al.*, 2018; Querido *et al.*, 2016). In the latter its binding to proteins induces the activation of signalling pathways that

lead to the enhancement of osteoblast proliferation, differentiation and activity. Simultaneously, such activation leads to the production of a glycoprotein (osteoprotegerin) which is able to inhibit the binding of a receptor activator of nuclear factor-κB ligand (RANKL) with the RANK receptor, suppressing osteoclast differentiation and activity (Boyce and Xing, 2007). In addition, the direct binding of strontium on the osteoclasts calcium receptors has been shown to induce cell apoptosis and therefore contributes to the reduction of bone resorption (Glenske *et al.*, 2018; Querido *et al.*, 2016). Thanks to these properties, strontium has been incorporated into a range of materials for bone regeneration, such us titanium implant coatings, bone cements and synthetic hydroxyapatite (Wong *et al.*, 2004; Capuccini *et al.*, 2008; Ravi *et al.*, 2012; Jiménez *et al.*, 2019).

Selenium is considered as one of the essential trace elements for the human body. Selenium deficiency has been associated with two diseases, the Keshan illness, which affects the heart in children, and the Kashin-Beck syndrome, which is a type of osteochondropathy characterized by cartilage and long bone degeneration (Moreno-Reyes *et al.*, 2001; Rodríguez-Valencia *et al.*, 2013). Selenium plays a crucial role in the human body through its incorporation in selenoproteins, which are proteins that possess in their active site a selenocysteine amino acid residue. Among this class of enzymes, one family, the glutathione peroxidase is particularly important due to its antioxidant role in the human body, protecting against oxidative stress (Ellwanger *et al.*, 2016). Such proteins catalyse the reduction of peroxides (i.e. hydrogen peroxide, and lipid and phospholipid hydroperoxides), reducing the formation of free radicals and reactive oxygen species, which can cause cell damage affecting membrane, lipids, phospholipids and DNA (Holben and Smith, 1999; Rayman, 2000). Selenium has also been linked with anticancer activity even though its mechanism of action is still not clear. It has been hypothesised that a number of pathways are involved including but not limiting to antioxidation effect (Wrobel *et al.*, 2016; Drake, 2006). This latter effect has been in fact ascribed to the capability of selenium to enhance cancer prevention, but it does not explain the anticancer effect that has been evidenced at high concentrations, exceeding the dosage that allows maximum expression of selenoproteins (Wrobel *et al.*, 2016). At these concentrations selenium has been associated with pro-oxidant activity, resulting in the formation of ROS species due to its metabolism inside the human body. To be incorporated into selenoproteins in fact hydrogen selenide (HSe^-) and methyl selenol (CH_3Se^-) intermediate metabolites are obtained by inorganic and organic selenium containing

compounds respectively. In the presence of low concentrations of Se, such metabolites will be converted into selenoproteins with an antioxidant effect. On the other hand, once a saturation level of synthesis of such antioxidant proteins has been reached, the presence of greater levels of selenium leads to a high accumulation of such metabolites which are highly redox reactive and are able to generate superoxide and hydrogen peroxide upon reaction with and oxidation of thiols (Misra *et al.*, 2015; Collery, 2018; Lee and Jeong, 2012). Moreover, selenium can interact with free thiols of enzymes or low molecular compounds, inducing thiol oxidation or formation of inter-molecular bonds (e.g. selenotrisulphide bonds (S–Se–S), selenenylsulphide bonds (Se–S), and diselenide bonds (Se–Se)). This can cause inactivation of the active site of critical enzymes or lead to protein unfolding and loss of biological activity (Gandin *et al.*, 2018; Fernandes and Gandin, 2015). Several studies have shown that selenium doped materials (e.g hydroxyapatite) induced apoptosis of bone cancer cells *in vitro* and inhibits the growth of bone tumours *in vivo* (Yanhua *et al.*, 2016; He *et al.*, 2019; Wang *et al.*, 2012). The selectivity towards cancer cells has been linked to the fact that high levels of ROS are present in such cells due to their abnormal metabolism, especially in early stages of tumour, which leads to a high expression of antioxidant activity. Such a condition might leave these cells to be more sensitive to an increase in the levels of ROS, inducing cell death. On the contrary, healthy cells are usually characterized by low levels of ROS and can counterbalance an increment by upregulating antioxidant systems. Therefore, a system that induces an increment of ROS necessary to kill cancer cells but still not harmful for healthy cells might represent an effective anticancer therapy (Gorrini *et al.*, 2013; Gandin *et al.*, 2018). Finally, recently selenium has been shown to possess an antibacterial activity against a range of bacteria (Huang *et al.*, 2016b; Medina Cruz *et al.*, 2018; Nguyen *et al.*, 2017). Even though the mechanism of action has not been fully elucidated, it has been attributed to the same principles of the anticancer activity, the induction of oxidative stress by the generation of ROS species and the depletion of thiol groups, inducing membrane and cell wall damage as well as permanent changes in cell components leading to bacterial death (Kolmas *et al.*, 2014b; Huang *et al.*, 2019).

In this chapter, the development of novel antibacterial composite 2D structures was investigated by the combination of PHAs with a novel hydroxyapatite. The hydroxyapatite was developed by Dr. Muhammad Maqbool (Early stage researcher of the Marie Curie HyMedPoly project) and it is characterized by a co-substitution of selenium and strontium

ions. The presence of such ions should confer to the material both osteoinductive and antibacterial properties. Two of the three PHAs produced were selected as bulk materials (as discussed in the Discussion section of Chapter 3): one scl-PHA and one mcl-PHA. P(3HB) was selected as it is an scl-PHA commonly used for bone applications due to it is mechanical properties. For the mcl-PHAs, P(3HO-co-3HD-co-3HDD) was selected over P(3HO-co-HD) due to its higher polymer yield as the two materials showed comparable physical, mechanical and biocompatibility properties.

Firstly, preliminary *in vitro* characterization of the novel hydroxyapatite was conducted through MIC and MBC tests. Then the effect of the combination of Se-Sr-HA with the two different PHAs in the form of 2D films on their physical, thermal and mechanical properties was reported. Finally, the antibacterial properties of the produced materials against both *S. aureus* 6538P and *E. coli* 8739 were investigated using both a direct contact (ISO 22196) and an indirect (antibacterial ion release) test.

5.2. Results

5.2.1. Antibacterial properties of Se-Sr-HA

Preliminary *in vitro* characterization of the antibacterial properties of the novel Se-Sr-HA was conducted following the ISO 20776. Such standard procedure allows to determine the minimal inhibitory concentration (MIC) and the minimal bactericidal concentration (MBC) of a compound through the broth dilution test. The material activity was tested against *S. aureus* 6538P and *E. coli* 8739, chosen as examples of Gram positive and Gram negative bacteria as specified in the ISO 22196 used for the characterization of antibacterial plastics. Briefly, the material in form of powder was suspended in Mueller Hinton broth to obtain a series of concentrations between 5 to 100 mg/mL and plated in 96 multi-well plates. Each well was then inoculated with a final microbial suspension adjusted to 5x10^5 and incubated at 37ºC for 24 hours at 100 rpm. The test was performed in triplicates. After the incubation time the optical density was measured at 600 nm and the MIC was determined as the lowest concentration of an antimicrobial agent that inhibits the visible growth of the bacteria analysed.

Figure 5.1 a and b show the variation of the optical density as a function of the Se-Sr-HA concentration against *S. aureus* 6538P and *E. coli* 8739 respectively. In both curves a similar

trend could be detected characterized by the inhibition of bacterial growth with increasing concentration of Se-Sr-HA. The MIC against *S. aureus* 6538P was 40 mg/mL, while the value for *E. coli* 8739 was 60 mg/mL.

Following the MIC test, the entire volume of the well containing the concentration of Se-Sr-HA identified as the MIC and of the wells with a concentration higher than the MIC were removed and spreaded onto agar plates to determine the MBC. The plates were incubated 37ºC for 24 hours. The MBC was determined as the lowest concentration of compound that induced 99.9% killing of the bacteria, corresponding to a visible reduction in the bacterial growth compared to the control conditions. Figure 5.2 a and b show the agar plates for both bacteria for the wells with concentration between 40 and 100 mg/mL for *S. aureus* 6538P and between 60 and 100 mg/mL *E. coli* 8739. In both cases, a uniform layer of bacteria could still be detected even at the highest concentrations tested (100 mg/mL).

a)

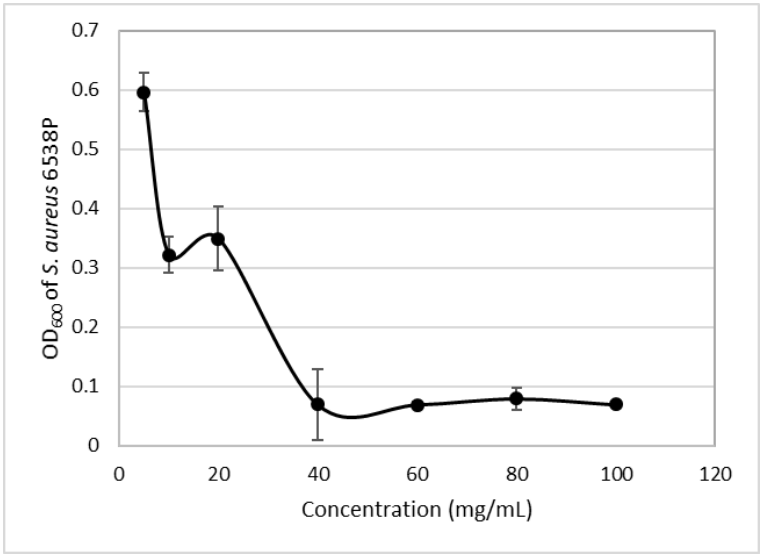

b)

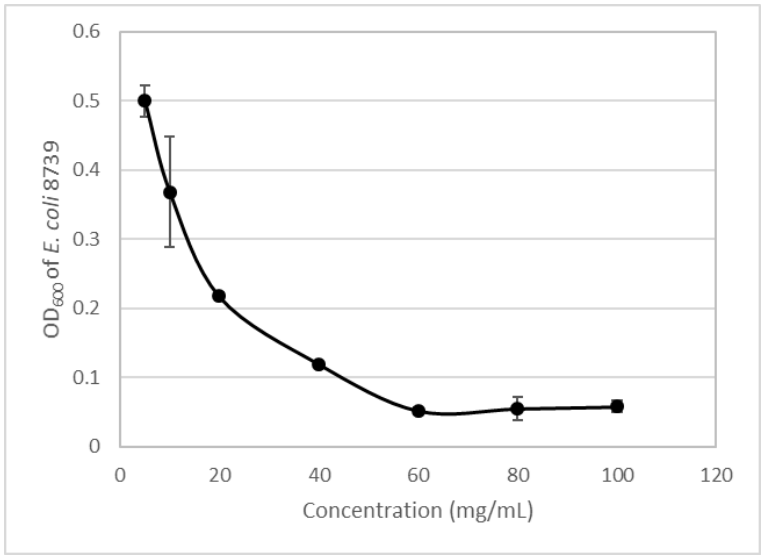

Figure 5.1 Variations of the OD_{600} of a) *S. aureus* 6538P and B) *E. coli* 8739 with the increase in the concentration of Se-Sr-HA powders (5 mg/mL-100 mg/mL). The Minimal Inhibitory Concentration (MIC) was determined as the lowest concentration of Se-Sr-HA that inhibits the visible growth of the bacteria analysed (OD_{600} lower than 0.1). The MIC against *S. aureus* 6538P was 40 mg/mL, while the value for *E. coli* 8739 was 60 mg/mL.

To better understand and quantify whether a reduction in the number of bacteria had occurred, the number of colony forming units of the bacteria present at the highest concentration investigated (100 mg/mL) was determined using the drop plate technique and compared to the CFU of the initial inoculum. The results are reported in Table 5.1 and expressed as a % reduction of the number of CFU compared with the positive control. Against both bacteria Se-Sr-HA induced a comparable *ca.* 99% reduction of bacterial cell count.

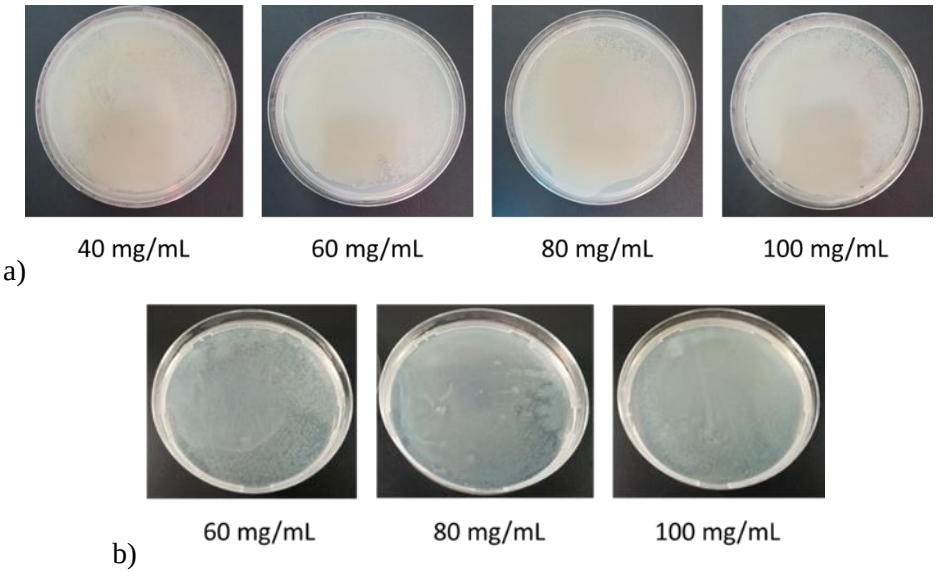

Figure 5.2 Representative images of the results of the MBC tests against a) *S. aureus* 6538P and b) *E. coli* 8739. The nutrient agar plates were treated with the entire volume (100 µL) of the well containing the concentration of Se-Sr-HA identified as the MIC and of the wells with a concentration higher than the MIC (i.e. 40, 60,80 and 100 mg/mL for *S. aureus* 6538P and 60, 80 and 100 mg/mL against *E. coli* 8739).

Table 5.1 Percentage reduction of the number of CFU of Se-Sr-HA at a concentration of 100 mg/mL.

Sample	***% CFU reduction***	
	***S. aureus* 6538P**	***E.coli* 8739**
Se-Sr-HA (100 mg/mL)	98.9 ± 0.1	98.3 ± 0.5

5.2.2. Fabrication of 2D antibacterial composite scaffolds

To obtain 2D antibacterial composite scaffolds, three different loading compositions of Se-Sr-HA were investigated, 10, 20 and 30 wt% using P(3HB) or P(3HO-co-3HD-co-3HDD) as the bulk material.

Figure 5.3 shows the composite films obtained with P(3HB) and P(3HO-co-3HD-co-3HDD) composites. From macroscopic observation the presence of hydroxyapatite in the films could be detected, as the material looked more white and opaque.

Complete characterization of the materials in terms of physical, chemical, thermal and mechanical is described in the following sections.

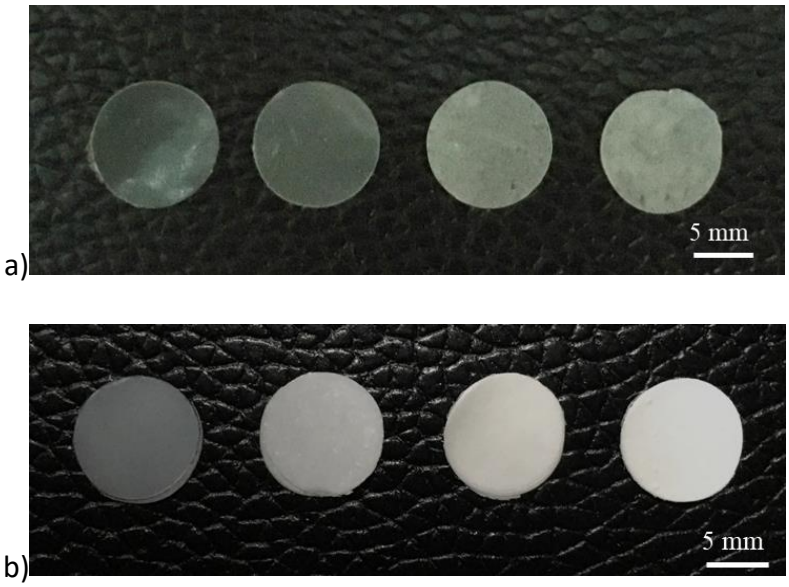

Figure 5.3 Representative image of a) P(3HO-co-3HD-co-3HDD) composite films and b) P(3HB) composite films. In each image the samples are in the following order from left to right: neat film, 10 wt% Se-Sr-HA, 20 wt% Se-Sr-HA and 30 wt% Se-Sr-HA composite films.

5.2.2.1. Chemical characterization

Preliminary characterization of the composite films was conducted by FT-IR analysis. Figure 5.4 shows the spectra for P(3HO-co-3HD-co-3HDD) composites and Figure 5.5 shows the ones for P(3HB). In all the spectra the characteristic peak of PHAs was identified related to the stretching of the carbonyl group (1720-1740 cm^{-1}) in the ester bond. Moreover, the mcl-PHA composites showed more prominent peaks around 2900 cm^{-1} (i.e. stretching of carbon-hydrogen bond of methyl and methylene group (CH_3, CH_2)) compared to the scl-PHAs (Kann *et al.*, 2014; Randriamahefa *et al.*, 2003). The spectra of all the composite films showed new bands at 1072–1032, 601, 571, and 474 cm^{-1}, which were assigned to the vibrations of the phosphate group, PO_4^{-3}, present in the hydroxyapatite. In particular the area between 1072-1032 cm^{-1} is related to the stretching mode of the phosphate oxygen (P-O) bond in the phosphate group, while the area below 600 cm^{-1} is due to the bending mode of the O-P-O bond in the phosphate group (Koutsopoulos, 2002; Li *et al.*, 2007).

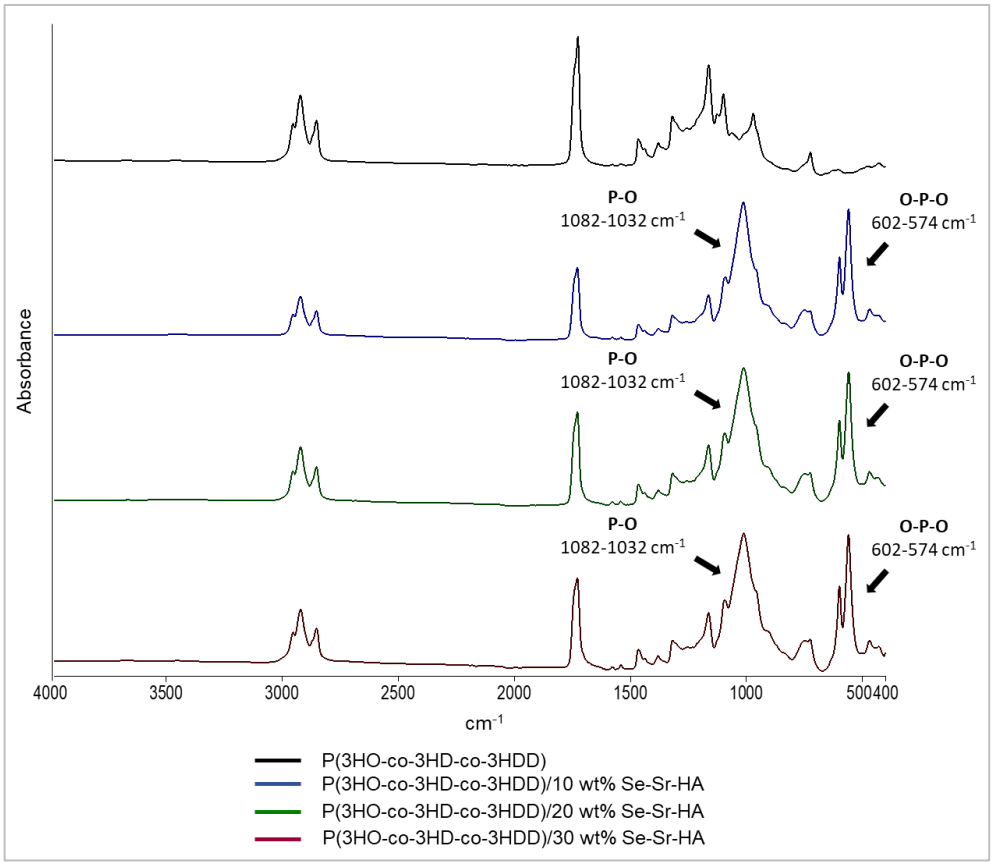

Figure 5.4 FT-IR spectra of a) P(3HO-co-3HD-co-3HDD) neat film, b) P(3HO-co-3HD-co-3HDD)/10 wt% Se-Sr-HA c) P(3HO-co-3HD-co-3HDD)/20 wt% Se-Sr-HA and c) P(3HO-co-3HD-co-3HDD)/30 wt% Se-Sr-HA composite films.

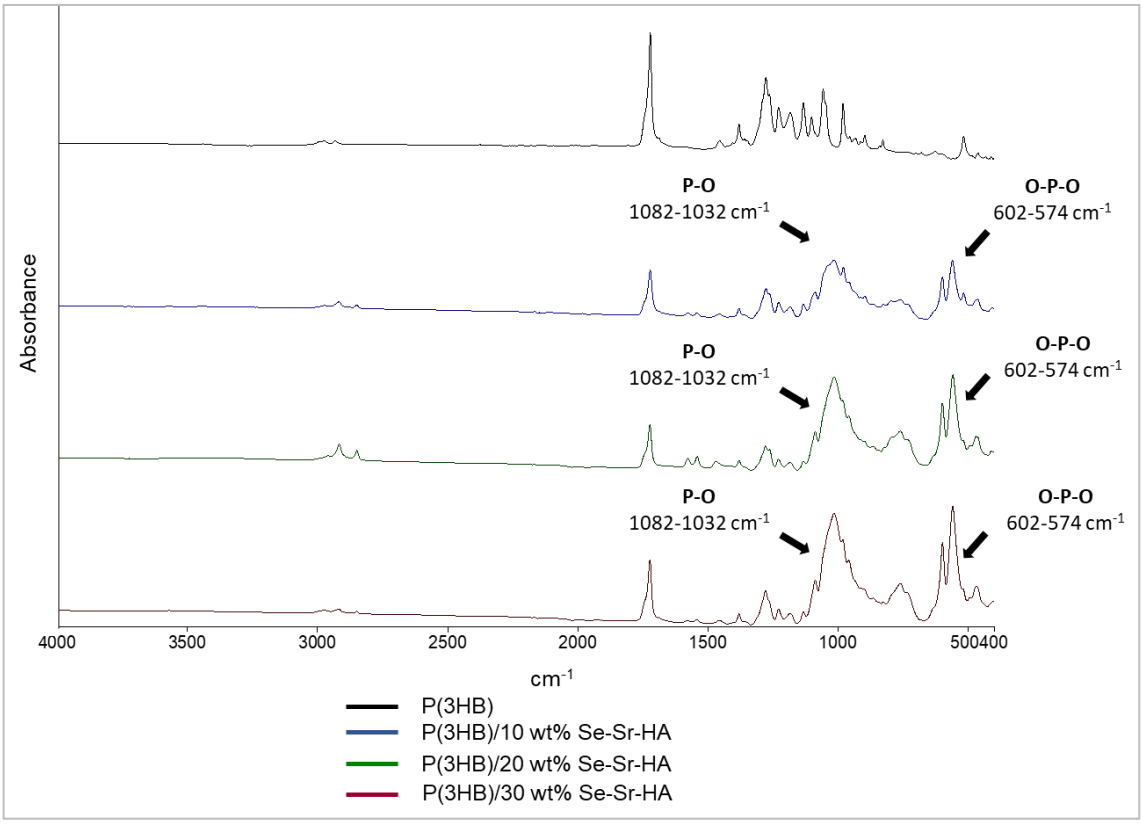

Figure 5.5: FT-IR spectra of a) P(3HB) neat film, b) P(3HB)/10 wt% Se-Sr-HA c) P(3HB)/20 wt% Se-Sr-HA and c) P(3HB)/30 wt% Se-Sr-HA composite films

5.2.2.2. Surface characterization

The surface morphology of the composite films was investigated using SEM analysis as shown in Figure 5.6 for P(3HO-co-3HD-co-3HDD) composites films and in Figure 5.8 for P(3HB) composite films.

The surface of the composite films appeared less uniform than neat P(3HO-co-3HD-co-3HDD) films due to the presence of hydroxyapatite particles. EDX analyses confirmed the presence of Se-Sr-HA particles in the materials as shown in Figure 5.7. EDX spectra of the neat P(3HO-co-3HD-co-3HDD) film showed only the presence of peaks assigned to carbon and oxygen (Figure 5.7a), while for all the composite films the presence of other four elements (i.e. calcium, phosphorus, selenium and strontium) could be detected (Figure 5.7 b,c and d).

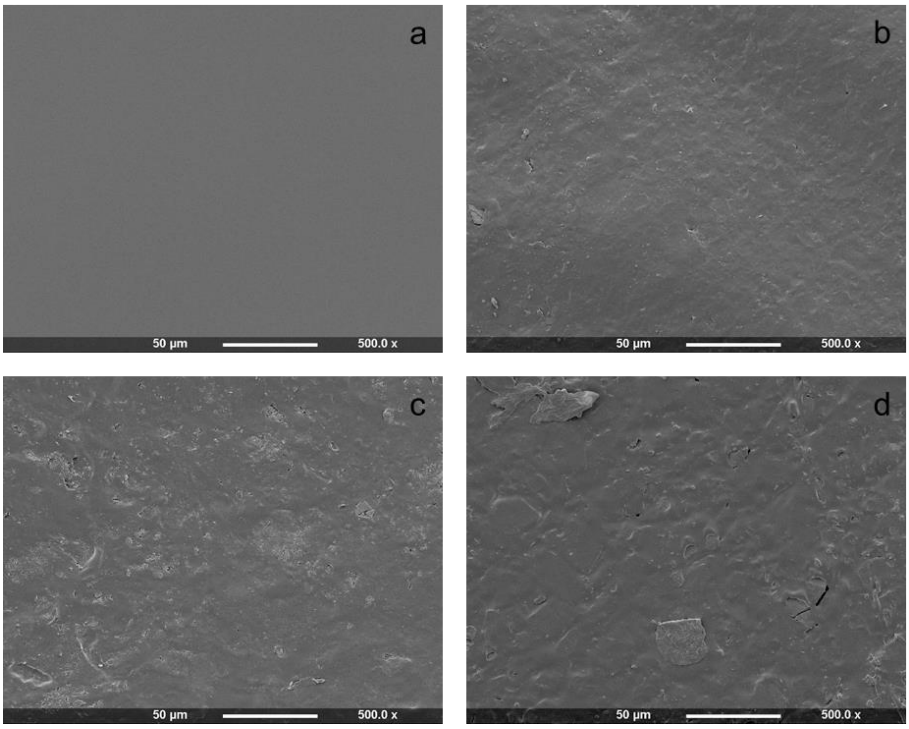

Figure 5.6 SEM images (500x) of the surface of a) P(3HO-co-3HD-co-3HDD) film b) composite films of P(3HO-co-3HD-co-3HDD) with 10 wt% Se-Sr-HA as filler c) composite films of P(3HO-co-3HD-co-3HDD) with 20 wt% Se-Sr-HA as filler d) composite films of P(3HOco-3HD-co-3HDD)

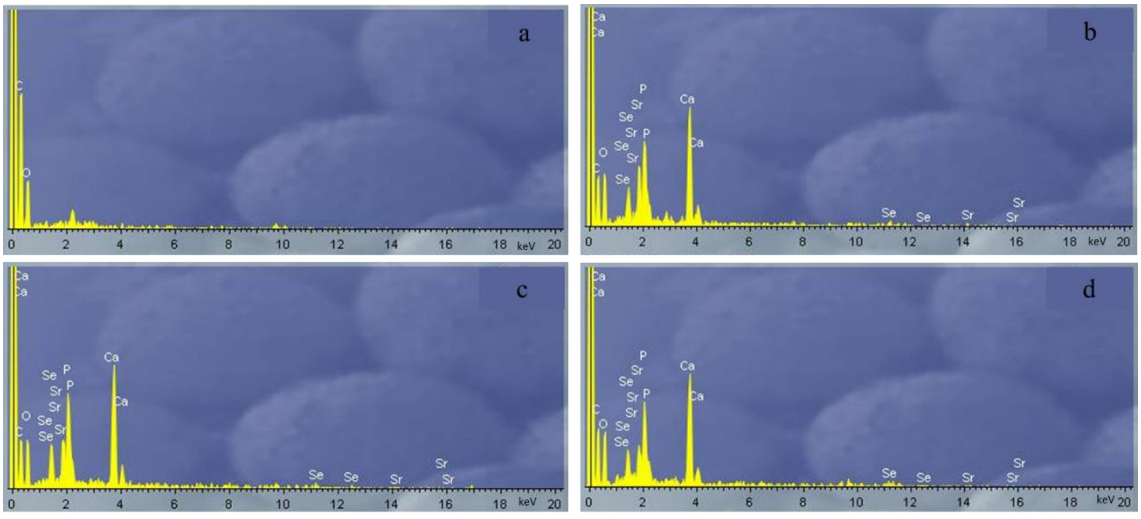

Figure 5.7 EDX spectra of a) P(3HO-co-3HD-co-3HDD) neat film, b) P(3HO-co-3HD-co-3HDD)/10 wt% Se-Sr-HA c) P(3HO-co-3HD-co-3HDD)/20 wt% Se-Sr-HA and c) P(3HO-co-3HD-co-3HDD)/30 wt% Se-Sr-HA composite films

For P(3HB), SEM analyses of the surface of the composite films is shown in Figure 5.8. For all the composite films the presence of Se-Sr-HA resulted in a rougher surface morphology, and the presence of Se-Sr-HA was further confirmed by EDX analyses, as already described for P(3HO-co-3HD-co-3HDD) samples (Figure 5.9). As expected, the EDX spectra of the neat P(3HB) film showed only the presence of peaks assigned to carbon and oxygen (Figure 5.9a), while for all the composite films the presence of other four elements associated with Se-Sr-HA (i.e. calcium, phosphorus, selenium and strontium) could be detected (Figure 5.9 b,c and d).

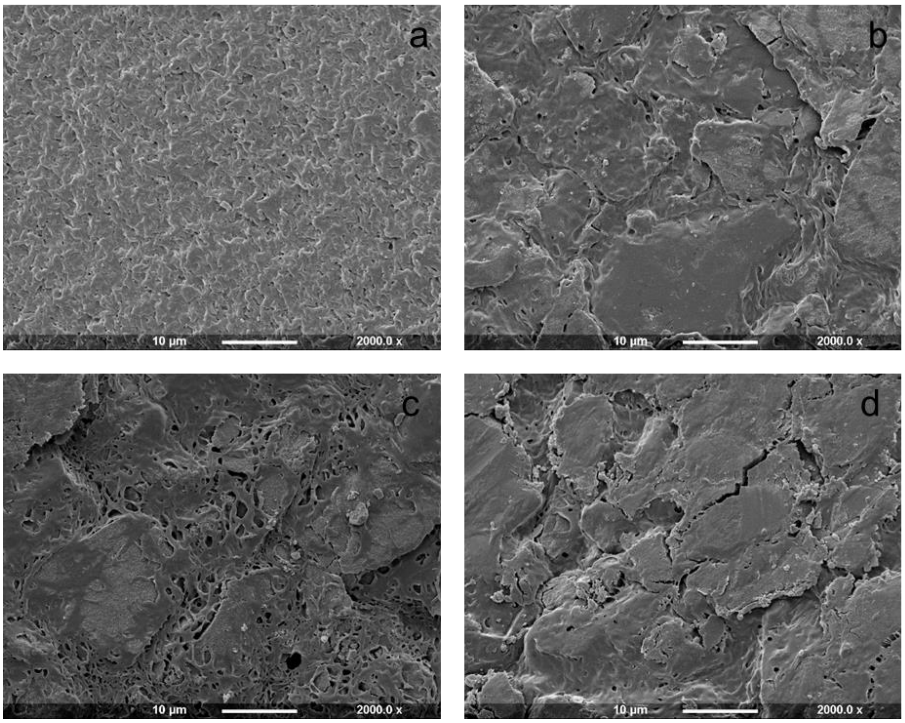

Figure 5.8 SEM images (2000x) of the surface of a) P(3HB) film b) composite films of P(3HB) with 10% w/v Se-Sr-HA as filler c) composite films of P(3HB) with 20% w/v Se-Sr-HA as filler d) composite films of P(3HB) with 30% w/v Se-Sr-HA as filler.

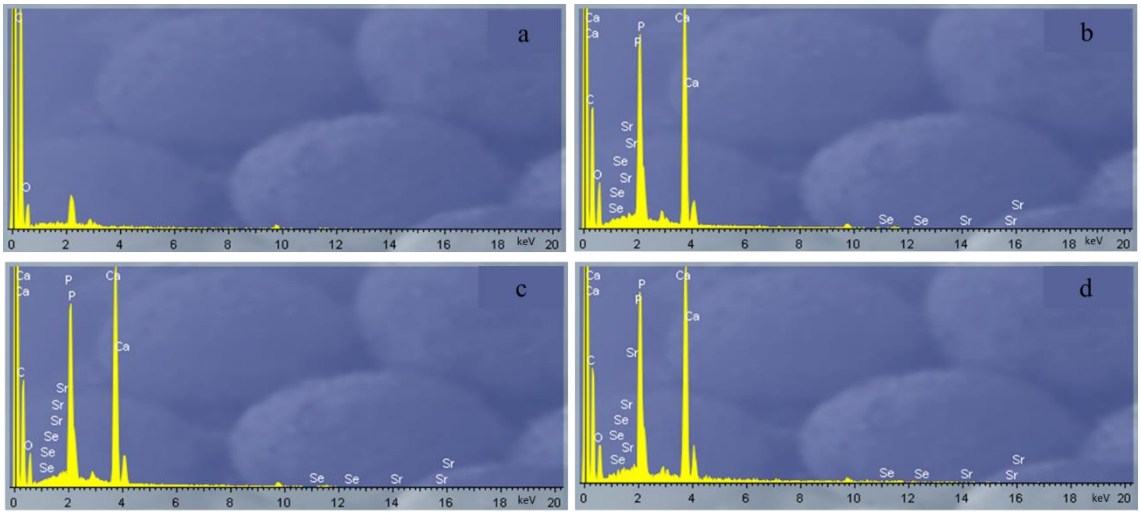

Figure 5.9 EDX spectra of a) P(3HB) neat film, b) P(3HB)/10 wt% Se-Sr-HA c) P(3HB)/ 20wt% Se-Sr-HA and c) P(3HB)/30 wt% Se-Sr-HA composite films

5.2.2.3. Thermal characterization

The effect of the incorporation of Se-Sr-HA on the thermal properties was evaluated by DSC analyses.

The thermal properties of P(3HO-co-3HD-co-3HDD) composites are reported in Table 5.2. The loading of hydroxyapatite did not induce statistically significant differences for both the melting temperature peak and the glass transitions of the composite films compared to the neat P(3HO-co-3HD-co-3HDD) sample. In terms of enthalpy of fusion, the sample with 10 wt% of Se-Sr-HA did not show statistically significant difference as compared to the neat films. On the contrary, the samples with the highest concentrations of filler (i.e. 20 and 30 wt%) showed statistically lower values of enthalpy of fusion as compared to the neat films (p-value<0.05 for 20 wt% and p-value<0.01 for 30 wt%). However, no statistically significant differences in the enthalpy of fusion were detected between the composite films (i.e. 10 wt% vs 20 wt% vs 30wt%). As described in chapter 3, the value of crystallinity for mcl-PHA-based composites could not be calculated from the enthalpy of fusion of the material as the enthalpy of fusion for a 100% crystalline polymer was not known (Suchitra, 2004). Since the enthalpy of fusion is directly proportional to the degree of crystallinity (as described in the formula in Chapter 2 section 2.11.4), the decrease in the enthalpy of fusion of the composite indicated that the presence of filler affected P(3HO-co-3HD-co-3HDD) crystallization.

Table 5.2 Thermal properties obtained from DSC analyses of P(3HO-co-3HD-co-3HDD) film and composite films of P(3HO-co-3HD-co-3HDD) with 10 wt%, 20 wt% and 30 wt% Se-Sr-HA as filler. T_m is the melting peak, T_g is the glass transition, ΔH^n_m is the enthalpy of fusion normalized to the mass fraction of P(3HHx-co-3HO-co-3HD). The results are expressed as average ± standard deviation (n=3).

Sample	T_m (°C)	T_g (°C)	ΔH^n_m (J/g)
P(3HO-co-3HD-co-3HDD)	53 ± 5	-44 ± 2	24.5 ± 1
10 wt% Se-Sr-HA	52 ± 0.5	-40.5 ± 2	21.5 ± 1.5
20 wt% Se-Sr-HA	52.5 ± 0.5	-42 ± 2	19 ± 1.5
30 wt% Se-Sr-HA	52 ± 0.5	-42 ± 0.5	18 ± 2

For P(3HB) composite films, the thermal properties are reported in Table 5.3. All the composite films did not show any statistically significant differences of the melting, crystallization and glass transition temperature compared to the neat samples. Statistically significant differences were detected in the enthalpy of fusion (normalized to the content of the filler, as described in materials and methods section 2.11.4) and consequently the percentage crystallinity of the materials. As discussed already in Chapter 3, the crystallinity of the scl-PHAs samples was obtained by comparing the observed values of enthalpy of fusion of the materials to that of a 100 % crystalline sample of the same polymer, which for P(3HB) is 146 J/g (Ho *et al.*, 2014). For the samples with the lowest concentrations of Se-Sr-HA (i.e. 10 and 20 wt%) no significant differences in the values of crystallinity could be detected compared to neat P(3HB) films. On the contrary, a statistically significant reduction in the crystallinity of the composite samples containing 30 wt% of filler was evidenced as compared to the neat samples (p-value<0.01). Moreover, the sample with 30 wt% of filler showed a statistically significant reduction in the values of enthalpy of fusion as compared to both 20 wt% and 10 wt% samples (p-value<0.01 for 10 wt%, p-value<0.05 for 20 wt%).

Table 5.3 Thermal properties obtained from DSC analyses of P(3HB) with 10%, 20% and 30% wt% of Se-Sr-HA as filler (n=3). T_m is the melting peak, T_g is the glass transition, ΔH^n_m is the enthalpy of fusion normalized to the mass fraction of P(3HB), and X_c is the % polymer crystallinity. The results are expressed as average ± standard deviation (n=3).

Polymer	T_m (°C)	T_g (°C)	ΔH^n_m (J/g)	X_c (%)
P(3HB)	169 ± 2	1.7 ± 2.6	82 ± 4	56 ± 4
10 wt% Se-Sr-HA	169 ± 1	0 ± 3	83 ± 4	57 ± 3
20 wt% Se-Sr-HA	170 ± 1	1 ± 5	78.5 ± 4	54 ± 3
30 wt% Se-Sr-HA	169±1.5	0.5 ± 4	61 ± 4.5	42 ± 3

5.2.2.4. Mechanical characterization

Tensile testing of the composite films was conducted to assess the influence of the incorporation of Se-Sr-HA on the mechanical properties of the material.

For P(3HO-co-3HD-co-3HDD) based composites, the representative strain-stress curves of the materials are shown in Figure 5.10. The mechanical properties are shown in Table 5.4. For the elastic modulus, all concentrations showed an increase in the average value as compared to the neat films (p-value<0.001 for 10 and 20 wt% and p-value<0.0001 for 30 wt% as compared to the neat films). However, variation in the amount of Se-Sr-HA did not show an increase of the elastic modulus as no statistically significant difference was evidenced between the three composite films. The ultimate tensile strength did not show any significant differences for the sample with 10 wt% and 20 wt% as compared to the neat films. While for the sample with 30 wt%, a statistically significant decrease was evidenced (p-value<0.5 as compared to the neat films). All the composite samples showed a significantly reduced elongation at break compared to the neat samples (p-value<0.0001). The film with 30 wt% showed a statistically lower average elongation at break value as compared to both 20 wt% and 10 wt% samples (p-value<0.001 compared to 20 wt% and p-value<0.0001 compared to 10 wt%). No statistically significant difference in the elongation at break was detected between the 10 wt% and 20 wt% composite films.

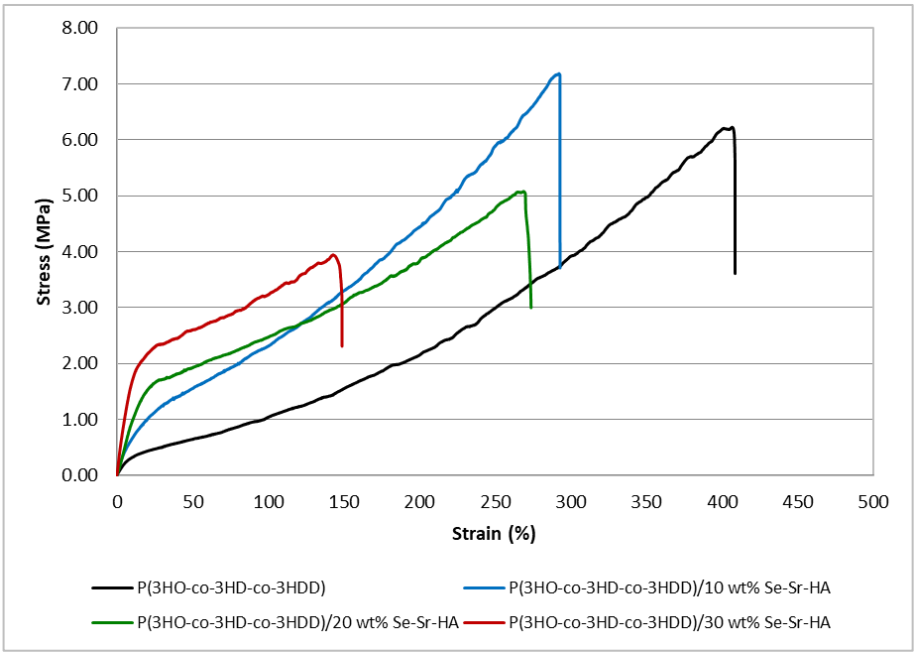

Figure 5.10 Representative stress-strain curve for P(3HO-co-3HD-co-3HDD) film (black) and composite films of P(3HO-co-3HD-co-3HDD) with 10 wt% (blue), 20 wt% (green) and 30 wt% (red) Se-Sr-HA as filler.

Table 5.4 Mechanical properties of composite films of P(3HO-co-3HD-co-3HDD) with 10 wt%, 20 wt% and 30 wt% Se-Sr-HA as filler. E is the Young's modulus, σ_U is the ultimate tensile strength and ε_U is the elongation at break. The results are expressed as average ± standard deviation (n=9).

Sample	E (MPa)	σ (MPa)	ε (%)
P(3HO-co-3HD-co-3HDD)	5.3±2	6.6± 1	414±32
P(3HO-co-3HD-co-3HDD)/10 wt% Se-Sr-HA	14± 4	7 ± 1.5	299± 44
P(3HO-co-3HD-co-3HDD)/20 wt% Se-Sr-HA	14± 6	5.7± 1.5	284± 31
P(3HO-co-3HD-co-3HDD)/30 wt% Se-Sr-HA	16± 2	4 ± 1	173± 32

The representative stress-strain curves of P(3HB) antibacterial composite films are shown in Figure 5.11, while the mechanical properties are reported in Table 5.5. The addition of hydroxyapatite did not induce a significant change in the elastic modulus of the materials containing 10 wt% and 30 wt% as compared to the neat sample. The sample with 20 wt% showed a higher elastic modulus as compared to the neat sample (p-value<0.01). As regards the ultimate tensile strength, all the composite samples showed a

significant increase in the ultimate tensile strength as compared to the neat film, with the 20 wt% films showing the highest increase (p-value<0.05 for 10 wt% and 30 wt%, p-value < 0.001 for 20 wt%). Moreover, the ultimate tensile strength of the composite with 20 wt% was significantly higher as compared to the other two filler compositions investigated (p-value<0.05 for 10 wt% and 30 wt%). Finally, the elongation at break for all the samples was significantly lower than the neat film (p-value<0.05 for 10 wt%, p-value < 0.001 for 20 wt% and 30 wt%). However, no statistically significant difference was evidenced between the three different loadings of hydroxyapatite.

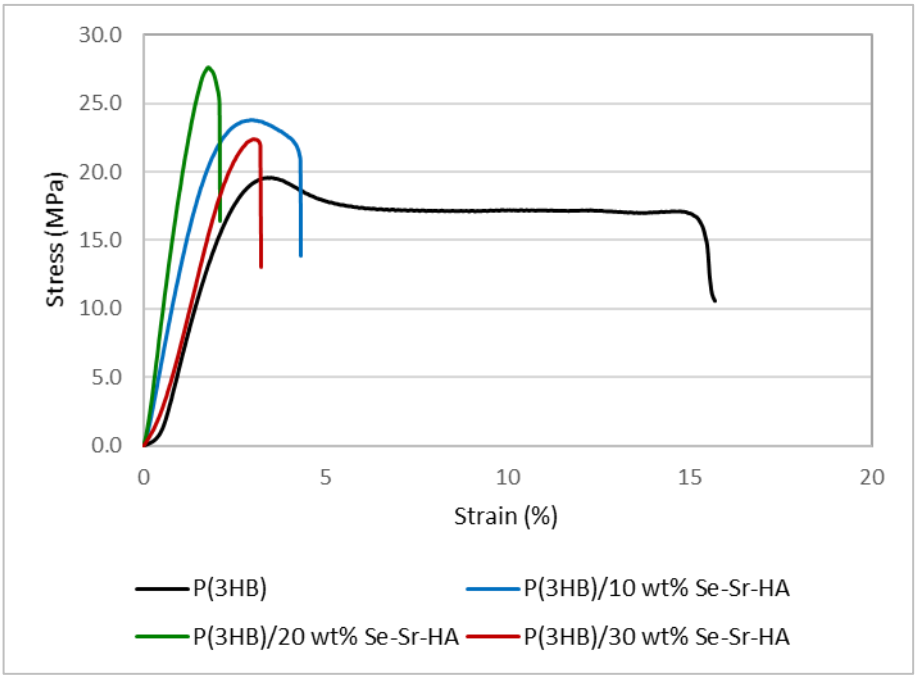

Figure 5.11 Representative stress-strain curve for P(3HB) film (black) and composite films of P(3HB) with 10 wt% (blue), 20 wt% (green) and 30 wt% (red) Se-Sr-HA as filler.

Table 5.5 Mechanical properties composite films of P(3HB) with 10 wt%, 20 wt% and 30 wt% of Se-Sr-HA as filler. E is the Young's modulus, σ_U is the ultimate tensile strength and ε_U is the elongation at break. The results are expressed as average ± standard deviation (n=9).

Sample	E (GPa)	σ (MPa)	ε (%)
P(3HB)	0.9 ± 0.12	19 ± 1.5	16 ± 8
P(3HB)/10 wt% Se-Sr-HA	1.1 ± 0.1	23.5 ± 1	5 ± 2
P(3HB)/20 wt% Se-Sr-HA	1.7 ± 0.2	30 ± 3	2.3 ± 1
P(3HB)/30 wt% Se-Sr-HA	0.9 ± 0.2	24 ± 2	3 ± 1

5.2.2.5. Biological characterization

5.2.2.5.1. Antibacterial ion release studies

The capability of the developed 2D antibacterial composite films to release ions with antibacterial properties was tested using an indirect antimicrobial ion release study. Briefly, the materials were incubated in Mueller Hinton broth for 1, 3, 6 and 24 hours. After each time point the media of each well was collected and replaced with fresh media. The eluates obtained were mixed with a microbial suspension of *S. aureus* 6538P or *E. coli* 8739, adjusted to 0.5 McFarland (final concentration in the well) and incubated for 24h at 37°C. The optical density at 600 nm was recorded after 24 hours and used to determine the reduction of the bacterial cell count, calculated as a percentage of the control (i.e. bacteria cultured with eluates from neat samples).

P(3HO-co-3HD-co-3HDD) composite films showed a reduction in the OD of both *S. aureus* 6538P and *E. coli* 8739 cells as compared to the control throughout the duration of the experiment as shown in Figure 5.12

In the case of *S. aureus* 6538P, all three composite samples showed at least a 30% average reduction of the bacterial cell count as compared to the control after 1h, 3h and 6h incubation. The antibacterial activity was higher for the samples containing 30 wt% of Se-Sr-HA, displaying an average reduction of the OD around 70% for all the time points evaluated as compared to the control (p-value<0.0001). For the eluates obtained after 24 hours of incubation, the materials containing 10 wt% of filler showed a 20% average OD

reduction as compared to the control, although no statistically significant difference could be detected with the control samples. On the other hand, the films with 20 wt% and 30 wt% of hydroxyapatite induced a significant reduction of the bacterial cells as compared to the control, with an average reduction value of 70% (p-value<0.0001).

The mcl-based composite films also showed activity against *E. coli* 8739, although the effect was lower than that against *S. aureus* 6538P. Overall, the eluates obtained after 1h, 3h and 6 hours of incubation with the polymeric composite samples induced an average 20% reduction of the bacterial cell count. A similar trend was obtained for the composite samples with 20 wt% and 30 wt% of Se-Sr-HA after 24 hours, showing a statistically significant reduction of the OD as compared to the control (p-value<0.001 for 20 wt% and p-value<0.05 for 30 wt% samples). On the contrary, the samples with the lowest concentration of the filler did not show a significant difference as compared to the control.

a)

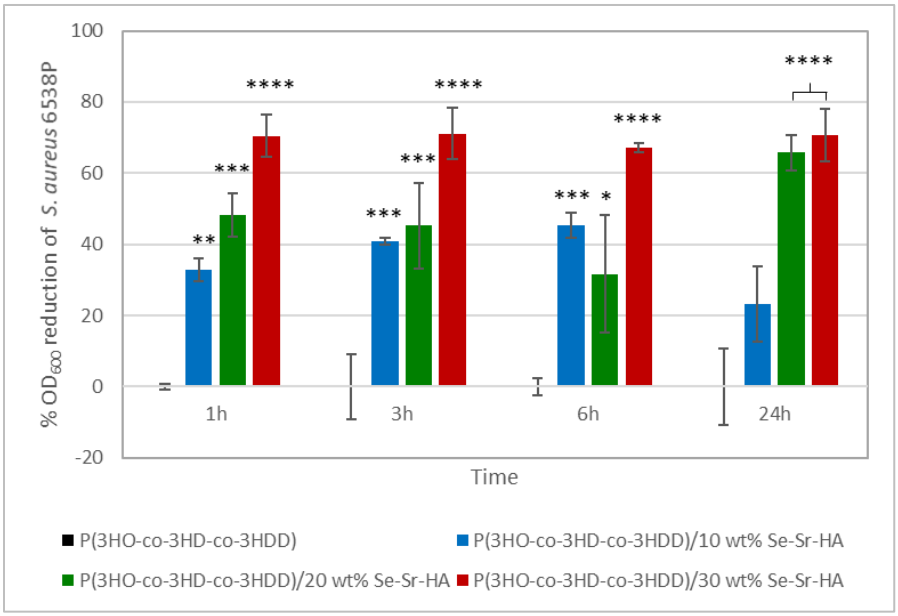

b)

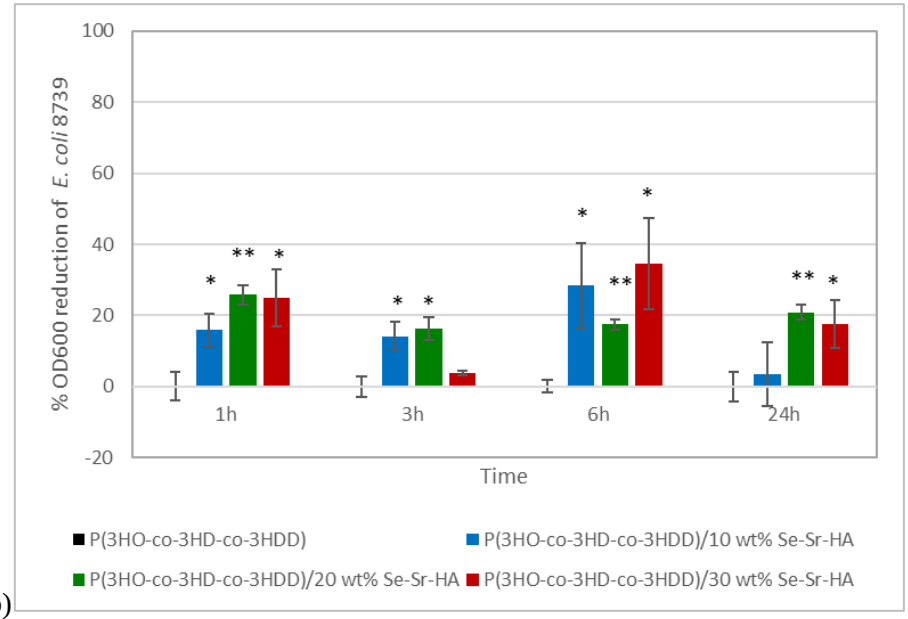

Figure 5.12 Indirect antibacterial ion release study of the eluates of P(3HO-co-3HD-co-3HDD) antibacterial composite films with 10 wt%(blue), 20 wt% (green) and 30 wt% (red) of Se-Sr-HA as a filler against a) *S. aureus* 6538P and b) *E. coli* 8739 (n=3). Control consists of bacterial cells cultured in eluates of neat P(3HO-co-3HD-co-3HDD) (black). *, **, *,**** indicate statistically significant difference between the composite samples and the positive control (*p*-value<0.05, *p*-value<0.01, *p*-value<0.001, *p*-value<0.0001).**

The reduction of OD of the bacterial cells in contact with the eluates of the P(3HB) composite films with respect to *S. aureus* 6538P and *E. coli* 8739 are shown in Figure 5.13 a and b. A reduction of the bacterial cell count could be detected for both type of bacteria, indicating an antimicrobial effect against both Gram positive and Gram negative species.

In the case of *S. aureus* 6538P, the eluates obtained after 1h incubation with the composite films with 20 wt% and 30 wt% of Se-Sr-HA showed a similar 40% average reduction of the OD, significantly lower OD than that of the control (p-value<0.001). On the contrary, the composite with the lowest concentration of hydroxyapatite did not show an antibacterial effect after 1h incubation. For all the other time points evaluated, all the samples showed a statically significant reduction of the bacterial cell count, inducing at least a 30% average reduction of the OD. Moreover, the composite with the highest concentrations of hydroxyapatite (i.e. 20 wt% and 30 wt%) showed a higher antibacterial activity than that of samples with 10 wt% of filler at all the time points evaluated.

The P(3HB) composite samples showed antibacterial activity against *E. coli* 8739 even though the effect was lower than that against *S. aureus* 6538P. For all the three composite films, the eluates obtained after 1, 3, 6 and 24 hours of incubation showed at least a 20% average reduction of the OD as compared to the control (p-value<0.05 for 10 wt% and p-value<0.001 for 20 wt% and 30 wt% samples).

a)

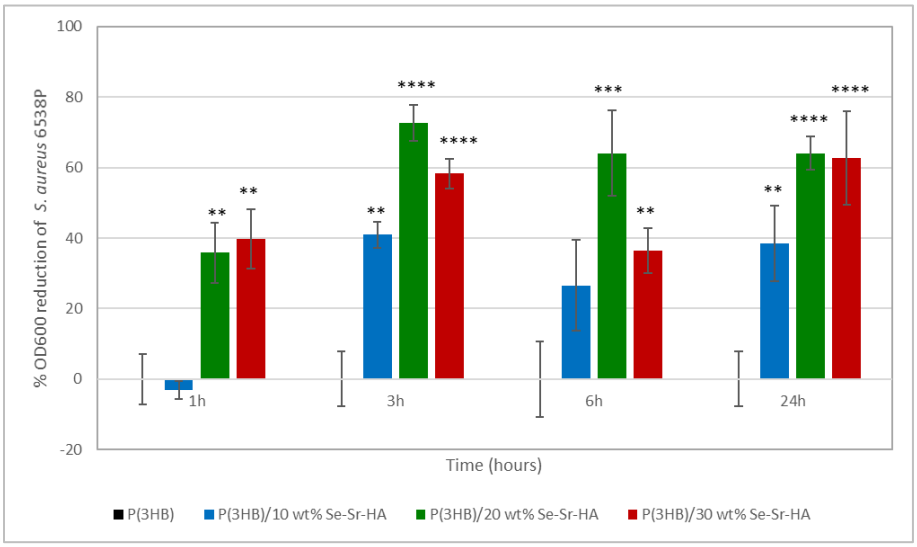

b)

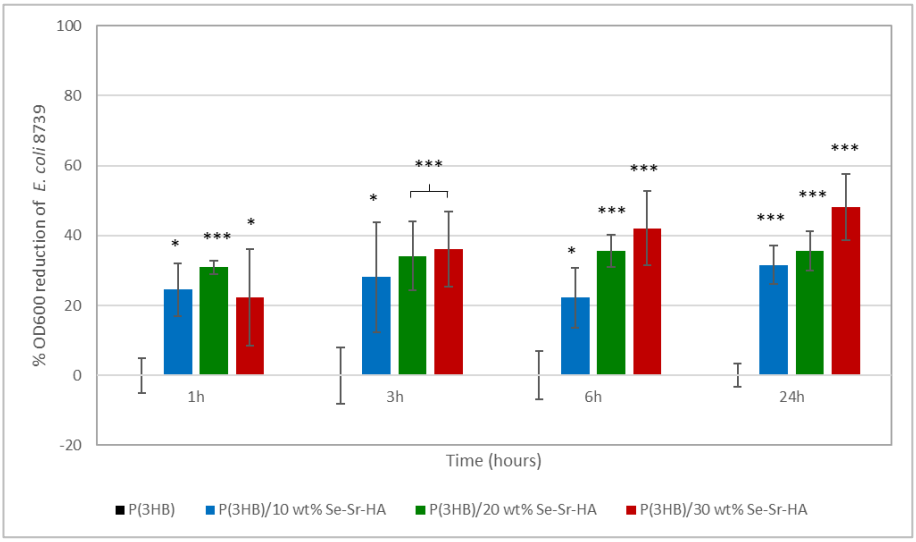

Figure 5.13 Indirect antibacterial ion release study of the eluates P(3HB) antibacterial composite films with 10 wt%(blue), 20 wt% (green) and 30 wt% (red) of Se-Sr-HA as a filler against a) *S. aureus* 6538P and b) *E. coli* 8739 (n=3). Control consists of bacterial cells cultured in eluates of neat P(3HB)(black). *, **, *,**** indicate statistically significant difference between the composite samples and the positive control (*p*-value<0.05, *p*-value<0.01, *p*-value<0.001, *p*-value<0.0001).**

5.2.2.5.2. Direct contact test- ISO 22196

The antibacterial properties of the composite films were investigated using the ISO 22196 against *S. aureus* 6538P and *E. coli* 8739. As described in Chapter 4, this standard procedure involved the seeding of a known number of bacteria directly on the surface of the samples for 24 hours. After the incubation time, the number of viable cells were counted by colony forming assay, normalized to the surface area of the materials and compared to the control specimens, i.e. neat P(3HO-co-3HD-co-3HDD) and P(3HB) samples. The antibacterial activity (R) was expressed as the difference between the logarithm of the bacterial cell count of the composite films and the logarithm of the bacterial cell count of the control. Moreover, the percentage antibacterial activity (R%) was also calculated as the percentage reduction of the number of colony forming units of the composite materials compared to the control.

P(3HO-co-3HD-co-3HDD) composites were active against both bacterial strains at all the concentrations tested (Figure 5.14 and Table 5.6). The composite films showed a bactericidal effect against *S. aureus* 6538P, increasing with the increase in hydroxyapatite content. The composite with the lowest concentration of filler, 10 wt%, showed an antibacterial activity R of 1, inducing an almost 90% reduction (R%) of the number of bacterial cells (p-value<0.001). The sample with 20 wt% of Se-Sr-HA displayed an antibacterial activity R of 1.25, corresponding to a 94% reduction of the bacterial cell (R%) (p-value<0.0001). The highest efficacy was obtained with the highest concentration of filler, 30 wt% of Se-Sr-HA, showing an average 96% reduction of bacterial cells (R%), corresponding to an average R value of 1.4 (p-value<0.0001).

A higher effect was detected against *E. coli* 8739, as all the compositions investigated showed at least a 99% reduction of the bacterial cell count (p-value<0.0001).

a)

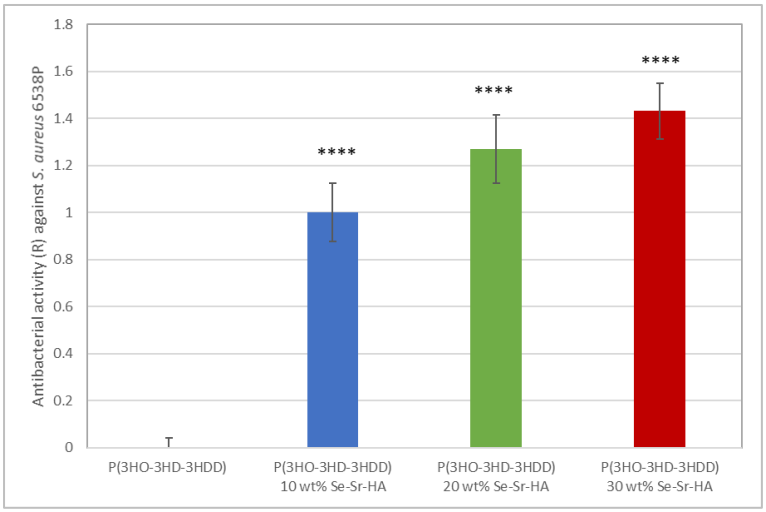

b)

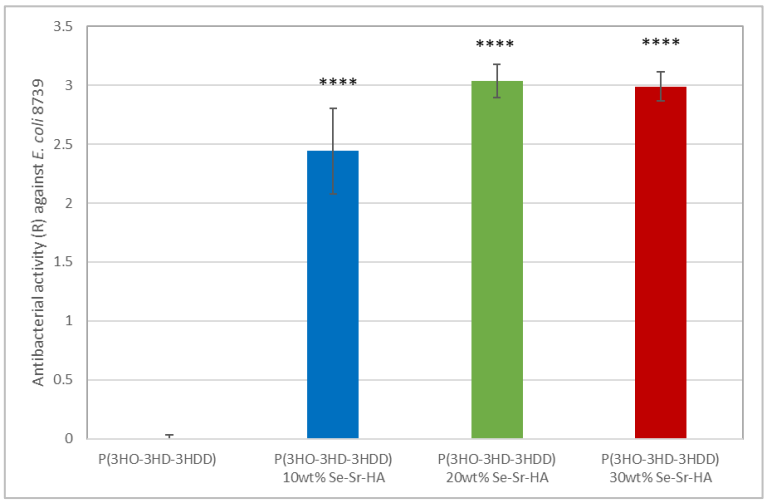

Figure 5.14 Antibacterial Activity (R) (ISO 22196) of P(3HO-co-3HD-co-3HDD) neat film (grey) and P(3HO-co-3HD-co-3HDD) antibacterial composite films with 10 wt%(blue), 20 wt% (green) and 30 wt% (red) of Se-Sr-HA as a filler against a) *S. aureus* 6538P and b) *E. coli* 8739.** indicates statistically significant difference between P(3HO-co-3HD-co-3HDD) antibacterial composite films and P(3HO-co-3HD-co-3HDD) neat films (*p*-value<0.0001).**

Table 5.6 Percentage antibacterial activity (R%) and Antibacterial activity (R) values of P(3HO-co-3HD-co-3HDD) antibacterial composite films with 10 wt%, 20 wt% and 30 wt% of Se-Sr-HA as the filler against *S. aureus* 6538P and *E. coli* 8739.

Sample	*S. aureus* 6538P		*E.coli* 8739	
	R	***R(%)***	***R***	***R(%)***
P(3HO-co-3HD-co-3HDD)/ 10 wt% Se-Sr-HA	1 ± 0.1	89.8 ± 2.8	2.4 ± 0.3	99.5 ±0.4
P(3HO-co-3HD-co-3HDD)/ 20 wt% Se-Sr-HA	1.25 ± 0.15	94.5 ± 1.6	3 ± 0.15	99.9 ± 0.03
P(3HO-co-3HD-co-3HDD)/ 30 wt% Se-Sr-HA	1.43 ± 0.1	96.2 ± 1.1	3 ± 0.1	99.8 ± 0.8

P(3HB) composite films showed a high antibacterial activity at all the concentrations tested against both bacterial strains (Figure 5.15 and Table 5.7). For both *S. aureus* 6538P and *E. coli* 8739 the materials showed a 100% killing of the bacterial cells at all the concentrations tested (p-value<0.0001).

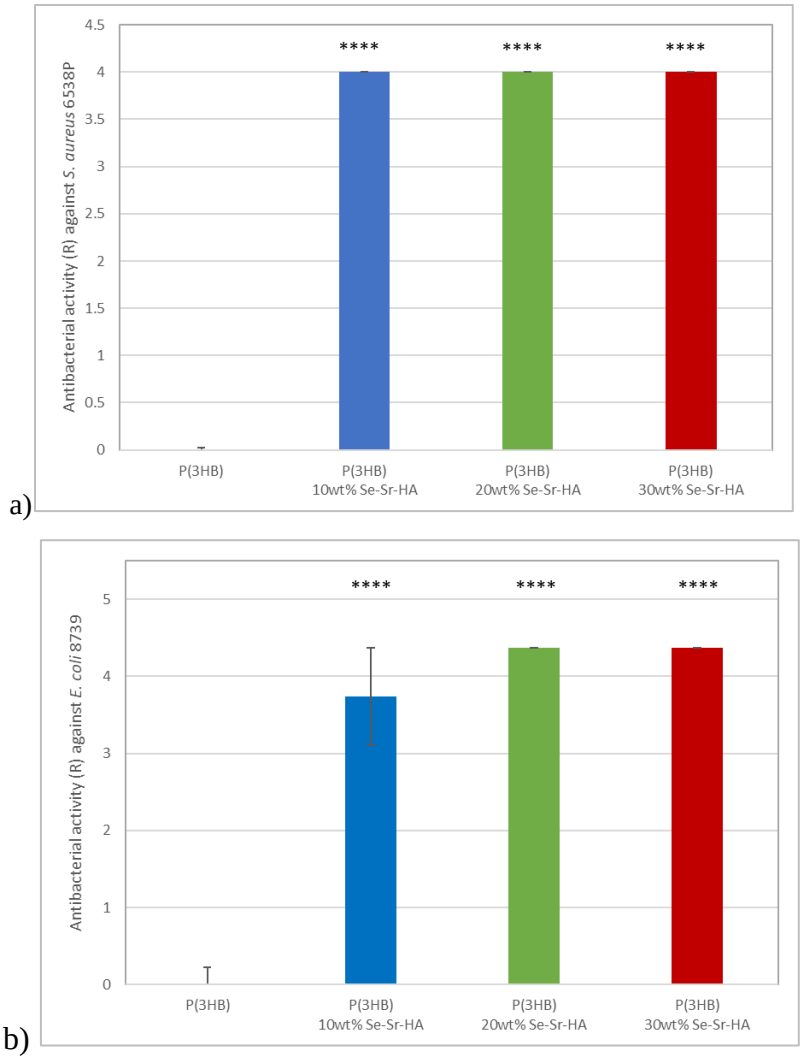

Figure 5.15 Antibacterial activity (R) (ISO 22196) of P(3HB) neat film (grey) and P(3HB) antibacterial composite films with 10 wt%(blue), 20 wt% (green) and 30 wt% (red) of Se-Sr-HA as a filler against a) *S. aureus* 6538P and b) *E. coli* 8739. ** indicates statistically significant difference between P(3HB) antibacterial composite films and P(3HB) neat films (*p*-value<0.0001).**

Table 5.7 Percentage antibacterial activity (R%) and Antibacterial activity (R) values of P(3HB) antibacterial composite films with 10 wt%, 20 wt% and 30 wt% of Se-Sr-HA as a filler against A) *S. aureus* 6538P and B) *E. coli* 8739.

Sample	***S. aureus* 6538P**		***E.coli* 8739**	
	R	***R(%)***	***R***	***R(%)***
P(3HB)/10 wt% Se-Sr-HA	4 ± 0	100 ± 0	3.8± 0.7	99.9 ±0.1
P(3HB)/20 wt% Se-Sr-HA	4 ± 0	100 ± 0	4.4 ± 0	100 ± 0
P(3HB)/30 wt% Se-Sr-HA	4 ± 0	100 ± 0	4.4 ± 0	100 ± 0

5.3. Discussion

In this chapter the development of 2D antibacterial composite films was investigated through the combination of PHAs with a novel antibacterial hydroxyapatite containing selenium and strontium ions (Se-Sr-HA). This material was developed by Dr. Muhammad Maqbool, an early stage researcher involved in the same Marie Curie European Doctoral Programme HyMedPoly.

In the first part of this chapter a preliminary *in vitro* characterization of the antibacterial properties of Se-Sr-HA, a novel co-substituted hydroxyapatite was conducted. In literature, the introduction of either strontium or selenium in the crystal structure of such calcium phosphates has been explored (Uskokovic *et al.*, 2017; Laskus *et al.*, 2019; Zarins *et al.*, 2019), but to date no study regarding the simultaneous co-substitution of such ions has been published. The material was produced using a wet precipitation method with sodium selenite and strontium nitrate as the sources of selenite and strontium ions respectively. From literature it is known that strontium ions partially substitute calcium ions through cationic substitutions, while anionic substitution occurs between selenite and phosphate groups (Šupová, 2015; Uskokovic *et al.*, 2017; Ratnayake *et al.*, 2017). The final material had a selenium content of 1.4 wt% and 2.7 wt% of strontium.

The antimicrobial effect was assessed by the determination of the minimal inhibitory concentration (MIC) and the minimal bactericidal concentration (MBC) through the broth dilution test against both Gram positive and Gram negative bacteria. The produced Se-Sr-

HA in powder form showed activity against both types of bacteria, inducing inhibition of the microbial cell growth. The MBC is defined as the concentration of the compound that leads to 99.9% of bacterial death. This was not achieved even at the highest concentration of Se-Sr-HA tested indicating that at the current concentration the material can be classified as bacteriostatic rather than bactericidal. Further tests should therefore be conducted to investigate whether an MBC value for this novel substituted hydroxyapatite could be obtained at higher concentrations.

Only a few studies have been conducted in literature to investigate the antibacterial properties of selenium doped hydroxyapatite and they differ in the content of selenium, form of hydroxyapatite utilized and method tested, making it difficult to compare the results obtained. Nevertheless, overall the materials produced have shown activity against both Gram positive and Gram negative bacteria, in line with the preliminary results obtained in this study. Uskokovic *et al.* produced a substituted HA with four concentrations of selenium (0.1, 1.2, 1.9 and 3 wt%) and showed that these materials in the form of powders were able to produce a zone of inhibition for all the four bacterial strains tested, i.e. *E. coli, S. aureus, S. enteritidis* and *P. aeruginosa* at all the concentrations investigated. In another study, Se-HA coatings on titanium discs containing 0.6 wt% of selenium resulted in a reduction in biofilm formation of both *P. aeruginosa* 19582 and *S. aureus* 6538P (Rodríguez-Valencia *et al.*, 2013). Finally, Kolmas, *et al.* evaluated the antimicrobial properties of a co-substituted hydroxyapatite with selenium (3.5 wt%) and manganese (0.6 wt%) by incubation of this material in the form of pellets with a microbial suspension of *S. aureus* 25293 and *E.coli* 2592 for 24h. The material induced reduction in the cells count of *S. aureus* 25293, while it showed no activity against *E.coli* 2592 (Kolmas *et al.*, 2015b). The difference in the form of hydroxyapatite used, pellet discs, compared to the powder used in this study and in the work of Uskokovic *et al.* might be the reason for the discrepancy in the results obtained against *E.coli*, as the former might have led to a lower release of antimicrobial ions compared to the free powder form. Nevertheless, further tests should be conducted to obtain a better understanding of the antimicrobial efficacy of such substituted hydroxyapatite.

The Se-Sr-HA was used as a filler for the development of 2D antibacterial PHA-based composite scaffolds by mixing it with two PHAs, P(3HB) and P(3HO-co-3HD-co-3HDD). Combination of PHAs with hydroxyapatite has been investigated in literature to produce composites for bone tissue engineering (Lim *et al.*, 2017; Goonoo *et al.*, 2017).

The main polymer investigated is P(3HB) due to its mechanical properties in terms of elastic modulus which are more similar to those of native bone (Hayati *et al.*, 2012; Degli Esposti *et al.*, 2019; Saadat *et al.*, 2015). However, the brittle nature of the material limits its *in vivo* application (Obat *et al.*, 2013; Wang *et al.*, 2008). Therefore recently mcl-PHA have also been investigated as an alternative material for bone regeneration (Ansari *et al.*, 2016). For this reason, both types of PHAs were selected and the effect of the addition of the novel antibacterial filler was investigated.

The 2D composite films were produced by solvent casting technique using the two PHAs and three different loadings of the filler (10, 20 and 30 wt%). To validate the presence of Se-Sr-HA, the 2D composite structures were investigated in terms of chemical, thermal and mechanical properties. The presence of the hydroxyapatite in the films was confirmed via FT-IR analyses, which showed the characteristics peaks of phosphate groups typical of such material. Moreover, the chemical analysis by EDX further evidenced the presence of Se-Sr-HA specifically, as all the elements present in such filler could be identified (i.e. selenium, strontium, calcium, phosphorus).

The morphology of the surface of the films was also assessed through SEM analysis. The composite materials showed differences that can be related to the two types of PHAs used. The surface of films of mcl-PHAs obtained by solvent evaporation is usually smooth, while P(3HB) usually shows a rougher surface characterized by the presence of protrusions and pores (Rai *et al.*, 2011b; Anbukarasu *et al.*, 2015). Such distinctive characteristics are attributed to the higher degree of crystallization and a more rapid crystallization rate of scl-PHAs compared to mcl-PHAs (Kai *et al.*, 2003; Li *et al.*, 2016c). These typical features were still present in the composite films containing Se-Sr-HA. In particular, P(3HB) composites showed a higher exposure of the hydroxyapatite compared to the P(3HO-co-3HD-co-3HDD) ones. A similar behaviour was reported by Wang *et al.* when comparing the surface of P(3HB) and P(3HB-co-3HHx) loaded with hydroxyapatite. A higher amount of the filling could be detected on the surface of the former composites, which was attributed to the higher crystallinity of the bulk material (Wang *et al.*, 2008).

The thermal properties of the 2D composite films developed were evaluated by DSC analysis to investigate the influence of the addition of the filler in the polymer matrices. For both types of PHA-based composite, the main effect of the introduction of the hydroxyapatite was a decrease in the enthalpy of fusion (and consequently the crystallinity) of the materials with high content of filler compared to the neat samples. A similar behaviour has been described

in literature for both scl and mcl-PHA based composites with hydroxyapatite (Ansari *et al.*, 2016; Bergmann and Owen, 2003). These results showed that the introduction of high quantities of filler reduced the mobility of the chains, hindering the material crystallization (Liu *et al.*, 2014a; Zhan *et al.*, 2014; Misra *et al.*, 2007). On the contrary, Noohom *et al.*and Sadat-Shojai *et al.* evidenced a nucleating effect of the hydroxyapatite on the crystallization of P(3HB) or P(3HB-co-3HV) composites. Such different outcome was probably related to the difference in the particle size of the filler used. In this study in fact micro-sized hydroxyapatite (data not shown) was utilized while Noohom *et al.*and Sadat-Shojai *et al.* used smaller particles in the nano-range. Nano-hydroxyapatite has been shown to create a better interface with the polymeric matrix due to a higher dispersion compared to micro-size which have higher tendency to form agglomerates (Sadat-Shojai *et al.*, 2013; Misra *et al.*, 2008, 2007).

The mechanical properties of the composite films were investigated through tensile testing. As mentioned in the introduction, one of the main reasons for the use of composites is to create a final material that has a higher strength and modulus than the polymeric component and at the same time better toughness and processability than the inorganic filler. In the case of P(3HO-co-3HD-co-3HDD) samples, the introduction of the hydroxyapatite led to an improvement in the strength and stiffness of the material. On the contrary, an embrittlement of the constructs was evidenced through the reduction of the elongation at break. This behaviour was particularly pronounced with the highest concentration of filler investigated (30 wt%), reaching almost 60% reduction of the elongation at break of the neat films. However, the composite samples with 30 wt% of Se-Sr-HA still showed a high elongation at break with an average value of 170%. Even though no other studies in literature have investigated the mechanical properties of mcl-PHA composites, preventing a direct comparison, this behaviour is known in literature and it is due to the intrinsic characteristics of hydroxyapatite, possessing high strength but brittle nature (Rezwan *et al.*, 2006; Chocholata *et al.*, 2019).

A similar embrittlement behaviour was evidenced for the P(3HB) films composites, where the average elongation at break decreased from 16% to 2%. These results are in agreement with literature studies for both P(3HB) and P(3HB-co-3HV) (Noohom *et al.*, 2009; Rai *et al.*, 2008; Bergmann and Owen, 2003). The hydroxyapatite showed a reinforcement effect also in these scl-PHA systems. In particular, the samples with 20 wt% of filler content showed an increase in the tensile strength of the material, showing a higher elastic modulus (1.7 GPa)

and tensile strength (30 MPa) than the neat P(3HB) films (0.9 GPa and 19 MPa respectively). Such values are again in agreement with the majority of the work conducted in literature using similar polymers with hydroxyapatite (Bergmann and Owen, 2003; Noohom *et al.*, 2009; Sadat-Shojai *et al.*, 2013). On the contrary, the sample with the highest filler concentration (30 wt%) did not induce an increase in the elastic modulus of the composite compared to the neat sample. Furthermore, the elastic modulus of samples containing 30 wt% was statistically lower than the composite with 20 wt% of filler. This mechanism has been evidenced in a variety of composite systems (i.e. polyesters with inorganic filler) evaluated where higher amounts of particles did not lead to further changes or even had a detrimental effect on the final strength of the structures (Tasdemir *et al.*, 2017; Ferri *et al.*, 2018; Rai *et al.*, 2008; Fu *et al.*, 2012). It has been proposed that each composite system is characterized by an upper limit of filler content that can be incorporated into the final constructs. Moreover, it has been hypothesized that above such limit the particles might hinder the material crystallization or even exert a disruptive effect on the crystalline structure of the polymers, leading to no further improvement in the mechanical properties or even inducing lower mechanical properties than the original material (Goonasekera *et al.*, 2016; Grøndahl *et al.*, 2017). Such correlation between the variation in crystallinity and the mechanical properties can be evidenced in this study, as P(3HB) composite samples with 30 wt% filler showed a significant reduction in the crystallinity of the samples. The P(3HO-co-3HD-3HDD) samples followed the same principle, but with a lower filler concentration of 10 wt%. No increase in the elastic modulus was in fact evidenced for P(3HO-co-3HD-3HDD) samples containing 20 and 30 wt% of Se-Sr-HA compared to the ones with 10 wt% of filler and in parallel a reduction of the enthalpy of fusion (and consequently crystallinity) was obtained with the materials with 20 wt% and 30 wt% of hydroxyapatite. The difference between the two types of PHAs might be related to the higher crystallinity of the scl-PHAs compared to the mcl ones. It has in fact been hypothesized that in polymers with high crystallinity low quantities of filler present in the amorphous region do not impact significantly on the final bulk mechanical properties, therefore requiring higher concentrations compared to less crystalline materials (Grøndahl *et al.*, 2017; Kaur and Shofner, 2009; Wei and Ma, 2004).

The mechanical properties of natural bone have been extensively described in literature. It has been reported that for cortical bone the elastic modulus and the strength are in the range of 7–20 GPa and 100–180 MPa respectively, while for cancellous bone 0.2–2 GPa and 2–20 MPa respectively (Bose *et al.*, 2012; Kashirina *et al.*, 2019). The P(3HB) composite

containing Se-Sr-HA showed mechanical features similar to those of cancellous bone, making them good candidate for the development of materials the reconstruction of defects of such type of tissue (Gao *et al.*, 2017; Fernandez de Grado *et al.*, 2018). However, future work should still be conducted to improve the brittleness of these materials, which might limit their *in vivo* application. On the other hand, P(3HO-co-3HD-co-3HDD) still showed a ductile behaviour after the incorporation of the hydroxyapatite, which make them suitable for possible application in bone regeneration even though the mechanical strength of the materials is lower than that of native tissue. The targeted application for such elastomer composite materials is indeed for bone filling agents in not-load bearing applications, where their elastic nature might be an advantage for the development of flexible and easily shaped materials able to adapt to the defected site (Ural *et al.*, 2000; Chen *et al.*, 2012;). Nevertheless, improvement of the final mechanical properties should be further optimized and could be achieved by improving the interface between the polymers and the filler with the use for example of nano-sized hydroxyapatite (Misra *et al.*, 2008; Rai *et al.*, 2008).

The main reason for using a co-substituted hydroxyapatite compared to traditional calcium phosphates was to develop a scaffold possessing antibacterial properties. Therefore, the 2D composite films were investigated using two methodologies, an indirect contact test (i.e. antibacterial ion release) and a direct one (i.e. ISO 22196). The former one was chosen to evaluate whether the materials were able to release ions possessing antimicrobial activity. The latter is a standard well-established procedure used for the quantification of the antimicrobial properties of materials (Molling *et al.*, 2014). The 2D composite films developed should in fact exhibit an antibacterial activity by two mechanisms, by direct contact between the bacteria and the selenite ions present in the hydroxyapatite structure and by contact with the ions released in the surrounding environment. In this way the two tests performed enable to analyse the two systems independently of each other.

Both P(3HB) and P(3HO-co-3HD-co-3HDD) composites showed a reduction in the growth of *S. aureus* 6538P and *E. coli* 8739 during the *in vitro* antibacterial indirect tests. Such results can be used as an indication of the capability of such materials to release ions. In particular, the release of the ions seemed to possess an early onset as a reduction of the number of bacteria could be detected with the eluates obtained after 1 hour of incubation for both types of PHAs. Moreover, the release seemed to be extended over time, as the media obtained at 24 hours of incubation still possessed an antimicrobial activity. Finally, as expected the materials containing a higher percentage of hydroxyapatite showed a higher antimicrobial

effect which could be associated with an increased amount of selenite ions. Nevertheless, further studies should be conducted to quantify the ionic content using inductively coupled plasma/optical emission spectroscopy (ICP-OES) and to investigate the release over a longer period of time (Gritsch *et al.,* 2019). Only a few studies have been conducted on the antibacterial properties of selenite and the mechanism behind its efficacy has not been elucidated yet. Overall the activity of selenite seems to be concentration dependent (Turner *et al.,* 1998; Kramer and Ames, 1988; Bébien *et al.,* 2002). The main hypothesis formulated is the induction of oxidative stress through the production of ROS species at high concentrations (Kolmas *et al.,* 2014b; Bébien *et al.,* 2002). For both P(3HB) and P(3HO-co-3HD-co-3HDD) composites, the growth inhibition was slightly more effective against Gram positive bacteria than negative ones. In a few studies in literature low concentrations of selenite did not induce significant reduction in *E. coli* cultures (Alam *et al.*, 2016; Vasić *et al.,* 2011). It is known in literature that some species are capable of reducing inorganic selenite ions to elemental selenium nano-particles which are then deposited within the cell (e.g. in the cytoplasm or in the periplasmic space) or pumped outside the cells (Kessi *et al.,* 1999; Kolmas *et al.,* 2014a; Kramer and Ames, 1988; Gonzalez-Gil *et al.,* 2016). *E. coli* has been shown to possess such features probably making them less susceptible to the antimicrobial activity of such ions at lower concentrations (Turner *et al.,* 1998). These results are also in agreement with the slightly higher MIC value obtained for *E. coli* 8739 compared to the *S. aureus* 6538P for the Se-Sr-HA, described at the beginning of the chapter.

The second antibacterial test performed was the ISO 22196 procedure, which was used to investigate the antibacterial properties of the produced 2D composite films in direct contact with the bacteria. For this test in fact *S. aureus* 6538P and *E. coli* 8739 were incubated directly on the surface of the film samples for 24 hours and their antimicrobial effect was indicated as the reduction in the number of viable bacterial cells. The composites obtained from both types of PHAs exhibited activity against both bacterial strains. Once more these results confirm the activity of selenium containing compound against both Gram positive and Gram negative species, as already evidenced in MIC and indirect contact test and in literature studies (Alam *et al.,* 2016; Uskokovic *et al.,* 2017; Rodríguez-Valencia *et al.,* 2013). P(3HB) composites showed a higher effect compared to the P(3HO-co-3HD-co-3HDD) ones, as they induced a 100% reduction for both Gram positive and Gram negative cells. Such higher activity might be due to the differences in the surface properties of the two types of composites that were evidenced in the SEM analyses. The scl-PHAs samples possessed in

fact a more porous surface which might have led to a higher exposure of hydroxyapatite on surface of the films, therefore potentially increasing the amount of selenite ions in contact with the bacterial cells.

On the other hand, in case of mcl-PHA based composites, a slightly lower antibacterial activity was observed as mentioned, even though a reduction of over 90% was obtained at all concentrations for both strains. For the samples containing lower filler concentrations (i.e. 10 and 20 wt%), a slightly although statistically significant higher activity towards *E. coli* 8739 compared to *S. aureus* 6538P was obtained, with values of bacterial reduction 10% (for 10 wt% composite) and 5% (for 20 wt% composite) lower for the Gram negative bacteria compared to the positive one. Such results seem to be in contrast with the findings obtained from the previous assays. This is most probably related to the presence of the polymer in the system, which can have an effect on the growth of bacteria as well as the distribution of the agent on the surface. It is possible, in fact, that the surface topography of the film played a role in the action of selenium, as a variation in the micro-concentration of such ions can affect the growth of bacteria locally, whereas in the case of the MIC assay and the indirect antibacterial ion release test such a variable is not present (Sharifahmadian *et al.*, 2013; Zdraveva *et al.*, 2019). Moreover, the intrinsic variability of a biological system can affect the outcome of an assay, therefore further studies with a larger statistical population might be required in order to assess if there is a significant difference in the activity of selenite ions towards Gram positive and Gram negative bacteria using the direct contact method in the case of P(3HO-co-3HD-co-3HDD) composites.

5.4. Conclusions

In this chapter the development of novel 2D composite scaffolds for bone regeneration was investigated through the combination of PHAs with a novel co-substitute hydroxyapatite containing selenium and strontium ions. The influence of the introduction of the hydroxyapatite on the thermal and mechanical properties of both scl and mcl-PHA based films was investigating, showing an enhancement in the mechanical strength of the materials but a parallel embrittlement of the final constructs. The antibacterial testing of the 2D composite films revealed that such materials are active on contact against both Gram positive and Gram negative bacteria, inducing a reduction of the bacterial cell count higher than 90%. Finally, the materials are also capable of releasing active ions in a prolonged manner up to 24 hours and at a concentration capable of inhibiting both *E. coli* 8739 and *S. aureus* 6538P.

Chapter 6

Development of mcl-PHA based 3D printed scaffolds by melt 3D printing

6.1. Introduction

Traditional methods of scaffolds production include solvent casting, particulate leaching, freeze drying and phase separation. Even though widely investigated, such techniques possess drawbacks and limitations in their applications for the development of structure for tissue regeneration due to their lack of reproducibility and control of geometry, porosity, pore structure and interconnectivity (Ma *et al.*, 2018; Chiulan *et al.*, 2018). For these reasons, in recent years additive manufacturing has attracted great interest in the field of tissue engineering. The basic principle of 3D printing is the construction of a final object by the successive additions of layers of materials. The model of the structure that is needed is developed using a computer-aided design (CAD) software, and is expressed as a sequence of layers that are then implemented by the 3D printer machine to create a physical structure (Gloria *et al.*, 2009; Tao *et al.*, 2019). In this way highly complex structures can be reproduced in a repetitive manner. Moreover, 3D printing allows product customization in the medical field by its combination with several imaging techniques (e.g. magnetic resonance and computer tomography imaging) to develop structures that are patient specific and are able to recreate the shape of the specific defects that need to be regenerated (Ji *et al.*, 2018; Yang *et al.*, 2018). Several types of 3D printing techniques have been developed and can be classified based on the fabrication methods into inkjet, laser and extrusion-based technologies. In inkjet-based systems, the material is deposited in the form of droplets, which can be obtained by thermal or piezoelectric induction (Tao *et al.*, 2019). Stereolithography (SLA) and Selective Laser Sintering (SLS) are the two techniques based on the use of laser. In the former, UV light is used to induce polymerization of liquid monomer solutions or

resins (Ngo *et al.*, 2018; Ma *et al.*, 2018). In the latter the difference is that the laser is applied to a powder form, inducing sintering of the particles (Ji *et al.*, 2018). Finally, extrusion-based technologies are characterized by the application of mechanical or pneumatic pressure to obtain a continuous flow of material (Jammalamadaka and Tappa, 2018). Fuse deposition modelling (FDM) is one of the most investigated techniques of this category and is based on the use of a filament of the material, usually polymer or polymer and ceramics, that is extruded from a heated nozzle and then deposited on the printer bed where solidification occurs (Bose *et al.*, 2013; Yang *et al.*, 2018). The printer used in this study (CellInk Inkredible +) is a type of extrusion-based bioprinter, where pressurized air is applied to create a continuous filament of material. In such a system PHAs can be used either in liquid form as a chloroform solution or in the solid pellet form, as the heat can be applied in the printer cartridge (Gloria *et al.*, 2009). The latter has the advantage of eliminating the possible toxicity related to the use of organic solvents and was therefore chosen as the printing method for the polyesters produced in this work (Pfister *et al.*, 2004).

Limited research has been conducted on the 3D printing of PHAs and only a few of the obtained materials have been characterized in terms of their biocompatibility for medical applications. Two studies investigated the use of P(3HB) for the development of structures using SLS. Pereira *et al.*, carried out preliminary studies on the feasibility of such polyesters for SLS and were able to produce porous cubes that closely mimicked the virtual model, showing no degradation of the materials in terms of mechanical and thermal properties after the printing process (Pereira *et al.*, 2012). In another study, Duan *et al.* produced P(3HB) microspheres loaded with calcium phosphate through oil-in-water emulsion. Such microparticles were used as the raw material for the fabrication of scaffolds with complex structures by SLS technology (Duan *et al.*, 2011). Extrusion-based technology have been employed for the development of 3D structures based on P(3HB-co-3HHx) and bioglass (BG) for bone tissue engineering. Zhao *et al.* employed a solution-based system by dissolving the polyester in chloroform and dimethyl sulfoxide and mixing it with BG. The 3D scaffolds was tested *in vivo* for the repair of bone defects in a rat model and showed their ability to stimulate bone repair after 8 weeks of implantation (Zhao *et al.*, 2014). In another study, melt printing of P(3HB-co-3HHx) was employed to produced 3D scaffolds that were then surface coated by immersion in a solution containing BG. This material showed enhanced cell proliferation and ALP activity of human mesenchymal stem cells compared to non-loaded

P(3HB-co-3HHx) (Yang *et al.*, 2014). The rest of the work present in literature is mainly focused on the development and production of PHA-based filament for FDM. Valentini *et al.*, produced P(3HB-co-3HHx) filaments reinforced with fibrillated nanocellulose with three loadings (0.5, 1 and 3 wt%). The samples with the lowest percentage of filler showed increment of the elastic modulus compared to the neat material, while higher loading percentages induced fibres aggregation and interface debonding between the filler and the matrix (Valentini *et al.*, 2019). In another study, P(3HB) was mixed with 20% w/w lignin to produce filaments and developed 3D printed structures by FDM (Vaidya *et al.*, 2019). Lastly, a 3D printing filament containing PHA is commercially available and distributed by ColorFabb, Belfeld, The Netherlands. The filament is characterized by a blend of PLA and P(3HB-co-3HV) with a 88:22 ratio (PLA: P(3HB-co-3HV)) (Gonzalez-Ausejo *et al.*, 2018). Such composition was developed to improve the ductility of neat PLA filament, inducing an 40% increase of the elongation at break, but a 25% of reduction of the mechanical strength (Kaygusuz and Özerinç, 2019; Gonzalez-Ausejo *et al.*, 2018). 3D printed constructs obtained with such materials by FDM were shown to be able to support the growth and proliferation of human embryonic kidney 293 cells cultured directly on the surface of the materials for 7 days (Gonzalez-Ausejo *et al.*, 2018).

In recent years, a few studies have been focused on the developing polyester–based scaffolds with intrinsic dual porosity, a macro-one obtained by printing the designed model by 3D printing, and a micro one present within the fibre of the construct obtained by combination with salt leaching or phase separation technique (Visscher *et al.*, 2018; Jakus *et al.*, 2018; Dang *et al.*, 2019; Kang *et al.*, 2019; Kim *et al.*, 2017). Porosity is a key parameter for the design of a scaffolds for tissue engineering applications. An open and interconnected porosity has been described as pivotal for an adequate exchange of nutrients, for a better migration and proliferation of cells (Loh and Choong, 2013). Moreover, higher binding between the scaffolds and the surrounding tissues has been evidenced with highly porous surfaces (Hannink and Arts, 2011; Zhang *et al.*, 2018). Scaffold obtained by extrusion or SLS of polyesters usually do not possess porosity within their fibres (Chiulan *et al.*, 2018). Kim *et al.* developed a PCL based scaffold containing hydroxyapatite with dual porosity by non-solvent induced phase separation. A PCL/HA solution in tetrahydrofuran was 3D printing via extrusion in an ethanol bath (non-solvent for the polymer), inducing solvent exchange and phase separation. The scaffolds showed highly microporous struts, improving the

mechanical and cytocompatibility properties of the materials (Kim *et al.*, 2017). In another study, the combination of melt extrusion printing with salt leaching was applied using PCL, polyethylene glycol (PEG) and NaCl. The scaffolds were leached out to remove both the salt and PEG (water soluble polymer) producing a structured that enable better attachment and proliferation of cells compared to neat PCL constructs (Kang *et al.*, 2019). The introduction of micro-porosity could also favour a rapid and specific loading of drug (e.g. Cefazolin) in the PCL based scaffolds, which were obtained using only salt as the porogen (Dang *et al.*, 2019; Visscher *et al.*, 2018). Finally, Jakus *et al.* obtained PLGA scaffolds with dual porosity by combining melt extrusion with salt leaching, using in this case $CuSO_4$ as the porogen. By varying the ratio of salt, the scaffold displayed a wide range of porosity that significantly changed the mechanical and physical properties of the materials. Moreover, the constructs with high porosity showed enhanced promotion of cellular attachment and proliferation (Jakus *et al.*, 2018).

In the first part of this chapter, a screening study was conducted to evaluate the optimal printing conditions for the melt 3D printing of P(3HO-co-3HD-co-3HDD). The physical properties of the 3D printed scaffolds were investigated. The *in vitro* degradation of the obtained scaffold was studied by incubation of the sample in PBS for 6 months. Moreover, the possibility of using these materials for bone regeneration was assessed through *in vitro* compatibility studies and differentiation studies using MC3T3-E1 cells.

In the second section, the possibility of producing scaffolds with dual porosity was also evaluated through the combination of melt printing and salt leaching. A preliminary feasibility study was conducted to investigate the optimal ratio between polymer and salt, and the physical properties of the materials were investigated. Finally, preliminary *in vitro* cytotoxicity studies on the developed materials were conducted using MC3T3-E1 cells.

6.2. Results

In this chapter the development of mcl-PHA based 3D printed constructs by melt 3D printing was investigated. P(3HO-co-3HD-co-3HDD) was chosen as a representative mcl-PHA based on the results already discussed in Chapter 3 and 5. Melt 3D printing of P(3HB) could not be achieved due to the intrinsic limitation of the machine used. The highest temperature that could be achieved was 120°C, lower than the polymer melting temperature of 170 °C.

In order to optimize the melt printing of P(3HO-co-3HD-co-3HDD), the following parameters were considered: the writing speed (i.e. movement of the printer head), the melting temperature and the pressure of extrusion. Structures with a rectilinear pattern with a 1.5 mm distance between the filaments (i.e. pore size) and the deposition of 2 layers of materials were used as a template for the investigation of such features using a nozzle with an internal diameter of 600 µm. The range of the different parameters tested is described in Table 2.6. The range of values of such parameters was chosen based on literature studies and the physical limitations of the 3D printer used. Overall, a combination of the lowest feasible pressure and the maximum feasible writing speed that allow to obtain reproducible and well-formed scaffolds was considered optimal from an efficiency point of view, as it reduces the energy consumption and the fabrication time (Domingos *et al.*, 2012; Hoque *et al.*, 2009; Sheshadri and Shirwaiker, 2015). The applied temperature needs to be higher than the melting temperature of the polymer used, but not too high to cause polymer degradation (Hoque *et al.*, 2009; Sheshadri and Shirwaiker, 2015). Moreover, the lowest temperature achievable is preferred as it should allow a more rapid solidification of the material For P(3HO-co-3HD-co-3HDD) a minimal temperature of 80°C was required to obtain extrusion of material, higher than its melting range between 40-60°C, as described in Chapter 3.
Each parameter was varied one at the time (e.g. varying printing velocity while keeping the temperature constant at 90°C and pressure at 50 kPa). Visual analysis of the printed structures was conducted to determine the feasibility of the tested parameters. A combination of parameters was considered feasible if a well-defined structure was obtained, matching that of the implemented design (obtained using the software Slic3r). Moreover, if a structure could be printed, quantitative analysis of the filament width was performed using ImageJ software to evaluate if continuous and uniform struts were achieved and the values are reported in Table 6.2.

The aim of the experimental study was to obtain a structure with a filament width of 600 µm and a uniform dimension (i.e. low standard deviation) in order to achieve a pore size of 1.5 mm x 1.5mm. As shown in Table 6.2, using 80°C as the melting temperature, none of the conditions applied could yield the desired features. For 90°C and 100°C, the two conditions marked in yellow gave the best results for the related temperatures but not optimal overall, as either the filament dimension was not the targeted one (i.e. higher average value for writing temperature of 90 °C, a pressure of 200 kPa and a writing speed of 1 mm/s) or the uniformity of the strut was not maintained (i.e. high standard deviation for writing temperature of 100 °C, a pressure of 200 kPa and a writing speed of 1 mm/s). Finally, one condition gave the optimal result and was highlighted in green and corresponded to a writing temperature of 110 °C, a pressure of 100 kPa and a writing speed of 1 mm/s.

Table 6.1 Summary of the parameters investigated in the screening experiment to optimize the melt 3D printing of P(3HO-co-3HD-co-3HDD).

Parameter	**Values considered**			
Temperature (°C)	80	90	100	110
Velocity (mm/s)	0.5	1	2	4
Pressure (kPa)	50	100	200	-

Table 6.2 Filament dimension (mm) expressed as average ± std. dev. for all the feasible combinations investigated (i.e. yielding well-defined structures). The data highlighted in green represents the optimal conditions obtained, while the yellow ones identified the best conditions for 90°C and 100°C.

		Velocity (mm/s)			
Temperature (°C)	**Pressure (kPa)**	**0.5**	**1**	**2**	**4**
80	**50**	-	-	-	-
	100	0.40 ±0.1	-	-	-
	200	0.53 ± 0.1	0.41 ±0.14	-	-
90	**50**	0.30 ±0.01	-	-	-
	100	0.51 ±0.1	0.4 ± 0.07	-	-
	200	0.96 ±0.14	0.64 ± 0.06	0.54 ±0.13	-
100	**50**	0.37 ±0.06	-	-	-
	100	0.5 ±0.09	0.4 ± 0.07	-	-
	200	1 ±0.1	0.60 ± 0.14	0.4 ±0.1	0.36 ±0.1
110	**50**	0.45±0.07	0.44 ±0.17	-	-
	100	0.7±0.1	0.60 ± 0.07	0.44 ±0.21	-
	200	1.2 ±0.12	0.845 ±0.096	0.51 ± 0.06	0.34 ± 0.1

To better investigate the effect of the processing parameters on the strut width, statistical analysis of the values reported in Table 6.2 was conducted. Figure 6.1, 6.2 and 6.3 describe the effect of each parameter (i.e. velocity, pressure and temperature) on the filament width of the 3D printed structures while keeping the other two fixed (e.g. temperature while keeping velocity and pressure constant), underling the statistically significant differences. For each parameter considered, the condition with a complete set of all the variables investigated was selected (e.g. velocity 0.5 mm/s was the only velocity with a complete set of parameters for all the variations of pressure and temperature investigated).

Figure 6.1 describes the effect of the variation of pressure for each temperature while keeping the velocity fixed at 0.5 mm/s (i.e. only velocity with a complete set of data for all the parameters tested). For each temperature, the strut dimension significantly increased with increasing pressure. In particular, the filament width at 200 kPa was significantly higher than that at 50 kPa and 100 kPa for 90°C, 100 °C and 110°C (p-value < 0.001). As regards the

comparison between the lower pressures investigated, overall the values for 100 kPa were statistically higher than those at 50 kPa (i.e. *p*-value < 0.05 for 80°C, *p*-value < 0.01 for 90°C and 100°C and *p*-value<0.0001 for 110 °C).

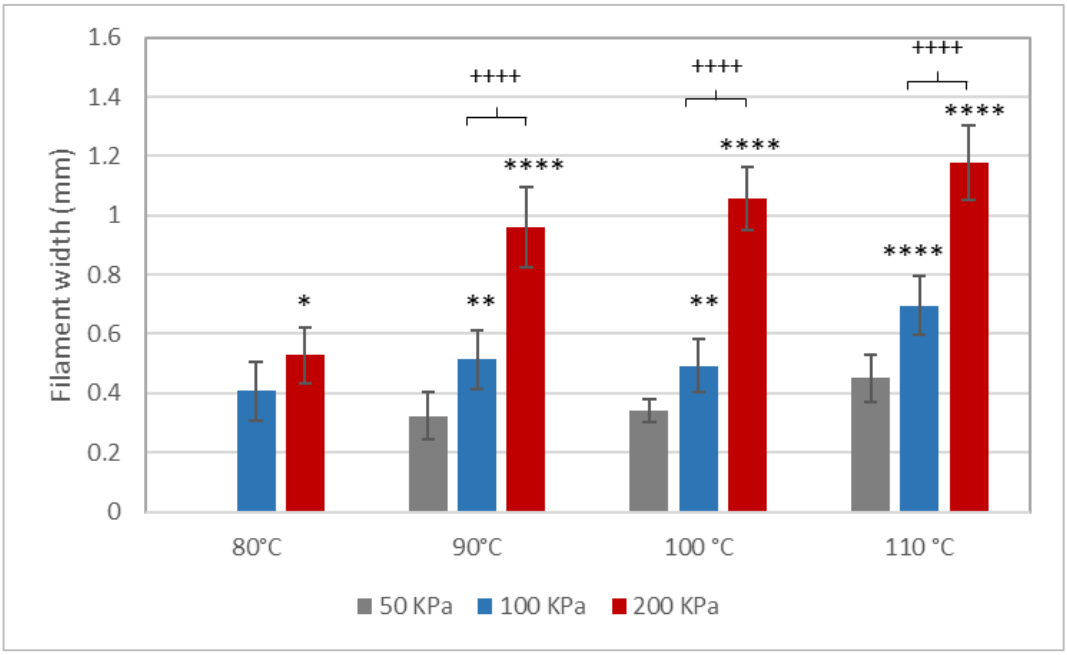

Figure 6.1 Variation of the filament width (i.e. average ± std. dev.) with processing parameters. Variation of pressure for each temperature while keeping velocity constant (0.5 mm/s) (n=10). Statistical analysis was performed between samples belonging to the same group. *, **,** indicate statistically significant difference between the lowest parameter considered and all the other levels (*p*-value<0.05, *p*-value<0.01, *p*-value<0.0001). $^{++}$,$^{++++}$ indicate statistically significant difference between two consecutive parameters (*p*-value<0.01 and *p*-value<0.0001).**

A similar trend could be observed for variations in temperature for each pressure while keeping the velocity fixed at 0.5 mm/s, as described in Figure 6.2. Overall the width of the struts at 110°C were significantly higher than those at the lowest temperature considered (i.e. 110°C vs 80°C for 100 and 200 kPa and 110°C vs 90°C for 50 kPa) (*p*-value <0.01 for 50 kPa, *p*-value <0.001for 100 kPa and *p*-value <0.0001 for 200 kPa). However, for all the pressures analysed no statistically significant differences could be detected between the samples at 90°C and 100 °C.

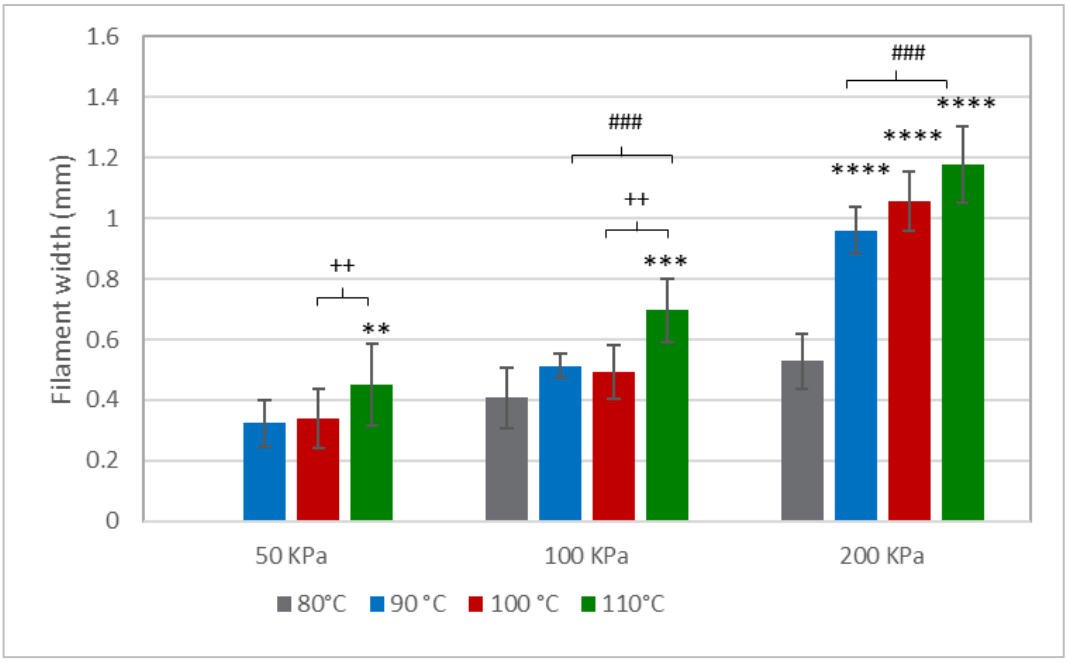

Figure 6.2 Variation of the filament width (i.e. average ± std. dev.). Variation of temperature for each pressure while keeping velocity (0.5 mm/s) constant. Statistical analysis was performed between samples belonging to the same group (n=10). **,*,**** indicate statistically significant difference between the lowest parameter considered and all the other levels (*p*-value<0.01, *p*-value<0.001, *p*-value<0.0001). $^{++}$ indicates statistically significant difference between two consecutive parameters (*p*-value<0.01).$^{###}$ indicates statistically significant difference between two consecutive parameters of the samples belonging to the same group (*p*-value < 0.001).**

An opposite trend was obtained by variation of the velocity for each temperature analysed while keeping the pressure constant at 200 kPa (i.e. only pressure with a complete set of data for all the parameters tested) (Figure 6.3). The dimensions of the filament significantly decreased with the increase of velocity. For all the temperature evaluated, the dimensions of the strut at 0.5 mm/s was significantly higher than the filament dimension obtained for all the other velocities (*p*-value <0.05 for 80°C and *p*-value <0.0001 for the other three temperatures). Moreover, for the sample at 110°C the filament size statistically decreased with each change of temperature (*p*-value < 0.0001 between 1 mm/s and 2 mm/s and *p*-value< 0.01 for 2 mm/s and 4 mm/s). For 100°C, a significant reduction was evidenced between 1 mm/s and 2 mm/s samples (*p*-value<0.001), while no difference could be detected between 2 mm/s and 4 mm/s. Finally, for 90°C no significance differences in the filament dimension was observed between the samples at 1 mm/s and 2 mm/s.

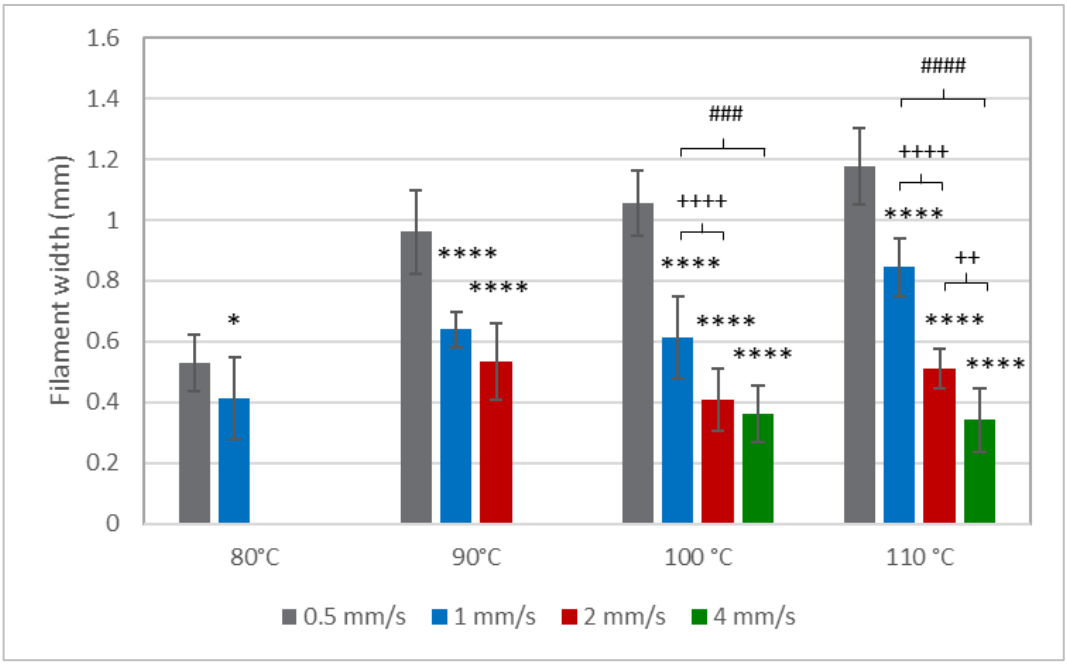

Figure 6.3 Variation of the filament width (i.e. average ± std. dev.) with processing parameters. Variation of writing velocity for each temperature while keeping pressure (200 kPa) constant (n=10). Statistical analysis was performed between samples belonging to the same group. *, ** indicate statistically significant difference between the lowest parameter considered and all the other levels (*p*-value<0.05, *p*-value<0.0001). $^{++++}$ indicates statistically significant difference between two consecutive parameters (*p*-value<0.0001). $^{###}$, $^{####}$indicate statistically significant difference between two consecutive parameters of the samples belonging to the same group (*p*-value<0.01, *p*-value<0.0001).**

Using the optimized conditions described above, structures with different macro porosities ranging from 1.5 mm to 0.5 mm could be obtained, as shown in Figure 6.4 a, b and c. Moreover, constructs with a honeycomb pattern could be obtained as shown in Figure 6.4 d. All the scaffolds produced possessed a well-defined structure, closely matching that of the implemented design, confirming the printability of the material.

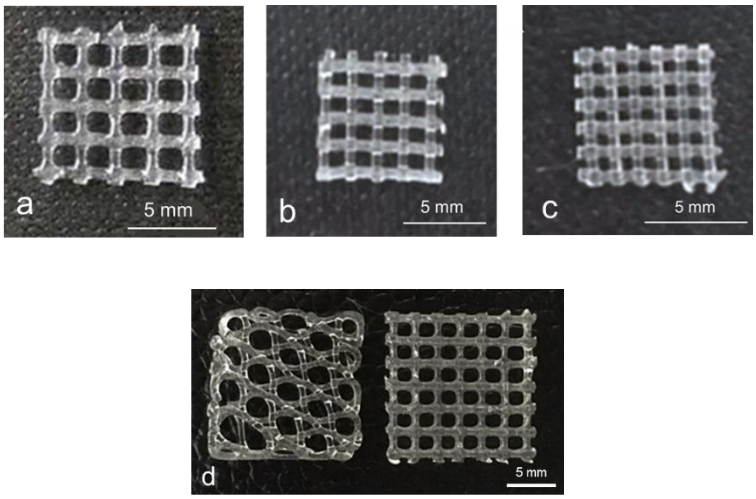

Figure 6.4 3D printed scaffolds of P(3HO-co-3HD-co-3HDD) with macro porosities of a)1.5mm , b) 1 mm, c) 0.5 mm pore size and d) with different patterns, honeycomb (left image) and rectilinear (right image).

Another important parameter for 3D printing is the layer height, the distance between layers of materials deposited on top of each other. Using the optimal conditions obtained in the screening experiment, a layer distance of 0.4 mm was found to be the best for the development of 3D printed constructs. In particular a targeted scaffold height of 6 mm could be achieved by the deposition of 22 layers of materials, as shown in Figure 6.5. Such scaffolds dimensions (1.5x1.5 of pore size and 6 mm height) were designed in collaboration with the Orthopaedic Surgery and Traumatology and Cell Therapy Department of the University of Navarra and will be discussed in more details in Chapter 7. However, the structure obtained did not show porosity in the zeta axes, an indication of sagging of the material between layers (Chen *et al.*, 2019).

Figure 6.5 3D printed scaffolds of P(3HO-co-3HD-co-3HDD) with 6 mm of height obtained by deposition of 22 layers of material.

6.2.1. Surface characterization

SEM analyses of the 3D printed P(3HO-co-3HD-co-3HDD) scaffolds was conducted to investigate the surface properties of the materials. As shown in Figure 6.6, the scaffolds obtained has a smooth surface without the presence of micro pores.

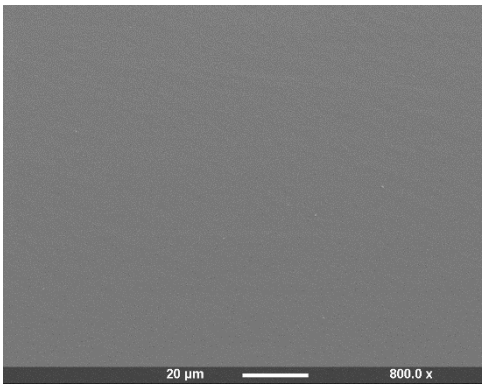

Figure 6.6 SEM analyses of the surface of a 3D printed P(3HO-co-3HD-co-3HDD) scaffold.

6.2.2. Evaluation of the effect of the printing process on the molecular weight properties

To evaluate whether the melt 3D printing process could induce a variation of the properties of the polymeric material, GPC analyses were performed on the extruded material. For this reason, three samples were taken at specific time points through the printing process and the material properties were analysed and compared to the starting material. The first interval considered was 15 minutes as that is the time used to allow the polymer to melt inside the aluminium cartridge. The final sample was taken after 2 hours, which based on laboratory practise was the longest time that the polyester would be heated for. Two middle points of 30 minutes and 1 hour were chosen to characterize the printing process.

Table 6.3As shown in Table 6.3, no statistical variation of the weight average molar mass, the number average molar mass and the polydispersity index for all the time points were evaluated as compared to the control conditions (i.e. polymer not 3D printed).

Table 6.3 Molecular weight of 3D printed P(3HO-co-3HD-co-3HDD) samples after 15 minutes, 30 minutes, 1 hour and 2 hours of printing. M_w is the weight average molar mass, M_n is the number average molar mass and PDI is the polydispersity index (Mw/Mn) The results are expressed as average ± standard deviation (n=3).

Time	M_w (kDa)	M_n (kDa)	PDI
Time 0 CTR	273 ± 12	65 ± 15	4.2 ± 0.8
15 minutes	280 ± 10	56 ± 13	5.2 ± 1.4
30 minutes	290 ± 7.5	57 ± 18	5.2 ± 2.4
1 hour	279 ± 12	60 ± 6	4.1 ± 0.4
2 hours	284 ± 10	59 ± 6	4.8 ± 0.5

6.2.3. Degradation study

The *in vitro* degradation of the 3D printed structures was investigated by incubating the samples in PBS at 37°C for 6 months. For such experimental tests, samples of 1.5x 1.5 mm pore size and 1 mm of layer height were produced. The materials maintained their shape throughout the duration of the study.

After each month, the samples were weighted, and the % water uptake was calculated. As shown in Figure 6.7 a, the 3D printed structures showed an average wet weight slightly higher than the initial weight even though not significantly different. Moreover, the weight remained constant throughout the course of the experiments, without statistically significant differences. The samples were then dried at room temperature until constant weight was achieved. Figure 6.7 b shows the % dried weight variation of the samples over time. No statistically significant difference was detected for all the samples analysed, indicating that the weight remained constant over time.

a)

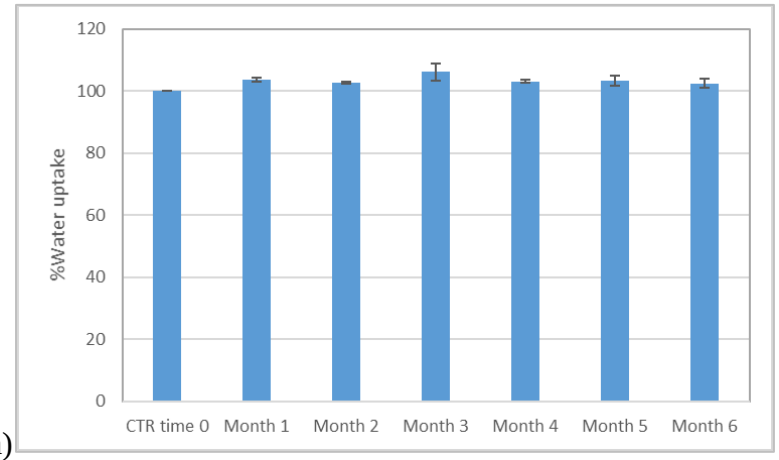

b)

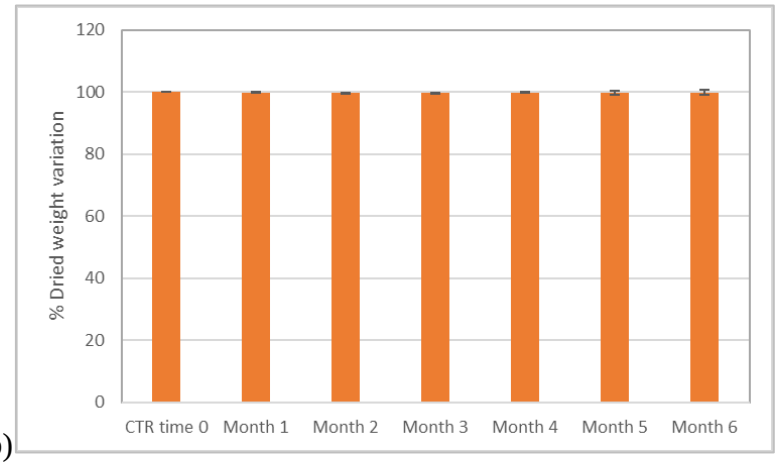

Figure 6.7 a)% water uptake and b) % dried weight variation of 3D P(3HO-co-3HD-co-3HDD) printed scaffolds after incubation in PBS for 6 months at 37 °C (n=3). For both graphs no statistically significant difference was detected between the samples (*p*-value >0.05).

The variation of the pH of the solutions was recorded over time and is reported in Figure 6.8. No change in the pH was observed after 1 month of incubation of the 3D printed scaffolds. After 2 months, a slight but statistically significant decrease of the pH was detected

from 7.4 to 7.2 (p-value < 0.05), and this value remained constant for the rest of the duration of the degradation tests.

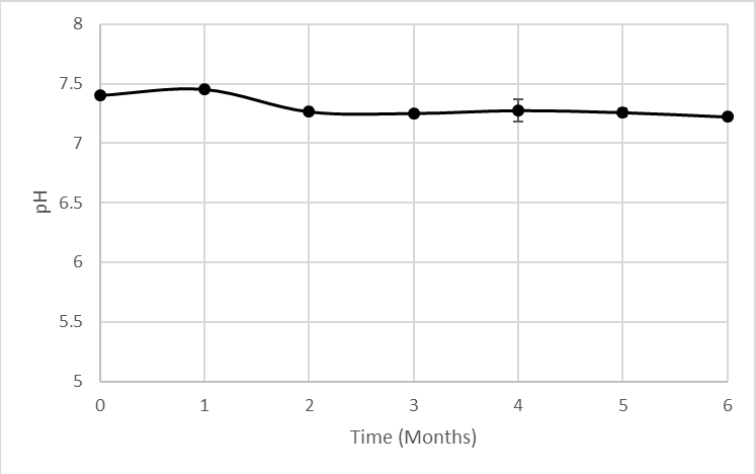

Figure 6.8 Variation of the pH of 3D P(3HO-co-3HD-co-3HDD) printed scaffolds during the degradation studies in PBS over 6 months of incubation at 37° C (n=3).

The variation of the molecular weight of the samples over time was investigated through GPC analyses. Table 6.4 shows the weight average molar mass (M_w), the number average molar mass (M_n) and the polydispersity index (PDI)(M_w/M_n) for all the time points evaluated. Figure 6.9a shows the variation of the M_w over time, evidencing the statistically significant differences between the samples. Overall, the M_w decreased significantly over time as compared to the sample at time zero. After one month a significant decrease in the average M_w was detected as compared to the sample at time zero (average reduction of 10%, p-value< 0.05). After 2 months, the average M_w was significantly lower than both the M_w at time zero (average reduction of 32%, p-value < 0.0001) and the M_w of the samples after 1 month (average relative reduction of 25% as compared to samples after 1 month, p-value < 0.0001). After 3 months of incubation, the samples showed a further statistically significant decrease in the molecular weight, with an average of 45% of reduction as compared to the initial sample (p-value < 0.0001) and an average of 19% of relative reduction as compared to the samples after 2 months (p-value < 0.01). No statistically significant changes in the M_w of the samples after 4 months could be detected as compared to the samples after 3 months of incubation. After 5 months, the samples showed a significant decreased value of the M_w as compared to both the initial samples (average reduction of 57%, p-value < 0.0001) and the samples after 4 months (average relative reduction of 15%, p-value < 0.05). Finally, an average reduction of the M_w by 66% was obtained after 6 months of incubation as compared

to the initial sample (p-value < 0.0001). Moreover, the M_w of the samples at 6 months was significantly lower than the M_w of the samples at 5 months (average relative reduction of 20%, p- value < 0.01).

The variation of the M_n over time is describe in Figure 6.9 b. No statistically significant difference could be noticed after one month of incubation as compared to the control conditions. After 2 months a significant decrease of the M_n was detected as compared to the initial samples (average reduction of 19%, p-value<0.05). No statistically significant changes in the M_n of the samples after 3 months could be detected as compared to the samples after 2 months of incubation. After 4 months, the samples showed a significant decrease of the M_n as compared to both the initial samples (average reduction of 45%, p-value < 0.0001) and the samples after 4 months (average relative reduction of 25%, p-value < 0.01). No statistically significant changes in the M_n of the samples after 5 months could be detected as compared to the samples after 4 months of incubation. A final average 57% reduction of the M_n was obtained after 6 months of incubation as compared to the initial sample (p-value < 0.0001).

Finally, a significant decrease in the average value of the PDI was detected after 2 and 3 months of incubation as compared to the initial samples (p-value<0.05). No statistically significant difference was detected between the other time points evaluated and the initial conditions.

Table 6.4 Variation of the molecular weight of 3D P(3HO-co-3HD-co-3HDD) printed scaffolds during the degradation studies in PBS over 6 months of incubation at 37° C (n=3). M_w is the weight average molar mass, M_n is the number average molar mass and PDI is the polydispersity index (Mw/Mn)

Time	M_w (kDa)	M_n (kDa)	PDI
CTR Time 0	274 ± 6	52.7 ±1.8	5.1 ± 0.3
Month 1	244 ± 7	51 ± 3	4.8 ± 0.2
Month 2	185 ± 10	42.5 ±1.5	4.3 ± 0.1
Month 3	150 ± 3	38.5 ± 2	3.9 ± 0.2
Month 4	138 ± 14	29 ± 2.5	4.6 ± 0.3
Month 5	117.5 ± 2	25 ± 2	4.6 ± 0.1
Month 6	93.5 ± 3.5	22.5 ± 4.5	4.3 ± 1

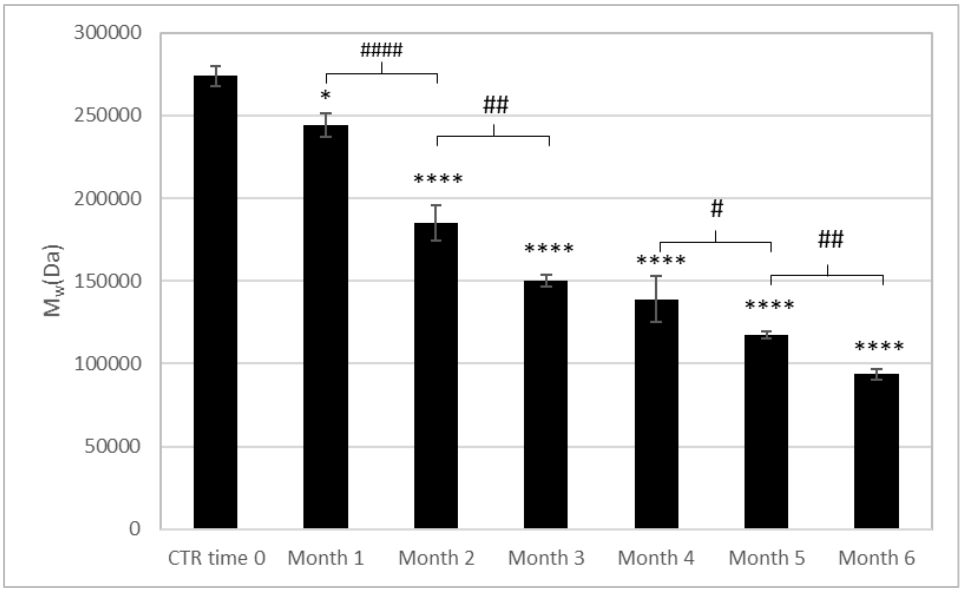

a)

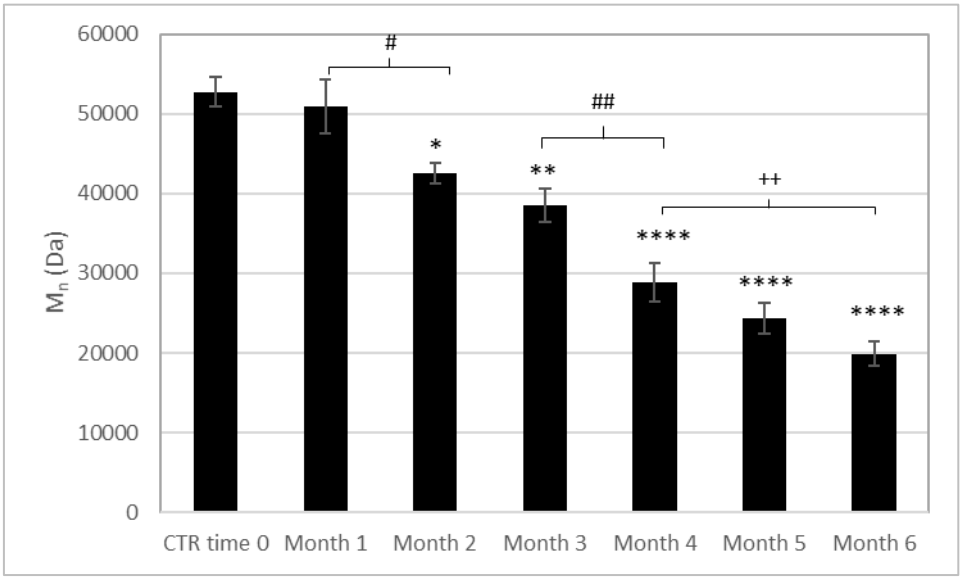

b)

Figure 6.9 Variations of the a) M_w and b) M_n of 3D P(3HO-co-3HD-co-3HDD) printed scaffolds after incubation in PBS for 6 months at 37 °C(n=3). *, **,** indicate statistically significant difference between the samples at time 0 and all the other time points (*p*-value<0.05, , *p*-value<0.01, *p*-value<0.0001).$^{\#}$, $^{\#\#}$, $^{\#\#\#\#}$indicate statistically significant difference between two consecutive time points (*p*-value<0.05, *p*-value<0.01, *p*-value<0.0001). $^{++}$ indicate statistically significant difference between the Mn after 4 months and after 6 months (*p*-value<0.01).**

The variation of the thermal properties during the *in vitro* degradation studies over 6 months are reported in Table 6.5 and Figure 6.10. No statistically significant differences of the glass transition temperature could be detected between the samples during the study. After one month of incubation, a distinct bimodal pattern was detected for the melting peak, characterized by the presence of two melting peaks as shown in Figure 6.10. The main peak was around 51°C, while the second was around 39°C, and the values remained constant over time for all the samples evaluated, without statistically significant differences.

Variation of the enthalpy of fusion of the materials could be detected during the duration of the experiment. No statistically significant differences were evidenced after 1 month of incubation. The enthalpy of fusion increased significantly after 2, 3 and 4 months as compared to the starting material (p-value < 0.001 for moth 3, p-value < 0.01 for both month 3 and 4). However, no statistically significant differences were evidenced between these time points (i.e. month 2 vs month 3, month 3 vs month 4 and month 2 vs month 4). Finally, no statistically significant differences were detected between the variation of enthalpy after 5 and 6 months as compared to the initial values.

Table 6.5 Thermal properties of 3D printed P(3HO-co-3HD-co-3HDD) samples after incubation in PBS for 6 months at 37 °C. T_m is the melting peak, T_g is the glass transition temperature and ΔHm is the enthalpy of fusion. The results are expressed as average ± standard deviation (n=3).

Polymer	T_m (°C)		T_g (°C)	ΔH_m (J/g)
	T_1	T_2		
Time 0	-	50.5 ± 0.5	-43 ± 1.8	17.5 ± 0.5
1 Month	39 ± 0.5	50.5 ± 0.5	-42 ± 0.5	16.7 ± 0.5
2 Months	39.1 ± 0.3	50.5 ± 0.6	-43± 1.2	22.6 ± 1.4
3 Months	40 ± 1	51 ± 0.5	-42± 0.5	21.2 ± 1
4 Months	38.7 ± 1	52.3 ± 0.5	-42.6 ± 2	21 ± 1.9
5 Months	38.5 ± 0.5	52.3 ± 0.6	-42 ±0.5	18.4 ± 1
6 Months	38.5 ± 1	51.7 ± 1.4	-42.6 ± 1.2	19± 0.5

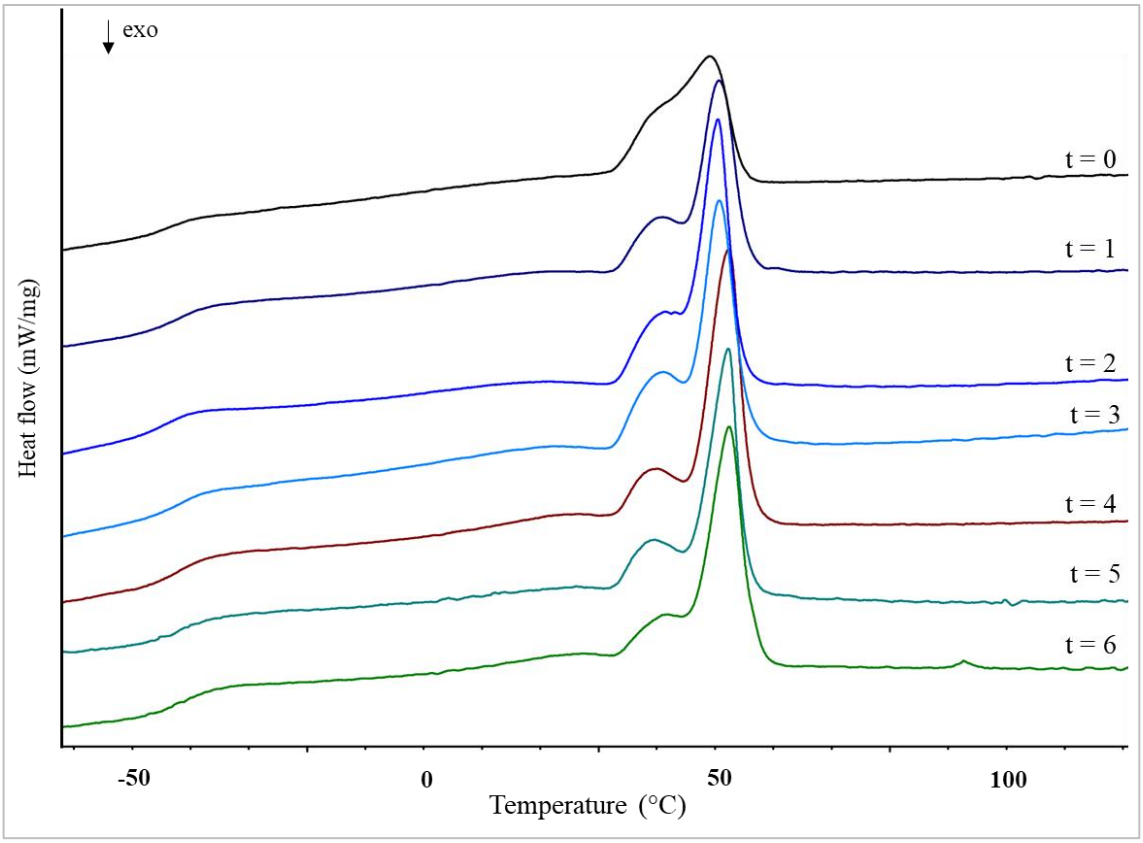

Figure 6.10 Representative thermographs for the 3D P(3HO-co-3HD-co-3HDD) scaffolds during the degradation studies in PBS at 37 °C for six months. Thermograms were shifted vertically for better visibility.

6.2.4. Biological characterization

6.2.4.1. *In vitro* cell compatibility studies

In vitro preliminary cell studies were conducted to assess the compatibility of the 3D printed scaffolds using MC3T3-E1 cell line. Indirect cytotoxicity studies were performed to evaluate the potential release of toxic material from the structure. As shown in Figure 6.11 , 3D P(3HO-co-3HD-co-3HDD) printed scaffolds showed a cell viability comparable to the positive control. This result indicated the absence of toxic degradation products potentially released from the structures developed using melt 3D printing.

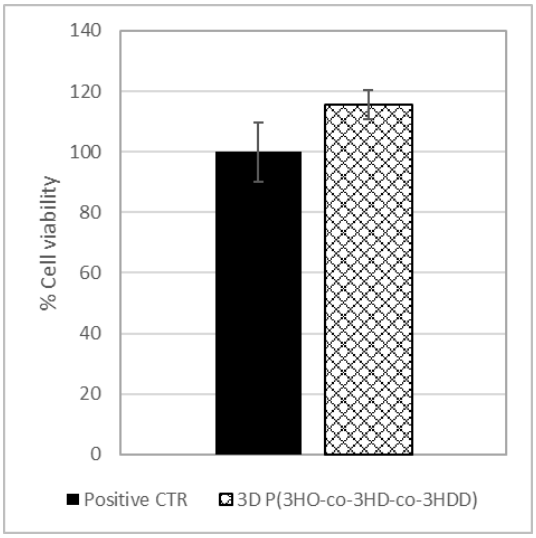

Figure 6.11 Indirect cytotoxicity studies of 3D P(3HO-co-3HD-co-3HDD) using MC3T3-E1 cell line (n=3, error bars =± SD).). The values were expressed as % positive control, i.e. cells cultured directly on Tissue Culture Plastic (TCP). There was no statistically significance difference between the samples.

Cell viability studies were conducted to investigate the growth of MC3T3-E1 on the produced materials at 1, 3 and 7 days. As shown in Figure 6.12, the cell viability was comparable to the positive control (tissue culture plastic, TCP) for all the time points evaluated.

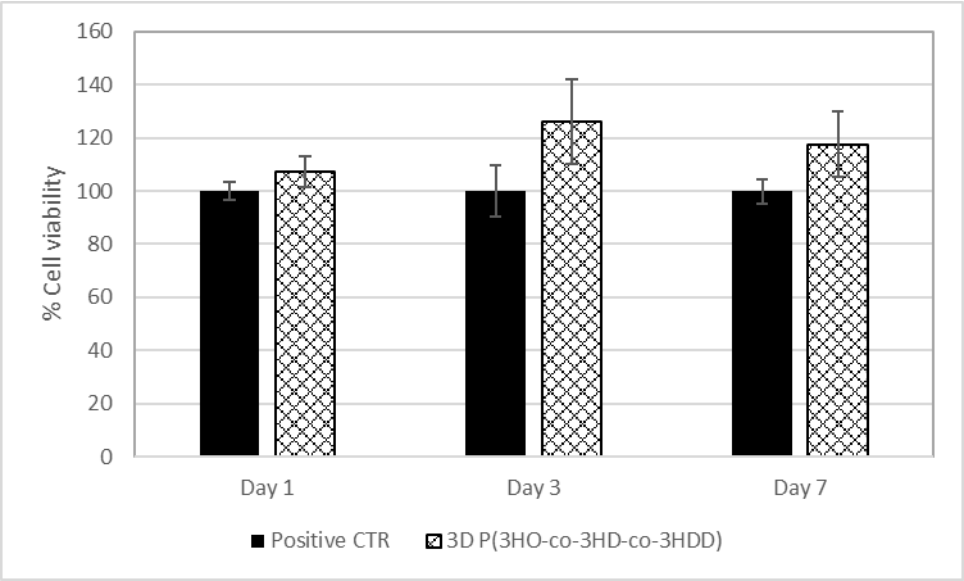

Figure 6.12 Cell viability studies of MC3T3-E1 cultured directly on 3D P(3HO-co-3HD-co-3HDD) at day 1, 3 and 7 (n = 3, error bars =± SD). The values were expressed as % positive control, i.e. cells cultured directly on Tissue Culture Plastic (TCP). There was no statistically significant difference between the samples for all the time point evaluated.

A live and dead test was conducted after 7 days of incubation of the MC3T3-E1 cells on the 3D scaffolds to confirm the cell viability results of the Alamar blue assay and evaluate the distribution of the cells on the surface of the materials. The test uses two dyes to distinguish between alive and dead cells. Calcein-AM is a non-fluorescent dye that can permeate the cell membrane of cells and can be converted by esterases into green-fluorescent calcein. Ethidium homodimer-1 is a weakly fluorescent dye that can bind to DNA, increasing its red fluorescence. Since this dye is impermeable to the cell membrane, only cells with damaged plasma membrane can be labelled with this dye. Therefore, using this staining method live cells appear green while dead cells appear red. Figure 6.13 shows the images obtained by fluorescent microscopy of the MC3T3-E1 cells on the surface of the scaffold. Two sections of the constructs are shown, a fibre of the scaffold and the middle section, characterized by a "cross shape" due to the crossing of two fibres. In both figures a uniform layer of live cells was detected, confirming the capability of the scaffold to favour the attachment and proliferation of the cells.

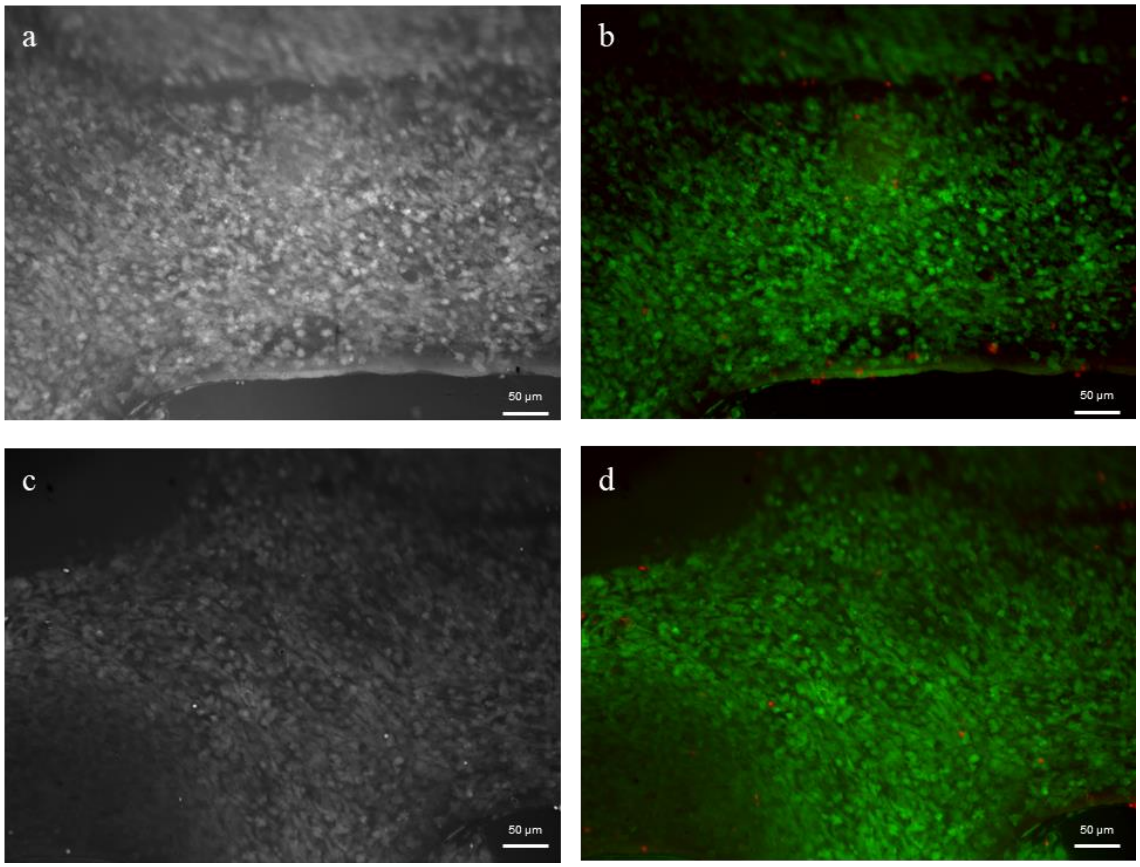

Figure 6.13 Images of the MC3T3–E1 cells cultured on of the 3D P(3HO-co-3HD-co-3HDD) scaffolds for 7 days: a-c) microscopic images at phase contrast b-d), fluorescence microscopic images by live/dead assay. Two sections of the scaffolds were selected a) and b) represent the filament part, while c) and d) represent the central part with a "cross shape".

6.2.4.2. *In vitro* cell differentiation studies

To further investigate the possibility of using 3D P(3HO-co-3HD-co-3HDD) scaffolds for bone tissue engineering, differentiation studies were conducted culturing MC3T3-E1 cells in osteogenic media containing ascorbic acid and β-glycerophosphate. MC3T3-E1 is a preosteoblastic cell line that has been extensively investigated for preliminary compatibility studies of materials for bone regeneration due to its capability to differentiate into osteoblast cells in the presence of the aforementioned supplements. The cells were seeded on the surface of the materials and incubated for 21 days.

Preliminary investigation of the cell viability was conducted using Alamar blue assay and the results are reported in Figure 6.14. The cell viability was comparable with the control

(i.e. cell cultured on tissue culture plastic) for all the time points evaluated without statistically significant differences.

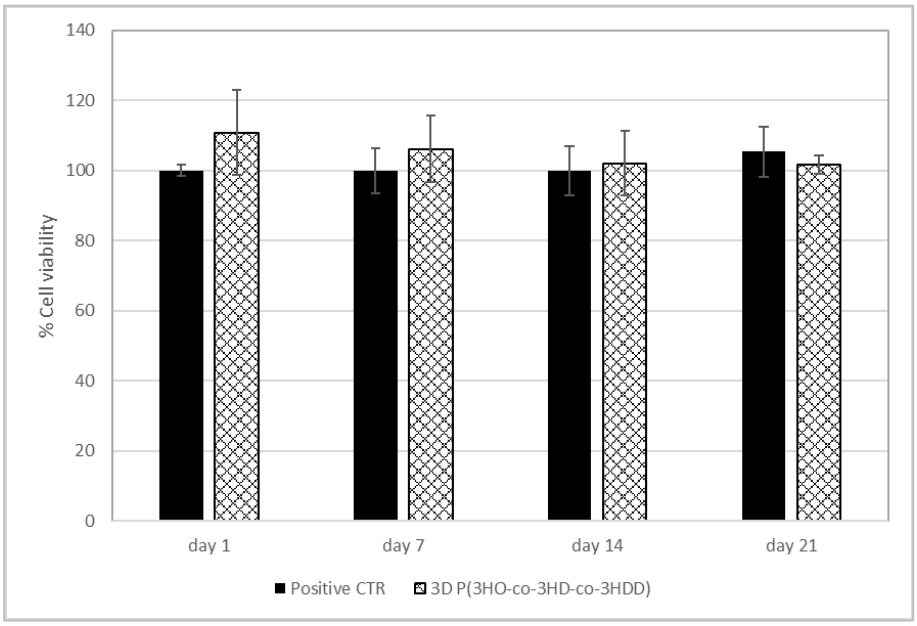

Figure 6.14 Cell viability studies of MC3T3-E1 cells cultured directly on 3D P(3HO-co-3HD-co-3HDD) at day 1, 7, 14 and 21 days cultured using osteogenic media (n = 3). The values were expressed as % positive control, i.e. cells cultured directly on Tissue Culture Plastic (TCP). There was no statistically significant difference between the samples.

To evaluate the differentiation of MC3T3-E1 cells into osteoblasts the expression of the alkaline phosphatase (ALP) was investigated. This enzyme is able to hydrolyse phosphate esters bonds and has been shown to promote mineralization by increasing the concentration of inorganic phosphates through the hydrolysis of pyrophosphate (Golub and Boesze-Battaglia, 2007). To quantify the presence of ALP in the *in vitro* cell culture a colorimetric assay was employed based on the use of p-nitrophenyl phosphate as the substrate which is turned into a yellow compound (i.e. *p*-nitrophenol, *p*NP) when dephosphorylated by the enzyme. The final activity of ALP expressed in nmol was then normalized to the total content of DNA (ng) present in each sample. Figure 6.15 shows the ALP activity for the MC3T3-E1 cells cultured on the 3D P(3HO-co-3HD-co-3HDD) scaffolds at 7, 14 and 21 days. The average values of ALP activity increased over time for the 3D constructs with statistically significant difference at both day 14 and day 21 as compared to day 7 (p-value <0.02 for Day 14 and p-value <0.0001 for day 21). At day 7 no statistically significant differences were evidenced between the sample and the positive control. A statically lower average was detected at day 14 for the cells cultured on the scaffolds as compared to the control (p-value

< 0.01). However, the ALP activity of the scaffolds increased between day 14 and day 21 (p-value < 0.05) reaching the same values of the positive control. No statistically significant difference was in fact observed between the 3D constructs and the TCP after 21 days of incubation.

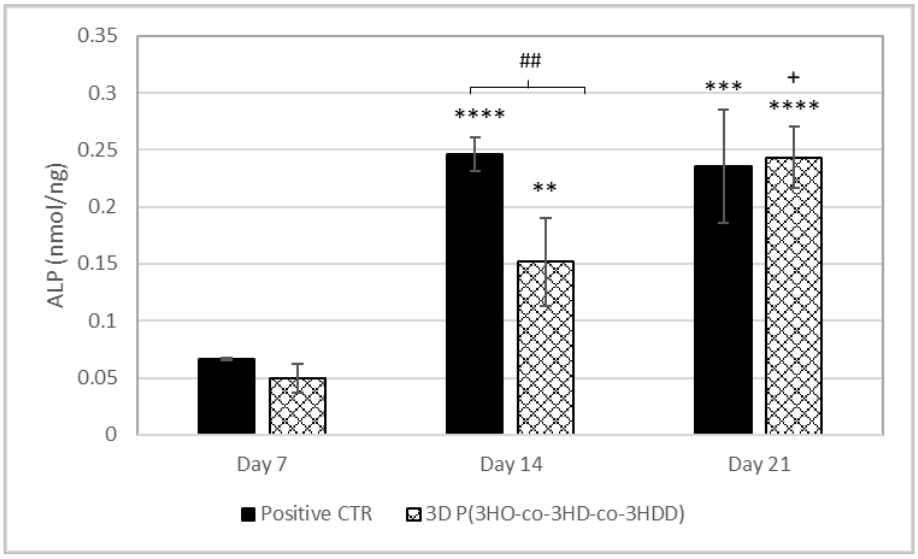

Figure 6.15 Alkaline phosphatase activity of MC3T3-E1 cells cultured on 3D P(3HO-co-3HD-co-3HDD) using osteogenic media after 7, 14 and 21 days (n=3). The ALP activity normalized to the DNA content and expressed as nmol/ng. The positive control was Tissue Culture Plastic (TCP). **,*,**** indicate statistically significant difference between the same samples at day 14 and 21 compared to day 7 (p-value<0.01, p-value<0.001, p-value<0.0001). ## indicate statistically significant difference between the scaffold and the TCP at day 14 (p-value<0.01). + indicate statistically significant difference between the scaffolds at day 21 and the scaffolds at day 21(p-value<0.05).**

The Alizarin red S staining solution was used for evaluating the mineralization of the scaffolds at 7, 14 and 21 days. The dye is able to bind with calcium deposited by a chelation mechanism, allowing the formation of a red complex which can then be extracted and analysed by colorimetric detection at 540 nm (Gregory *et al.*, 2004). Figure 6.16 shows the results of the Alizarin red S staining for the scaffolds compared to the control. A significant increase in the absorbance was detected for both the scaffold and the positive control from day 7 to day 14 and from day 14 to day 21 (p-value < 0.0001). No statistically significant difference was evidenced between the 3D printed scaffolds and the positive control for all the three time points considered.

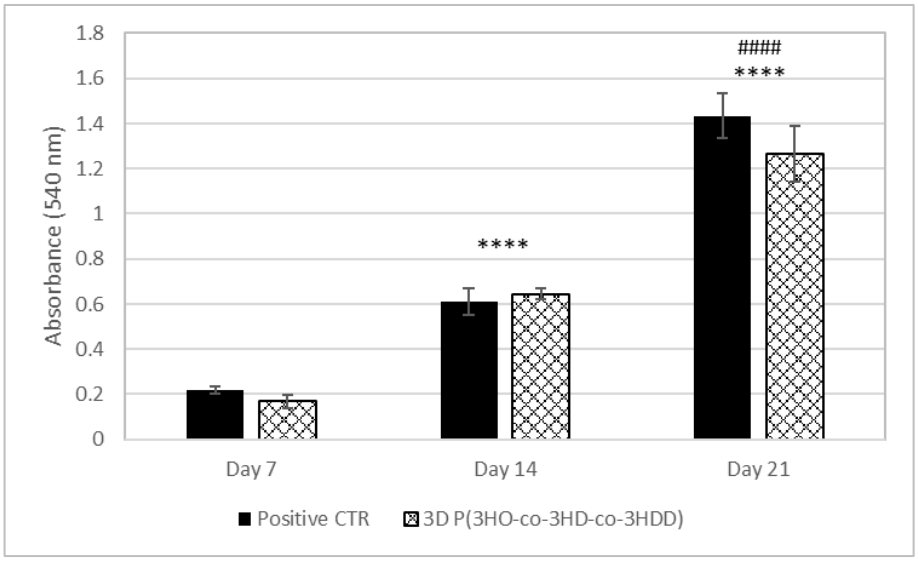

Figure 6.16 Alizarin red S staining of MC3T3-E1 culture on 3D P(3HO-co-3HD-co-3HDD) using osteogenic media after7 and 21 days (n=3). The positive control was Tissue Culture Plastic (TCP). ** indicate significant statistically difference between the same samples at day 14 and day 21 compared to day 7 (*p*-value<0.0001). #### indicate statistically significant difference between the same samples at day 21 compared to day 14 (*p*-value<0.0001). There was no statistically significant difference between the scaffolds and TCP at day 7 and day 21.**

6.2.5. Development of 3D printed scaffolds with dual porosity: macro and micro porosity

In the second part of this chapter, the possibility of combining salt-leaching with melt 3D printing was investigated to create scaffolds with dual porosity. The macro-porosity was created by the 3D model used for the printing (i.e. 1.5x 1.5 mm pore size and 1 mm height) and a micro-porosity was created inside the fibres through the addition of salt particles.

To optimize the production of such structures, P(3HO-co-3HD-co-3HDD) was mixed with salt particles of different size and in different ratios, as described in Table 6.6. In particular salt particles of two sizes (<100 µm and 100-300 µm) and three ratios of P(3HO-co-3HD-co-3HDD)/NaCl (50:50, 35:65 and 25:75 wt/wt) were considered. Compositions with a higher content of salt could not be printed. Slurry solutions of each composition were obtained by mixing the polymer with salt in chloroform. The mixtures were then poured in glass Petri dishes to obtain films with a homogeneous distribution of salt. Such films were cut into pieces and used as the starting materials for the printing of scaffolds with dual porosity.

All the samples listed in the table could be printed but a higher temperature 120 °C and a higher pressure between 170-200 kPa was required to extrude the material compared to neat constructs (100:0 P(3HO-co-3HD-co-3HDD)/NaCl).

Table 6.6 Composition of 3D P(3HO-co-3HD-co-3HDD)/NaCl samples

Sample	***Polymer Content (%wt/wt)***	***NaCl Content (% wt/wt)***	***NaCl Size (µm)***
50:50 P(3HO-co-3HD-co-3HDD)/$NaCl_{100µm}$	50	50	<100
35:65 P(3HO-co-3HD-co-3HDD)/$NaCl_{100µm}$	35	65	<100
25:75 P(3HO-co-3HD-co-3HDD)/$NaCl_{100µm}$	25	75	<100
50:50 P(3HO-co-3HD-co-3HDD)/$NaCl_{300µm}$	50	50	100-300
35:65 P(3HO-co-3HD-co-3HDD)/$NaCl_{300µm}$	35	65	100-300
25:75 P(3HO-co-3HD-co-3HDD) $NaCl_{300µm}$	25	75	100-300

6.2.5.1. Surface morphology characterization

A preliminary investigation of the surface morphology of the 3D scaffolds before salt leaching was conducted using the sample with the highest concentration of salt 25:75 P(3HO-co-3HD-co-3HDD)/ NaCl and salt dimension <100 µm as an example. The SEM analyses are reported in Figure 6.17. The surface of the samples containing salt appeared less uniform compared to the neat samples due to the presence of the porogen. Moreover, Figure 6.17c shows the cross section of a fibre of the 25:75 P(3HO-co-3HD-co-3HDD)/ $NaCl_{100\mu m}$. NaCl particles appeared embedded within the fibre and uniformly distributed, with grains of NaCl of dimensions lower than 100 µm as expected.

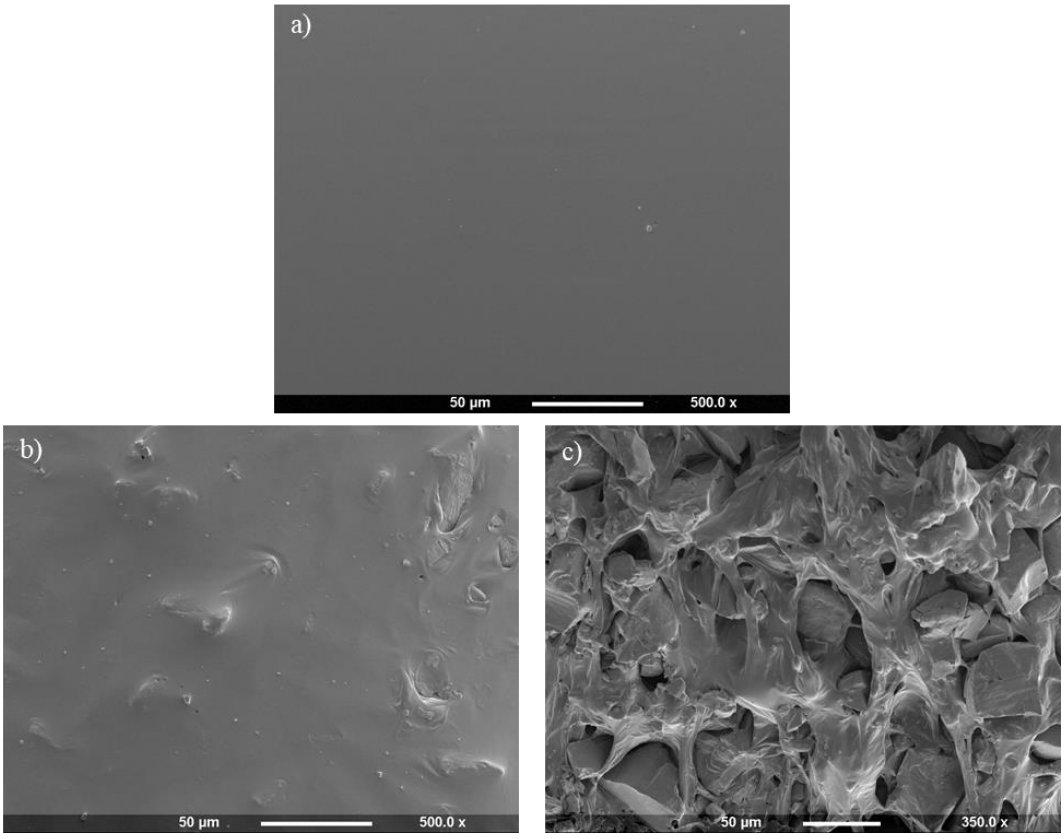

Figure 6.17 Representative SEM analyses of the surface of a) 3D P(3HO-co-3HD-co-3HDD) without salt, b) 3D 25:75 P(3HO-co-3HD-co-3HDD)/$NaCl_{100\mu m}$. Figure c represents the inside cross section of a fibre of 3D 25:75 P(3HO-co-3HD-co-3HDD)/$NaCl_{100\mu m}$.

Figure 6.18 shows the SEM analyses of the surface of 3D P(3HO-co-3HD-co-3HDD)/NaCl samples with a particle salt particle size <100µm and between 100 and 300 µm after leaching in water. ImageJ software was used to quantify the dimension of the pores present and to

give an indication of % area of the surface occupied by the pores (Figure 6.19), as described in the material and methods section 2.11.1.

For the smaller dimension of porogen (i.e. < 100 µm), the sample with the lowest concentration of salt 50:50 P(3HO-co-3HD-co-3HDD)/$NaCl_{100µm}$ showed a smooth surface characterized by the presence of a few pores with a diameter < 20µm. The relative % area covered with pores was low, less than 1%. The effect of the presence of salt was more evident in the samples with a higher concentration of porogen, 35:65 and 25:75 P(3HO-co-3HD-co-3HDD)/ $NaCl_{100µm}$. A change in the morphology of the surface from smooth to rough could be detected. Moreover, the presence of salt induced the formation of pores with an irregular shape and a range of dimensions. For both loadings of porogen in fact three classes of pores dimensions could be detected, large one with a diameter from 50-30 µm, medium ones from 30 to 5 µm and small ones with a diameter lower than < 5 µm. Moreover, the area of the surface occupied by the pores was significantly higher for both concentrations compare to the lowest one (*p*-value <0.001), with an average value of 11%. No statistically significant differences could be detected between the two concentrations.

For the 3D P(3HO-co-3HD-co-3HDD)/$NaCl_{300µm}$ samples with a salt particle size between 100 and 300µm, the SEM analysis showed that the effect of salt could be detected for all the concentrations tested. The scaffold with the lowest amount of pororgen,50:50 P(3HO-co-3HD-co-3HDD)/$NaCl_{300µm}$, showed a rough surface with a few pores of diameter < 10 µm. The relative % area of the pore was lower than 1%. The surface of the samples with the intermediate concentration of NaCl appeared similar to that of 35:65 and 25:75 P(3HO-co-3HD-co-3HDD)/$NaCl_{100µm}$. Pores of irregular geometry were in fact present with dimensions lower than 50 µm. Moreover, the amount of the surface area occupied by the pores was higher than the one for the lowest concentration of salt (average 11%, *p*-value < 0.001). Finally, the increase in the amount of porogen induced the formation of bigger pores with a length between 90-100 µm on the surface of 25:75 P(3HO-co-3HD-co-3HDD)/$NaCl_{300µm}$. The presence of smaller pores with dimensions between 50-30 µm, 30-5 µm and <5 µm was also detected. The % area occupied by the pores was statistically higher than that of 50:50 and 35:65 P(3HO-co-3HD-co-3HDD)/$NaCl_{300µm}$ samples (*p*-value< 0.001 for both concentrations), with an average value of 22%. This percentage was also significantly higher than that obtained by the sample with the same composition but lower salt particle size (i.e. 25:75 P(3HO-co-3HD-co-3HDD)/$NaCl_{100µm}$, *p*-value< 0.001).

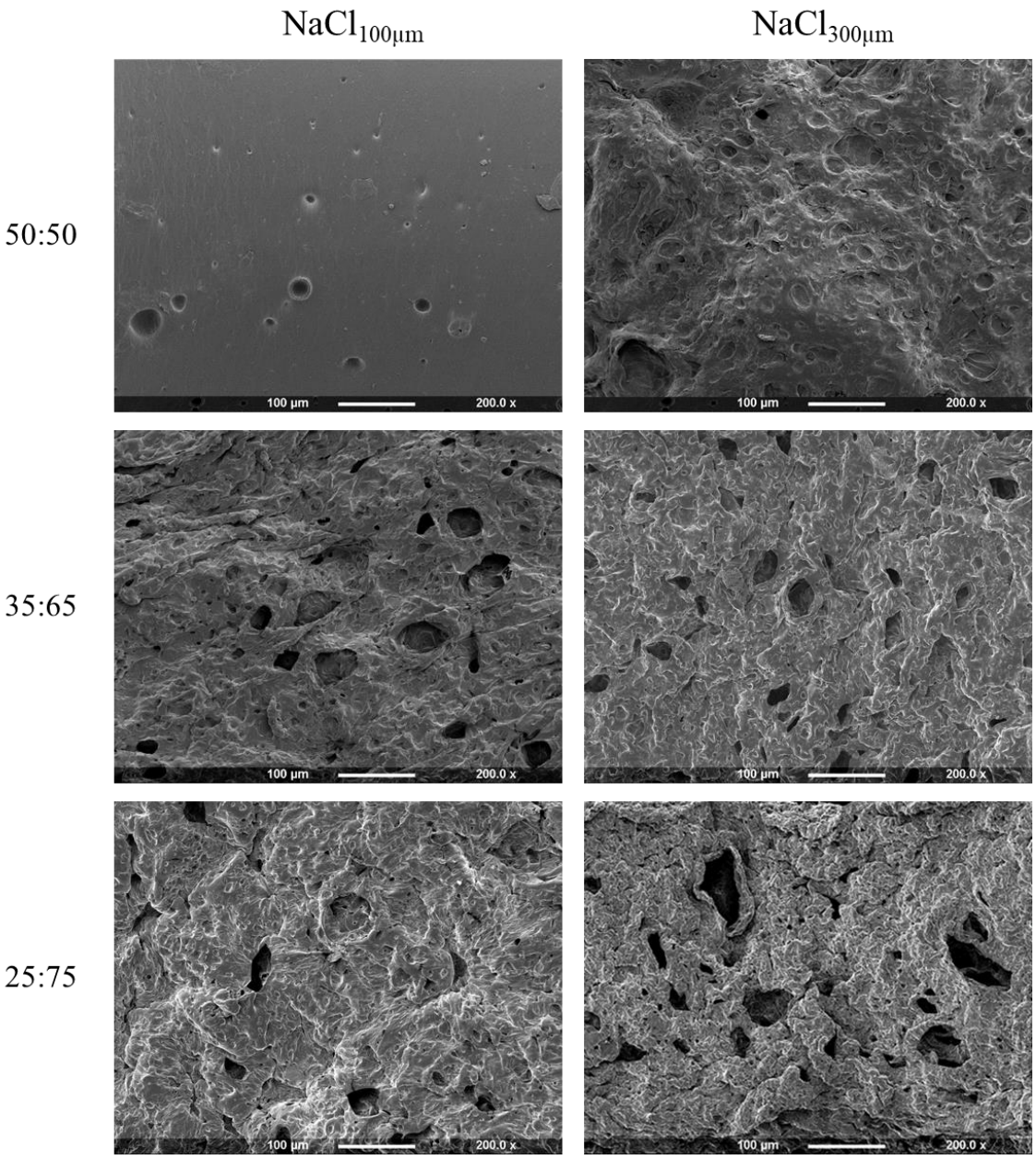

Figure 6.18 SEM analyses of the surface of 3D P(3HO-co-3HD-co-3HDD)/NaCl samples with a salt particle size <100µm (right column) and 100-300µm (left column) after leaching in water (200x). The first row shows samples with 50:50 ration of P(3HO-co-3HD-co-3HDD):NaCl, the second 35:65, the third 25:75.

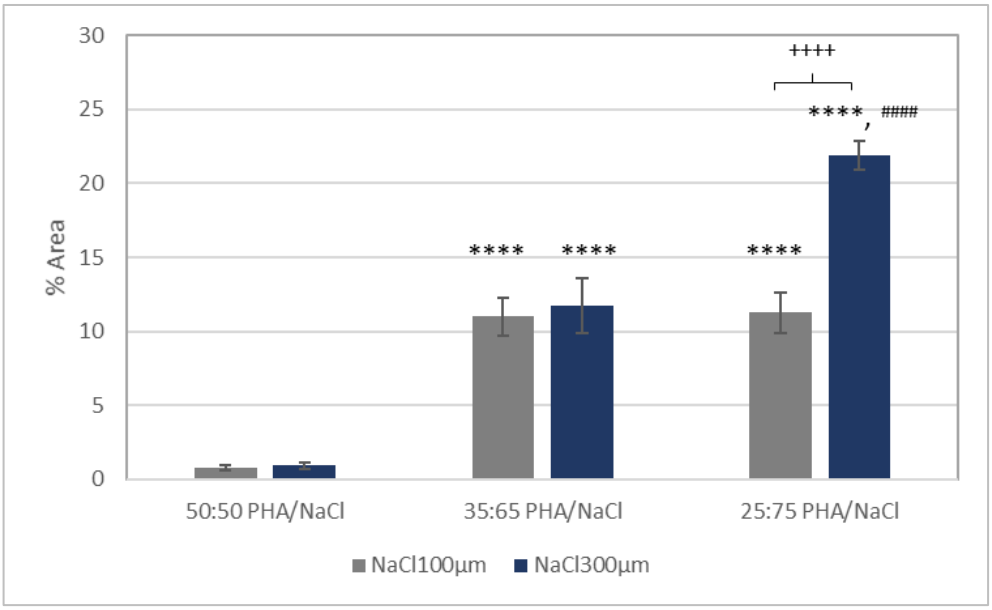

Figure 6.19 Percentage area of the surface occupied by the pores calculated using ImageJ software for 3D P(3HO-co-3HD-co-3HDD)/NaCl samples with a salt particle size <100µm (grey) and 100-300µm (blue) (n=3). ** indicate statistically significant difference between the same samples with 35:65 and 25:75 ratio compared to 50:50 ratio (*p*-value<0.0001). #### indicate statistically significant difference for P(3HO-co-3HD-co-3HDD)/$NaCl_{300µm}$ samples between 25:75 and 35:65 ratio (*p*-value<0.0001). ++++ indicate statistically significant difference for 25:75 ratio between samples with NaCl size <100µm and 100-300µm (*p*-value<0.0001)**

6.2.5.2. Porosity study

The intra-strut porosity of the 3D P(3HO-co-3HD-co-3HDD)/NaCl samples was calculated using the gravimetric method as described in the materials and methods section 2.11.7 and is reported in Figure 6.20.

For the smaller dimension of porogen (i.e. < 100 µm), the sample with the lowest concentration of salt 50:50 P(3HO-co-3HD-co-3HDD)/$NaCl_{100um}$ showed a low intra-strut porosity of 1%. The constructs with higher concentrations of salt showed a significantly higher percentage as compared to 50:50 P(3HO-co-3HD-co-3HDD)/$NaCl_{100um}$, with an average value of 22% for 35:65 P(3HO-co-3HD-co-3HDD)/$NaCl_{100um}$ and 36% for 35:75 P(3HO-co-3HD-co-3HDD)/$NaCl_{100um}$ (*p*-value <0.001 and *p*-value <0.0001 respectively). However, no statistically significant differences could be detected between the two concentrations with the highest amounts of salt (i.e. 35:65 vs 35:75).

A similar behaviour could be observed for the 3D P(3HO-co-3HD-co-3HDD)/$NaCl_{300um}$ samples with a salt particle size between 100 and 300 µm. The scaffold with the lowest

amount of porogen showed a low average value of 6.5%. The intra-strut porosity increased significantly for the constructs with higher content of salt as compared to 50:50 P(3HO-co-3HD-co-3HDD)/$NaCl_{300um}$, showing an average value of 23 for 35:65 P(3HO-co-3HD-co-3HDD)/$NaCl_{300um}$, and 36% for 25:75 P(3HO-co-3HD-co-3HDD)/$NaCl_{300um}$, (*p*-value <0.05 and *p*-value <0.001 respectively). As for the samples with porogen size < 100 µm, no statistically significant differences were detected between the samples with the highest amounts of salt (i.e. 35:65 vs 25:75).

Finally, no statistically significant differences could be detected between the sample with the same composition but different porogen dimensions (i.e. $NaCl_{100µm}$ vs $NaCl_{300µm}$).

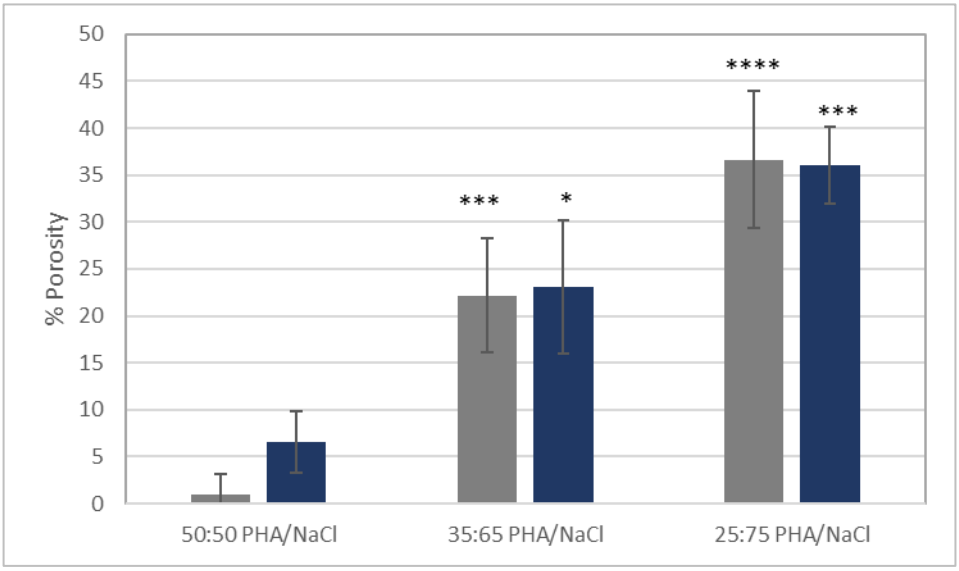

Figure 6.20 % Porosity of 3D P(3HO-co-3HD-co-3HDD)/NaCl samples with a salt particle size <100µm (grey) and between 100 and300µm (blue) (n=3). *,*,**** indicate statistically significant difference between the same samples with 35:65 and 25:75 ratio compared to 50:50 ratio (*p*-value<0.05, *p*-value<0.001, *p*-value<0.0001).**

6.2.5.3. *In vitro* compatibility studies

Preliminary *in vitro* compatibility studies were conducted using MC3T3-E1 cells. Indirect cytotoxicity studies were investigated using the eluates obtained after incubation of the scaffolds for 24 hours in the media, to evaluate the potential release of toxic substances from the 3D P(3HO-co-3HD-co-3HDD)/NaCl with a porogen size < 100 µm and between 100 and 300 µm. The results were expressed as percentage compared to the positive control, tissue culture plastic, and are shown in Figure 6.21. No statistically significant difference was

detected between the samples and the TCP for all the three concentrations of salt tested and the two porogen sizes.

a)

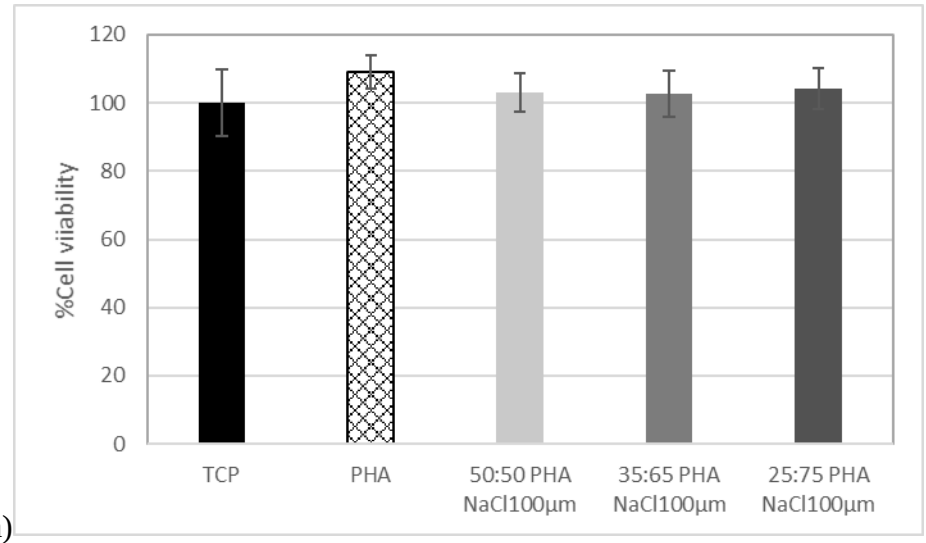

b)

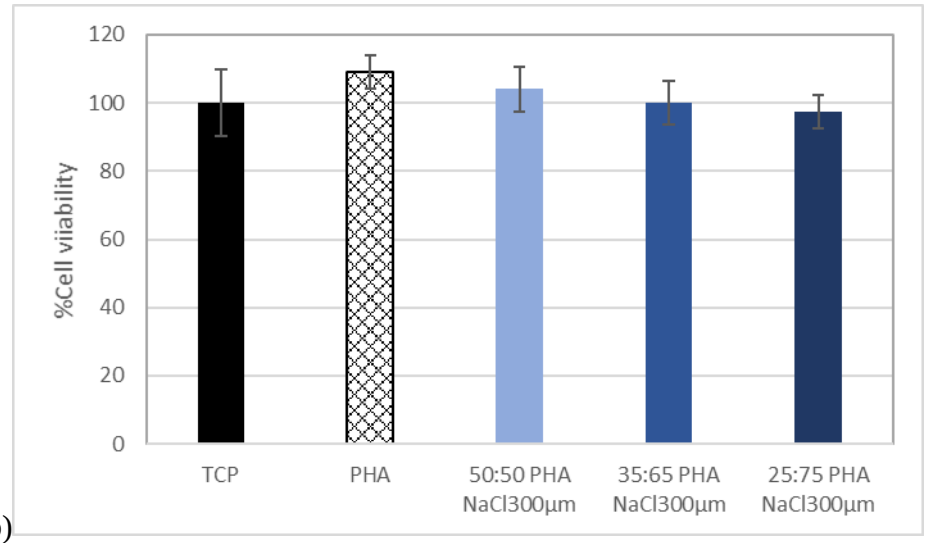

Figure 6.21 Indirect cytotoxicity studies using MC3T3-E1 cell line of 3D P(3HO-co-3HD-co-3HDD)/NaCl with a salt particle size a) <100 µm) and b) 100-300µm (n = 3). The positive control was Tissue Culture Plastic (TCP). There was no statistically significance difference between the samples (*p*-value>0.05).

6.3. Discussion

In the first part of this chapter, the possibility of developing 3D scaffolds through melt extrusion printing of P(3HO-co-3HD-co-3HDD) was investigated. As described in the introduction section, additive manufacturing allows to create controlled and well-defined structures with high reproducibility. Moreover, this technique can ultimately allow the development of customized and patient -specific scaffolds that match the shape and dimensions of the tissue to be replaced (Gloria *et al.*, 2009; Chiulan *et al.*, 2018). To date only a limited number of studies have been conducted on the 3D printing of PHAs, and none have investigated the use of mcl-PHA (Vaidya *et al.*, 2019; Pereira *et al.*, 2012; Duan *et al.*, 2011; Zhao *et al.*, 2014; Yang *et al.*, 2014). In this work for the first time a screening study was conducted to evaluate the optimal printing conditions for this polyester. Due to the thermoplastic properties of PHAs, these materials can be processed using extrusion-based systems by applying heat above their melting temperature, avoiding the use of toxic solvents (Gleadall *et al.*, 2018; Pfister *et al.*, 2004; Guo *et al.*, 2013). Based on literature studies, the melting temperature, the writing speed and the extrusion pressure are known to be key process parameters and were therefore investigated in this study (Gloria *et al.*, 2009; Hoque *et al.*, 2009; Sheshadri and Shirwaiker, 2015; Trachtenberg *et al.*, 2014; Domingos *et al.*, 2012). Assuming the molten polymer as a viscous Newtonian fluid with a laminar flow profile, the flow rate of the material (Q) can be described by the following Hagen-Poiseuille equation:

$$Q = \frac{\pi \Delta P}{128\, L \eta} * d^4$$

Where ΔP is the pressure, d is the nozzle inner diameter, L is the nozzle length, and η is the polymer viscosity. Keeping the nozzle parameters constant, Q is directly proportional to the applied pressure and inversely proportional to the material viscosity (Trachtenberg *et al.*, 2014; Gloria *et al.*, 2009; Turner *et al.*, 2014). In this work, the behaviour of P(3HO-co-3HD-co-3HDD) in terms of variation of filament width was in agreement with this equation. An increase in the filament width with increasing pressure was observed, which is explained by the fact that an increase of pressure leads to an higher flow of material while maintaining the other parameters constant (Hoque *et al.*, 2009; Trachtenberg *et al.*, 2014). A similar trend was observed for the extrusion temperature and can be correlated to the its relationship with

viscosity. An inverse relationship exists in fact between such parameters (i.e. increase in temperature causes a decrease of the viscosity) (Sheshadri and Shirwaiker, 2015; Domingos *et al.*, 2012). Therefore, the higher values of filament width induced by increments of temperature can be explained by the fact that in such conditions a lower viscosity is induced, consequently leading to higher flow rate, as described by the equation (Hoque *et al.*, 2009; Domingos *et al.*, 2012). Finally, a decrease of the filament width was obtained with increased writing speed. Under such conditions (i.e. fixed pressure, temperature and nozzle parameters), the flow rate of the material is kept constant and the cross section of the filament (A) can be described by the following equation:

$$A = \frac{\mathrm{Q}}{v}$$

Where Q is the flow rate and *v* the printing velocity (Hoque *et al.*, 2009; Turner *et al.*, 2014). This formula shows an inverse relationship between A and *v* which describes the results obtained in this work. Overall, the screening study allowed to obtain the optimal combination of parameters to successfully print well-defined and reproducible 3D structures using P(3HO-co-3HD-co-3HDD), for the selected nozzle size (i.e. 600 µm). Future work should be conducted to investigate the effect of the nozzle dimensions on the process, as such parameter directly linked with the flow rate of the material (as described by the Hagen-Poiseuille equation) and also determine the minimal printable resolution feature (Munaz *et al.*, 2016; Turner *et al.*, 2014).

Visual observation of the final 3D scaffolds printed (i.e. 6 mm height) revealed that no porosity on the z- direction could be achieved due to sagging of the material. During the printing process, solidification of each layer needs to occur before a following layer can be applied to avoid lateral collapse. Such feature depends on both processing parameters (e.g. temperature of printing, the writing speed, the layer height) and the materials properties (Ortega *et al.*, 2019; Domingos *et al.*, 2012). In this work, the optimal conditions to develop pores in the z direction could not be obtained, indicating a possible intrinsic limitation of the polyester used. Several studies in literature have indeed shown that PHAs possess low solidification properties from melt (Nerkar *et al.*, 2015; Li *et al.*, 2016c; Wang *et al.*, 2016b). A possible solution could be explored in future through the use of dual printing the polyesters with other materials to be used as sacrificial support layers (Alom-Ruiz and Chen, 2007; Birol *et al.*, 2006).

Finally, investigation of the effect of the printing process on the material properties was conducted, as the exposure of the polymer to high temperatures could lead to its degradation (Turner *et al.*, 2014). No decrease of the molecular weight of the material was detected in the GPC studies conducted, confirming the suitability of such techniques for mcl-PHAs.

Understanding the degradation behaviour of the scaffold obtained is essential for biomedical applications. Biodegradable constructs should be able to support cell attachment and proliferation and allow the cell to produce their own extracellular matrix, replacing over time the materials. Therefore, the scaffolds should be able to degrade in a manner suitable for the regeneration of a specific tissue. Moreover, the degradation product should be non-toxic and should not elicit an adverse reaction in the site of implantation. The degradation *in vivo* is a complex mechanism, depending on both the environmental characteristic (e.g. pH, temperature, presence of cells and enzymes) and the material properties (e.g. polymer chemical structure, molecular weight, crystallinity, morphology)(Gil-Castell *et al.*, 2019; Woodard and Grunlan, 2018). For this reason preliminary *in vitro* investigations are required to understand the degradation mechanism under simpler conditions (Domingos *et al.*, 2010). In this study, the degradation of the 3D P(3HO-co-3HD-co-3HDD) scaffolds was investigated using a simple set up by immersion of the samples in PBS at 37°C and pH of 7.4 over 6 months (Dong *et al.*, 2009; Woodard and Grunlan, 2018). In such conditions, polyesters are known to be degraded by hydrolysis of the ester bonds and two main mechanism can occur, bulk or surface degradation (Woodard and Grunlan, 2018). The former is characterized by random chain scission throughout the matrix of the material due to water diffusion inside the structure, causing reduction in the molecular weight. When the reaction produces small enough oligomers that can diffuse out of the scaffolds, drop in the weight of the materials can be evidenced (Ferreira *et al.*, 2017; Lam *et al.*, 2008). Surface degradation is instead localized in the outer layers of the constructs as the hydrolysis of the material is faster than the water penetration, leading to the release of the degradation products in the surrounding media with a reduction in the weight of the scaffolds, but not in its molecular weight (Ferreira *et al.*, 2017; Lam *et al.*, 2008; Beslikas *et al.*, 2011). The results obtained in this study suggested that the 3D printed scaffolds underwent bulk degradation, as no change in the weight of the material could be detected, while a decrease of the molecular weight (M_w) of up to 66% was observed after six months. Moreover, the overall structure of the constructs remained unchanged as the degradation occurred at a molecular level. In literature

a few studies have been conducted on the *in vitro* degradation for scl-PHA based scaffolds, while to date no study has been conducted on the *in vitro* degradation of mcl-PHAs materials. Freier *et al.* showed a reduction of 50% of the molecular weight (M_w) of P(3HB) films after 14 months of incubation, while for P(3HB) electrospun fibres a 54% decreased of M_n was achieved after 21 months (Freier *et al.*, 2002; Gil-Castell *et al.*, 2019). The degradation of P(3HB-co-HV) fibres has also been investigated showing a similar rate with a 47% loss of M_n after 11 months (Sultana and Khan, 2012). These results evidenced that the PHAs studied in this study showed a faster rate of degradation compared to the polyester studied in literature. This behaviour could be ascribed to the possible lower crystallinity of P(3HO-co-3HD-co-3HDD) compare to scl-PHAs. Crystalline regions in fact reduce the rate of construct degradation as they limit water penetration due to their tightly packed conformation (Woodard and Grunlan, 2018; Lam *et al.*, 2008). For example, poly(D,L-lactic) acid, an amorphous polymer, is characterized by a faster degradation rate compared to the semi crystalline poly(L-lactic acid)(Azevedo *et al.*, 2003). The higher susceptibility of the amorphous region compared to the crystalline one could also explain the increase in the enthalpy of fusion (and therefore increase in crystallinity) detected after 2, 3 and 4 months of incubation of the scaffolds. Such a behaviour has been evidenced for several polyesters including PHAs and it has been attributed to the fact that the hydrolysis of the amorphous areas leads to the presence of smaller fragments that can rearrange into crystalline structures (Bartnikowski *et al.*, 2019; Foster and Tighe, 2005; Domingos *et al.*, 2010; You *et al.*, 2005). Such mechanism was further confirmed by the presence of two distinct peaks in the melting area, suggesting that two different crystalline populations were present in the materials. In particular the recrystallized areas of the amorphous regions seemed to possess a less perfect structure, therefore melting at a lower temperature (40 °C compared to 50 °C)(Gil-Castell *et al.*, 2019). The increase in the enthalpy of fusion could also be related to the decrease in the rate of reduction of the molecular weight over time, as the new crystalline regions can act as a barrier to water diffusion and hence hydrolysis (Lam *et al.*, 2008).

Finally, a slight decrease in the pH of the solution was detected from 7.4 to 7.2 over the degradation tests. These results are encouraging for the application of such device for tissue engineering, as polyesters like PLLA or PLGA are usually associated with a reduction of the local pH due to their degradation products, with possible adverse effects such as the rise of a late inflammation at the implantation site (Liu *et al.*, 2006; Sung *et al.*, 2004). In literature PHAs have been shown to possess less acid degradation products than the aforementioned

polyesters, making them a valid alternative (Manavitehrani *et al.*, 2016; Bonartsev *et al.*, 2019). Based on these preliminary results, the designed 3D P(3HO-co-3HD-co-3HDD) scaffolds seemed to be suitable in terms of degradation for long term applications such as bone regeneration. For bone tissue regeneration in fact the scaffold should maintain its properties and structure during the first 3 months of implantation, allowing the deposition of new bone, and degradation should progress up to 12 months favouring bone remodelling (Woodruff *et al.*, 2012). Nevertheless, further studies should be conducted to evaluate the degradation of the polyester in the presence of enzymes such us eukaryotic lipases and esterases that have been shown to contribute to their degradation *in vivo* (Ong *et al.*, 2017; Freier *et al.*, 2002).

The compatibility of the 3D printed scaffolds was evaluated by preliminary *in vitro* studies using MC3T3-E1 cells. The indirect cytotoxicity test confirmed the absence of toxic leachable compounds in the developed constructs. Moreover, the materials were able to support the growth and proliferation of the cells, and a continuous and uniform layer of cells was detected after 7 days of incubation, showing the potential of this material for its application in bone tissue engineering. To further investigate the use of these materials in the bone regeneration, differentiation studies were conducted where the cells were cultured in a media containing ascorbic acid and β-glycerophosphate to favour their differentiation into osteoblasts. In a typical tissue engineering approach in fact the scaffold is combined with stem cells and needs to support and/or induce their differentiation into mature osteoblasts either before or after implantation (Sheehy *et al.*, 2019; Rai *et al.*, 2010; Cai *et al.*, 2015). Alternatively, if acellular constructs are implanted, the same requirement is needed for the differentiation of the host cells that are recruited during the bone healing process (Sheehy *et al.*, 2019; Su *et al.*, 2018; Lin *et al.*, 2017). Therefore, when novel constructs are developed, preliminary *in vitro* studies are usually conducted to evaluate if the material possess such features. In particular in this work the MC3T3-E1 cell line was chosen as it is a well-established model to study bone differentiation and mineralization *in vitro*, and its interaction with a wide range of materials has been investigated (Czekanska *et al.*, 2012; Hwang and Horton, 2019; Quarles *et al.*, 1992). This cell line is able to produce a mineralized extracellular matrix when cultured using ascorbic acid and β-glycerophosphate. The former is associated with the synthesis, deposition and maturation of collagen type 1, which has also been shown to induce differentiation as a direct contact between the cells and an ECM

containing collagen has been hypothesized to be essential for the cells to differentiate (Yan *et al.*, 2014; Langenbach and Handschel, 2013). β-glycerophosphate represent a source of phosphate for the ECM mineralization through its hydrolysis by the alkaline phosphatase enzyme leading to the release of inorganic phosphate (Pi). Moreover, Pi have also been described to be involved in the regulation of several osteogenic genes, acting as intracellular signalling molecules (Langenbach and Handschel, 2013; Hwang and Horton, 2019). In this work MC3T3-E1 cells were seeded on the 3D P(3HO-co-3HD-co-3HDD) scaffolds and cultured in osteogenic media, and the differentiation was evaluated in terms of ALP activity and calcium deposition (i.e. alizarin red s assay). From literature it is known that in such conditions the cell line undergoes three stages, proliferation, maturation and mineralization. During the first phase the cells attach and grow on the surface of the material but are still at an immature stage with low levels of ALP and calcium deposition (McCauley *et al.*, 1996; Quarles *et al.*, 1992). In this study such behaviour was detected as both markers were low after 7 days of incubation of MC3T3-E1 cell on both the scaffolds and the control (i.e. Tissue culture plastic). The maturation phase usually starts after 10 days of incubation and is characterized by a peak of ALP production, which then remains constant or even decreases during the final phase. Such stage is the final and typically begins after 16 days and is characterized by the deposition of inorganic calcium in the extracellular matrix, with the highest peak at the end of the incubation (St-Pierre *et al.*, 2005; Marsh *et al.*, 1995; Li *et al.*, 2019b; Choi *et al.*, 1996). The cells cultured on the positive control showed such typical behaviour, with an ALP activity peak after 14 days of incubation followed by the highest increment of calcium deposition after 21 days. For the 3D printed scaffolds, the ALP peak increased over time, but the highest value was detected at 21 days, indicating a possible slower maturation of the cells on such constructs compared to the positive control. Nevertheless, the maximum ALP activity was comparable to that of the positive control and a high level of mineralization was achieved after 21, without significant differences with the TCP, indicating that the 3D P(3HO-co-3HD-co-3HDD) are able to support the differentiation of the cells *in vitro*. Moreover, the similar behaviour in the mineralization might be an indication that the highest peak of ALP activity was actually achieved before 21 days, as a delay between the maximum expression of such markers is usually noticed (St-Pierre *et al.*, 2005; Choi *et al.*, 1996; Liu *et al.*, 2018). To obtain a better understanding of the influence of the 3D structure on the differentiation of the MC3T3-E1 cells compared to 2D systems, the use of the same material should be evaluated for future studies, using P(3HO-co-3HD-

co-3HDD) solvent cast films, eliminating possible differences due to intrinsic material properties (Kaur *et al.*, 2019b; Wu *et al.*, 2018). Finally, an osteoinductive behaviour for such materials was not detected in this study, which was expected as PHAs are not bioactive polyesters. In the studies where an increase in differentiation was achieved in fact the polymers were always mixed with materials such as bioactive glasses and hydroxyapatite, capable of inducing better biological performances (Ansari *et al.*, 2016; Yang *et al.*, 2014; Wang *et al.*, 2005).

In the second part of this chapter a feasibility study was conducted to evaluate the possibility of creating dual porosity in 3D printed P(3HO-co-3HD-co-3HDD) scaffolds through the combination of melt printing and salt leaching. As described in the previous sections the constructs obtained by melt printing of the mcl-PHAs showed a smooth surface without the presence of pores. Moreover, the absence of pores in the z-direction of the scaffolds was detected which could be detrimental for the application in a biological environment. An open and interconnective porosity is in fact a key parameter for the development of any scaffold for tissue engineering applications as it allows the exchange of nutrients and waste substances and favours cell proliferation and migration and tissue vascularization (Loh and Choong, 2013; Petrochenko and Narayan, 2010). Furthermore, higher binding between the scaffolds and the surrounding tissues has been evidenced with highly porous surfaces (Hannink and Arts, 2011; Zhang *et al.*, 2018). For these reasons recently there has been an interest in developing scaffolds with two types of porosity, a macro and structured one to allow diffusion of nutrients in the constructs and a micro one to promote cellular adhesion and proliferation and infiltration of the cells within the scaffolds (Mohanty *et al.*, 2016; Kang *et al.*, 2019; Cho *et al.*, 2014; Park *et al.*, 2007). In this work the macro porosity was obtained through the design achieved with the 3D printing process, while the micro porosity was obtained by mixing the polymer with salt crystals. The macro-porosity was kept constant by using the same design with a 1.5x1.5 mm pore size to evaluate the effect of the introduction of salt particles. When using the salt leaching technique, the size and the amount of porosity is strictly controlled by the porogen/polymer ratio and the porogen dimensions (Prasad *et al.*, 2017; Loh and Choong, 2013). Three ratios of P(3HO-co-3HD-co-3HDD)/NaCl were investigated, 50:50, 35:65 and 25:75, using two sizes of porogen dimensions, <100 µm and between 100 and 300 µm. A higher amount of salt could not be incorporated as the material could not be extruded. Jakus *et al.* observed a similar threshold of the amount of $CuSO_4$

(70%) that could be introduced in PLGA scaffolds, as higher concentrations led to nozzle clogging, while for PCL-based scaffolds a maximum of 55% of salt could be extruded (Visscher *et al.*, 2018; Dang *et al.*, 2019). Successful 3D printing of all the six compositions was achieved and the scaffolds obtained were characterized to evaluate the effect of salt in creating porosity inside the printed struts. For both salt dimensions, the samples with the lowest amount of porogen 50:50 P(3HO-co-3HD-co-3HDD)/NaCl did not show a high porosity. A similar behaviour was evidenced with PCL and PLGA scaffolds, where lower amounts of porogen (33% and 25% respectively), did not lead to high porous constructs due to the fact that the polymers acted as a barrier to the dissolution and leaching out of the crystals (Jakus *et al.*, 2018; Kang *et al.*, 2019). In such systems in fact the creation of pores is guided by the ability of water to penetrate inside the material. As the polymers used are hydrophobic, they limit the diffusion of water, making it necessary for the porogen to be present on the surface of the material to achieve porosity (Kang *et al.*, 2019; Cho *et al.*, 2017; Jakus *et al.*, 2018). To produce such features in extrusion-based 3D process a high amount of porogen is required because the polymer extruded, as the viscous material, tends to cover and entrap the particulate used within the fibres (Cho *et al.*, 2017; Kang *et al.*, 2019). The work conducted in this study confirms such behaviour as 35:65 and 25:75 P(3HO-co-3HD-co-3HDD)/NaCl samples showed the formation of pores on the surface of the scaffold and an increase in the overall intra-strut porosity. In particular, constructs with the highest salt content and dimension (25:75 P(3HO-co-3HD-co-3HDD)/NaCl $_{300\mu m}$) showed the formation of the largest surface pores, which was expected as in the salt leaching technique the pore size is strictly dependent on that of the porogen used (Prasad *et al.*, 2017; Loh and Choong, 2013). However, the largest size of the pores obtained (i.e. 100 µm) was lower than the largest dimension of the NaCl used (i.e. 300 µm). Such apparently contradictory results could be explained by the fact that only surface pores were investigated by SEM analyses in this study and not the one present inside the struts. As mentioned above and as shown in the SEM images of the 3D P(3HO-co-3HD-co-3HDD)/NaCl$_{100\mu m}$ before the salt leaching, the porogen particles are mainly distributed inside the struts, leading to larger pores inside the fibres compared to the surface, as confirmed in studies on both PCL and PLGA constructs (Kang *et al.*, 2019; Visscher *et al.*, 2018; Jakus *et al.*, 2018). An attempt to analyse the cross-section areas of the leached materials was carried out, but the material could not withstand the forces applied through the surgical blade resulting in a distorted structure (data not shown). Therefore, future SEM analyses should be conducted to obtain a direct correlation between

the pore size and the porogen dimension by preparing the material either using a microtome or the direct freeze fracture method (i.e. freeze the scaffold in liquid nitrogen to make it brittle and quickly breaking) (Ferlita *et al.*, 2008). Investigation of the intra-strut porosity revealed that the samples with the highest concentration of salt crystals (25:75) possessed the highest average value of 36%. This result is in agreement with literature results, showing a range of porosity between 30-41% in dual porosity scaffolds obtained with PCL using a similar printing technique (Dang *et al.*, 2019; Visscher *et al.*, 2018; Kang *et al.*, 2019). As expected no statistically significant differences were detected between the porosity of the samples with the same composition but different porogen size (i.e. $NaCl_{100\mu m}$ vs $NaCl_{300\mu m}$), as the in salt leaching technique the ratio of material/porogen determines the overall porosity of the construct (Lin-Gibson *et al.*, 2007; Loh and Choong, 2013). However, the comparison of the porosity between the samples with 35:65 and 25:75 ratio did not show any statically significant differences, even though an increase in the average values of porosity was detected with increasing concentration of porogen. The reason behind such behaviour could be related to the intrinsic limits of the gravimetric method used for the calculation of the scaffold porosity. This technique is a simple, fast and non-disruptive method extensively used for the characterization of materials for tissue engineering, however it relies on the determination of the volume of the material which can lead to rough estimations. Moreover, only the estimation of the total porosity of the material can be obtained with, without any indication of pore size geometry or distribution. Therefore, to better understand the relationship between the porosity and the composition of the samples, future studies should be conducted employing more precise methods such us mercury porosimetry or microcomputed tomography (Micro-CT). Such methods allow to obtain a better and more precise characterization of the porosity of the materials through the calculation of the total pore volume fraction, the average pore diameter and pore size distribution (Loh and Choong, 2013; Lin-Gibson *et al.*, 2007).

Finally, a preliminary *in vitro* cytotoxicity test was conducted to evaluate the potential toxicity of substances released form the 3D P(3HO-co-3HD-co-3HDD)/NaCl constructs, as the presence of residual salt could have potential detrimental effect on the cell viability. All the samples investigated did not show any toxic effect after 24 hours of incubation, confirming the complete removal of salt particles with the leaching treatment.

6.4. Conclusions

In this chapter the possibility of developing scaffolds using melt 3D printing of medium chain length PHAs was investigated for the first time. The use of additive manufacturing can expand the applications of PHAs in the medical field, as the technique can ultimately allow the development of customized and patient -specific scaffolds that match the shape and dimensions of the tissue to be replaced. The process parameters were successfully optimized to produce well-defined and reproducible 3D P(3HO-co-3HD-co-3HDD) scaffolds. Moreover, molecular weight analyses of the materials further confirmed the suitability of melt 3D printing for the polyester, as no alteration of its properties was detected. An *in vitro* degradation study in PBS was conducted to investigate the potential of the printed constructs for long term application, like bone regeneration. The samples showed a reduction of the molecular weight, but no apparent change in their physical structure during the period investigated. The 3D scaffolds developed showed good cytocompatibility towards both undifferentiated and differentiated MC3T3-E1 cells, showing that the material can be used as a suitable substrate for bone regeneration. Finally, a feasibility study was conducted to investigate the possibility of developing 3D printed scaffolds with dual porosity through the combination of melt 3D printing and salt leaching. Optimization of the ratio between the porogen and the polymer resulted in the production of structures with different levels of intra-strut porosity. All the scaffolds produced showed no sign of cytotoxicity towards MC3T3-E1 cells.

Chapter 7

PHA-based Antibacterial Bone substitutes

7.1. Introduction

Even though bone has an intrinsic capability of self-healing, it is one of the most transplanted tissues in the world, second only to blood (Hasan *et al.*, 2018; Porter *et al.*, 2009; Tao *et al.*, 2019). In the presence of large-size defects, mechanical fixation on its own is not able to induce bone healing, requiring the use of additional material. These critical-size defects can be caused by a variety of scenarios including trauma, tumour resection, infections or congenital diseases (De Witte *et al.*, 2018; Hasan *et al.*, 2018; Porter *et al.*, 2009). Moreover, external intervention is also required in the presence of non-unions, which are defined as fractures not healed after 6 months or not showing an appropriate healing advancement over 3 months period (Jones and Mayo, 2005; Marsh, 2003). Autologous osseous material is still considered the gold standard in clinical practise, due to its inherent osteogenic, osteoconductive and osteoinductive properties. However, the restricted availability of this material combined with the possible complications of donor site morbidity limit its applications, especially for the treatment of large bone defects (Fernandez de Grado *et al.*, 2018; Zeng *et al.*, 2018). Allografts and xenografts represent possible alternatives but are associated with the risk of an immunogenic response and diseases transmission correlated with a reduction in the osteoinductive properties and a lack of viable cells (Haugen *et al.*, 2019; Baldwin *et al.*, 2019). In light of the limitations of the current transplanted osseous grafts, great attention in literature has been brought to the development of synthetic bone substitutes, thanks to their unlimited availability and longer shelf life. As already discussed in the introduction chapter, one of the main alternatives investigated is to restore or regenerate the damaged tissue through a tissue engineering approach by combining cells with a scaffold able to provide a suitable environment for cell anchorage and proliferation (Fernandez de Grado *et al.*, 2018; Hasan *et al.*, 2018).

Among the characteristics of an ideal material for bone regeneration, increasing interest has been placed on the antibacterial properties. Infections represent a major complications in the orthopaedic field, hindering tissue healing and ultimately leading to non-union fractures or implant failure (Thomas and Puleo, 2011). The main prevention technique employed is the systemic delivery of antibiotics which can result in systemic toxicity and low concentration at the implant site (Mouriño and Boccaccini, 2010; Van Vugt *et al.*, 2016). Alternatively, grafts loaded with antibiotics are used, allowing a controlled release of the therapeutics at the targeted site and lowering possible side effects (Johnson and García, 2015). However, the increasing rise of antibiotic resistant species due to the overuse or misuse of antibiotics requires the investigation of new alternatives for the prevention and treatment of infections.

In this chapter the possibility of developing PHA-based antibacterial bone substitutes was investigated. The work was conducted in collaboration with the Orthopaedic Surgery and Traumatology and Cell Therapy Department of the University of Navarra, Pamplona, Spain. In their recent work, González-Gil *et al.* developed a tissue-engineered construct using a 3D PCL scaffold combined with rat periosteal mesenchymal cells and tested its ability to favour bone regeneration *in vivo* in critical-size defects in Sprague–Dawley rats (González-Gil *et al.*, 2019). In this chapter, an alternative solution to such implants was investigated through the development of antibacterial PHA-based constructs.

Two strategies were investigated based on the production of 3D structures using the antimicrobial materials developed in Chapter 4 and 5.

For the first strategy, 3D antibacterial composite scaffolds were produced by the combination of P(3HO-co-3HD-co-HDD) as the bulk material and Se-Sr-HA (Chapter 7 – Part A). For the second strategy, thioester-PHAs and P(3HHx-co-3HO-co-3HD) were blended to develop 3D inherently antibacterial scaffolds using melt 3D printing (Chapter 7 – Part B). All the materials were characterized in terms of morphological, chemical, biological and antibacterial properties.

7.2. Results

7.2.1. Part A: Development of 3D printed antibacterial composite scaffolds

To develop antibacterial composite scaffolds by melt 3D printing, the P(3HO-co-3HD-co-3HDD) composite films developed in Chapter 5 were used as the starting materials.

All the three compositions, 10, 20 and 30 wt% of Se-Sr-HA were successfully printed as shown in Figure 7.1. Starting from the optimized printing conditions obtained in Chapter 6, a higher temperature of 120 °C and a higher pressure between 170-200 kPa were required to extrude the three composite compositions investigated as compared to the neat constructs (i.e. 3D P(3HO-co-3HD-co-3HDD)). Moreover, scaffolds with a targeted height of 6 mm could also be printed using all three compositions investigated.
From visual observation it was possible to see the presence of hydroxyapatite in the composite scaffolds. Such materials were characterized by a white colour and were more opaque as compared to the scaffolds obtained with only P(3HO-co-3HD-co-3HDD).

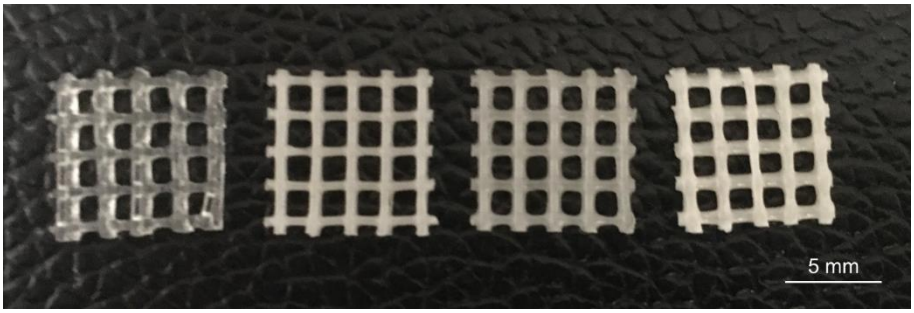

Figure 7.1 Representative image of 3D printed composite scaffolds. The samples are in the following order from left to right: neat scaffolds, 10 wt% Se-Sr-HA, 20 wt% Se-Sr-HA and 30 wt% Se-Sr-HA composite scaffolds.

7.2.2. Chemical characterization

Preliminary characterization of the 3D composite structures was conducted through FT-IR analysis, as shown in Figure 7.2. In all the spectra the characteristic peaks of PHAs could be detected. All the spectra showed the peak around 1720-1740 cm^{-1} related to the stretching of the carbonyl group of the ester bond and around 2900 cm^{-1} related to the stretching of carbon-hydrogen bond of methyl and methylene group (CH_3, CH_2) (Kann *et al.*, 2014; Randriamahefa *et al.*, 2003). In all the composite scaffolds new bands at 1072–1032, 601, 571, and 474 cm^{-1} could be detected compared to neat 3D constructs. Such peaks were assigned to vibrations of the phosphate group, PO_4^{3-}, present in the Se-Sr-HA (Li *et al.*, 2007). For all the composite materials, a peak at 630 cm^{-1} could be detected, which was assigned to the vibration of hydroxyl groups (OH) present in the hydroxyapatite (Gritsch *et al.*, 2019).

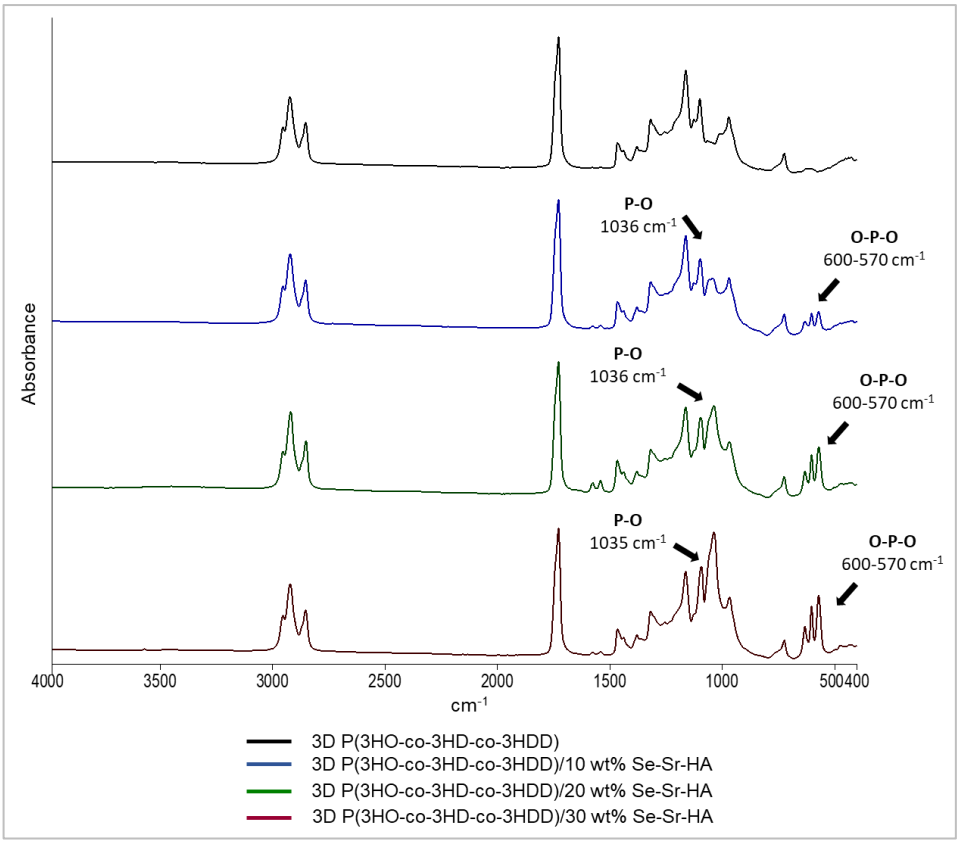

Figure 7.2 FT-IR spectra of a) 3D P(3HO-co-3HD-co-3HDD) scaffold, b) P(3HO-co-3HD-co-3HDD)/10 wt% Se-Sr-HA c) P(3HO-co-3HD-co-3HDD)/20 wt% Se-Sr-HA and c) P(3HO-co-3HD-co-3HDD)/30 wt% Se-Sr-HA composite scaffolds.

7.2.3. Surface characterization

The surface morphology of the scaffolds was investigated by SEM analysis. Figure 7.3 shows that the composite materials showed a smooth surface without the presence of pores, similar to the neat scaffolds. The presence of Se-Sr-HA could be detected through EDX analyses as shown in Figure 7.4. The spectra of the neat 3D P(3HO-co-3HD-co-3HDD) scaffold showed only the presence of peaks related to carbon and oxygen, while for all the composite constructs new bands related to characteristic elements of Se-Sr-HA (i.e. calcium, phosphorus, selenium and strontium) were identified.

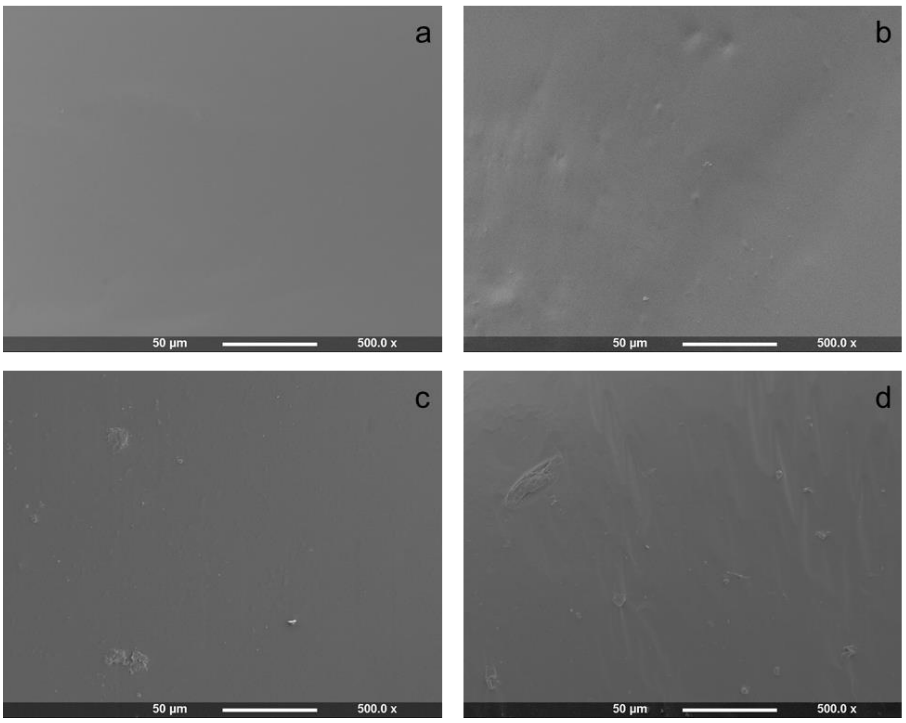

Figure 7.3 SEM images of the surface of a) 3D P(3HO-co-3HD-co-3HDD) scaffold, b) P(3HO-co-3HD-co-3HDD)/10 wt% Se-Sr-HA c) P(3HO-co-3HD-co-3HDD)/20 wt% Se-Sr-HA and c) P(3HO-co-3HD-co-3HDD)/30 wt% Se-Sr-HA composite scaffolds

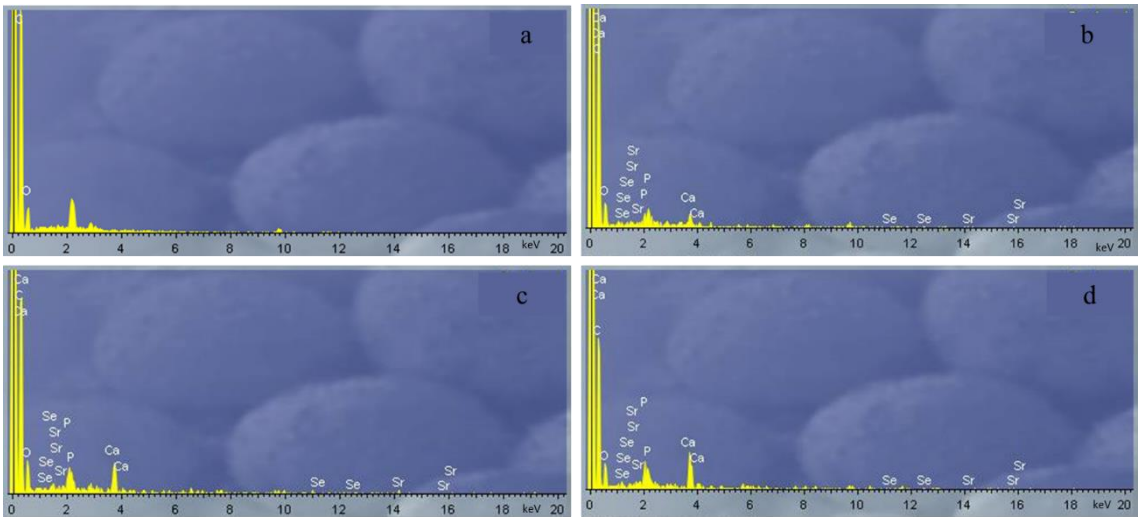

Figure 7.4 EDX spectra of a) 3D P(3HO-co-3HD-co-3HDD) scaffold, b) P(3HO-co-3HD-co-3HDD)/10 wt% Se-Sr-HA c) P(3HO-co-3HD-co-3HDD)/20 wt% Se-Sr-HA and c) P(3HO-co-3HD-co-3HDD)/30 wt% Se-Sr-HA composite scaffolds.

7.2.4. Micro-CT analysis

Micro-CT analyses of the 3D P(3HO-co-3HD-co-3HDD) composite scaffolds containing 10 wt% of Se-Sr-HA were performed to qualitatively evaluate the distribution of the filler inside the constructs. This technique is based on the irradiation of the sample with X-rays from different angles. When passing through the material the radiation is attenuated based on the properties of the sample, such as the density, thickness and composition. Reconstruction of the different projection images from all the angles analysed results in 2D or 3D grey-scale maps of the specimen (Ho and Hutmacher, 2006; Cengiz *et al.*, 2018). Figure 7.5 shows the 2D cross-sectional area of two filaments of 3D P(3HO-co-3HD-co-3HDD) /10 wt% Se-Sr-HA. The two phases of the composite materials could be differentiated thanks to their difference in absorption of the radiation. Using the Bruker Micro-CT CTan software, two different colours were used to identify the two components present in the composite material. The organic part (i.e. the polymer) leads to a lower attenuation and was coloured in blue, while higher attenuation is caused by the inorganic phase (i.e. Se-Sr-HA), which was coloured in red. Overall, Figure 7.5 showed a uniform distribution of the filler inside the 3D printed struts.

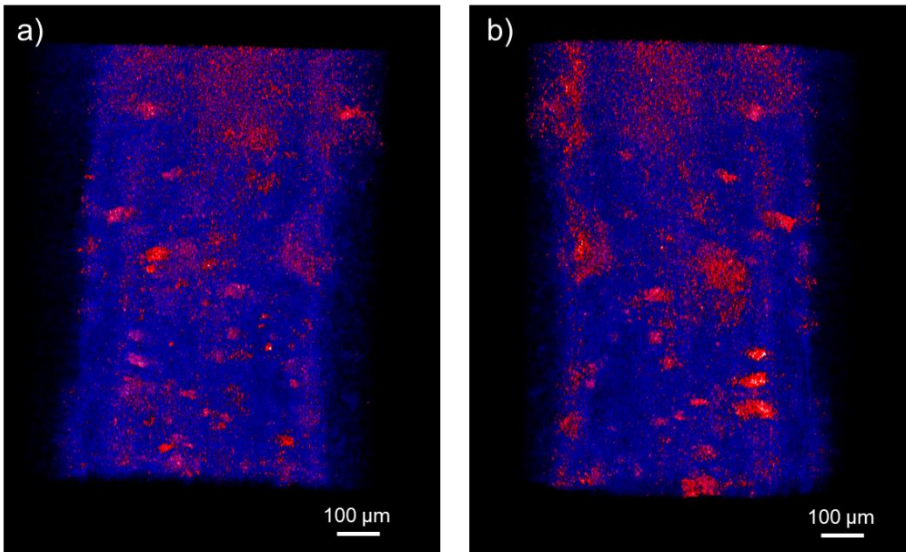

Figure 7.5 Micro-CT reconstructed image of two filaments (a and b) of 3D P(3HO-co-3HD-co-3HDD)/10 wt% Se-Sr-HA composite scaffolds. The area in blue represent the polymer, while the area in red represents the Se-Sr-HA.

7.2.5. Biological characterization

7.2.5.1. *In vitro* cell compatibility studies

The biocompatibility of the 3D printed antibacterial composite scaffolds was tested using the MC3T3-E1 cell line to investigate the potential of such materials for bone regeneration.

To investigate the potential release of toxic substances from the materials over time, an indirect cytotoxicity test was conducted on all the composites produced for 1, 3 and 7 days. The cell viability was calculated as a percentage of the positive control (cells cultured on tissue culture plates) and is shown in Figure 7.6. The composite materials with 10 and 20 wt% of Se-Sr-HA as filler showed a cell compatibility comparable to both the positive controls and neat 3D P(3HO-co-3HD-co-3HDD) samples, without any statistically significant differences. On the contrary, the material with the highest concentration of Se-Sr-HA (i.e. 30 wt%) showed a significantly lower cell viability as compared to both the control and the 3D samples for all the time points evaluated (p-value<0.0001). The average cell viability was lower than 40% for all the time points investigated and no statistically significant differences were detected between day 1, 3 and 7.

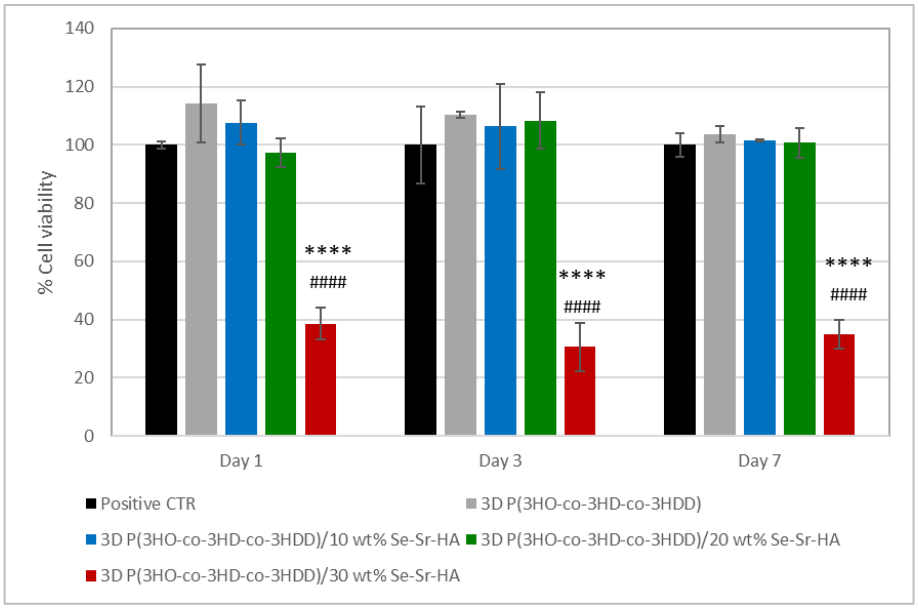

Figure 7.6 Indirect cytotoxicity studies using MC3T3-E1 of 3D printed P(3HO-co-3HD-co-3HDD) neat scaffolds and 3D printed P(3HO-co-3HD-co-3HDD) antibacterial composite scaffolds with 10 wt%(blue), 20 wt% (green) and 30 wt% (red) of Se-Sr-HA as a filler (n=3). The positive control was Tissue Culture Plastic (TCP)(black). ** indicates statistically significant difference between 3D P(3HO-co-3HD-co-3HDD)/30 wt% Se-Sr-HA and the positive control (p-value<0.0001). #### indicates statistically significant difference between 3D P(3HO-co-3HD-co-3HDD)/30 wt% Se-Sr-HA and the neat scaffolds (*p*-value<0.0001).**

Preliminary direct compatibility tests were performed on all the composite scaffolds produced. MC3T3-E1 cells were seeded directly on the surface of the materials and cultured for 1, 3 and 7 days. Figure 7.7 shows the cell viability, which was calculated as a percentage of the positive control (cells cultured on tissue culture plates). For all the time points evaluated, the cell viability of the 3D composites with 10 wt% of Se-Sr-HA was comparable to both the positive control and the 3D neat samples, without statistically significant differences. The material with 20 wt% of Sr-Sr-HA showed a reduction of the cell viability over time. At day 1 no statistically significant difference could be detected with the positive control and the neat samples. However, for the following time points 3D P(3HO-co-3HD-co-3HDD)/20 wt% Se-Sr-HA showed a significantly lower cell viability, with an average value of 65% at day 3 (p-value<0.05 compared to the control and p-value<0.01 compared to the neat samples) and 52% at day 7 (p-value<0.01 compared to the positive control and p-value<0.001 compared to the neat samples). Finally, the sample with the highest concentration of the filler, 3D P(3HO-co-3HD-co-3HDD)/30 wt% Se-Sr-HA, showed a statistically significant reduction in cell viability compared to both the positive control and

the neat specimen for all the time points evaluated. At day 1 the average cell viability was 51% (*p*-value<0.001 compared to the both positive control and neat samples), at day 3 of 36% (*p*-value<0.0001 compared to the both positive control and neat samples) and at day 7 of 50% (*p*-value<0.001 compared to the both positive and neat samples).

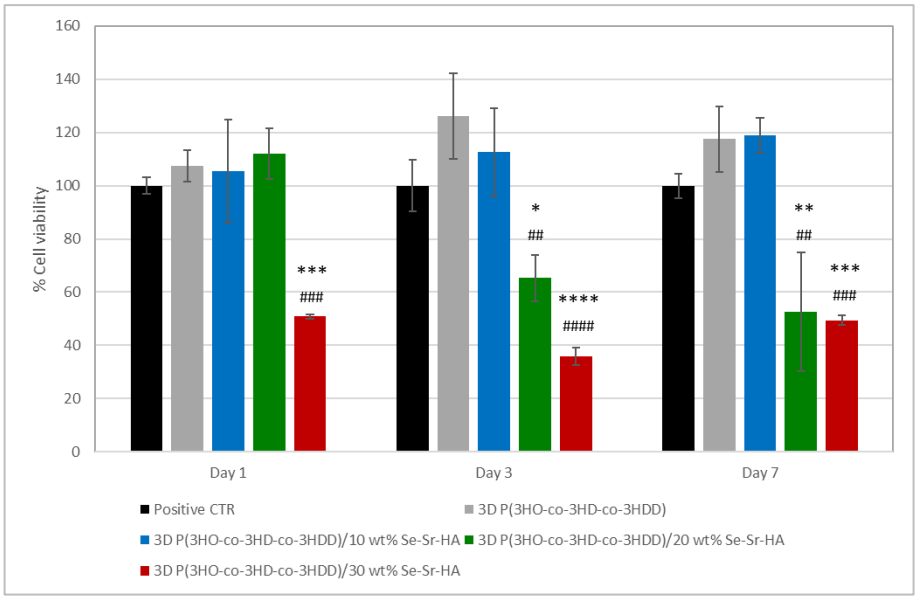

Figure 7.7 Cell viability study of MC3T3-E1 cells seeded on 3D printed P(3HO-co-3HD-co-3HDD) neat scaffolds and 3D printed P(3HO-co-3HD-co-3HDD) antibacterial composite scaffolds with 10 wt%(blue), 20 wt% (green) and 30 wt% (red) of Se-Sr-HA as a filler. The positive control was Tissue Culture Plastic (TCP)(black) (n=3). *,, ***,**** indicates statistically significant difference between the composite samples and the positive control (*p*-value<0.05, *p*-value<0.01,*p*-value<0.001,p-value<0.0001). ##, ###, #### indicates statistically significant difference between 3D P(3HO-co-3HD-co-3HDD)/30 wt% Se-Sr-HA and the neat scaffolds**

7.2.5.2. Antibacterial studies – ISO 22196

The antibacterial properties of the 3D printed composite scaffolds were investigated using the ISO 22196 against *S. aureus* 6538P and *E. coli* 8739. As described in Chapter 4 and 7, the standard procedure consisted on the incubation of a known number of bacteria on the surface of the materials for 24 hours, followed by the recovery of the bacterial cells and their quantification through a colony forming assay. The antibacterial activity (R) was calculated as the difference between the logarithm of the bacterial cell count of the composite scaffolds and the logarithm of the bacterial cell count of the control (i.e. 3D neat P(3HO-co-3HD-co-3HDD) scaffolds. Moreover, the percentage antibacterial activity (R%) was calculated as the reduction of the number of bacterial cells on the composite materials compared to the control.

As shown in Figure 7.8 and Table 7.1, the materials were active against both bacterial strains at all the concentration tested, and the activity increased with the increase in the hydroxyapatite content. Both compositions showed a similar level of bactericidal effect against the two types of bacteria.

Against *S. aureus* 6538P the composite with the lowest concentration of filler, 3D P(3HO-co-3HD-co-3HDD)/10 wt% Se-Sr-HA, showed an average antibacterial activity R of 0.8, inducing an average 83% reduction of the number of bacterial cells (p-value<0.01). 3D P(3HO-co-3HD-co-3HDD)/20 wt% Se-Sr-HA displayed an antibacterial activity R of 1.5, corresponding to a 96 % bacterial cells reduction (p-value<0.001). The highest efficacy was obtained with the highest concentration of filler, 30 wt% of Se-Sr-HA, showing a 99.8% reduction of bacterial cells, corresponding to an average antibacterial activity R of 2.7 (p-value<0.0001).

A similar behaviour was detected for the Gram negative bacteria, *E. coli* 8739. 3D P(3HO-co-3HD-co-3HDD)/30 wt% Se-Sr-HA exhibited the highest activity with a 99.7% reduction of bacterial cells, corresponding to an average antibacterial activity R of 2.4 (p-value<0.0001 compared to 3D neat samples). The samples with 20 wt% of Se-Sr-HA induced a 97% reduction of viable bacterial cells (average antibacterial activity R of 1.7) (p-value<0.001 compared to 3D neat samples). Finally, the composite with the lowest concentration of filler, 3D P(3HO-co-3HD-co-3HDD)/10 wt% Se-Sr-HA, lead to an average antibacterial activity R of 0.72, corresponding to an 80% reduction of the bacterial cell count (p-value<0.01 compared to 3D neat samples).

a)

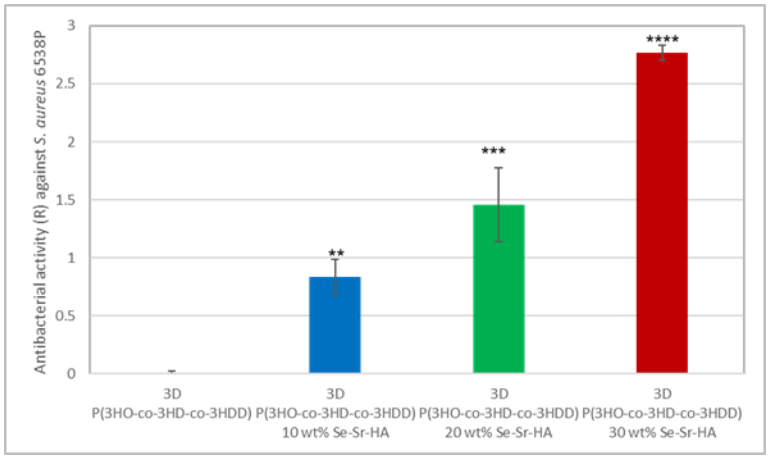

b)

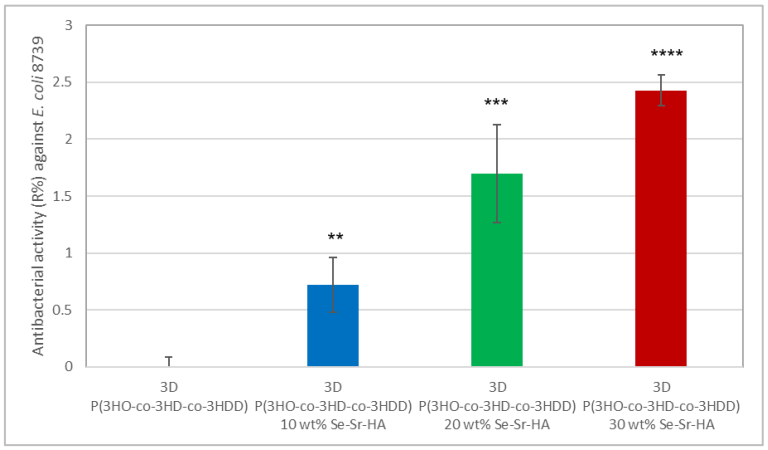

Figure 7.8 Antibacterial activity (R) (ISO 22196) of 3D printed P(3HO-co-3HD-co-3HDD) (grey) and 3D printed P(3HO-co-3HD-co-3HDD) antibacterial composite scaffolds with 10 wt%(blue), 20 wt% (green) and 30 wt% (red) of Se-Sr-HA as a filler against a) *S. aureus* 6538P and b) *E. coli* 8739. **,*,**** indicate statistically significant difference between 3D printed P(3HO-co-3HD-co-3HDD) and 3D printed P(3HO-co-3HD-co-3HDD) antibacterial composite scaffolds (*p*-value<0.01, *p*-value<0.001, *p*-value<0.0001).**

Table 7.1 Percentage antibacterial activity (R%) and Antibacterial activity (R) values of P(3HO-co-3HD-3HDD) antibacterial composite films with 10 wt%, 20 wt% and 30 wt% of Se-Sr-HA as a filler against *S. aureus* 6538P and *E. coli* 8739.

Sample	*S. aureus* 6538P		*E.coli* 8739	
	R	***R(%)***	***R***	***R(%)***
3D P(3HO-co-3HD-co-3HDD)/ 10 wt% Se-Sr-HA	0.8 ± 0.15	83.3 ± 5	0.72 ± 0.2	80 ± 8
3D P(3HO-co-3HD-co-3HDD)/ 20 wt% Se-Sr-HA	1.45 ± 0.3	96 ± 2	1.7 ± 0.4	97 ± 2.7
3D P(3HO-co-3HD-co-3HDD)/ 30 wt% Se-Sr-HA	2.7 ± 0.1	99.8 ± 0.1	2.4 ± 0.1	99.7±0.15

7.2.5.3. Antibacterial ion release studies

Based on the cell compatibility results obtained with the MC3T3-E1 cell line and the antibacterial studies performed using ISO 22196, 3D P(3HO-co-3HD-co-3HDD)/10 wt% Se-Sr-HA was selected to investigate the potential of the material to release ions with antibacterial properties using an indirect antimicrobial ion release study. Briefly, the materials were incubated in Mueller Hinton broth for 1, 3 and 7 days. After each time point the media of each well was collected and replaced with fresh media. The eluates obtained were mixed with a microbial suspension of *S. aureus* 6538P or *E. coli* 8739, adjusted to 0.5 McFarland and incubated for 24h at 37°C. The optical density at 600 nm was recorded after 24h and used to determine the reduction of the bacterial cell count, calculated as a percentage of the positive control (i.e. bacteria cultured in eluates obtained from 3D neat P(3HO-co-3HD-co-3HDD)).

The 3D composite containing 10 wt% of Se-Sr-HA resulted in a reduction in the OD of both *S. aureus* 6538P and *E. coli* 8739 cells as compared to the positive control throughout the duration of the experiment as shown in Figure 7.9.

In the case of *S. aureus* 6538P, the materials showed a 54% and 49% reduction of the bacterial cell count at day 1 and 3 respectively as compared to the control (p-value<0.01).

For day 7, a lower but still significant reduction of the OD could be detected as compared to the control, showing an average value of 24% (p-value<0.05).

3D P(3HO-co-3HD-co-3HDD)/10 wt% Se-Sr-HA showed activity against *E. coli* 8739, although the effect was lower than that against *S. aureus* 6538P. After 1 day, an average 30% reduction of the OD was obtained as compared to the control (p-value<0.001). A significant reduction of the bacterial cell count of 17% could be detected with the eluates obtained after 3 days of incubation with the polymeric samples (p-value<0.05). Finally, the eluates obtained after 7 days of incubation showed an average reduction of the bacterial OD of 11%, but no statistically significant difference was detected as compared to the control samples.

a)

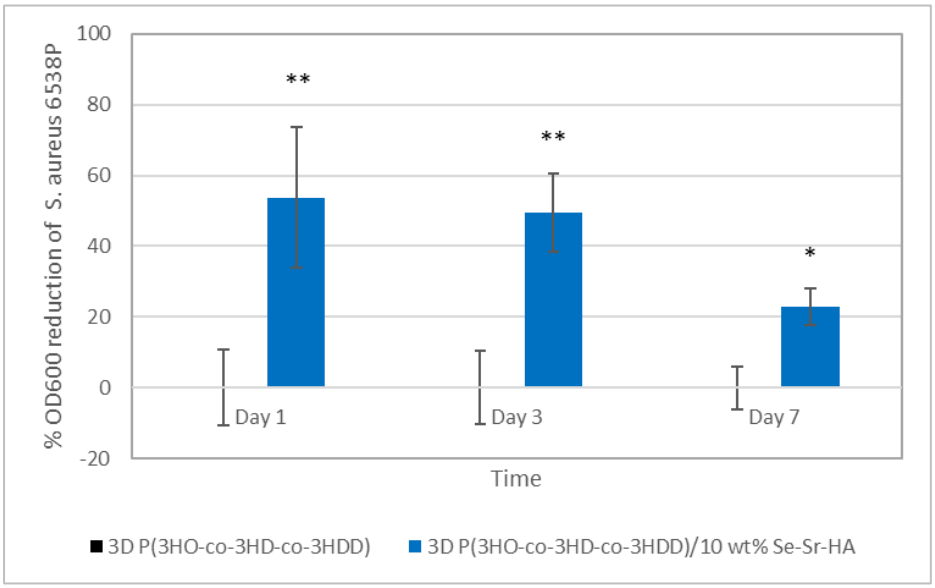

b)

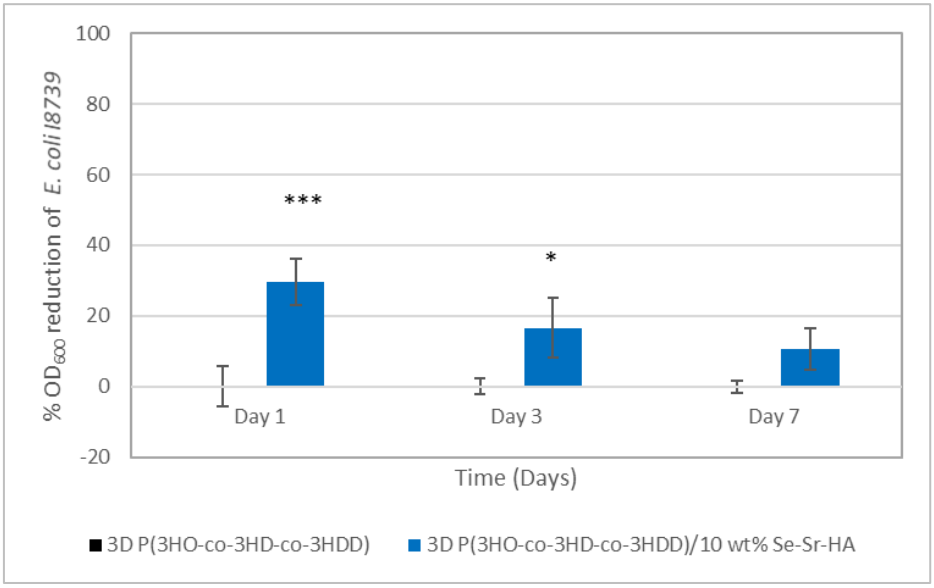

Figure 7.9 Indirect antibacterial ion release study of the P(3HO-co-3HD-co-3HDD) antibacterial composite films with 10 wt%(blue) of Se-Sr-HA as a filler against a) *S. aureus* 6538P and b) *E. coli* 8739 (n=3). Control consists of bacterial cells cultured in eluates of 3D neat P(3HO-co-3HD-co-3HDD (black). *, **, * indicate statistically significant difference between the composite samples and the positive control (*p*-value<0.05, *p*-value<0.01, *p*-value<0.001).**

7.3. Part B: Development of 3D printed inherently antibacterial scaffolds

To develop inherently antibacterial scaffolds for bone tissue engineering, the thioester-PHAs described in Chapter 4 were used. These materials showed activity against *S. aureus* 6538P (ISO 22196) due to the presence of the thioester groups. The produced thioester-PHAs were completely amorphous and could not be used as the bulk material for the scaffold production. For this reason, thioester-PHAs were blended with P(3HHx-co-3HO-co-3HD) (not active material obtained by control conditions) to produce inherently antibacterial 3D printed constructs. 20:80 ratio was chosen as this ratio showed antibacterial activity in blend films. As shown in Figure 7.10, the 3D printed inherently antibacterial scaffolds could be successfully processed using melt 3D printing. The same printing conditions obtained in Chapter 6 were applied for the extrusion (110°C, 1 mm/s and 100 kPa). However, the constructs of 6 mm height could not be developed using these materials.

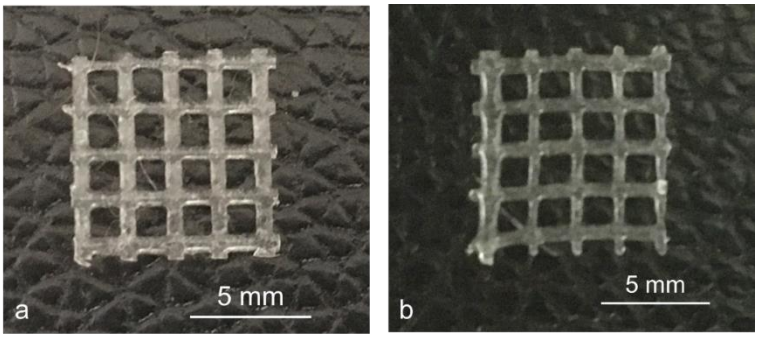

Figure 7.10 Optical image of 3D scaffolds of a) P(3HHx-co-3HO-co-3HD) scaffold and b) 3D printed blend scaffolds of thioester-PHA and P(3HHx-co-3HO-co-3HD).

7.3.1. Chemical characterization

Preliminary FT-IR analyses were conducted on the 3D inherently antibacterial scaffolds and are reported in Figure 7.11. In all the spectra the characteristic peaks of PHAs could be detected (i.e. 1720-1740 cm^{-1} related to the stretching of the carbonyl group of the ester bond and around 2900 cm^{-1} related to the stretching of carbon-hydrogen bond of methyl and methylene group (CH_3, CH_2)) (Kann *et al.*, 2014; Randriamahefa *et al.*, 2003). The spectrum of the 3D blend scaffolds showed an extra peak at 1690 cm^{-1} which is related to the stretching of the carbonyl group present in thioester groups (Lütke-Eversloh *et al.*, 2001).

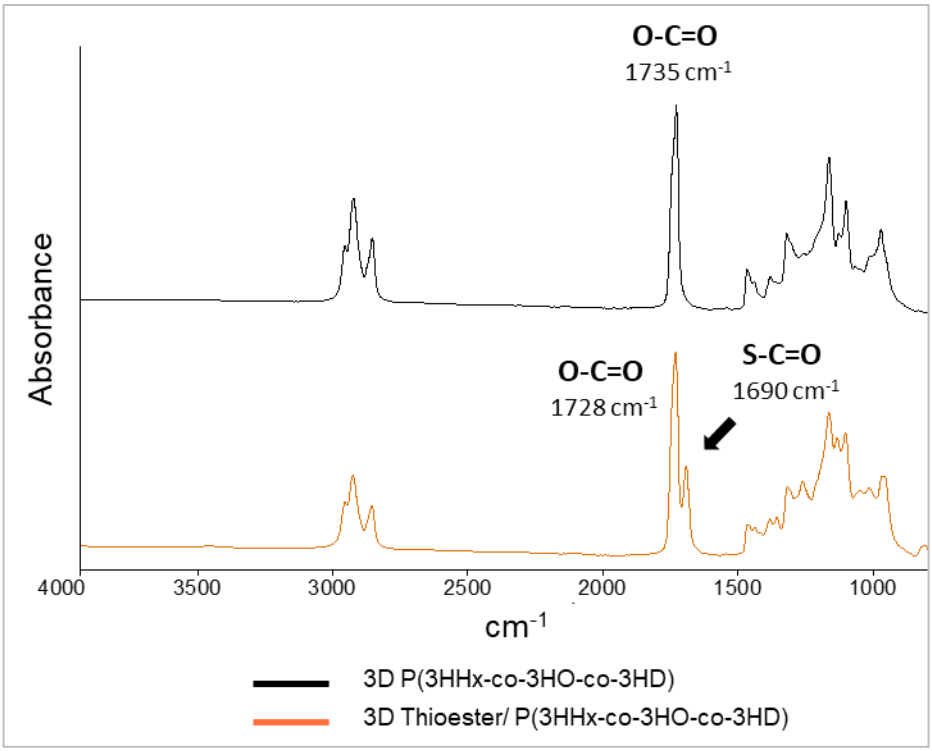

Figure 7.11 FT-IR spectra of 3D printed scaffolds of P(3HHx-co-3HO-co-3HD) and 3D printed blend scaffolds of thioester-PHA and P(3HHx-co-3HO-co-3HD).

7.3.2. Surface characterization

The surface morphology of the scaffolds was investigated by SEM analysis. Figure 7.12 shows that 3D printed inherently antibacterial scaffolds possess a smooth surface without porosity comparable to the 3D printed neat scaffolds. EDX analysis confirmed the presence of sulphur in the blend scaffolds of thioester-PHA and P(3HHx-co-3HO-co-3HD), as shown in Figure 7.13. The spectra of the neat 3D P(3HHx-co-3HD-co-3HDD) scaffold showed the presence of the peaks related to carbon and oxygen, while for 3D thioester/P(3HHx-co-3HD-co-3HDD) new bands related to sulphur were identified.

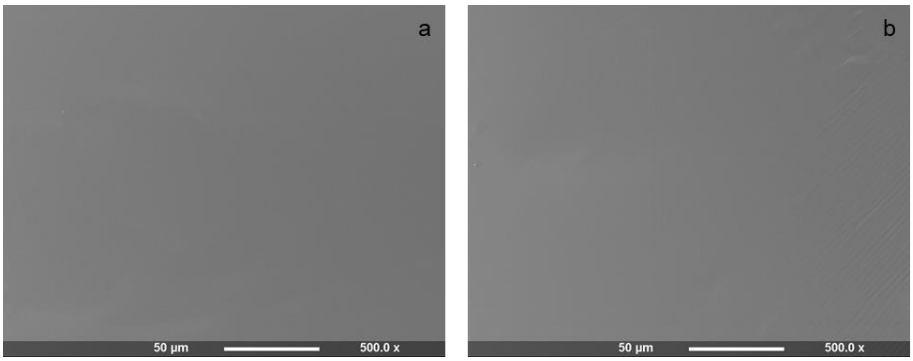

Figure 7.12 SEM images of a) 3D printed scaffolds of P(3HHx-co-3HO-co-3HD) and b) 3D printed blend scaffolds of thioester-PHA and P(3HHx-co-3HO-co-3HD).

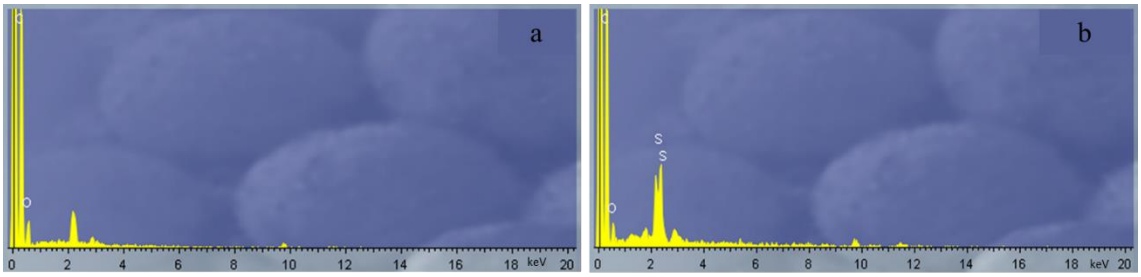

Figure 7.13 EDX spectra of a) 3D printed scaffolds of P(3HHx-co-3HO-co-3HD) and b) 3D printed blend scaffolds of thioester-PHA and P(3HHx-co-3HO-co-3HD)

7.3.3. Biological characterization

The antibacterial activity of the scaffolds was evaluated using ISO 22196 against *S. aureus* 6538P and compared to 3D scaffolds composed only of P(3HHx-co-3HO-co-3HD).

As shown in Figure 7.14 and Table 7.2, the 3D printed blend scaffolds showed antibacterial activity against *S. aureus* 6538P. A decrease in the number of cells growing on the surface of the material could be detected compared to the neat materials. The average antibacterial activity R was 0.55, corresponding to a 70% reduction of the number of cells (p-value<0.01).

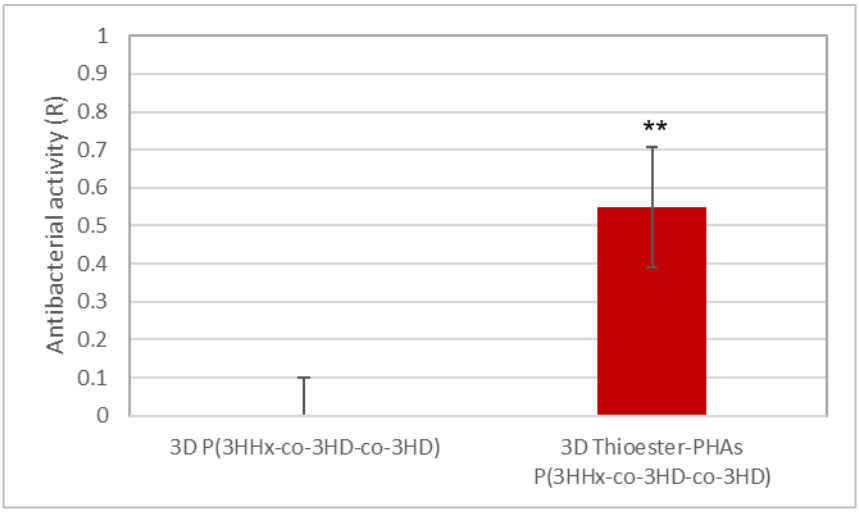

Figure 7.14 Antibacterial activity (R) (ISO 22196) against *S. aureus* 6538P evaluated through ISO 22196 of 3D P(3HHx-co-3HO-co-3HD) scaffolds and 3D thioester-PHA/ P(3HHx-co-3HO-co-3HD) scaffolds. indicates statistically significant difference between of 3D P(3HHx-co-3HO-co-3HD) scaffolds and 3D thioester/ P(3HHx-co-3HO-co-3HD) scaffolds (*p*-value<0.01).**

Table 7.2 Antibacterial reduction (R%) and Antibacterial activity (R) values of 3D P(3HHx-co-3HO-co-3HD) scaffolds and 3D thioester/ P(3HHx-co-3HO-co-3HD) scaffolds *S. aureus* 6538P.

Sample	***S. aureus* 6538P**	
	R	***R(%)***
3D P(3HHx-co-3HD-co-3HD)	0	0
3D thioester-PHA/P(3HHx-co-3HD-co-3HD)	0.55 ± 0.15	70 ± 9

7.3.4. *In vitro* cells compatibility studies

Preliminary *in vitro* cell compatibility studies were conducted using MC3T3-E1 cell line for day 1, 2 and 7. The cell viability was compared to the positive control (tissue culture plate, TCP) and is reported in Figure 7.15. For all the time point considered the cell viability on the 3D thioester-PHA/P(3HHx-co-3HD-co-3HD) antibacterial scaffolds was comparable with both the tissue culture plastic and 3D P(3HHx-co-3HD-co-3HD) scaffolds (average cell viability 109% at day 1, 106% at day 3, 111% at day 7).

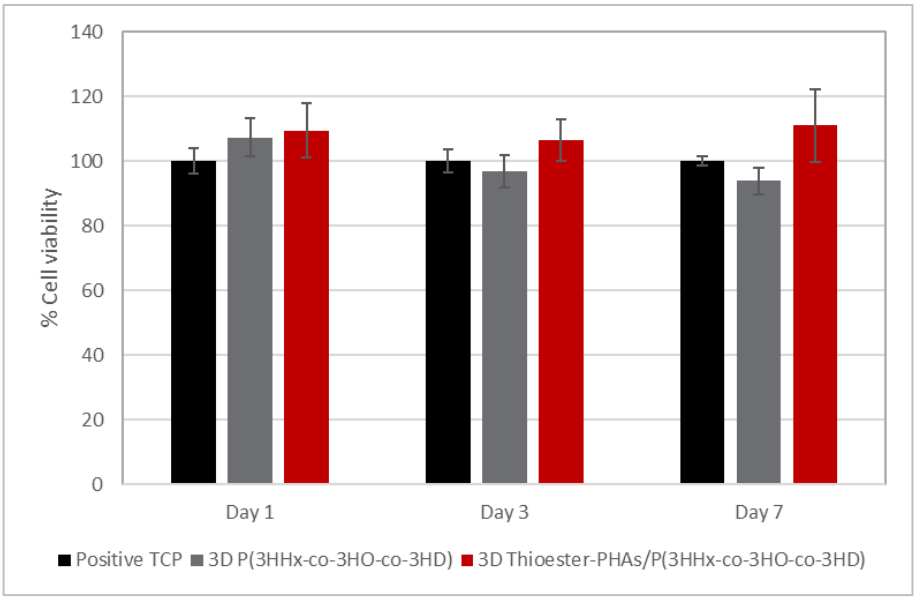

Figure 7.15 Cell viability study of MC3T3-E1 cells on 3D thioester-PHA/P(3HHx-co-3HD-co-3HD) antibacterial scaffolds (red) and 3D P(3HHx-co-3HD-co-3HD) scaffolds (grey) at day 1, 3 and 7 (n = 3). Positive control was Tissue Culture Plastic (TCP). There was no statistically significant difference between the samples and the positive control for all the time points evaluated (*p*-value > 0.5).

7.4. Discussion

In this work, PHA-based antibacterial bone grafting substitutes were developed using the materials produced in Chapter 4 and 5. The melt 3D printing technique optimized in Chapter 6 was applied for the scaffold development. This technology will allow to produce well-defined and highly reproducible constructs, able to be tailored to specific patient's requirements allowing to recreate the tissues defects to be regenerated (Turnbull *et al.*, 2018). For this study, the dimensions of the final scaffolds were defined in collaboration with the Orthopaedic Surgery and Traumatology and Cell Therapy Department of the University of Navarra. The aim was to develop a construct with a pore dimension of 1.5 x 1.5 mm and a height of 6 mm to be tested in a bone critical-size defect model. Such dimensions were chosen to compare the new constructs with a 3D PCL-based construct recently developed by our collaborators (González-Gil *et al.*, 2019). In this chapter, an alternative solution to such implants was investigated through the development of antibacterial PHA-based constructs. In particular, the addition of antimicrobial properties to the bone substitutes was proposed due to the high risk of infections in bone regeneration combined with the challenges of using antibiotics caused by the rise of resistant strains. For these reasons, two strategies were

investigated, the development of 3D antibacterial composites substitutes and of 3D inherently antibacterial materials.

For the first strategy, 3D composite scaffolds were developed by the combination of P(3HO-co-3HD-co-HDD) as the bulk material and Se-Sr-HA as the filler. As described in Chapter 4, composite materials represent one of the best candidates for bone regeneration as they can better mimic the intrinsic heterogenous composite structure of the native tissue (Chocholata *et al.*, 2019; Qu *et al.*, 2019).

The 2D composite films containing three different loadings of the filler (10, 20 and 30 wt%) were used as the starting materials for the production of the 3D printed constructs. Successful printing of all the three compositions could be obtained. Moreover, the final structure required for the *in vivo* test was also achieved. Chemical analysis of the developed materials through FT-IR confirmed the presence of the hydroxyapatite in the scaffolds, showing the characteristics peaks of phosphate groups typical of HA. Interestingly, in the FT-IR spectra of the 3D composite materials the presence of a peak associated with vibration of hydroxyl group could be detected (i.e. 630 cm^{-1}). This peak could not be detected in the original Se-Sr-HA and in the 2D P(3HO-co-3HD-co-HDD) composite samples used as the starting materials for the 3D printing process (as shown in Chapter 5, Figure 5.4). In literature FT-IR analyses of hydroxyapatite doped with strontium or selenite ions showed reduction in the intensity of the peak at 630 cm^{-1}, and the intensity of the peak decreased with the increase in the concentration of the doped ion (Gritsch *et al.*, 2019; Kolmas *et al.*, 2015b; He *et al.*, 2016). Frasnelli *et al.* suggested that for strontium containing HA the vibration mode of the hydroxyl groups could be affected by the perturbation in the crystal lattice of the material due to the presence of strontium, resulting in a reduction in the FT-IR absorption signal (Frasnelli *et al.*, 2017). In the case of selenite containing hydroxyapatite, Kolmas *et al.* postulated that the reduction in the absorption bands of hydroxyl group could be associated with perturbation of the lattice, the presence of intracrystalline water and the charge compensation mechanism caused by the substitution of trivalent phosphate anions (PO_4^{3-}) with bivalent selenite anion (SeO_3^{2-}), leading to the loss of hydroxyl anions (Kolmas *et al.*, 2015a). In this work, the detection of the hydroxyl peak in the FTIR spectra of 3D composite samples might suggest that the applied heating process led to changes in the 2D composite materials, possibly by removal of water or by inducing changes in the structure of the Se-Sr-HA (Ahmed *et al.*, 2015; Kaflak and Kolodziejski, 2011). However, an in-depth analysis of

the materials (e.g. XRD and solid-state NMR) is required to gain understanding of this mechanism.

EDX analysis of the 3D composite scaffolds further confirmed the presence of Se-Sr-HA, as all the elements present in this filler could be identified (i.e. selenium, strontium, calcium, phosphorus). To our knowledge, no previous work investigated the possibility of developing mcl-PHA based 3D composite constructs using melt printing to date. A similar processing technique was employed by Yang *et al.* to produce P(3HB-co-3HHx) scaffolds which were then coated with bioactive glasses to improve the osteogenic properties of the material surface. Even though the scaffolds showed higher attachment, proliferation and osteogenic differentiation of human mesenchymal stem cells compared to neat ones, no improvements in the mechanical properties was detected (Yang *et al.*, 2014). In another study, the same PHA was used as an additive material to produce 3D constructs based on bioactive glasses through a solution-based 3D printed system using a mixture of the polyester and the particles in a chloroform and dimethyl sulfoxide solution. The role of the polymer was to act as a polymer binder to improve the material toughness and reduction of its brittleness (Zhao *et al.*, 2014). In this work, P(3HO-co-3HD-co-HDD) was used as the main material to produce bone substitute for no-load bearing applications, where the elastomeric nature of the polyester would allow the development of surgically-friendly, flexible and easily shaped constructs able to adapt to the injured or diseased site (Jakus *et al.*, 2016; Chen *et al.*, 2012). The introduction of the hydroxyapatite as a filler is expected to improve both the mechanical and biological properties of the grafts. As described in Chapter 5, the novel Se-Sr-HA was chosen to produce a material with superior biological features thanks to the presence of therapeutic metals able to induce bone formation and display antimicrobial properties.

When using metal ions for biomedical applications, it is important to control the quantity of the materials incorporated to minimize their potential toxic effects against eukaryotic cells (Mouriño and Boccaccini, 2010; Marie *et al.*, 2001; Wrobel *et al.*, 2016). For this reason, biological characterization of the 3D composite materials was investigated in terms of both *in vitro* compatibility with mammalian cells and antibacterial properties.

The compatibility of the 3D printed scaffolds was evaluated by preliminary *in vitro* studies using MC3T3-E1 cells through both an indirect and a direct test. For the indirect cytotoxicity evaluation, the effect of the eluates obtained upon incubation of the materials for 1, 3 and 7 days on the cell viability was investigated. The 3D P(3HO-co-3HD-co-HDD) scaffolds with 10 and 20 wt% did not show any toxic effect for the time points evaluated. However, the

materials containing the highest percentage of filler (i.e. 30 wt%) showed a significant reduction of the cell viability of the pre-osteoblast cell line. Such an effect can be correlated with the capability of the material to release ions, which was already demonstrated in Chapter 5 using the 2D composite films. The toxic effect of the samples with a higher content of filler can be associated with a higher release of ions from such matrices compared to the ones containing 10 and 20 wt% of Se-Sr-HA. Moreover, the toxic effect after 7 days is also an indication of a prolonged release of the ions from the scaffolds. The reduction of the cell viability could probably be related to the toxicity of the selenite ions present in the media rather than that of strontium ones. In literature, high concentrations of selenite are known to exert a toxic effect on mammalian cells due to the induction of oxidative stress (Misra *et al.*, 2015; Huawei, 2009). On the contrary, a range of strontium substituted HA have been developed with a content of strontium from 1-10 wt% showing good compatibility towards a range of mammalian cells (e.g. MG63, MC3T3-E1, Saos-2) (Aina *et al.*, 2013; Frasnelli *et al.*, 2017; Capuccini *et al.*, 2008; Tite *et al.*, 2018; Ge *et al.*, 2018). Moreover, a hydroxyapatite doped with the similar content of strontium (i.e. 3 wt%) and produced using the same technique was used to fabricate chitosan composites for bone regeneration. The introduction of strontium did not show any toxic effect against MG63 cells even at the highest loading concentrations investigated (i.e. 80 wt%) (Gritsch *et al.*, 2019). Nevertheless, further tests should be conducted to quantify the amount of ions present in the media and to obtain a correlation between the concentration and the toxicity of each specific ion.

A direct cytocompatibility experiment was conducted by seeding the cells directly on the surface of the 3D printed composite scaffolds and culturing them for 1,3 and 7 days. As already evidenced in the indirect test, the composite with the highest percentage of filler showed cytotoxicity against MC3T3-E1 cells. A similar behaviour could be evidenced for the samples with 20 wt% of Se-Sr-HA, as from day 3 a reduction in the cell viability was detected with average values lower than 70% (i.e. the threshold value for a material to be considered biocompatible according to ISO 10993-5:2009 for the Biological Evaluation of Medical Devices). The combined effect of the metal ions present in the hydroxyapatite structure and the ones release in the surrounding environment could be the reason for the toxicity of such materials in such tests compared to the indirect study. On the contrary the material with the lowest percentage of antibacterial hydroxyapatite showed good cell viability for all the time points evaluated, displaying potential for the use of such substitutes in bone regeneration.

The antibacterial properties of the 3D composite materials were investigated using the ISO 22196, a standard procedure that enables to evaluate the antimicrobial activity of the samples in direct contact with the bacteria. All the three compositions investigated induced a reduction in the bacterial cell count against both to *S. aureus* 6538P and *E. coli* 8739. This activity confirms the activity of selenium containing compound against both Gram positive and Gram negative species, as already evidenced in Chapter 5 through the MIC studies and the antimicrobial tests on the 2D composite films. In particular the 3D P(3HO-co-3HD-co-HDD) with 10 wt% of Se-Sr-HA exhibited an average 80% reduction in the number of both bacterial species. Based on the antibacterial and cell compatibility studies, the composite materials with 10 wt% of Se-Sr-HA as a filler was chosen as the optimal candidate for the development of scaffolds for bone regeneration possessing good antimicrobial properties without resulting in cytotoxicity towards the pre-osteoblastic cell line.

Further investigation of the antimicrobial properties of the selected 3D P(3HO-co-3HD-co-HDD) with 10 wt% of Se-Sr-HA scaffold was carried out through an indirect antibacterial ion release study. Like the 2D composite films used as the starting material, the 3D composites should display antimicrobial properties by direct contact, through the ions present in the matrix, and indirect mechanism, through the ions released in the environment. The samples showed an effect against both *S. aureus* 6538P and *E. coli* 8739. These results confirmed the capability of the matrix to release ions in the surrounding media, already evidenced in the indirect *in vitro* cytotoxicity studies. The ion release seems to be prolonged over time, as a reduction of the bacterial cell count was detected with the eluates obtained after seven days of incubation with the materials. A slightly higher effect against Gram positive bacteria compared to negative ones was evidenced. These results are in agreement with those in Chapter 5 for the 2D composite films and with literature studies (Alam *et al.*, 2016; Vasić *et al.*, 2011). Finally, the time points selected (i.e. 1, 3 and 7 days) for the indirect release study were the same as the *in vitro* cytotoxicity one, showing once more the potential of the 3D P(3HO-co-3HD-co-HDD) with 10 wt% of Se-Sr-HA to inhibit bacterial growth while showing good cell viability of mammalian cells.

The second strategy to develop 3D PHA-based antibacterial was based on the use of thioester-containing PHAs in order to obtain inherently antibacterial materials. The advantages of using these inherently antibacterial materials is the possibility to obtain constructs possessing long-term activity and durability due to their chemical stability (Xue

et al., 2015). In Chapter 4, 2D 80:20 blend films of thioester-PHA and P(3HHx-co-3HO-co-3HD) showed antimicrobial properties against *S. aureus* and compatibility towards MC3T3-E1 cells, while still maintaining good handleability and processability. For these reasons, such a combination was chosen as the starting material for the production of 3D printed scaffolds. As mentioned in Chapter 4, limited research has been conducted on the use of thioester-PHAs for the development of scaffolds for medical applications. In this work for the first time, successful printing of the blend composite was obtained, showing potential to broaden the utilization of such materials. However, the targeted constructs of 6 mm height could not be achieved with such blend composition.

Chemical characterization of the scaffold was conducted through FT-IR analysis, confirming the presence of thioester groups on the surface of the produced scaffolds. The 3D blend samples showed in fact the presence of an additional peak at 1690 cm^{-1} related to the stretching of the carbonyl group of the thioester bond (Ewering *et al.*, 2002). Moreover, the presence of sulphur was also confirmed through EDX analysis.

The antibacterial properties of the 3D printed blend scaffolds were investigated using the ISO 22196 against *S. aureus* 6538P, as the thioester-PHAs only showed an antibacterial effect against such species (as described in Chapter 4). Reduction of the bacterial cell count was detected, showing that the 3D materials still preserved the antibacterial properties of the 2D samples used as starting materials.

Finally, preliminary *in vitro* compatibility studies were performed by seeding MC3T3-E1 cells on the scaffolds for 1, 3 and 7 days. The materials showed good cell viability for all the time points evaluated, showing potential for bone regeneration.

7.5. Conclusions

In this chapter, two strategies were investigated for the development of novel 3D antibacterial substitutes based on PHAs for bone regeneration.

The first strategy involved the production of novel 3D composite scaffolds using the 2D films developed in Chapter 5, obtained by the combination of P(3HO-co-3HD-co-3HDD) and Se-Sr-HA. All the 3 compositions tested, 10, 20 and 30 wt% of Se-Sr-HA were successfully printed and characterized in terms of chemical, antibacterial and biological properties. Based on the antibacterial and cell compatibility studies, the composite materials with 10 wt% of

Se-Sr-HA as a filler, 3D P(3HO-co-3HD-co-3HDD)/10 wt% Se-Sr-HA, was chosen as the optimal candidate for the development of antibacterial scaffolds for bone regeneration.

In the second strategy, inherently antibacterial scaffolds were produced by melt 3D printing of 20:80 blend films of thioester-PHAs with P(3HHx-co-3HO-co-3HD), developed in Chapter 4. The structures developed showed antibacterial activity against *S. aureus* 6538P by direct contact. The material exhibited good cytocompatibility towards MC3T3-E1 cells, showing potential for bone regeneration.

Chapter 8

Conclusions and Future work

8.1. Conclusions

The world-wide concerns on the threats associated with the spreading and increase of antimicrobial resistance have highlighted the need for new therapeutics as alternatives to antibiotics to prevent and fight infections. In such a scenario, this work focused on the development of novel antibiotic-free materials based on polyhydroxyalkanoates for bone regeneration. PHAs represent an attractive option in this field thanks to their biocompatibility, biodegradability and sustainability. Two strategies were investigated to obtain antibacterial PHA-based materials, the production of inherently antibacterial polyesters and the development of composite materials through loading of PHAs with a novel antimicrobial hydroxyapatite. Such compounds were then used as starting materials for the development of 3D scaffolds for antibacterial synthetic bone substitutes using an optimized melt printing process.

Firstly, the production of three PHAs through bacterial fermentation were studied. A short chain length PHA, P(3HB) was produced by *B. subtilis* OK2 using glucose as the carbon source. The physical, thermal and mechanical properties of this polyester were comparable to those present in literature. In particular, P(3HB) is a relatively highly crystalline material (i.e. average crystallinity of 56%) with a melting temperature range between 155-175 °C and low glass transitions temperature (2°C), and characterized by a stiff and brittle mechanical behaviour, with a high Young's modulus (1 GPa) and low elongation at break (16%). Two novel medium chain length PHAs, P(3HO-co-3HD) and P(3HO-co-3HD-co-3HDD), were produced by *P. mendocina* CH50 using glucose and coconut oil as the carbon sources respectively. In particular, the use of coconut oil was investigated as a cheaper alternative to glucose. One of the major deterrents for the commercialization of PHAs is indeed their high production cost, with the price of the carbon source accounting for 50% of the overall cost. Using coconut oil, a higher polymer yield of 58 %dcw was obtained as compared to 47%dcw

with glucose. The two mcl-PHAs were characterized in terms of physical, thermal and mechanical properties, showing comparable features. The two polyesters possessed a low melting range (between 40-60 °C for both PHAs) and glass transition temperature (-45°C for both PHAs), and an elastomeric behaviour characterized by a high elongation at break (536% for P(3HO-co-3HD) and 414% for P(3HO-co-3HD-co-3HDD)) and low Young's modulus (5.7 MPa for P(3HO-co-3HD) and 5.3 MPa for P(3HO-co-3HD-co-3HDD)). Lastly, the preliminary *in vitro* biological properties of the three PHAs were investigated, showing that all the polyesters exhibited good cytocompatibility towards MC3T3-E1 cells, a pre-osteoblastic cell line. Based on the result obtained, P(3HO-co-3HD-co-3HDD) was selected over P(3HO-co-HD) as a more promising candidate for the development of antibacterial materials thanks to the higher productivity combined with the cheaper cost of the carbon source compared to glucose.

The first strategy investigated to develop novel antibacterial PHA-based materials was the production of inherently antibacterial PHAs, thioester-PHAs. Inherently antibacterial polymers have the advantage of possessing long-lasting and durable properties against bacteria. Thioester-PHAs were successfully produced using bacterial fermentation by *P. putida* KT2442 using decanoic acid and 6-acetylthiohexanoic acid as carbon sources, following a protocol developed by Escapa *et al.*, 2011. A co-feeding strategy was essential to obtain thioester-PHAs, as the compound containing the desired functional group (6-acetylthiohexanoic acid) was identified as a poor substrate not able to support neither bacterial growth nor polymer accumulation. FT-IR, GC-MS and NMR analyses confirmed the presence of the thioester group in the side chain of the polymers, with 45.5% of the monomeric units possessing this functional group. Thermal analysis of the material showed that the presence of the thioester moieties hindered the crystallization of the polymer, as no melting peak could be detected in the DSC thermogram, indicating the complete amorphous nature of such PHAs. Moreover, a quantitative standard procedure (ISO 22196) was employed to investigate the antibacterial properties of the produced PHAs, through the evaluation of the reduction of the number of bacterial cells in direct contact with the materials. The thioester PHAs showed an inhibitory effect against *S. aureus* 6538P, while no activity was evidenced against *E.coli* 8739. Even though the mechanism of action of thioester-PHAs has not been elucidated, it seemed to be related to the presence of thioester groups, as the polymer obtained using control conditions (i.e. only decanoic acid as the

carbon source) did not show an antibacterial effect against both species. Moreover, the preferential activity towards Gram positive species could be related to the presence of the additional outer membrane of Gram negative bacteria, which is known to act as an extra barrier to the action of active compounds. The possibility to use such polymers in bone tissue engineering was investigated for the first time in this study. Preliminary *in vitro* biocompatibility studies showed that the thioester-PHAs possessed good cytocompatibility towards MC3T3-E1 cells. However, the amorphous nature of such polymers prevents their application as bulk materials for the development of scaffolds. For this reason, physical blending of thioester-PHA with P(3HHx-co-3HO-co-3HD) (i.e. polymer obtained using control conditions) was investigated to produce 2D inherently antibacterial films. A polymer ratio of 80:20 (P(3HHx-co-3HO-co-3HD): thioester-PHA) was identified as optimal to develop handleable and processable samples possessing antibacterial and *in vitro* biocompatibility properties.

The second strategy investigated involved the production of 2D antibacterial composite films. Composite materials are excellent candidates for regeneration of bone as they can better mimic the inherent heterogenous composition of this tissue and allow the combination of the positive features of two or more compounds. In this work, the combination of PHAs with a novel antibacterial co-substituted hydroxyapatite, developed by Dr. Muhammad Maqbool (early stage researcher involved in the same Marie Curie European Doctoral Programme HyMedPoly), was investigated. This novel HA was used as the filler agent and was chosen as it contained two therapeutic ions, selenium and strontium, conferring osteoinductive and antibacterial properties to the ceramic. P(3HB) and P(3HO-co-3HD-co-3HDD) were selected as the bulk materials as representatives of scl and mcl-PHAs respectively. Firstly, the antibacterial properties of the novel Se-Sr-HA were investigated by MIC and MBC analysis. The material showed a bacteriostatic effect against both *S. aureus* 6538P and *E.coli* 8739 at the concentration investigated. In literature selenium ions have been shown to possess antimicrobial activity and the mechanism has been associated with the induction of oxidative stress (Estevam *et al.*, 2015; Alam *et al.*, 2016). 2D composite films with three filler percentages (10, 20 and 30 wt% of Se-Sr-HA) were then developed and characterized in terms of physical, mechanical and thermal properties. The introduction of the Se-Sr-HA induced an increase of the elastic modulus and ultimate tensile strength in both P(3HB) and P(3HO-co-3HD-co-3HDD). However, embrittlement of the films was also

evidenced by the reduction of the elongation at break of the materials compared to neat samples. Finally, the antibacterial properties of the composite samples were investigated against both Gram positive and Gram negative bacteria through both indirect and direct assay. The materials developed were shown to be able to induce an inhibitory effect against both bacterial species through two mechanisms, by direct contact between the bacteria and the selenite ions present in the hydroxyapatite structure and by contact with the ions released in the surrounding environment.

The possibility of developing 3D scaffolds using melt 3D printing of mcl-PHAs was investigated in this study for the first time. The use of 3D printing technology has a great potential in the medical field, as it allows to obtain controlled and repeatable structures that can be tailored to the specific patients' requirements. P(3HO-co-3HD-co-3HDD) was chosen as the representative mcl-PHA, while printing of P(3HB) could not be conducted due to the intrinsic limitation of the 3D printer used. The process parameters were successfully optimized to produce structures with a specific porosity and thickness. Moreover, the melt process did not induce degradation of the polyester, as the molecular weight of P(3HO-co-3HD-co-3HDD) remained unaltered after printing. The degradation behaviour of the 3D printed scaffold was tested *in vitro* in PBS for 6 months. During the testing period, no changes in the weight of the samples were evidenced, while a reduction of the molecular weight was detected, indicating that the materials underwent bulk degradation in such conditions. Moreover, the suitability of the developed constructs for bone regeneration was shown *in vitro* as the scaffold were able to support the growth, proliferation and differentiation of MC3T3-E1 cells into osteoblast when culture in an appropriate osteogenic media. Finally, the possibility to develop dual porous structure was investigated by combining the 3D printing with salt leaching. Effective structures for bone tissue engineering have been shown to be characterized by a range of porosity, both macro and micro, allowing the attachment and migration of cells, the flow of nutrients and waste and the vascularization of the scaffolds. Moreover, the scaffold produced with melt printing using P(3HO-co-3HD-co-3HDD) did not show side porosity (in the z-direction). In this study, the macro-porosity was created and controlled through the 3D model used for the printing (i.e. 1.5x 1.5 mm pore size), while the micro-porosity was created inside the fibres through the addition of salt particles. Scaffolds with different levels of intra-strut porosity were obtained by varying the polymer/salt ratio (50:50, 35:65 and 25:75, P(3HO-co-3HD-co-3HDD):NaCl) and the dimension of the

porogen (i.e. <100 µm and between 100 and 300 µm). All the material produced showed no sign of indirect cytotoxicity towards MC3T3-E1 cells.

Finally, the possibility of using the obtained materials for the development of antimicrobial synthetic bone grafts through melt 3D printing was investigated. The constructs were designed in collaboration with the Orthopaedic Surgery and Traumatology and Cell Therapy Department of the University of Navarra. The targeted scaffold dimensions were of 6 mm height and 1.5 x 1.5 mm of pore size to be tested *in vivo* in a mouse critical bone defect model. The need of antimicrobial materials in such an application has recently attracted great attention due to the high risk of infection associated with the treatment of bone repair and the challenges raised by the spreading of antimicrobial resistance. Commercially available antimicrobial strategies currently applied in the clinic rely heavily on the use of antibiotics, either through systemic administration or through the use of drug-loaded spacers or grafts. For these reasons, in the last years researchers have been focusing on developing antibiotic-free scaffolds for bone regeneration. In terms of 3D printed polymer-based materials, a few studies have been conducted on the production of antibacterial PCL or PLA scaffolds through the incorporation of therapeutic ions (i.e. copper, zinc or silver) or natural products (i.e. chitosan and poly- epsilon lysine) (Li *et al.*, 2019a; Luo *et al.*, 2020; Tian *et al.*, 2020; Zou *et al.*, 2020). 3D PHA-based materials offer advantages over such polyesters thanks to their natural origin, sustainability and less acidic degradation products (as compared to PLA). To our knowledge, no previous work investigated the possibility of developing 3D PHA-based bone scaffolds with antimicrobial properties. Based on the two different types of 2D films developed, two strategies were investigated for the production of novel 3D antibacterial PHA-based bone grafts. The first strategy involved the production of novel 3D composite scaffolds using the 2D composite P(3HO-co-3HD-co-3HDD) films as starting materials for the melt printing process. All the three compositions tested, 10, 20 and 30 wt% of Se-Sr-HA could be successfully processed in the final shape required for the *in vivo* test. Biological characterization of the 3D composite materials was investigated in terms of both *in vitro* compatibility with mammalian cells and antibacterial properties, due to the potential toxic effect of high quantity of metal ions against eukaryotic cells. All the 3D scaffolds showed a high antibacterial effect against both *S. aureus* 6538P and *E. coli* 8739, increasing with the increase of filler concentration. However, the samples with the highest concentrations of Se-Sr-HA (i.e. 20 and 30 wt%) showed a reduction of the viability of MC3T3-E1 cells.

Therefore, the composite materials with 10 wt% of Se-Sr-HA as a filler, 3D P(3HO-co-3HD-co-3HDD)/10 wt% Se-Sr-HA, was chosen as the optimal candidate for the development of 3D scaffolds possessing both antibacterial effect and biocompatibility towards pre-osteoblastic cell line.

For the second strategy, inherently antibacterial scaffolds were produced by melt 3D printing of 20:80 blend films of the thioester-PHA with P(3HHx-co-3HO-co-3HD). The materials could be successfully printed into controlled and repeatable geometries, but the targeted height of 6 mm could not be achieved. The 3D blend scaffolds showed an inhibitory effect against *S. aureus* 6538P by direct contact testing. Moreover, the material showed cytocompatibility towards MC3T3-E1 cells, showing potential for bone regeneration.

8.2. Future work

This thesis focused on the development of novel antibiotic-free PHA-based antibacterial materials for bone regeneration. Based on the promising results obtained in this work, many potential areas that could be further explored and improved have emerged.

As the main obstacle to the commercialization of PHAs is related to their high cost, further optimization studies should be conducted. For mcl-PHAs, the production using coconut oil showed promising results in terms of polymer yield over glucose. The fermentation process could be further analysed and optimized through a full design of experiment (DOE) factorial study with pH, carbon/nitrogen ratio and rpm as varying parameters (Sun *et al.*, 2007; Kniewel *et al.*, 2017). Moreover, different modes of fermentation could be investigated like fed-batch fermentation. For scl-PHAs, the production using cheaper and renewable carbon sources could be investigated and optimized (Singh *et al.*, 2009; Kumar *et al.*, 2009). Finally, the production of thioester-PHAs has only been conducted on a shaken flask level. Therefore, full optimization studies should be carried out using fermenters to improve the polymer yield.

The thioester-PHAs represent an interesting material for medical applications thanks to their inherent antibacterial activity. In this work, blending of the material was carried out to expand and explore its application in tissue engineering. Combination with mcl-PHAs was investigated due to the similar nature of the materials and the possibility to obtain miscible systems. Nevertheless, limitations in the amount of thioester-PHAs that could be incorporated was evidenced, with higher concentrations resulting in the poor handleability

and processability of the films. Future work could investigate the modification of the thioester-PHAs into oligomers through for example acid hydrolysis and their incorporation in both mcl and scl-PHA systems (Lukasiewicz *et al.*, 2018). Finally, investigation into the mechanism of action of such polymers should be conducted to understand their selectivity toward Gram positive bacteria and its possible dependence on membrane disruption activity (O'Neill and Chopra, 2004).

As regards the 2D composite materials developed containing Se-Sr-HA, investigation of the incorporation of the filler in nano-size form could be conducted to evaluate if the mechanical properties of the final constructs could be further improved (Misra *et al.*, 2008). Moreover, investigation of the surface of the properties of the films could also be analysed in terms of roughness, wettability and protein adsorption. The bioactivity of the constructs should be studied by evaluating the ability of the material to induce hydroxyapatite formation on its surface in simulated body fluids (Kokubo and Takadama, 2006). Finally, quantification of the ions released by the films should be analysed using Inductively coupled plasma/optical emission spectroscopy (ICP-OES) to have a better understanding of their antibacterial activity.

In this work, for the first time melt 3D printing of mcl-PHAs was conducted. A feasibility study was conducted to optimize the printing parameters for the production of well-defined, reproducible and controlled geometries. The interactions between the materials properties and the process parameters could be further investigated through a statistical design of experiment (DoE), taking into account variation in the nozzle dimension as well as extrusion temperature, pressure and writing speed. A full understanding of such interactions is needed for process standardization and for their scale-up and clinical translation (Sheshadri and Shirwaiker, 2015). Mechanical characterization of the printed constructs should be investigated as such properties are essential for any tissue engineering scaffold. An *in vitro* degradation study of the scaffolds was conducted in PBS over six months. The degradation in environment better simulating the *in vivo* condition should be investigated, such as the addition of enzymes like lipases and esterases (Ong *et al.*, 2017).

A preliminary investigation of the possibility to obtain structures with dual porosity was conducted by combining melt printing with salt leaching. The results obtained showed that the porosity could be modulated through the variation of the polymer/porogen ratio and the porogen dimensions. However, this work was only preliminary, and an in-depth

characterization of the developed constructs needs to be conducted investigating better the porosity obtained and its influence on the mechanical, biocompatibility and degradation properties.

Overall a more in-depth characterization of the 3D printed antibacterial PHA-based material should be conducted for the further development of such materials in the context on bone regeneration. Investigation of the surface, mechanical and degradation properties of the scaffolds should be conducted and compared with the neat 3D scaffolds, to evaluate the effect of the incorporation of Se-Sr-HA and thioester-PHA. For the 3D composite materials, the release of the ions from the 3D scaffolds should also be investigated to have a better understanding of its biological properties. Moreover, the same *in vitro* differentiation studies of MC3T3-E1 cells conducted with 3D neat scaffold should be conducted on the 3D composite materials. The use of hydroxyapatite with strontium ions should in fact conferrer osteoinductive properties to the materials. Furthermore, the possibility of using these constructs for bone-defects related to tumours treatment could also be evaluated thanks to the anticancer properties of selenium (Hosnedlova *et al.*, 2018). Finally, the two strategies investigated for the development of 3D antibacterial PHAs scaffold could be combined together in the future. The limitation of the printing of the thioester-PHAs could be overcame by the combination of both thioester-PHA and Se-Sr-HA with mcl-PHAs, producing osteoinductive, osteoconductive structures possessing long lasting antibacterial properties by contact and through the ion release.

Finally, a deeper understanding of the biological properties of all the developed materials is required for their application in bone regeneration. The antibacterial activity against other strains (e.g. *S. epidermidis*, *Streptococci* sp., *Pseudomonas* sp.) associated with bone infection should be investigated. Moreover, the long-lasting effect of the antimicrobial action of the materials should be evaluated. In terms of biocompatibility, the materials developed were designed to be combined with periosteum stem cells and tested *in vivo*. Therefore, *in vitro* compatibility studies with such mouse-derived primary cells should be conducted, followed by the implantation of the constructs in a *in vivo* critical-size defect model to assess their potential to promote bone regeneration.

References

Abdelwahab, M. A., El-Barbary, A. A., El-Said, K. S., El Naggar, S. A. & ElKholy, H. M. (2019) Evaluation of antibacterial and anticancer properties of poly(3-hydroxybutyrate) functionalized with different amino compounds. *International Journal of Biological Macromolecules*. 122, 793–805.

Abe, H., Ishii, N., Sato, S. & Tsuge, T. (2012) Thermal properties and crystallization behaviors of medium-chain-length poly(3-hydroxyalkanoate)s. *Polymer*. 53 (14), 3026–3034.

Ahmed, I., Salmon, L. J., Waller, A., Watanabe, H., Roe, J. P., Pinczewski, L. A., Orthopaedic Clinical Fellow, S. & Physiotherapist, R. (2016) Bone grafts and their substitutes. *Bone Joint Journal*. 9858–64.

Ahmed, Y. M. Z., El-Sheikh, S. M. & Zaki, Z. I. (2015) Changes in hydroxyapatite powder properties via heat treatment. *Bulletin of Materials Science*. 38 (7), 1807–1819.

Aina, V., Bergandi, L., Lusvardi, G., Malavasi, G., Imrie, F. E., Gibson, I. R., Cerrato, G. & Ghigo, D. (2013) Sr-containing hydroxyapatite: Morphologies of HA crystals and bioactivity on osteoblast cells. *Materials Science and Engineering C*. 33 (3), 1132–1142.

Akaraonye, E., Keshavarz, T. & Roy, I. (2010) Production of polyhydroxyalkanoates: The future green materials of choice. *Journal of Chemical Technology and Biotechnology*. 85 (6), 732–743.

Alam, M. F., Safhi, M. M., Moni, S. S. & Jabeen, A. (2016) *In vitro* Antibacterial Spectrum of Sodium Selenite against Selected Human Pathogenic Bacterial Strains. *Scientifica*. 2016, 1–5.

Albrektsson, T. & Johansson, C. (2001) Osteoinduction, osteoconduction and osseointegration. *European Spine Journal*. 10, 96–101.

Aldor, I. S. & Keasling, J. D. (2003) Process design for microbial plastic factories: Metabolic engineering of polyhydroxyalkanoates. *Current Opinion in Biotechnology*. 14 (5), 475–483.

Ali, I. & Jamil, N. (2016) Polyhydroxyalkanoates: Current applications in the medical field. *Frontiers in Biology*. 11 (1), 19–27.

Alom-Ruiz, S. & Chen, C. S. (2007) Microcontact printing: A tool to pattern. *Soft Matter*. 3 (2), 168–177.

Álvarez-Chávez, C. R., Edwards, S., Moure-Eraso, R. & Geiser, K. (2012) Sustainability of bio-based plastics: General comparative analysis and recommendations for improvement. *Journal of Cleaner Production*. 23 (1), 47–56.

Anbukarasu, P., Sauvageau, D. & Elias, A. (2015) Tuning the properties of polyhydroxybutyrate films using acetic acid via solvent casting. *Scientific Reports*. 51–14.

Ansari, N. F., Annuar, M. S. M. & Murphy, B. P. (2016) A porous medium-chain-length poly(3-hydroxyalkanoates)/hydroxyapatite composite as scaffold for bone tissue engineering. *Engineering in Life Sciences*. 17 (4), 1–29.

Appaiah, P., Sunil, L., Prasanth Kumar, P. K. & Gopala Krishna, A. G. (2014) Composition of coconut testa, coconut kernel and its oil. *JAOCS, Journal of the American Oil Chemists' Society*. 91 (6), 917–924.

Aróstegui, S. M., Aponte, M. A., Díaz, E. & Schröder, E. (1999) Bacterial polyesters produced by *Pseudomonas oleovorans* containing nitrophenyl groups. *Macromolecules*. 32 (9), 2889–2895.

Ashby, R. D., Solaiman, D. K. Y., Foglia, T. A. & Liu, C. K. (2001) Glucose/lipid mixed substrates as a means of controlling the properties of medium chain length poly(hydroxyalkanoates). *Biomacromolecules*. 2 (1), 211–216.

Ashby, R. D. & Foglia, T. A. (1998) Poly(hydroxyalkanoate) biosynthesis from triglyceride substrates. *Applied Microbiology and Biotechnology*. 49 (4), 431–437.

Auta, A., Hadi, M. A., Oga, E., Adewuyi, E. O., Abdu-Aguye, S. N., Adeloye, D., Strickland-Hodge, B. & Morgan, D. J. (2019) Global access to antibiotics without prescription in community pharmacies: A systematic review and meta-analysis. *Journal of Infection*. 78 (1), 8–18.

Azevedo, M. C., Reis, R. L., Claase, M. B., Grijpma, D. W. & Feijen, J. (2003) Development and properties of polycaprolactone/hydroxyapatite composite biomaterials. *Journal of Materials Science: Materials in Medicine*. 14 (2), 103–107.

Babinot, J., Renard, E. & Langlois, V. (2010) Preparation of *Clickable* Poly(3-hydroxyalkanoate) (PHA): Application to Poly(ethylene glycol) (PEG) Graft Copolymers Synthesis. *Macromolecular Rapid Communications*. 31 (7), 619–624.

Bajić, M., Jalšovec, H., Travan, A., Novak, U. & Likozar, B. (2019) Chitosan-based films with incorporated supercritical CO2 hop extract: Structural, physicochemical, and antibacterial properties. *Carbohydrate Polymers*. 219, 261–268.

Baldwin, P., Li, D. J., Auston, D. A., Mir, H. S., Yoon, R. S. & Koval, K. J. (2019) Autograft, Allograft, and Bone Graft Substitutes: Clinical Evidence and Indications for Use in the Setting of Orthopaedic Trauma Surgery. *Journal of orthopaedic trauma*. 33 (4), 203–213.

Barbuzzi, T., Giuffrida, M., Impallomeni, G., Carnazza, S., Ferreri, A., Guglielmino, S. P. P. & Ballistreri, A. (2004) Microbial Synthesis of Poly(3-hydroxyalkanoates) by *Pseudomonas aeruginosa* from Fatty Acids: Identification of Higher Monomer Units and Structural Characterization. *Biomacromolecules*. 5 (6), 2469–2478.

Bartnikowski, M., Dargaville, T. R., Ivanovski, S. & Hutmacher, D. W. (2019) Degradation mechanisms of polycaprolactone in the context of chemistry, geometry and environment. *Progress in Polymer Science*. 96, 1–20.

Basnett, P., Ravi, S. & Roy, I. (2017a) 'Natural bacterial biodegradable medical polymers: Polyhydroxyalkanoates', in *Science and Principles of Biodegradable and Bioresorbable Medical Polymers: Materials and Properties*. Woodhead Publishing Limited. pp. 257–277.

Basnett, P., Lukasiewicz, B., Marcello, E., Gura, H. K., Knowles, J. C. & Roy, I. (2017b) Production of a novel medium chain length poly(3- hydroxyalkanoate) using unprocessed biodiesel waste and its evaluation as a tissue engineering scaffold. *Microbial Biotechnology*. 10 (6), 1384–1399.

Bébien, M., Lagniel, G., Garin, J., Touati, D., Verméglio, A. & Labarre, J. (2002) Involvement of superoxide dismutases in the response of Escherichia coli to selenium oxides. *Journal of Bacteriology*. 184 (6), 1556–1564.

Bergander, K., Luftmann, H. & Steinbu, A. (2001) Biosynthesis of Poly (3-hydroxybutyrate-co-3-mercaptobutyrate) as a Sulfur Analogue to Poly (3-hydroxybutyrate) (PHB). *Biomacromolecules*. 2 (3), 1061–1065.

Bergmann, A. & Owen, A. (2003) Hydroxyapatite as a filler for biosynthetic PHB homopolymer and P(HB-HV) copolymers. *Polymer International*. 52 (7), 1145–1152.

Beslikas, T., Gigis, I., Goulios, V., Christoforides, J., Papageorgiou, G. Z. & Bikiaris, D. N. (2011) Crystallization study and comparative *in vitro-in vivo* hydrolysis of PLA reinforcement ligament. *International Journal of Molecular Sciences*. 12 (10), 6597–6618.

Birol, H., Maeder, T. & Ryser, P. (2006) Processing of graphite-based sacrificial layer for microfabrication of low temperature co-fired ceramics (LTCC). *Sensors and Actuators, A: Physical*. 130–131, 560–567.

Blair, J. M. A., Webber, M. A., Baylay, A. J., Ogbolu, D. O. & Piddock, L. J. V. (2015) Molecular mechanisms of antibiotic resistance. *Nature Reviews Microbiology*. 13 (1), 42–51.

Blom, A. (2007) (V) Which scaffold for which application? *Current Orthopaedics*. 21 (4), 280–287.

Blunt, W., Lagassé, A., Jin, Z., Dartiailh, C., Sparling, R., Gapes, D. J., Levin, D. B. & Cicek, N. (2019) Efficacy of medium chain-length polyhydroxyalkanoate biosynthesis from different biochemical pathways under oxygen-limited conditions using *Pseudomonas putida* LS46. *Process Biochemistry*. 82, 19–31.

Bonartsev, A. P., Bonartseva, G. A., Reshetov, I. V., Kirpichnikov, M. P. & Shaitan, K. V. (2019) Application of polyhydroxyalkanoates in medicine and the biological activity of natural poly(3-hydroxybutyrate). *Acta Naturae*. 11 (2), 4–16.

Borsagli, F. G. L. M., Ciminelli, V. S. T., Ladeira, C. L., Haas, D. J., Lage, A. P. & Mansur, H. S. (2019) Multi-functional eco-friendly 3D scaffolds based on N-acyl thiolated chitosan for potential adsorption of methyl orange and antibacterial activity against *Pseudomonas aeruginosa*. *Journal of Environmental Chemical Engineering*. 7 (5), 103286.

Bose, S., Vahabzadeh, S. & Bandyopadhyay, A. (2013) Bone tissue engineering using 3D printing. *Materials Today*. 16 (12), 496–504.

Bose, S., Roy, M. & Bandyopadhyay, A. (2012) Recent advances in bone tissue engineering scaffolds. *Trends in biotechnology*. 30 (10), 546–554.

Boyce, B. F., Xing, L. & Schwarz, E. M. (2011) The Role of the Immune System and Bone Cells in Acute and Chronic Osteomyelitis. *Osteoimmunology*. 369–389.

Boyce, B. F. & Xing, L. (2007) Biology of RANK, RANKL, and osteoprotegerin. *Arthritis Research and Therapy* 9 (1) p.S1.

Bridges, C. C. & Zalups, R. K. (2010) Ionic and molecular mimicry and the transport of metals. *Cellular and Molecular Biology of Metals*. 204 (3), 241–294.

Brigham & Sinskey (2012) Applications of Polyhydroxyalkanoates in the Medical Industry. *International Journal of Biotechnology for Wellness Industries*. 1 (1), 53–60.

Bugnicourt, E., Cinelli, P., Lazzeri, A. & Alvarez, V. (2014) Polyhydroxyalkanoate (PHA): Review of synthesis, characteristics, processing and potential applications in packaging. *Express Polymer Letters*. 8 (11), 791–808.

Butler, M. S., Blaskovich, M. A. & Cooper, M. A. (2013) Antibiotics in the clinical pipeline in 2013. *Journal of Antibiotics*. 66 (10), 571–591.

Butt, F. I., Muhammad, N., Hamid, A., Moniruzzaman, M. & Sharif, F. (2018) Recent progress in the utilization of biosynthesized polyhydroxyalkanoates for biomedical applications – Review. *International Journal of Biological Macromolecules*. 120, 1294–1305.

Cai, X., Yang, F., Yan, X., Yang, W., Yu, N., Oortgiesen, D. A. W., Wang, Y., Jansen, J. A. & Walboomers, X. F. (2015) Influence of bone marrow-derived mesenchymal stem cells pre-implantation differentiation approach on periodontal regeneration *in vivo*. *Journal of Clinical Periodontology*. 42 (4), 380–389.

Calori, G. M., Mazza, E., Colombo, M. & Ripamonti, C. (2011) The use of bone-graft substitutes in large bone defects: Any specific needs? *Injury*. 42, S56–S63.

Cao, Z., Jiang, D., Yan, L. & Wu, J. (2017) *In vitro* and *in vivo* drug release and antibacterial properties of the novel vancomycin-loaded bone-like hydroxyapatite/poly amino acid scaffold. *International Journal of Nanomedicine*. 12, 1841–1851.

Cao, Z. & Sun, Y. (2008) N-Halamine-based chitosan: Preparation, characterization, and antimicrobial function. *Journal of Biomedical Materials Research - Part A*. 85 (1), 99–107.

Capuccini, C., Torricelli, P., Sima, F., Boanini, E., Ristoscu, C., Bracci, B., Socol, G., Fini, M., Mihailescu, I. N. & Bigi, A. (2008) Strontium-substituted hydroxyapatite coatings synthesized by pulsed-laser deposition: *In vitro* osteoblast and osteoclast response. *Acta Biomaterialia*. 4 (6), 1885–1893.

Castro-Mayorga, J., Fabra, M., Cabedo, L. & Lagaron, J. (2016) On the Use of the Electrospinning Coating Technique to Produce Antimicrobial Polyhydroxyalkanoate Materials Containing In Situ-Stabilized Silver Nanoparticles. *Nanomaterials*. 7 (1), 4.

Castro-Mayorga, J. L., Fabra Rovira, M. J., Cabedo Mas, L., Sánchez Moragas, G. & Lagarón Cabello, J. M. (2018) Antimicrobial nanocomposites and electrospun coatings based on poly(3-hydroxybutyrate-co-3-hydroxyvalerate) and copper oxide nanoparticles for active packaging and coating applications. *Journal of Applied Polymer Science*. 135 (2), 1–11.

Catanzano, O., Straccia, M. C., Miro, A., Ungaro, F., Romano, I., Mazzarella, G., Santagata, G., Quaglia, F., Laurienzo, P. & Malinconico, M. (2015) Spray-by-spray *in situ* cross-linking alginate hydrogels delivering a tea tree oil microemulsion. *European Journal of Pharmaceutical Sciences*. 66, 20–28.

CDC (2019), Antibiotic Resistance Threats in the United States,Atlanta, GA: US Department of Health and Human Services, Centers for Disease Control and Prevention (CDC)*;* 2019.

Cengiz, I. F., Oliveira, J. M. & Reis, R. L. (2018) Micro-CT – a digital 3D microstructural voyage into scaffolds: a systematic review of the reported methods and results. *Biomaterials Research*. 22 (1), 1–11.

Chanasit, W., Hodgson, B., Sudesh, K. & Umsakul, K. (2016) Efficient production of polyhydroxyalkanoates (PHAs) from *Pseudomonas mendocina* PSU using a biodiesel liquid waste (BLW) as the sole carbon source. *Bioscience, Biotechnology and Biochemistry*. 80 (7), 1440–1450.

Chanprateep, S. (2010) Current trends in biodegradable polyhydroxyalkanoates. *Journal of Bioscience and Bioengineering*. 110 (6), 621–632.

Chee, J., Yoga, S., Lau, N., Ling, S. & Abed, R. M. M. (2010) Bacterially Produced Polyhydroxyalkanoate (PHA): Converting Renewable Resources into Bioplastics. *Current research, technology and education topics in Applied Microbiology and Microbial Biotechnology*. 2, 1395–1404.

Chen, G.-Q. (2009) A microbial polyhydroxyalkanoates (PHA) based bio- and materials industry. *Chemical Society Reviews*. 38 (8), 2434.

Chen, G. Q. & Luo, R. C. (2009) 'Polyhydroxyalkanoate Blends and Composites', in *Biodegradable Polymer Blends and Composites from Renewable Resources*. pp. 191–207.

Chen, G. Q. & Wu, Q. (2005) The application of polyhydroxyalkanoates as tissue engineering materials. *Biomaterials*. 26 (33), 6565–6578.

Chen, G. Q. & Zhang, J. (2018) Microbial polyhydroxyalkanoates as medical implant biomaterials. *Artificial Cells, Nanomedicine and Biotechnology*. 46 (1), 1–18.

Chen, Q., Zhu, C. & Thouas, G. A. (2012) Progress and challenges in biomaterials used for bone tissue engineering: bioactive glasses and elastomeric composites. *Progress in Biomaterials*. 1 (1), 1–22.

Chen, Z., Li, Z., Li, J., Liu, Chengbo, Lao, C., Fu, Y., Liu, Changyong, Li, Y., Wang, P. & He, Y. (2019) 3D printing of ceramics: A review. *Journal of the European Ceramic Society*. 39 (4), 661–687.

Chiulan, I., Frone, A. N., Brandabur, C. & Panaitescu, D. M. (2018) Recent advances in 3D printing of aliphatic polyesters. *Bioengineering*. 5 (1), 1–18.

Cho, Yong Sang, Hong, M. W., Kim, S. Y., Lee, S. J., Lee, J. H., Kim, Y. Y. & Cho, Young Sam (2014) Fabrication of dual-pore scaffolds using SLUP (salt leaching using powder) and WNM (wire-network molding) techniques. *Materials Science and Engineering C*. 45, 546–555.

Cho, Yong Sang, Hong, M. W., Jeong, H. J., Lee, S. J., Kim, Y. Y. & Cho, Young Sam (2017) The fabrication of well-interconnected polycaprolactone/hydroxyapatite composite scaffolds, enhancing the exposure of hydroxyapatite using the wire-network molding technique. *Journal of Biomedical Materials Research - Part B Applied Biomaterials*. 105 (8), 2315–2325.

Chocholata, P., Kulda, V. & Babuska, V. (2019) Fabrication of scaffolds for bone-tissue regeneration. *Materials*. 12 (4), 1–25.

Choi, J. Y., Lee, B. H., Song, K. B., Park, R. W., Kim, I. S., Sohn, K. Y., Jo, J. S. & Ryoo, H. M. (1996) Expression patterns of bone-related proteins during osteoblastic differentiation in MC3T3-E1 cells. *Journal of Cellular Biochemistry*. 61 (4), 609–618.

Choi, U. & Lee, C. R. (2019) Antimicrobial agents that inhibit the outer membrane assembly machines of Gram-negative bacteria. *Journal of Microbiology and Biotechnology*. 29 (1), 1–10.

Chokshi, A., Sifri, Z., Cennimo, D. & Horng, H. (2019) Global contributors to antibiotic resistance. *Journal of Global Infectious Diseases*. 11 (1), 36–42.

Chung, M. G., Kim, H. W., Kim, B. R., Kim, Y. B. & Rhee, Y. H. (2012) Biocompatibility and antimicrobial activity of poly(3-hydroxyoctanoate) grafted with vinylimidazole. *International Journal of Biological Macromolecules*. 50 (2), 310–316.

Chung, Y. C. & Chen, C. Y. (2008) Antibacterial characteristics and activity of acid-soluble chitosan. *Bioresource Technology*. 99 (8), 2806–2814.

Ciesielski, S., Mozejko, J. & Pisutpaisal, N. (2015) Plant oils as promising substrates for polyhydroxyalkanoates production. *Journal of Cleaner Production*. 106, 408–421.

Clarke, B. (2008) Normal bone anatomy and physiology. *Clinical journal of the American Society of Nephrology*. 3, 131–139.

Coates, A. R., Halls, G. & Hu, Y. (2011) Novel classes of antibiotics or more of the same? *British Journal of Pharmacology*. 163 (1), 184–194.

Collery, P. (2018) Strategies for the development of selenium-based anticancer drugs. *Journal of Trace Elements in Medicine and Biology*. 50 (November 2017), 498–507.

Crétois, R., Chenal, J. M., Sheibat-Othman, N., Monnier, A., Martin, C., Astruz, O., Kurusu, R. & Demarquette, N. R. (2016) Physical explanations about the improvement of PolyHydroxyButyrate ductility: Hidden effect of plasticizer on physical ageing. *Polymer*. 102, 176–182.

Croce, M., Conti, S., Maake, C. & Patzke, G. R. (2016) Synthesis and screening of N-acyl thiolated chitosans for antibacterial applications. *Carbohydrate Polymers*. 151, 1184–1192.

da Cunha, B. R., Fonseca, L. P. & Calado, C. R. C. (2019) Antibiotic discovery: Where have we come from, where do we go? *Antibiotics*. 8 (45), 1–21.

Curley, J. M., Hazer, B., Lenz, R. W. & Fuller, R. C. (1996) Production of poly(3-hydroxyalkanoates) containing aromatic substituents by *Pseudomonas oleovorans. Macromolecules*. 29 (5), 1762–1766.

Cushnie, T. P. T., Cushnie, B. & Lamb, A. J. (2014) Alkaloids: An overview of their antibacterial, antibiotic-enhancing and antivirulence activities. *International Journal of Antimicrobial Agents*. 44 (5), 377–386.

Czaja, W. K., Young, D. J., Kawecki, M. & Brown, R. M. (2007) The future prospects of microbial cellulose in biomedical applications. *Biomacromolecules*. 8 (1), 1–12.

Czekanska, E. M., Stoddart, M. J., Richards, R. G. & Hayes, J. S. (2012) In search of an osteoblast cell model for *in vitro* research. *European Cells and Materials*. 24, 1–17.

Dang, H. P., Shabab, T., Shafiee, A., Peiffer, Q. C., Fox, K., Tran, N., Dargaville, T. R., Hutmacher, Di. W. & Tran, P. A. (2019) 3D printed dual macro-, microscale porous network as a tissue engineering scaffold with drug delivering function. *Biofabrication*. 11 (3).

Darouiche, R. O. (2003) Antimicrobial approaches for preventing infections associated with surgical implants. *Clinical infectious diseases : an official publication of the Infectious Diseases Society of America*. 36 (10), 1284–1289.

Darouiche, R. O. (2001) Device-Associated Infections: A Macroproblem that Starts with Microadherence. *Clinical Infectious Diseases*. 33 (9), 1567–1572.

Darouiche, R. O. (2004) Treatment of Infections Associated with Surgical Implants. *New England Journal of Medicine*. 350 (14), 1422–1429.

Degli Esposti, M., Chiellini, F., Bondioli, F., Morselli, D. & Fabbri, P. (2019) Highly porous PHB-based bioactive scaffolds for bone tissue engineering by *in situ* synthesis of hydroxyapatite. *Materials Science and Engineering C*. 100, 286–296.

Deng, C. M., He, L. Z., Zhao, M., Yang, D. & Liu, Y. (2007) Biological properties of the chitosan-gelatin sponge wound dressing. *Carbohydrate Polymers*. 69 (3), 583–589.

Díez-Pascual, A. M. & Díez-Vicente, A. L. (2016) Electrospun fibers of chitosan-grafted polycaprolactone/poly(3-hydroxybutyrate-co-3-hydroxyhexanoate) blends. *Journal of Materials Chemistry B*. 4 (4), 600–612.

Díez-Pascual, A. M. & Díez-Vicente, A. L. (2014) ZnO-reinforced poly(3-hydroxybutyrate-co-3-hydroxyvalerate) bionanocomposites with antimicrobial function for food packaging. *ACS Applied Materials and Interfaces*. 6 (12), 9822–9834.

Dinjaski, N., Fernández-Gutiérrez, M., Selvam, S., Parra-Ruiz, F. J., Lehman, S. M., San Román, J., García, E., García, J. L., García, A. J. & Prieto, M. A. (2014) PHACOS, a functionalized bacterial polyester with bactericidal activity against methicillin-resistant *Staphylococcus aureus*. *Biomaterials*. 35 (1), 14–24.

Djagny, K. B., Wang, Z. & Xu, S. (2001) Gelatin: A Valuable Protein for Food and Pharmaceutical Industries: Review. *Critical Reviews in Food Science and Nutrition*. 41 (6), 481–492.

Domingos, M., Chiellini, F., Gloria, A., Ambrosio, L., Bartolo, P. & Chiellini, E. (2012) Effect of process parameters on the morphological and mechanical properties of 3D Bioextruded poly(1-caprolactone) scaffolds. *Rapid Prototyping Journal*. 18 (1), 56–67.

Domingos, M., Chiellini, F., Cometa, S., De Giglio, E., Grillo-Fernandes, E., Bártolo, P. & Chiellini, E. (2010) Evaluation of *in vitro* degradation of pcl scaffolds fabricated via bioextrusion. part 1: Influence of the degradation environment. *Virtual and Physical Prototyping*. 5 (2), 65–73.

Dong, Y., Liao, S., Ngiam, M., Chan, C. K. & Ramakrishna, S. (2009) Degradation behaviors of electrospun resorbable polyester nanofibers. *Tissue Engineering - Part B: Reviews*. 15 (3), 333–351.

Dorati, R., DeTrizio, A., Modena, T., Conti, B., Benazzo, F., Gastaldi, G. & Genta, I. (2017) Biodegradable scaffolds for bone regeneration combined with drug-delivery systems in osteomyelitis therapy. *Pharmaceuticals*. 10 (96), 1–21.

Dragostin, O. M., Samal, S. K., Dash, M., Lupascu, F., Pânzariu, A., Tuchilus, C., Ghetu, N., Danciu, M., Dubruel, P., Pieptu, D., Vasile, C., Tatia, R. & Profire, L. (2016) New antimicrobial chitosan derivatives for wound dressing applications. *Carbohydrate Polymers*. 141, 28–40.

Drake, E. N. (2006) Cancer chemoprevention: Selenium as a prooxidant, not an antioxidant. *Medical Hypotheses*. 67 (2), 318–322.

Du, T., Chen, Z., Li, H., Tang, X., Li, Z., Guan, J., Liu, C., Du, Z. & Wu, J. (2016) Modification of collagen – chitosan matrix by the natural crosslinker alginate dialdehyde. *International Journal of Biological Macromolecules*. 82, 580–588.

Duan, B., Cheung, W. L. & Wang, M. (2011) Optimized fabrication of Ca-P/PHBV nanocomposite scaffolds via selective laser sintering for bone tissue engineering. *Biofabrication*. 3 (1).

Dufresne, A. & Vincendon, M. (2000) Poly(3-hydroxybutyrate) and poly(3-hydroxyoctanoate) blends: Morphology and mechanical behavior. *Macromolecules*. 33 (8), 2998–3008.

Eiff, C. Von, Jansen, B., Kohnen, W. & Becker, K. (2005) *Infections Associated with Medical Devices Pathogenesis , Management and Prophylaxis*. 65 (2), 179–214.

Einhorn, T. A. & Gerstenfeld, L. C. (2015) Fracture healing: Mechanisms and interventions. *Nature Reviews Rheumatology*. 11 (1), 45–54.

El-Hadi, A., Schnabel, R., Straube, E., Müller, G. & Henning, S. (2002) Correlation between degree of crystallinity, morphology, glass temperature, mechanical properties and biodegradation of poly (3-hydroxyalkanoate) PHAs and their blends. *Polymer Testing*. 21 (6), 665–674.

El-Rashidy, A. A., Roether, J. A., Harhaus, L., Kneser, U. & Boccaccini, A. R. (2017) Regenerating bone with bioactive glass scaffolds: A review of *in vivo* studies in bone defect models. *Acta Biomaterialia*. 62, 1–28.

Ellwanger, J. H., Franke, S. I. R., Bordin, D. L., Prá, D. & Henriques, J. A. P. (2016) Biological functions of selenium and its potential influence on Parkinson's disease. *Annals of the Brazilian Academy of Sciences*. 88, 1655–1674.

Elmowafy, E., Abdal-Hay, A., Skouras, A., Tiboni, M., Casettari, L. & Guarino, V. (2019) Polyhydroxyalkanoate (PHA): Applications in drug delivery and tissue engineering. *Expert Review of Medical Devices*. 16 (6), 467–482.

Ergene, C., Yasuhara, K. & Palermo, E. F. (2018) Biomimetic antimicrobial polymers: Recent advances in molecular design. *Polymer Chemistry*. 9 (18), 2407–2427.

Escapa, I.F., Ruiz, M.D.V.M., Lopez, J.L.G. and Jimenez, M.A.P., Consejo Superior de Investigaciones Cientificas (CSIC), 2013. Synthesis of polyhydroxyalkanoates (PHA) with thioester groups in the side chain. U.S. Patent Application 13/825,447.

Escapa, I. F., Morales, V., Martino, V. P., Pollet, E., Avérous, L., García, J. L. & Prieto, M. A. (2011) Disruption of β-oxidation pathway in *Pseudomonas putida* KT2442 to produce new functionalized PHAs with thioester groups. *Applied Microbiology and Biotechnology*. 89 (5), 1583–1598.

Estevam, E. C., Witek, K., Faulstich, L., Nasim, M. J., Latacz, G., Domínguez-Álvarez, E., Kieć-Kononowicz, K., Demasi, M., Handzlik, J. & Jacob, C. (2015) Aspects of a distinct cytotoxicity of selenium salts and organic selenides in living cells with possible implications for drug design. *Molecules*. 20 (8), 13894–13912.

De Eugenio, L. I., Galán, B., Escapa, I. F., Maestro, B., Sanz, J. M., García, J. L. & Prieto, M. A. (2010) The PhaD regulator controls the simultaneous expression of the pha genes involved in polyhydroxyalkanoate metabolism and turnover in *Pseudomonas putida* KT2442. *Environmental Microbiology*. 12 (6), 1591–1603.

Ewering, C., Lütke-Eversloh, T., Luftmann, H. & Steinbüchel, A. (2002) Identification of novel sulfur-containing bacterial polyesters: Biosynthesis of poly(3-hydroxy-S-proply-ω-thioalkanoates) containing thioether linkages in the side chains. *Microbiology*. 148 (5), 1397–1406.

Fair, R. J. & Tor, Y. (2014) Perspectives in Medicinal Chemistry Antibiotics and Bacterial Resistance in the 21st Century. *Perspectives in Medicinal Chemistry*. 25–64.

Fakoor-Yazdan-Abad, M., Rajabzadeh, G., Taghvaei Ganjali, S. & Tavakoli, R. (2016) Preparing Allicin Nanocapsules and Determining the Factors Controlling Their Particle Size through Artificial Intelligence. *International Journal of Food Engineering*. 12 (3), 257–264.

Fan, L., Li, M., Gong, Y., Peng, K. & Xie, W. (2012) Preparation and Characterization of Alginate / Hydroxypropyl Chitosan Blend Fibers. *Journal of Applied Polymer Science*. 125, 829–835.

Fan, L., Du, Y., Zhang, B. & Yang, J. (2006) Preparation and properties of alginate / carboxymethyl chitosan blend fibers. *Carbohydrate Polymers*. 65, 447–452.

Fan, L., Yu, L., Xu, Y., Yi, C., Cai, J., Li, M. & Huang, J. (2010) The Novel Alginate / N- Succinyl-Chitosan Antibacterial Blend Fibers. *Journal of Applied Polymer Science*. 116, 2151–2156.

Favaro, L., Basaglia, M. & Casella, S. (2019) Improving polyhydroxyalkanoate production from inexpensive carbon sources by genetic approaches: a review. *Biofuels, Bioproducts and Biorefining*. 13 (1), 208–227.

Ferlita, R. R., Phipps, D., Safarik, J. & Yeh, D. H. (2008) Cryo-snap: A simple modified freeze-fracture method for SEM imaging of membrane cross-sections. *Environmental Progress*. 27 (2), 204–209.

Fernandes, A. P. & Gandin, V. (2015) Selenium compounds as therapeutic agents in cancer. *Biochimica et Biophysica Acta - General Subjects*. 1850 (8), 1642–1660.

Fernandez de Grado, G., Keller, L., Idoux-Gillet, Y., Wagner, Q., Musset, A. M., Benkirane-Jessel, N., Bornert, F. & Offner, D. (2018) Bone substitutes: a review of their characteristics, clinical use, and perspectives for large bone defects management. *Journal of Tissue Engineering*. 91–18.

Ferreira, J., Gloria, A., Cometa, S., Coelho, J. F. J. & Domingos, M. (2017) Effect of *in vitro* enzymatic degradation on 3D printed poly(ε-caprolactone) scaffolds: Morphological, chemical and mechanical properties. *Journal of Applied Biomaterials and Functional Materials*. 15 (3), e185–e195.

Ferri, J. M., Jordá, J., Montanes, N., Fenollar, O. & Balart, R. (2018) Manufacturing and characterization of poly(lactic acid) composites with hydroxyapatite. *Journal of Thermoplastic Composite Materials*. 31 (7), 865–881.

Figueroa-Lopez, K. J., Vicente, A. A., Reis, M. A. M., Torres-Giner, S. & Lagaron, J. M. (2019) Antimicrobial and antioxidant performance of various essential oils and natural extracts and their incorporation into biowaste derived poly(3-hydroxybutyrate-co-3-hydroxyvalerate) layers made from electrospun ultrathin fibers. *Nanomaterials*. 9 (2), 1–22.

Flemming, H. (2011) Colloids and Surfaces B : Biointerfaces The perfect slime. *Colloids and Surfaces B: Biointerfaces*. 86 (2), 251–259.

Foster, L. J. R. & Tighe, B. J. (2005) Centrifugally spun polyhydroxybutyrate fibres: Accelerated hydrolytic degradation studies. *Polymer Degradation and Stability*. 87 (1), 1–10.

Frasnelli, M., Cristofaro, F., Sglavo, V. M., Dirè, S., Callone, E., Ceccato, R., Bruni, G., Cornaglia, A. I. & Visai, L. (2017) Synthesis and characterization of strontium-substituted hydroxyapatite nanoparticles for bone regeneration. *Materials Science and Engineering C*. 71, 653–662.

Freier, T., Kunze, C., Nischan, C., Kramer, S., Sternberg, K., Sa, M., Hopt, U. T. & Schmitz, K.-P. (2002) *In vitro* and *in vivo* degradation studies for development of a biodegradable patch based on poly(3-hydroxybutyrate). *Biomaterials*. 23, 2649–2657.

Fu, G., Zeng, L., Jiang, J., Xia, Z., Jing, B. & Zhang, X. (2012) Preparation and Characterization of Nanocomposites based on Poly(ε-caprolactone) and the Surface Grafted Nanohydroxyapatite with the Comb-shaped Poly(ε-caprolactone) Brushes. *Polymers and Polymer Composites*. 20 (5), 463–470.

Furuya, E. Y. & Lowy, F. D. (2006) Antimicrobial-resistant bacteria in the community setting. *Nature Reviews Microbiology*. 4 (1), 36–45.

Gandin, V., Khalkar, P., Braude, J. & Fernandes, A. P. (2018) Organic selenium compounds as potential chemotherapeutic agents for improved cancer treatment. *Free Radical Biology and Medicine*. 127, 80–97.

Gao, C., Peng, S., Feng, P. & Shuai, C. (2017) Bone biomaterials and interactions with stem cells. *Bone Research*. 5, 1–33.

García-Gareta, E., Coathup, M. J. & Blunn, G. W. (2015) Osteoinduction of bone grafting materials for bone repair and regeneration. *Bone*. 81, 112–121.

Ge, M., Ge, K., Gao, F., Yan, W., Liu, H., Xue, L., Jin, Y., Ma, H. & Zhang, J. (2018) Biomimetic mineralized strontium-doped hydroxyapatite on porous poly(L-lactic acid) scaffolds for bone defect repair. *International Journal of Nanomedicine*. 13, 1707–1721.

Ghai, I. & Ghai, S. (2018) Understanding antibiotic resistance via outer membrane permeability. *Infection and Drug Resistance*. 11, 523–530.

Ghasemi-Mobarakeh, L., Kolahreez, D., Ramakrishna, S. & Williams, D. (2019) Key terminology in biomaterials and biocompatibility. *Current Opinion in Biomedical Engineering*. 10, 45–50.

Ghassemi, T., Shahroodi, A., Ebrahimzadeh, M. H., Mousavian, A., Movaffagh, J. & Moradi, A. (2018) Current Concepts in Scaffolding for Bone Tissue Engineering. *The archives of bone and joint surgery*. 6 (2), 90–99.

Ghiasi, M. S., Chen, J., Vaziri, A., Rodriguez, E. K. & Nazarian, A. (2017) Bone fracture healing in mechanobiological modeling: A review of principles and methods. *Bone Reports*. 687–100.

Gil-Castell, O., Badia, J. D., Bou, J. & Ribes-Greus, A. (2019) Performance of polyester-based electrospun scaffolds under *in vitro* hydrolytic conditions: From short-term to long-term applications. *Nanomaterials*. 9 (786), 1–19.

Gleadall, A., Visscher, D., Yang, J., Thomas, D. & Segal, J. (2018) Review of additive manufactured tissue engineering scaffolds: relationship between geometry and performance. *Burns & Trauma*. 6 (1), 1–16.

Glenske, K., Donkiewicz, P., Köwitsch, A., Milosevic-Oljaca, N., Rider, P., Rofall, S., Franke, J., Jung, O., Smeets, R., Schnettler, R., Wenisch, S. & Barbeck, M. (2018) Applications of metals for bone regeneration. *International Journal of Molecular Sciences*. 19 (3), 1–43.

Gloria, A., Russo, T., De Santis, R. & Ambrosio, L. (2009) 3D fiber deposition technique to make multifunctional and tailor-made scaffolds for tissue engineering applications. *Journal of Applied Biomaterials and Biomechanics*. 7 (3), 141–152.

Gold, K., Slay, B., Knackstedt, M. & Gaharwar, A. K. (2018) Antimicrobial Activity of Metal and Metal-Oxide Based Nanoparticles. *Advanced Therapeutics*. 1 (3), 1700033.

Golub, E. & Boesze-Battaglia, K. (2007) The role of alkaline phosphatase in mineralization. *Current Opinion in Orthopaedics*. 18 (5), 444–448.

Gong, S. H., Lee, H., Pae, A., Noh, K., Shin, Y. M., Lee, J. H. & Woo, Y. H. (2013) Gene expression of MC3T3-E1 osteoblastic cells on titanium and zirconia surface. *Journal of Advanced Prosthodontics*. 5 (4), 416–422.

González-Gil, A. B., Lamo-Espinosa, J. M., Muiños-López, E., Ripalda-Cemboráin, P., Abizanda, G., Valdés-Fernández, J., López-Martínez, T., Flandes-Iparraguirre, M., Andreu, I., Elizalde, M. R., Stuckensen, K., Groll, J., De-Juan-Pardo, E. M., Prósper, F. & Granero-Moltó, F. (2019) Periosteum-derived mesenchymal progenitor cells in engineered implants promote fracture healing in a critical-size defect rat model. *Journal of Tissue Engineering and Regenerative Medicine*. 13 (5), 742–752.

Gonzalez-Gil, G., Lens, P. N. L. & Saikaly, P. E. (2016) Selenite reduction by anaerobic microbial aggregates: Microbial community structure, and proteins associated to the produced selenium spheres. *Frontiers in Microbiology*. 7 (571), 1–14.

Gonzalez-Ausejo, J. *et al.* (2018) A comparative study of three-dimensional printing directions: The degradation and toxicological profile of a PLA/PHA blend. *Polymer Degradation and Stability*. 152 (June), 191–207.

Goonasekera, C. S., Jack, K. S., Cooper-White, J. J. & Grøndahl, L. (2016) Dispersion of hydroxyapatite nanoparticles in solution and in polycaprolactone composite scaffolds. *Journal of Materials Chemistry B*. 4 (3), 409–421.

Goonoo, N., Bhaw-Luximon, A., Passanha, P., Esteves, S. R. & Jhurry, D. (2017) Third generation poly(hydroxyacid) composite scaffolds for tissue engineering. *Journal of Biomedical Materials Research - Part B Applied Biomaterials*. 105 (6), 1667–1684.

Gopi, S., Kontopoulou, M., Ramsay, B. A. & Ramsay, J. A. (2018) Manipulating the structure of medium-chain-length polyhydroxyalkanoate (MCL-PHA) to enhance thermal properties and crystallization kinetics. *International Journal of Biological Macromolecules*. 119, 1248–1255.

Gorrini, C., Harris, I. S. & Mak, T. W. (2013) Modulation of oxidative stress as an anticancer strategy. *Nature Reviews Drug Discovery*. 12 (12), 931–947.

Goss, C. H. *et al.* (2018) Gallium disrupts bacterial iron metabolism and has therapeutic effects in mice and humans with lung infections HHS Public Access One Sentence Summary. *Sci Transl Med*. 10 (460).

Gothard, D., Cheung, K., Kanczler, J. M., Wilson, D. I. & Oreffo, R. O. C. (2015) Regionally-derived cell populations and skeletal stem cells from human foetal femora exhibit specific osteochondral and multi-lineage differentiation capacity *in vitro* and *ex vivo*. *Stem Cell Research and Therapy*. 6 (1), 1–17.

Grass, G., Rensing, C. & Solioz, M. (2011) Metallic copper as an antimicrobial surface. *Applied and Environmental Microbiology*. 77 (5), 1541–1547.

Gregory, C. A., Gunn, W. G., Peister, A. & Prockop, D. J. (2004) An Alizarin red-based assay of mineralization by adherent cells in culture: Comparison with cetylpyridinium chloride extraction. *Analytical Biochemistry*. 329 (1), 77–84.

Grigore, M. E., Grigorescu, R. M., Iancu, L., Ion, R. M., Zaharia, C. & Andrei, E. R. (2019) Methods of synthesis, properties and biomedical applications of polyhydroxyalkanoates: a review. *Journal of Biomaterials Science, Polymer Edition*. 30 (9), 695–712.

Gritsch, L., Maqbool, M., Mourin, V., Ciraldo, F. E., Cresswell, M., Jackson, P. R., Lovell, C. & Boccaccini, A. R. (2019) Chitosan/hydroxyapatite composite bone tissue engineering scaffolds with dual and decoupled therapeutic ion delivery: copper and strontium. *Journal of Materials Chemistry B*. 7 (40), 6109–6124.

Gritsch, L., Lovell, C., Goldmann, W. H. & Boccaccini, A. R. (2018) Fabrication and characterization of copper(II)-chitosan complexes as antibiotic-free antibacterial biomaterial. *Carbohydrate Polymers*. 179, 370–378.

Grøndahl, L., Jack, K. & Goonasekera, C. S. (2017) 'Composite materials for bone repair', in *Biomedical Composites*. Second Edi Woodhead Publishing Limited. pp. 101–126.

Guo-Qiang, C., Jun, X., Qiong, W., Zengming, Z. & Kwok-Ping, H. (2001) Synthesis of copolyesters consisting of medium-chain-length β-hydroxyalkanoates by *Pseudomonas stutzeri* 1317. *Reactive and Functional Polymers*. 48 (1–3), 107–112.

Guo, S. Z., Gosselin, F., Guerin, N., Lanouette, A. M., Heuzey, M. C. & Therriault, D. (2013) Solvent-cast three-dimensional printing of multifunctional microsystems. *Small*. 9 (24), 4118–4122.

Guo, W., Song, C., Kong, M., Geng, W., Wang, Y. & Wang, S. (2011) Simultaneous production and characterization of medium-chain-length polyhydroxyalkanoates and alginate oligosaccharides by *Pseudomonas mendocina* NK-01. *Applied Microbial and Cell Physiology*. 92, 791–801.

Gupta, A., Low, W. L., Radecka, I., Britland, S. T., Mohd Amin, M. C. I. & Martin, C. (2016) Characterisation and *in vitro* antimicrobial activity of biosynthetic silver-loaded bacterial cellulose hydrogels. *Journal of Microencapsulation*. 33 (8), 725–734.

Gurikov, P. & Smirnova, I. (2018) Non-Conventional Methods for Gelation of Alginate. *Gels*. 4 (1), 14.

Haaber, J., Leisner, J. J., Cohn, M. T., Catalan-Moreno, A., Nielsen, J. B., Westh, H., Penadés, J. R. & Ingmer, H. (2016) Bacterial viruses enable their host to acquire antibiotic resistance genes from neighbouring cells. *Nature Communications*. 7 (1), 1–8.

Hafdani, F. N. & Sadeghinia, N. (2011) A Review on Application of Chitosan as a Natural Antimicrobial. *World Academic Science, Engineering and Technology*. 5 (2), 225–229.

Hajiali, F., Tajbakhsh, S. & Shojaei, A. (2018) Fabrication and Properties of Polycaprolactone Composites Containing Calcium Phosphate-Based Ceramics and Bioactive Glasses in Bone Tissue Engineering: A Review. *Polymer Reviews*. 58 (1), 164–207.

Hajiali, H., Karbasi, S., Hosseinalipour, M. & Rezaie, H. R. (2010) Preparation of a novel biodegradable nanocomposite scaffold based on poly (3-hydroxybutyrate)/bioglass nanoparticles for bone tissue engineering. *Journal of Materials Science: Materials in Medicine*. 21 (7), 2125–2132.

Hamano, Y. (2011) Occurrence, biosynthesis, biodegradation, and industrial and medical applications of a naturally occurring ε-poly-L-lysine. *Bioscience, biotechnology, and biochemistry*. 75 (7), 1226–1233.

Hamedi, H., Moradi, S., Tonelli, A. E. & Hudson, S. M. (2019) Preparation and Characterization of Chitosan–Alginate Polyelectrolyte Complexes Loaded with Antibacterial Thyme Oil Nanoemulsions. *Applied Sciences*. 9 (18), 3933.

Hannink, G. & Arts, J. J. C. (2011) Bioresorbability, porosity and mechanical strength of bone substitutes: What is optimal for bone regeneration? *Injury*. 42 (2), S22–S25.

Hasan, A., Byambaa, B., Morshed, M., Cheikh, M. I., Shakoor, R. A., Mustafy, T. & Marei, H. E. (2018) Advances in osteobiologic materials for bone substitutes. *Journal of Tissue Engineering and Regenerative Medicine*. 12 (6), 1448–1468.

Haugen, H. J., Lyngstadaas, S. P., Rossi, F. & Perale, G. (2019) Bone grafts: which is the ideal biomaterial? *Journal of Clinical Periodontology*. 46 (S21), 92–102.

Hayati, A. N., Hosseinalipour, S. M., Rezaie, H. R. & Shokrgozar, M. A. (2012) Characterization of poly(3-hydroxybutyrate)/nano-hydroxyapatite composite scaffolds fabricated without the use of organic solvents for bone tissue engineering applications. *Materials Science and Engineering C*. 32 (3), 416–422.

Hazer, B. & Steinbüchel, A. (2007) Increased diversification of polyhydroxyalkanoates by modification reactions for industrial and medical applications. *Applied Microbiology and Biotechnology*. 74 (1), 1–12.

He, L., Dong, G. & Deng, C. (2016) Effects of strontium substitution on the phase transformation and crystal structure of calcium phosphate derived by chemical precipitation. *Ceramics International*. 42 (10), 11918–11923.

He, L., Li, H., Chen, X., Xu, T., Sun, T., Huang, H., Lu, M., Yin, Y., Ge, J., Weng, J., Zhuo, N. & Duan, K. (2019) Selenium-substituted hydroxyapatite particles with regulated microstructures for osteogenic differentiation and anti-tumor effects. *Ceramics International*. 45 (11), 13787–13798.

Heilmann, C., Herrmann, M. & Peters, G. (1999) Basic Aspects of the Pathogenesis of Staphylococcal Polymer-Associated Infections. *Infection*. 27, 7–10.

Herigstad, B., Hamilton, M. & Heersink, J. (2001) How to optimize the drop plate method for enumerating bacteria. *Journal of microbiological methods*. 44 (2), 121–129.

Hyldgaard, M., Mygind, T., Vad, B.S. Stenvang, M., Otzen, D.E. & Meyer, R.L. (2014). The antimicrobial mechanism of action of epsilon-poly-l-lysine. *Applied and environmental microbiology*. 80(24), 7758-7770.

Ho, M. H., Li, S. Y., Ciou, C. Y. & Wu, T. M. (2014) The morphology and degradation behavior of electrospun poly(3- hydroxybutyrate)/Magnetite and poly(3-hydroxybutyrate-co-3-hydroxyvalerate)/ Magnetite composites. *Journal of Applied Polymer Science*. 131 (22).

Ho, S. T. & Hutmacher, D. W. (2006) A comparison of micro CT with other techniques used in the characterization of scaffolds. *Biomaterials*. 27 (8), 1362–1376.

Høiby, N., Bjarnsholt, T., Givskov, M., Molin, S. & Ciofu, O. (2010) Antibiotic resistance of bacterial biofilms. *International Journal of Antimicrobial Agents*. 35 (4), 322–332.

Holben, D. H. & Smith, A. M. (1999) The diverse role of selenium within selenoproteins: A review. *Journal of the American Dietetic Association*. 99 (7), 836–843.

Hollister, S. J. (2005) Porous scaffold design for tissue engineering. *Nature Materials*. 4 (7), 518–524.

Hoppe, A., Mouriño, V. & Boccaccini, A. R. (2013) Therapeutic inorganic ions in bioactive glasses to enhance bone formation and beyond. *Biomaterials Science*. 1 (3), 254–256.

Hoque, M. E., San, W. Y., Wei, F., Li, S., Huang, M. H., Vert, M. & Hutmacher, D. W. (2009) Processing of polycaprolactone and polycaprolactone-based copolymers into 3D scaffolds, and their cellular responses. *Tissue Engineering - Part A*. 15 (10), 3013–3024.

Hosnedlova, B., Kepinska, M., Skalickova, S., Fernandez, C., Ruttkay-Nedecky, B., Peng, Q., Baron, M., Melcova, M., Opatrilova, R., Zidkova, J., Bjørklund, G., Sochor, J. & Kizek, R. (2018) Nano-selenium and its nanomedicine applications: A critical review. *International Journal of Nanomedicine*. 13, 2107–2128.

Hosseini, S. M., Hosseini, H., Mohammadifar, M. A., Mortazavian, A. M., Mohammadi, A., Khosravi-Darani, K., Shojaee-Aliabadi, S., Dehghan, S. & Khaksar, R. (2013) Incorporation of essential oil in alginate microparticles by multiple emulsion/ionic gelation process. *International Journal of Biological Macromolecules*. 62, 582–588.

Hu, S., Jou, C. & Yang, M. (2003) Antibacterial and Biodegradable Properties of Polyhydroxyalkanoates Grafted With Chitosan and Chitooligosaccharides via Ozone Treatment. *Journal of Applied Polymer Science*. 88, 2797–2803.

Hu, Y. J., Wei, X., Zhao, W., Liu, Y. S. & Chen, G. Q. (2009) Biocompatibility of poly(3-hydroxybutyrate-co-3-hydroxyvalerate-co-3-hydroxyhexanoate) with bone marrow mesenchymal stem cells. *Acta Biomaterialia*. 5 (4), 1115–1125.

Hua, J., Li, Z., Xia, W., Yang, N., Gong, J., Zhang, J. & Qiao, C. (2016) Preparation and properties of EDC/NHS mediated crosslinking poly (gamma-glutamic acid)/epsilon-polylysine hydrogels. *Materials Science and Engineering C*. 61, 879–892.

Huang, D., Zuo, Y., Zou, Q., Zhang, L., Li, J., Cheng, L., Shen, J. & Li, Y. (2011) Antibacterial chitosan coating on nano-hydroxyapatite/polyamide66 porous bone scaffold for drug delivery. *Journal of Biomaterials Science, Polymer Edition*. 22 (7), 931–944.

Huang, K. S., Yang, C. H., Huang, S. L., Chen, C. Y., Lu, Y. Y. & Lin, Y. S. (2016a) Recent Advances in Antimicrobial Polymers: A Mini-Review. *International Journal of Molecular Sciences*. 17 (9), 1578.

Huang, T., Holden, J. A., Heath, D. E., O'Brien-Simpson, N. M. & O'Connor, A. J. (2019) Engineering highly effective antimicrobial selenium nanoparticles through control of particle size. *Nanoscale*. 11 (31), 14937–14951.

Huang, X., Chen, X., Chen, Q., Yu, Q., Sun, D. & Liu, J. (2016b) Investigation of functional selenium nanoparticles as potent antimicrobial agents against superbugs. *Acta Biomaterialia*. 30, 397–407.

Huawei, Z. (2009) Selenium as an essential micronutrient: Roles in cell cycle and apoptosis. *Molecules*. 14 (3), 1263–1278.

Hui, F. & Debiemme-Chouvy, C. (2013) Antimicrobial N -Halamine Polymers and Coatings: A Review of Their Synthesis, Characterization, and Applications. *Biomacromolecules*. 14 (3), 585–601.

Huijberts, G. N. M., Eggink, G., De Waard, P., Huisman, G. W. & Witholt2, B. (1992) *Pseudomonas putida* KT2442 Cultivated on Glucose Accumulates Poly(3-Hydroxyalkanoates) Consisting of Saturated and Unsaturated Monomers. *Applied and Environmental Microbiology*. 58 (2), 536–544.

Hwang, P. W. & Horton, J. A. (2019) Variable osteogenic performance of MC3T3-E1 subclones impacts their utility as models of osteoblast biology. *Scientific Reports*. 9 (1), 1–9.

Hyldgaard, M., Mygind, T. & Meyer, R. L. (2012) Essential oils in food preservation: Mode of action, synergies, and interactions with food matrix components. *Frontiers in Microbiology*. 3 (12), 1–24.

Iaquinta, M. R., Mazzoni, E., Manfrini, M., D'Agostino, A., Trevisiol, L., Nocini, R., Trombelli, L., Barbanti-Brodano, G., Martini, F. & Tognon, M. (2019) Innovative biomaterials for bone regrowth. *International Journal of Molecular Sciences*. 20 (3), 1–17.

Iron, R., Mehdikhani, M., Naghashzargar, E., Karbasi, S. & Semnani, D. (2019) Effects of nano-bioactive glass on structural, mechanical and bioactivity properties of Poly (3-hydroxybutyrate) electrospun scaffold for bone tissue engineering applications. *Materials Technology*. 34 (9), 540–548.

Ishii-Hyakutake, M., Mizuno, S. & Tsuge, T. (2018) Biosynthesis and characteristics of aromatic polyhydroxyalkanoates. *Polymers*. 10 (1267), 1–24.

Jakus, A. E., Geisendorfer, N. R., Lewis, P. L. & Shah, R. N. (2018) 3D-printing porosity: A new approach to creating elevated porosity materials and structures. *Acta Biomaterialia*. 72, 94–109.

Jakus, A. E., Rutz, A. L., Jordan, S. W., Kannan, A., Mitchell, S. M., Yun, C., Koube, K. D., Yoo, S. C., Whiteley, H. E., Richter, C. P., Galiano, R. D., Hsu, W. K., Stock, S. R., Hsu, E. L. & Shah, R. N. (2016) Hyperelastic 'bone': A highly versatile, growth factor-free, osteoregenerative, scalable, and surgically friendly biomaterial. *Science Translational Medicine*. 8 (358), 1–16.

Jammalamadaka, U. & Tappa, K. (2018) Recent advances in biomaterials for 3D printing and tissue engineering. *Journal of Functional Biomaterials*. 9 (22), 1–14.

Jeong, J., Kim, J. H., Shim, J. H., Hwang, N. S. & Heo, C. Y. (2019) Bioactive calcium phosphate materials and applications in bone regeneration. *Biomaterials Research*. 23 (1), 1–11.

Ji, K., Wang, Y., Wei, Q., Zhang, K., Jiang, A., Rao, Y. & Cai, X. (2018) Application of 3D printing technology in bone tissue engineering. *Bio-Design and Manufacturing*. 1 (3), 203–210.

Jiang, Q., Xu, J., Li, T., Qiao, C. & Li, Y. (2014) Synthesis and Antibacterial Activities of Quaternary Ammonium Salt of Gelatin. *Journal of Macromolecular Science, Part B: Physics*. 53 (1), 133–141.

Jiang, X., Ramsay, J. A. & Ramsay, B. A. (2006) Acetone extraction of mcl-PHA from *Pseudomonas putida* KT2440. *Journal of Microbiological Methods*. 67 (2), 212–219.

Jiang, X., Sun, Z., Marchessault, R. H., Ramsay, J. A. & Ramsay, B. A. (2012) Biosynthesis and properties of medium-chain-length polyhydroxyalkanoates with enriched content of the dominant monomer. *Biomacromolecules*. 13 (9), 2926–2932.

Jiménez, M., Abradelo, C., San Román, J. & Rojo, L. (2019) Bibliographic review on the state of the art of strontium and zinc based regenerative therapies. Recent developments and clinical applications. *Journal of Materials Chemistry B*. 7 (12), 1974–1985.

Johnson, C. T. & García, A. J. (2015) Scaffold-based Anti-infection Strategies in Bone Repair. *Annals of Biomedical Engineering*. 43 (3), 515–528.

Jones, C. B. & Mayo, K. A. (2005) Nonunion Treatment. *Journal of Orthopaedic Trauma*. 19 (Supplement), S11–S13.

Jones, J. R. (2015) Review of bioactive glass: From Hench to hybrids. *Acta Biomaterialia*. 23, 4457–4486.

Jun, I., Han, H. S., Edwards, J. R. & Jeon, H. (2018) Electrospun fibrous scaffolds for tissue engineering: Viewpoints on architecture and fabrication. *International Journal of Molecular Sciences*. 19 (3).

Kaflak, A. & Kolodziejski, W. (2011) Complementary information on water and hydroxyl groups in nanocrystalline carbonated hydroxyapatites from TGA, NMR and IR measurements. *Journal of Molecular Structure*. 990 (1–3), 263–270.

Kai, Z., Ying, D. & Guo-Qiang, C. (2003) Effects of surface morphology on the biocompatibility of polyhydroxyalkanoates. *Biochemical Engineering Journal*. 16 (2), 115–123.

Kang, N.-U., Hong, M. W., Kim, Y. Y., Cho, Y.-S. & Lee, S.-J. (2019) Development of a Powder Extruder System for Dual-pore Tissue-engineering Scaffold Fabrication. *Journal of Bionic Engineering*. 16 (4), 686–695.

Kann, Y., Shurgalin, M. & Krishnaswamy, R. K. (2014) FTIR spectroscopy for analysis of crystallinity of poly(3-hydroxybutyrate-co-4 -hydroxybutyrate) polymers and its utilization in evaluation of aging, orientation and composition. *Polymer Testing*. 40, 218–224.

Karageorgiou, V. & Kaplan, D. (2005) Porosity of 3D biomaterial scaffolds and osteogenesis. *Biomaterials*. 26 (27), 5474–5491.

Kashirina, A., Yao, Y., Liu, Y. & Leng, J. (2019) Biopolymers as bone substitutes: A review. *Biomaterials Science*. 7 (10), 3961–3983.

Kaur, G., Kumar, V., Baino, F., Mauro, J. C., Pickrell, G., Evans, I. & Bretcanu, O. (2019a) Mechanical properties of bioactive glasses, ceramics, glass-ceramics and composites: State-of-the-art review and future challenges. *Materials Science and Engineering C*. 104 (109895), 1–14.

Kaur, J. & Shofner, M. L. (2009) Surface area effects in hydroxyapatite/poly(ε-caprolactone) nanocomposites. *Macromolecular Chemistry and Physics*. 210 (8), 677–688.

Kaur, K., Das, S. & Ghosh, S. (2019b) Regulation of Human Osteoblast-to-Osteocyte Differentiation by Direct-Write 3D Microperiodic Hydroxyapatite Scaffolds. *ACS Omega*. 4 (1), 1504–1515.

Kavanagh, N., O'Brien, F. J. & Kerrigan, S. W. (2017) The Molecular Mechanics of Inflammatory Bone and Joint Disease Caused by Microbial Infection. *The Microbiology of Skin, Soft Tissue, Bone and Joint Infections*. 125–140.

Kavoosi, G., Shakiba, A., Ghorbani, M., Dadfar, S. M. M. & Purfard, A. M. (2015) Antioxidant, antibacterial, water binding capacity and mechanical behavior of gelatin-ferula oil film as a wound dressing material. *Galen Medical Journal*. 4 (2), 103–114.

Kawada, J., Lu, T., Steinbu, A. & Marchessault, R. H. (2003) Physical Properties of Microbial Polythioesters : Characterization of Poly (3-mercaptoalkanoates) Synthesized by Engineered Escherichia coli. *Biomacromolecules*. 4, 1698–1702.

Kawada, J. & Marchessault, R. H. (2002) Characterization of Microbial Polythioesters : Physical Properties of Novel Copolymers Synthesized by Ralstonia eutropha. *Biomacromolecules*. 3, 159–166.

Kaygusuz, B. & Özerinç, S. (2019) Improving the ductility of polylactic acid parts produced by fused deposition modeling through polyhydroxyalkanoate additions. *Journal of Applied Polymer Science*. 136 (43), 48154.

Kędziora, A., Speruda, M., Krzyżewska, E., Rybka, J., Łukowiak, A. & Bugla-Płoskońska, G. (2018) Similarities and differences between silver ions and silver in nanoforms as antibacterial agents. *International Journal of Molecular Sciences*. 19 (444), 1–27.

Kehail, A. A., Boominathan, V., Fodor, K., Chalivendra, V., Ferreira, T. & Brigham, C. J. (2017) *In vivo* and *In vitro* Degradation Studies for Poly(3-hydroxybutyrate-co-3-hydroxyhexanoate) Biopolymer. *Journal of Polymers and the Environment*. 25 (2), 296–307.

Kenawy, E., Omer, A. M., Tamer, T. M., Elmeligy, M. A. & Eldin, M. S. M. (2019) Fabrication of biodegradable gelatin/chitosan/cinnamaldehyde crosslinked membranes for antibacterial wound dressing applications. *International Journal of Biological Macromolecules*. 139, 440–448.

Keshavarz, T. & Roy, I. (2010) Polyhydroxyalkanoates: bioplastics with a green agenda. *Current Opinion in Microbiology*. 13 (3), 321–326.

Kessi, J., Ramuz, M., Wehrli, E., Spycher, M. & Bachofen, R. (1999) Reduction of selenite and detoxification of elemental selenium by the phototrophic bacterium *Rhodospirillum rubrum*. *Applied and Environmental Microbiology*. 65 (11), 4734–4740.

Kessler, B. & Witholt, B. (2001) Factors involved in the regulatory network of polyhydroxyalkanoate metabolism. *Journal of Biotechnology*. 86 (2), 97–104.

Khajavi, R., Abbasipour, M., Barzi, M. G., Rashidi, A., Rahimi, M. K. & Mirzababa, H. H. (2014) Eucalyptus essential oil-doped alginate fibers as a potent antibacterial wound dressing. *Advances in Polymer Technology*. 33 (2), 1–7.

Khameneh, B., Iranshahy, M., Soheili, V. & Fazly Bazzaz, B. S. (2019) Review on plant antimicrobials: A mechanistic viewpoint. *Antimicrobial Resistance and Infection Control*. 8 (118), 1–28.

Khanna, S. & Srivastava, A. K. (2005) Recent advances in microbial polyhydroxyalkanoates. *Process Biochemistry*. 40 (2), 607–619.

Khoshraftar, A., Noorani, B., Yazdian, F., Rashedi, H., Vaez Ghaemi, R., Alihemmati, Z. & Shahmoradi, S. (2018) Fabrication and evaluation of nanofibrous polyhydroxybutyrate valerate scaffolds containing hydroxyapatite particles for bone tissue engineering. *International Journal of Polymeric Materials and Polymeric Biomaterials*. 67 (17), 987–995.

Kim, J. W., Shin, K. H., Koh, Y. H., Hah, M. J., Moon, J. & Kim, H. E. (2017) Production of poly(ε-caprolactone)/hydroxyapatite composite scaffolds with a tailored macro/micro-porous structure, high mechanical properties, and excellent bioactivity. *Materials*. 10 (1123), 1–13.

Kim, M. S., Ahn, H. H., Shin, Y. N., Cho, M. H., Khang, G. & Lee, H. B. (2007) An *in vivo* study of the host tissue response to subcutaneous implantation of PLGA- and/or porcine small intestinal submucosa-based scaffolds. *Biomaterials.* 28 (34), 5137–5143.

Kim, Y., Rhee, Y. H., Han, S. H., Heo, G. S. & Kim, J. S. (1996) Poly-3-hydroxyalkanoates produced from *Pseudomonas oleovorans* grown with ω-phenoxyalkanoates. *Macromolecules*. 29 (10), 3432–3435.

Kim, Y. Do, Kim, B. Y. & Rhee, H. Y. (2000) Evaluation of various carbon substrates for the biosynthesis of polyhydroxyalkanoates bearing functional groups by *Pseudomonas putida*. *International Journal of Biological Macromolecules*. 28, 23–29.

Klinkajon, W. & Supaphol, P. (2014) Novel copper (II) alginate hydrogels and their potential for use as anti-bacterial wound dressings. *Biomedical Materials (Bristol)*. 9 (045008), 1–11.

Kniewel, R., Lopez, O. R. & Prieto, M. A. (2017) Biogenesis of Fatty Acids, Lipids and Membranes. *Biogenesis of Fatty Acids, Lipids and Membranes*. 1–25.

Knill, C. J., Kennedy, J. F., Mistry, J., Miraftab, M., Smart, G., Groocock, M. R. & Williams, H. J. (2004) Alginate fibres modified with unhydrolysed and hydrolysed chitosans for wound dressings. *Carbohydrate Polymers*. 55, 65–76.

Kokubo, T. & Takadama, H. (2006) How useful is SBF in predicting *in vivo* bone bioactivity? *Biomaterials*. 27 (15), 2907–2915.

Koller, M. (2018) Biodegradable and biocompatible polyhydroxy-alkanoates (PHA): Auspicious microbial macromolecules for pharmaceutical and therapeutic applications. *Molecules*. 23 (362), 1–20.

Koller, M. & Braunegg, G. (2018) Advanced approaches to produce polyhydroxyalkanoate (PHA) biopolyesters in a sustainable and economic fashion. *The EuroBiotech Journal*. 2 (2), 89–103.

Koller, M. & Braunegg, G. (2015) Potential and prospects of continuous polyhydroxyalkanoate (PHA) production. *Bioengineering*. 2 (2), 94–121.

Kolmas, J., Kuras, M., Oledzka, E. & Sobczak, M. (2015a) A solid-state NMR study of selenium substitution into nanocrystalline hydroxyapatite. *International Journal of Molecular Sciences*. 16 (5), 11452–11464.

Kolmas, J., Oledzka, E., Sobczak, M. & Nałęcz-Jawecki, G. (2014a) Nanocrystalline hydroxyapatite doped with selenium oxyanions: A new material for potential biomedical applications. *Materials Science and Engineering C*. 39 (1), 134–142.

Kolmas, J., Groszyk, E. & Piotrowska, U. (2015b) Nanocrystalline hydroxyapatite enriched in selenite and manganese ions: physicochemical and antibacterial properties. *Nanoscale Research Letters*. 10 (1), 1–9.

Kolmas, J., Groszyk, E. & Kwiatkowska-Rózycka, D. (2014b) Substituted hydroxyapatites with antibacterial properties. *BioMed Research International*. 2014.

Kong, M., Chen, X. G., Xing, K. & Park, H. J. (2010) Antimicrobial properties of chitosan and mode of action: A state of the art review. *International Journal of Food Microbiology*. 144 (1), 51–63.

Köse, S., Aerts Kaya, F., Denkbaş, E. B., Korkusuz, P. & Çetinkaya, F. D. (2016) Evaluation of biocompatibility of random or aligned electrospun polyhydroxybutyrate scaffolds combined with human mesenchymal stem cells. *Turkish Journal of Biology*. 40 (2), 410–419.

Kouhi, M., Prabhakaran, M. P., Shamanian, M., Fathi, M., Morshed, M. & Ramakrishna, S. (2015) Electrospun PHBV nanofibers containing HA and bredigite nanoparticles: Fabrication, characterization and evaluation of mechanical properties and bioactivity. *Composites Science and Technology*. 121, 115–122.

Kourmentza, C., Plácido, J., Venetsaneas, N., Burniol-Figols, A., Varrone, C., Gavala, H. N. & Reis, M. A. M. (2017) Recent Advances and Challenges towards Sustainable Polyhydroxyalkanoate (PHA) Production. *Bioengineering*. 4 (2), 55.

Koutsopoulos, S. (2002) Synthesis and characterization of hydroxyapatite crystals: A review study on the analytical methods. *Journal of Biomedical Materials Research*. 62 (4), 600–612.

Kozicki, M., Kołodziejczyk, M., Szynkowska, M., Pawlaczyk, A., Leśniewska, E., Matusiak, A., Adamus, A. & Karolczak, A. (2016) Hydrogels made from chitosan and silver nitrate. *Carbohydrate Polymers*. 140, 74–87.

Kramer, G. F. & Ames, B. N. (1988) Mechanims of mutagenicity and toxicity of sodium selenite (Na2SeO3) in *Salmonella typhimurium*. *Mutation Research - Fundamental and Molecular Mechanisms of Mutagenesis*. 201 (1), 169–180.

Kumar, P. & Kim, B. S. (2018) Valorization of polyhydroxyalkanoates production process by co-synthesis of value-added products. *Bioresource Technology*. 269, 544–556.

Kumar, T., Singh, M., Purohit, H. J. & Kalia, V. C. (2009) Potential of *Bacillus sp*. to produce polyhydroxybutyrate from biowaste. *Journal of Applied Microbiology*. 106 (6), 2017–2023.

Kundrat, V., Matouskova, P. & Marova, I. (2019) Facile Preparation of Porous Microfiber from Poly-3-(R)-Hydroxybutyrate and Its Application. *Materials*. 13 (1), 86.

Kuroda, K., Caputo, G. A. & DeGrado, W. F. (2009) The Role of Hydrophobicity in the Antimicrobial and Hemolytic Activities of Polymethacrylate Derivatives. *Chemistry*. 15 (5).

Lam, C. X. F., Savalani, M. M., Teoh, S. H. & Hutmacher, D. W. (2008) Dynamics of *in vitro* polymer degradation of polycaprolactone-based scaffolds: Accelerated versus simulated physiological conditions. *Biomedical Materials*. 3 (034108), 1–15.

Langenbach, F. & Handschel, J. (2013) Effects of dexamethasone, ascorbic acid and β-glycerophosphate on the osteogenic differentiation of stem cells *in vitro*. *Stem cell research & therapy*. 4 (5), 117–124.

Larrañaga, A., Fernández, J., Vega, A., Etxeberria, A., Ronchel, C., Adrio, J. L. & Sarasua, J. R. (2014) Crystallization and its effect on the mechanical properties of a medium chain length polyhydroxyalkanoate. *Journal of the Mechanical Behavior of Biomedical Materials*. 39, 87–94.

Lasanianos, N. G., Kanakaris, N. K. & Giannoudis, P. V. (2010) Current management of long bone large segmental defects. *Orthopaedics and Trauma*. 24 (2), 149–163.

Laskus, A., Zgadzaj, A. & Kolmas, J. (2019) Zn2+ and SeO32− co-substituted hydroxyapatite: Physicochemical properties and biological usefulness. *Ceramics International*. 45 (17), 22707-22715.

Lebeaux, D., Ghigo, J.-M. & Beloin, C. (2014) Biofilm-related infections: bridging the gap between clinical management and fundamental aspects of recalcitrance toward antibiotics. *Microbiology and Molecular Biology Reviews*. 78 (3), 510–543.

Lee, C. H., Singla, A. & Lee, Y. (2001) Biomedical applications of collagen. *International Journal of Pharmaceutics*. 22, 11–22.

Lee, G. N. & Na, J. (2013) Future of microbial polyesters. *Microbial Cell Factories*. 12 (54), 1–4.

Lee, K. H. & Jeong, D. (2012) Bimodal actions of selenium essential for antioxidant and toxic pro-oxidant activities: The selenium paradox (Review). *Molecular Medicine Reports*. 5 (2), 299–304.

Lee, K. J. & Mooney, D. J. (2013) Alginate : properties and biomedical applications. *Progress in Polymer Science (Oxford)*. 37 (1), 106–126.

Lee, Y., Kwon, J., Khang, G. & Lee, D. (2012) Reduction of inflammatory responses and enhancement of extracellular matrix formation by vanillin-incorporated poly(lactic-co-glycolic acid) scaffolds. *Tissue Engineering - Part A*. 18 (19–20), 1967–1978.

Lei, B., Guo, B., Rambhia, K. J. & Ma, P. X. (2019) Hybrid polymer biomaterials for bone tissue regeneration. *Frontiers of Medicine*. 13 (2), 189–201.

Lemire, J. A., Harrison, J. J. & Turner, R. J. (2013) Antimicrobial activity of metals: Mechanisms, molecular targets and applications. *Nature Reviews Microbiology*. 11 (6), 371–384.

Lenz, R. W., Kim, Y. B. & Fuller, R. C. (1992) Production of unusual bacterial polyesters by *Pseudomonas oleovorans* through cometabolism. *FEMS Microbiology Letters*. 103 (2–4), 207–214.

Lertsutthiwong, P., Noomun, K., Jongaroonngamsang, N., Rojsitthisak, P. & Nimmannit, U. (2008) Preparation of alginate nanocapsules containing turmeric oil. *Carbohydrate Polymers*. 74 (2), 209–214.

Leteve, M. & Passuti, N. (2018) Current Concepts in Bone Graft Substitutes. *New Journal of Glass and Ceramics*. 08 (03), 39–54.

Levy, S. B. & Bonnie, M. (2004) Antibacterial resistance worldwide: Causes, challenges and responses. *Nature Medicine*. 10 (12S), S122–S129.

Li, J., Li, L., Zhou, J., Zhou, Z., Wu, X.L., Wang, L. and Yao, Q. (2019a). 3D printed dual-functional biomaterial with self-assembly micro-nano surface and enriched nano argentum for antibacterial and bone regeneration. *Applied Materials Today*, 17, 206-215.

Li, J., Wu, Y. & Zhao, L. (2016a) Antibacterial activity and mechanism of chitosan with ultra high molecular weight. *Carbohydrate Polymers*. 148, 200–205.

Li, J., Yun, H., Gong, Y., Zhao, N. & Zhang, X. (2005) Effects of surface modification of poly (3-hydroxybutyrate-co-3- hydroxyhexanoate) (PHBHHx) on physicochemical properties and on interactions with MC3T3-E1 cells. *Journal of Biomedical Materials Research - Part A*. 75 (4), 985–998.

Li, J., Sha, Z., Zhang, W., Tao, F. & Yang, P. (2016b) Preparation and antibacterial properties of gelatin grafted with an epoxy silicone quaternary ammonium salt. *Journal of Biomaterials Science, Polymer Edition*. 7 (10), 1017–1028.

Li, X.-Z. Z., Li, X.-Z. Z., Nikaido, H. & Nikaido, H. (2004) Efflux-mediated drug resistance in bacteria. *Drugs*. 64 (2), 159–204.

Li, Y. (2017) Fabrication and Applications of Metal-Ion-Doped Hydroxyapatite Nanoparticles. *Juniper Online Journal Material Science*. 1 (2), 1–6.

Li, Y., Kim, J. H., Choi, E. H. & Han, I. (2019b) Promotion of osteogenic differentiation by non-thermal biocompatible plasma treated chitosan scaffold. *Scientific Reports*. 9 (1), 1–10.

Li, Z., Yang, J. & Loh, X. J. (2016c) Polyhydroxyalkanoates: Opening doors for a sustainable future. *NPG Asia Materials*. 8 (4), 1–20.

Li, Z. Y., Lam, W. M., Yang, C., Xu, B., Ni, G. X., Abbah, S. A., Cheung, K. M. C., Luk, K. D. K. & Lu, W. W. (2007) Chemical composition, crystal size and lattice structural changes after incorporation of strontium into biomimetic apatite. *Biomaterials*. 28 (7), 1452–1460.

Liakos, I., Rizzello, L., Scurr, D. J., Pompa, P. P., Bayer, I. S. & Athanassiou, A. (2014) All-natural composite wound dressing films of essential oils encapsulated in sodium alginate with antimicrobial properties. *International Journal of Pharmaceutics*. 463 (2), 137–145.

Lim, J., You, M., Li, J. & Li, Z. (2017) Emerging bone tissue engineering via Polyhydroxyalkanoate (PHA)-based scaffolds. *Materials Science and Engineering C*. 79, 917–929.

Lin-Gibson, S., Cooper, J. A., Landis, F. A. & Cicerone, M. T. (2007) Systematic Investigation of Porogen Size and Content on Scaffold Morphometric Parameters and Properties. *Biomacromolecule*. 8, 1511–1518.

Lin, W., Xu, L., Zwingenberger, S., Gibon, E., Goodman, S. B. & Li, G. (2017) Mesenchymal stem cells homing to improve bone healing. *Journal of Orthopaedic Translation*. 9, 19–27.

Liu, H., Slamovich, E. B. & Webster, T. J. (2006) Less harmful acidic degradation of poly(lactic-co-glycolic acid) bone tissue engineering scaffolds through titania nanoparticle addition. *International Journal of Nanomedicine*. 1 (4), 541–545.

Liu, Q., Zhou, Y. & Li, Z. (2018) PDGF-BB promotes the differentiation and proliferation of MC3T3-E1 cells through the Src/JAK2 signaling pathway. *Molecular Medicine Reports*. 18 (4), 3719–3726.

Liu, X., Wang, T., Chow, L. C., Yang, M. & Mitchell, J. W. (2014a) Effects of inorganic fillers on the thermal and mechanical properties of poly(lactic acid). *International Journal of Polymer Science*.

Liu, Y., Li, L., Li, X., Wang, Y., Ren, X. & Liang, J. (2016) Antibacterial modification of microcrystalline cellulose by grafting copolymerization. *BioResources*. 11 (1), 519–529.

Liu, Y., Cui, X., Hao, C., Tao, F. & Li, J. (2014b) Modified gelatin with quaternary ammonium salts containing epoxide groups. *Chinese Chemical Letters*. 25, 1193–1197.

Lizarraga-Valderrama, L. R., Nigmatullin, R., Taylor, C., Haycock, J. W., Claeyssens, F., Knowles, J. C. & Roy, I. (2015) Nerve tissue engineering using blends of poly(3-hydroxyalkanoates) for peripheral nerve regeneration. *Engineering in Life Sciences*. 15 (6), 612–621.

Lizarraga-Valderrama, L. R., Thomas, C., Juan Ignacio, C.-M. & Roy, I. (2018) Tissue Engineering: Polyhydroxyalkanoate-Based Materials and Composites. In *Encyclopedia of Polymer Applications*, CRC Press Taylor & Francis Group.

Lizarraga-Valderrama, L. D. R., Nigmatullin, R., Ladino, B., Taylor, C. S., Boccaccini, A. R., Knowles, J. C., Claeyssens, F., Haycock, J. W. & Roy, I. (2020) Modulation of neuronal cell affinity of composites scaffolds based on polyhydroxyalkanoates and bioactive glasses. *Biomedical materials (Bristol, England)*.

Loh, Q. L. & Choong, C. (2013) Three-Dimensional Scaffolds for Tissue Engineering Applications: Role of Porosity and Pore Size. *Tissue Engineering Part B: Reviews*. 19 (6), 485–502.

Di Lorenzo, M. L. & Righetti, M. C. (2013) Effect of thermal history on the evolution of crystal and amorphous fractions of poly[(R)-3-hydroxybutyrate] upon storage at ambient temperature. *European Polymer Journal*. 49 (2), 510–517.

Lu, H., Liu, Y., Guo, J., Wu, H., Wang, J. & Wu, G. (2016) Biomaterials with antibacterial and osteoinductive properties to repair infected bone defects. *International Journal of Molecular Sciences*. 17 (3), 1–18.

Lu, J., Tappel, R. C. & Nomura, C. T. (2009) Mini-Review: Biosynthesis of Poly(hydroxyalkanoates). *Journal of Macromolecular Science R , Part C: Polymer Reviews*. 49, 226–248.

Lu, L. X., Zhang, X. F., Wang, Y. Y., Ortiz, L., Mao, X., Jiang, Z. L., Xiao, Z. D. & Huang, N. P. (2013) Effects of hydroxyapatite-containing composite nanofibers on osteogenesis of mesenchymal stem cells *in vitro* and bone regeneration *in vivo*. *ACS Applied Materials and Interfaces*. 5 (2), 319–330.

Lukasiewicz, B., Basnett, P., Nigmatullin, R., Matharu, R., Knowles, J. C. & Roy, I. (2018) Binary Polyhydroxyalkanoate Systems for Soft Tissue Engineering. *Acta Biomaterialia*. 71, 225–234.

Luo, Y., Humayun, A. and Mills, D.K. (2020). Surface Modification of 3D Printed PLA/Halloysite Composite Scaffolds with Antibacterial and Osteogenic Capabilities. *Applied Sciences*, 10(11), 3971.

Lütke-Eversloh, T., Bergander, K., Luftmann, H. & Steinbüchel, A. (2001) Identification of a new class of biopolymer: Bacterial synthesis of a sulfur-containing polymer with thioester linkages. *Microbiology*. 147 (1), 11–19.

Ma, H., Feng, C., Chang, J. & Wu, C. (2018) 3D-printed bioceramic scaffolds: From bone tissue engineering to tumor therapy. *Acta Biomaterialia*. 79, 37–59.

Madison, L. L. & Huisman, G. W. (1999) Metabolic engineering of poly(3-hydroxyalkanoates): from DNA to plastic. *Microbiology and Molecular Biology Reviews*. 63 (1), 21–53.

Madzovska-Malagurski, I., Vukasinovic-Sekulic, M., Kostic, D. & Levic, S. (2016) Towards antimicrobial yet bioactive Cu-alginate hydrogels. *Biomedical Materials*. 11 (3), 35015.

Mah, T. F. C. & O'Toole, G. A. (2001) Mechanisms of biofilm resistance to antimicrobial agents. *Trends in Microbiology*. 9 (1), 34–39.

Manavitehrani, I., Fathi, A., Badr, H., Daly, S., Shirazi, A. N. & Dehghani, F. (2016) Biomedical applications of biodegradable polyesters. *Polymers*. 8 (20), 1–32.

Manecka, G. M., Labrash, J., Rouxel, O., Dubot, P., Lalevée, J., Andaloussi, S. A., Renard, E., Langlois, V. & Versace, D. L. (2014) Green photoinduced modification of natural poly(3-hydroxybutyrate- co -3-hydroxyvalerate) surface for antibacterial applications. *ACS Sustainable Chemistry and Engineering*. 2 (4), 996–1006.

Marchese, A., Barbieri, R., Sanches-Silva, A., Daglia, M., Nabavi, S. F., Jafari, N. J., Izadi, M., Ajami, M. & Nabavi, S. M. (2016) Antifungal and antibacterial activities of allicin: A review. *Trends in Food Science and Technology*. 52, 49–56.

Marie, P. J., Ammann, P., Boivin, G. & Rey, C. (2001) Mechanisms of action and therapeutic potential of strontium in bone. *Calcified Tissue International*. 69 (3), 121–129.

Marsell, R. & Einhorn, T. A. (2012) The biology of fracture healing. *Injury*. 42 (6), 551–555.

Marsh, J. (2003) Principles of Bone Grafting: Non-union, Delayed Union. *Surgery*. 21 (9), 213–216.

Marsh, M. E., Munne, A. M., Vogel, J. J., Cui, Y. & Franceschi, R. T. (1995) Mineralization of bone-like extracellular matrix in the absence of functional osteoblasts. *Journal of Bone and Mineral Research*. 10 (11), 1635–1643.

Martins, A. F., Facchi, S. P., Follmann, H. D. M., Pereira, A. G. B., Rubira, A. F. & Muniz, E. C. (2014) Antimicrobial activity of chitosan derivatives containing N-quaternized moieties in its backbone: A review. *International Journal of Molecular Sciences*. 15 (11), 20800–20832.

Marzona, L. & Pavolini, B. (2009) Play and players in bone fracture healing match. *Clinical Cases in Mineral and Bone Metabolism*. 6 (2), 159–162.

McCauley, L. K., Koh, A. J., Beecher, C. A., Cui, Y., Rosol, T. J. & Franceschi, R. T. (1996) PTH/PTHrP receptor is temporally regulated during osteoblast differentiation and is associated with collagen synthesis. *Journal of Cellular Biochemistry*. 61 (4), 638–647.

Medina Cruz, D., Mi, G. & Webster, T. J. (2018) Synthesis and characterization of biogenic selenium nanoparticles with antimicrobial properties made by *Staphylococcus aureus*, methicillin-resistant *Staphylococcus aureus* (MRSA), *Escherichia coli*, and *Pseudomonas aeruginosa*. *Journal of Biomedical Materials Research - Part A*. 106 (5), 1400–1412.

Medina, M., Legido-quigley, H. & Hsu, L. Y. (2020) Antimicrobial Resistance in One Health. in In *Global Health Security*, Springer, pp. 209-229.

Melendez-Rodriguez, B., Figueroa-Lopez, K. J., Bernardos, A., Martínez-Máñez, R., Cabedo, L., Torres-Giner, S. & Lagaron, J. M. (2019) Electrospun antimicrobial films of poly(3-hydroxybutyrate-co-3-hydroxyvalerate) containing eugenol essential oil encapsulated in mesoporous silica nanoparticles. *Nanomaterials*. 9 (227), 1–23.

Mikulcová, V., Bordes, R. & Kašpárková, V. (2016) On the preparation and antibacterial activity of emulsions stabilized with nanocellulose particles. *Food Hydrocolloids*. 61, 780–792.

Miller, G. L. (1959) Use of Dinitrosalicylic Acid Reagent for Determination of Reducing Sugar. *Analytical Chemistry*. 31 (3), 426–428.

Miller, S. I. (2016) Antibiotic resistance and regulation of the Gram-negative bacterial outer membrane barrier by host innate immune molecules. *MBio*. 7 (5), 5–7.

Misra, S., Boylan, M., Selvam, A., Spallholz, J. E. & Björnstedt, M. (2015) Redox-active selenium compounds—from toxicity and cell death to cancer treatment. *Nutrients*. 7 (5), 3536–3556.

Misra, S. K., Mohn, D., Brunner, T. J., Stark, W. J., Philip, S. E., Roy, I., Salih, V., Knowles, J. C. & Boccaccini, A. R. (2008) Comparison of nanoscale and microscale bioactive glass on the properties of P(3HB)/Bioglass® composites. *Biomaterials*. 29 (12), 1750–1761.

Misra, S. K., Nazhat, S. N., Valappil, S. P., Moshrefi-Torbati, M., Wood, R. J. K., Roy, I. & Boccaccini, A. R. (2007) Fabrication and characterization of biodegradable poly(3-hydroxybutyrate) composite containing bioglass. *Biomacromolecules*. 8 (7), 2112–2119.

Mohammadi, A., Hashemi, M. & Masoud Hosseini, S. (2016) Effect of chitosan molecular weight as micro and nanoparticles on antibacterial activity against some soft rot pathogenic bacteria. *LWT - Food Science and Technology*. 71, 347–355.

Mohanty, S., Sanger, K., Heiskanen, A., Trifol, J., Szabo, P., Dufva, M., Emnéus, J. & Wolff, A. (2016) Fabrication of scalable tissue engineering scaffolds with dual-pore microarchitecture by combining 3D printing and particle leaching. *Materials Science and Engineering C*. 61, 180–189.

Mohapatra, S., Maity, S., Ranjan Dash, H., Das, S., Pattnaik, S., Rath, C. C. & Samantaray, D. (2017) Bacillus and biopolymer: Prospects and challenges. *Biochemistry and Biophysics Reports*. 12, 206–213.

Molling, J. W., Seezink, J. W., Teunissen, B. E. J., Muijrers-Chen, I. & Borm, P. J. A. (2014) Comparative performance of a panel of commercially available antimicrobial nanocoatings in Europe. *Nanotechnology, Science and Applications*. 7, 97–104.

Moreno-Reyes, R., Egrise, D., Nève, J., Pasteels, J. L. & Schoutens, A. (2001) Selenium deficiency-induced growth retardation is associated with an impaired bone metabolism and osteopenia. *Journal of Bone and Mineral Research*. 16 (8), 1556–1563.

Mouriño, V., Cattalini, J. P. & Boccaccini, A. R. (2012) Metallic ions as therapeutic agents in tissue engineering scaffolds: An overview of their biological applications and strategies for new developments. *Journal of the Royal Society Interface*. 9 (68), 401–419.

Mouriño, V. & Boccaccini, A. R. (2010) Bone tissue engineering therapeutics: Controlled drug delivery in three-dimensional scaffolds. *Journal of the Royal Society Interface*. 7 (43), 209–227.

Mozejko-Ciesielska, J., Szacherska, K. & Marciniak, P. (2019) *Pseudomonas* Species as Producers of Eco-friendly Polyhydroxyalkanoates. *Journal of Polymers and the Environment*. 27 (6), 1151–1166.

Możejko-Ciesielska, J. & Kiewisz, R. (2016) Bacterial polyhydroxyalkanoates: Still fabulous? *Microbiological Research*. 192 (2016), 271–282.

Muangwong, A., Boontip, T., Pachimsawat, J. & Napathorn, S. C. (2016) Medium chain length polyhydroxyalkanoates consisting primarily of unsaturated 3-hydroxy-5-cis-dodecanoate synthesized by newly isolated bacteria using crude glycerol. *Microbial Cell Factories*. 15 (1), 55.

Müller, J. M. & Alegre, R. M. (2007) Alginate production by *Pseudomonas mendocina* in a stirred draft fermenter. *World Journal of Microbiology and Biotechnology*. 23, 691–695.

Munaz, A., Vadivelu, R. K., St. John, J., Barton, M., Kamble, H. & Nguyen, N. T. (2016) Three-dimensional printing of biological matters. *Journal of Science: Advanced Materials and Devices*. 1 (1), 1–17.

Munita, J. M. & Arias, C. A. (2016) Mechanisms of Antibiotic Resistance. *Microbiology Spectrum*. 4 (2), 1–37.

Muñoz-Bonilla, A. & Fernández-García, M. (2012) Polymeric materials with antimicrobial activity. *Progress in Polymer Science (Oxford)*. 37 (2), 281–339.

Muñoz-Bonilla, A. & Fernández-García, M. (2015) The roadmap of antimicrobial polymeric materials in macromolecular nanotechnology. *European Polymer Journal*. 65, 46–62.

Murphy, C. M. & O'Brien, F. J. (2010) Understanding the effect of mean pore size on cell activity in collagen-glycosaminoglycan scaffolds. *Cell Adhesion and Migration*. 4 (3), 377–381.

Muzzarelli, R. A. A. & Tanfani, F. (1985) The N-Permethylation of Chitosan and the Preparation of N-Trimethyi Chitosan Iodide Infrared spectrometry. *Carbohydrate Polymers*. 52, 97–307.

Natrajan, D., Srinivasan, S., Sundar, K. & Ravindran, A. (2015) Formulation of essential oil-loaded chitosan-alginate nanocapsules. *Journal of Food and Drug Analysis*. 23 (3), 560–568.

Nerkar, M., Ramsay, J. A., Ramsay, B. A., Vasileiou, A. A. & Kontopoulou, M. (2015) Improvements in the melt and solid-state properties of poly(lactic acid), poly-3-hydroxyoctanoate and their blends through reactive modification. *Polymer*. 64 (September 2014), 51–61.

Ngo, T. D., Kashani, A., Imbalzano, G., Nguyen, K. T. Q. & Hui, D. (2018) Additive manufacturing (3D printing): A review of materials, methods, applications and challenges. *Composites Part B: Engineering*. 143, 172–196.

Nguyen, T. H. D., Vardhanabhuti, B., Lin, M. & Mustapha, A. (2017) Antibacterial properties of selenium nanoparticles and their toxicity to Caco-2 cells. *Food Control*. 77, 17–24.

Nguyen, V. C., Nguyen, V. B. & Hsieh, M. F. (2013) Curcumin-loaded chitosan/gelatin composite sponge for wound healing application. *International Journal of Polymer Science*. 2013.

Niaounakis, M. (2015) 'Blending of Biodegradable polymer', in *Biopolymers: Processing and Products*. Elsevier Inc. pp. 117–185.

Nigmatullin, R., Thomas, P., Lukasiewicz, B., Puthussery, H. & Roy, I. (2015) Polyhydroxyalkanoates, a family of natural polymers, and their applications in drug delivery. *Journal of Chemical Technology and Biotechnology*. 90 (7), 1209–1221.

Nigmatullin, R. & Gao, F. (2012) Onium-functionalised polymers in the design of non-leaching antimicrobial surfaces. *Macromolecular Materials and Engineering*. 297 (11), 1038–1074.

No, H. K., Young Park, N., Ho Lee, S. & Meyers, S. P. (2002) Antibacterial activity of chitosans and chitosan oligomers with different molecular weights. *International Journal of Food Microbiology*. 74 (1–2), 65–72.

Noohom, W., Jack, K. S., Martin, D. & Trau, M. (2009) Understanding the roles of nanoparticle dispersion and polymer crystallinity in controlling the mechanical properties of HA/PHBV nanocomposites. *Biomedical Materials*. 4 (1), 1–13.

O'Neill, A. J. & Chopra, I. (2004) Preclinical evaluation of novel antibacterial agents by microbiological and molecular techniques. *Expert Opinion on Investigational Drugs*. 13 (8), 1045–1063.

Obat, A., Iwata, T., Maeda, H., Hirata, H. & Kasuga, T. (2013) Preparation of poly(3-hydroxybutyrate-co-4-hydroxybutyrate)-based composites releasing soluble silica for bone regeneration. *Journal of the Ceramic Society of Japan*. 121 (1417), 753–758.

Odermatt, E. K., Funk, L., Bargon, R., Martin, D. P., Rizk, S. & Williams, S. F. (2012) MonoMax suture: A new long-term absorbable monofilament suture made from poly-4-hydroxybutyrate. *International Journal of Polymer Science*. 2012.

OECD (2018). Stemming the superbug tide: just a few dollars more. Organisation for Economic Co-operation and Development (OECD) publishing, 2018.

Ong, S. Y., Chee, J. Y. & Sudesh, K. (2017) Degradation of Polyhydroxyalkanoate (PHA): a Review. *Journal of Siberian Federal University. Biology*. 10 (2), 21–225.

Ortega, E. S., Sanz-Garcia, A., Pernia-Espinoza, A. & Escobedo-Lucea, C. (2019) Efficient fabrication of polycaprolactone scaffolds for printing hybrid tissue-engineered constructs. *Materials*. 12 (4), 1–18.

Oryan, A., Alidadi, S., Moshiri, A. & Bigham-Sadegh, A. (2014) Bone morphogenetic proteins: A powerful osteoinductive compound with non-negligible side effects and limitations. *BioFactors*. 40 (5), 459–481.

Ouyang, S. P., Luo, R. C., Chen, S. S., Liu, Q., Chung, A., Wu, Q. & Chen, G. Q. (2007) Production of polyhydroxyalkanoates with high 3-hydroxydodecanoate monomer content by *fadB* and *fadA* knockout mutant of *Pseudomonas putida* KT2442. *Biomacromolecules*. 8 (8), 2504–2511.

Palermo, E. F., Lienkamp, K., Gillies, E. R. & Ragogna, P. J. (2019) Antibacterial Activity of Polymers: Discussions on the Nature of Amphiphilic Balance. *Angewandte Chemie*. 58 (12), 3690–3693.

Palza, H. (2015) Antimicrobial polymers with metal nanoparticles. *International Journal of Molecular Sciences*. 16 (1), 2099–2116.

Park, B. K. & Kim, M. (2010) Applications of Chitin and Its Derivatives in Biological Medicine. *International Journal of Molecular Sciences*. 11, 5152–5164.

Park, K., Jung, H., Son, J. S., Park, K. D., Kim, J. J., Ahn, K. D. & Han, D. K. (2007) Preparation of biodegradable polymer scaffolds with dual pore system for tissue regeneration. *Macromolecular Symposia*. 249, 145–150.

Percival, S. L., Suleman, L. & Donelli, G. (2015) Healthcare-Associated infections, medical devices and biofilms: Risk, tolerance and control. *Journal of Medical Microbiology*. 64 (4), 323–334.

Pereira dos Santos, E., Nicácio, P. H. M., Coêlho Barbosa, F., Nunes da Silva, H., Andrade, A. L. S., Lia Fook, M. V., de Lima Silva, S. M. & Farias Leite, I. (2019) Chitosan/Essential Oils Formulations for Potential Use as Wound Dressing: Physical and Antimicrobial Properties. *Materials*. 12 (14), 2223.

Pereira, T. F., Oliveira, M. F., Maia, I. A., Silva, J. V. L., Costa, M. F. & Thiré, R. M. S. M. (2012) 3D Printing of Poly(3-hydroxybutyrate) Porous Structures Using Selective Laser Sintering. *Macromolecular Symposia*. 319 (1), 64–73.

Petrochenko, P. & Narayan, R. J. (2010) Novel approaches to bone grafting: Porosity, Bone morphogenetic proteins, stem cells, and the periosteum. *Journal of Long-Term Effects of Medical Implants*. 20 (4), 303–315.

Pfister, A., Landers, R., Laib, A., Hübner, U., Schmelzeisen, R. & Mülhaupt, R. (2004) Biofunctional Rapid Prototyping for Tissue-Engineering Applications: 3D Bioplotting versus 3D Printing. *Journal of Polymer Science, Part A: Polymer Chemistry*. 42 (3), 624–638.

Phukon, P., Pokhrel, B., Konwar, B. K. & Dolui, S. K. (2013) Biosynthesis and characterization of a new copolymer, poly(3-hydroxyvalerate-co-5-hydroxydecenoate), from *Pseudomonas aeruginosa*. *Biotechnology Letters*. 35 (4), 607–611.

Pirak, T., Jangchud, A. & Jantawat, P. (2012) Characterisation of physical, chemical and antimicrobial properties of allicin-chitosan complexes. *International Journal of Food Science and Technology*. 47 (7), 1339–1347.

Poblete-Castro, I., Rodriguez, A. L., Chi Lam, C. M. & Kessler, W. (2014) Improved production of medium-chain-length polyhydroxyalkanoates in glucose-based fed-batch cultivations of metabolically engineered *Pseudomonas putida* strains. *Journal of Microbiology and Biotechnology*. 24 (1), 59–69.

Pors-Nielsen, S. (2004) The biological role of strontium. *Bone*. 35 (3), 583–588.

Porter, J. R., Ruckh, T. T. & Popat, K. C. (2009) Bone tissue engineering: A review in bone biomimetics and drug delivery strategies. *Biotechnology Progress*. 25 (6), 1539–1560.

Pountos, I. & Giannoudis, P. V (2018) Fracture Reduction and Fixation Techniques. *Fracture Reduction and Fixation Techniques*.

Pramanik, N., Dutta, K., Basu, R. K. & Kundu, P. P. (2016) Aromatic π-Conjugated Curcumin on Surface Modified Polyaniline/Polyhydroxyalkanoate Based 3D Porous Scaffolds for Tissue Engineering Applications. *ACS Biomaterials Science & Engineering*. 2 (12), 2365–2377.

Pramanik, N., Mitra, T., Khamrai, M., Bhattacharyya, A., Mukhopadhyay, P., Gnanamani, A., Basu, R. K. & Kundu, P. P. (2015) Characterization and evaluation of curcumin loaded guar gum/polyhydroxyalkanoates blend films for wound healing applications. *RSC Adv.* 5 (78), 63489–63501.

Prasad, A., Sankar, M. R. & Katiyar, V. (2017) State of Art on Solvent Casting Particulate Leaching Method for Orthopedic ScaffoldsFabrication. *Materials Today: Proceedings*. 4 (2), 898–907.

Pratt, S., Vandi, L.-J., Gapes, D., Werker, A., Oehmen, A. & Laycock, B. (2019) Polyhydroxyalkanoate (PHA) Bioplastics from Organic Waste. *Biorefinery*. 615–638.

Prieto, A., Escapa, I. F., Martínez, V., Dinjaski, N., Herencias, C., de la Peña, F., Tarazona, N. & Revelles, O. (2016) A holistic view of polyhydroxyalkanoate metabolism in *Pseudomonas putida*. *Environmental Microbiology*. 18 (2), 341–357.

Puppi, D., Pecorini, G. & Chiellini, F. (2019) Biomedical processing of polyhydroxyalkanoates. *Bioengineering*. 6 (4), 1–20.

Qin, Y. (2005) Silver-containing alginate fibres and dressings. *International Wound Journal*. 2 (2), 172–176.

Qu, H., Fu, H., Han, Z. & Sun, Y. (2019) Biomaterials for bone tissue engineering scaffolds: a review. *RSC Advances*. 9 (45), 26252–26262.

Quarles, L. D., Yohay, D. A., Lever, L. W., Caton, R. & Wenstrup, R. J. (1992) Distinct proliferative and differentiated stages of murine MC3T3-E1 cells in culture: An *in vitro* model of osteoblast development. *Journal of Bone and Mineral Research*. 7 (6), 683–692.

Querido, W., Rossi, A. L. & Farina, M. (2016) The effects of strontium on bone mineral: A review on current knowledge and microanalytical approaches. *Micron*. 80, 122–134.

Raafat, D., Von Bargen, K., Haas, A. & Sahl, H. G. (2008) Insights into the mode of action of chitosan as an antibacterial compound. *Applied and Environmental Microbiology*. 74 (12), 3764–3773.

Rabea, E. I., Badawy, M. E. T., Stevens, C. V., Smagghe, G. & Steurbaut, W. (2003) Chitosan as antimicrobial agent: Applications and mode of action. *Biomacromolecules*. 4 (6), 1457–1465.

Rai, B., Noohom, W., Kithva, P. H., Grøndahl, L. & Trau, M. (2008) Bionanohydroxyapatite/poly(3-hydroxybutyrate-co-3-hydroxyvalerate) composites with improved particle dispersion and superior mechanical properties. *Chemistry of Materials*. 20 (8), 2802–2808.

Rai, B., Lin, J. L., Lim, Z. X. H., Guldberg, R. E., Hutmacher, D. W. & Cool, S. M. (2010) Differences between *in vitro* viability and differentiation and *in vivo* bone-forming efficacy of human mesenchymal stem cells cultured on PCL-TCP scaffolds. *Biomaterials*. 31 (31), 7960–7970.

Rai, R., Keshavarz, T., Roether, J. A., Boccaccini, A. R. & Roy, I. (2011a) Medium chain length polyhydroxyalkanoates, promising new biomedical materials for the future. *Materials Science and Engineering R: Reports*. 72 (3), 29–47.

Rai, R., Yunos, D. M., Boccaccini, A. R., Knowles, J. C., Barker, I. A., Howdle, S. M., Tredwell, G. D., Keshavarz, T. & Roy, I. (2011b) Poly-3-hydroxyoctanoate P(3HO), a Medium Chain Length Polyhydroxyalkanoate Homopolymer from *Pseudomonas mendocina*. *Biomacromolecules*. 12 (6), 2126–2136.

Ramier, J., Bouderlique, T., Stoilova, O., Manolova, N., Rashkov, I., Langlois, V., Renard, E., Albanese, P. & Grande, D. (2014) Biocomposite scaffolds based on electrospun poly(3-hydroxybutyrate) nanofibers and electrosprayed hydroxyapatite nanoparticles for bone tissue engineering applications. *Materials Science and Engineering C*. 38 (1), 161–169.

Ramsay, B. A., Lomaliza, K., Chavarie, C., Dube, B., Bataille, P. & Ramsay, J. A. (1990) Production of poly-(β-hydroxybutyric-co-β-hydroxyvaleric) acids. *Applied and Environmental Microbiology*. 56 (7), 2093–2098.

Randriamahefa, S., Renard, E., Guérin, P. & Langlois, V. (2003) Fourier Transform Infrared Spectroscopy for Screening and Quantifying Production of PHAs by *Pseudomonas* Grown on Sodium Octanoate. *Biomacromolecules*. 4 (4), 1092–1097.

Ratnayake, J. T. B., Mucalo, M. & Dias, G. J. (2017) Substituted hydroxyapatites for bone regeneration: A review of current trends. *Journal of Biomedical Materials Research - Part B Applied Biomaterials*. 105 (5), 1285–1299.

Ravi, N. D., Balu, R. & Sampath Kumar, T. S. (2012) Strontium-substituted calcium deficient hydroxyapatite nanoparticles: Synthesis, characterization, and antibacterial properties. *Journal of the American Ceramic Society*. 95 (9), 2700–2708.

Rayman, M. P. (2000) The importance of selenium to human health. *The Lancet*. 356 (9225), 233–241.

Raza, Z. A., Tariq, M. R., Majeed, M. I. & Banat, I. M. (2019) Recent developments in bioreactor scale production of bacterial polyhydroxyalkanoates. *Bioprocess and Biosystems Engineering*. 42 (6), 901–919.

Reidy, B., Haase, A., Luch, A., Dawson, K. A. & Lynch, I. (2013) Mechanisms of silver nanoparticle release, transformation and toxicity: A critical review of current knowledge and recommendations for future studies and applications. *Materials*. 6 (6), 2295–2350.

Requena, R., Jiménez, A., Vargas, M. & Chiralt, A. (2016) Poly[(3-hydroxybutyrate)-co-(3-hydroxyvalerate)] active bilayer films obtained by compression moulding and applying essential oils at the interface. *Polymer International*. 65 (8), 883–891.

Rezwan, K., Chen, Q. Z., Blaker, J. J. & Boccaccini, A. R. (2006) Biodegradable and bioactive porous polymer/inorganic composite scaffolds for bone tissue engineering. *Biomaterials*. 27 (18), 3413–3431.

Righetti, M. C., Aliotta, L., Mallegni, N., Gazzano, M., Passaglia, E., Cinelli, P. & Lazzeri, A. (2019) Constrained Amorphous Interphase and Mechanical Properties of Poly(3-Hydroxybutyrate-co-3-Hydroxyvalerate). *Frontiers in Chemistry*. 7 (November), 1–16.

Rodríguez-Tobías, H., Morales, G., Ledezma, A., Romero, J., Saldívar, R., Langlois, V., Renard, E. & Grande, D. (2016) Electrospinning and electrospraying techniques for designing novel antibacterial poly(3-hydroxybutyrate)/zinc oxide nanofibrous composites. *Journal of Materials Science*. 51 (18), 8593–8609.

Rodríguez-Valencia, C., Lopez-Álvarez, M., Cochón-Cores, B., Pereiro, I., Serra, J. & González, P. (2013) Novel selenium-doped hydroxyapatite coatings for biomedical applications. *Journal of Biomedical Materials Research - Part A*. 101 A (3), 853–861.

Roilides, E., Simitsopoulou, M., Katragkou, A. & Walsh, T. J. (2015) How Biofilms Evade Host Defenses. *Microbiology Spectrum*. 1–10.

van Rooijen, M. M. J. *et al*. (2018) A post-market, prospective, multi-center, single-arm clinical investigation of Phasix™ mesh for VHWG grade 3 midline incisional hernia repair: a research protocol. *BMC Surgery*. 18 (1), 104.

Rosellini, E., Cristallini, C., Barbani, N., Vozzi, G. & Giusti, P. (2009) Preparation and characterization of alginate/gelatin blend films for cardiac tissue engineering. *Journal of Biomedical Materials Research - Part A*. 91 (2), 447–453.

Ruddaraju, L. K., Pammi, S. V. N., Guntuku, G. sankar, Padavala, V. S. & Kolapalli, V. R. M. (2019) A review on anti-bacterials to combat resistance: From ancient era of plants and metals to present and future perspectives of green nano technological combinations. *Asian Journal of Pharmaceutical Sciences*. 1–18.

Rui-Rodrigues, J. & Lagoa, R. (2006) Copper ions binding in Cu-alginate gelation. *Journal of Carbohydrate Chemistry*. 25 (2–3), 219–232.

Runt, J. & Huang, J. (2002) 'Polymer blends and copolymers', in *Handbook of Thermal Analysis and Calorimetry*. Elsevier Science Inc. pp. 273–294.

Saadat, A., Karbasi, S., Ghader, A. A. B. & Khodaei, M. (2015) Characterization of Biodegradable P3HB/HA Nanocomposite Scaffold for Bone Tissue Engineering. *Procedia Materials Science*. 11, 217–223.

Saadat, A., Behnamghader, A., Karbasi, S., Abedi, D., Soleimani, M. & Shafiee, A. (2013) Comparison of acellular and cellular bioactivity of poly 3-hydroxybutyrate/hydroxyapatite nanocomposite and poly 3-hydroxybutyrate scaffolds. *Biotechnology and Bioprocess Engineering*. 18 (3), 587–593.

Sabokbar, A., Millett, P. J., Myer, B. & Rushton, N. (1994) A rapid, quantitative assay for measuring alkaline phosphatase activity in osteoblastic cells *in vitro*. *Bone and Mineral*. 27, 57–67.

Sadat-Shojai, M., Khorasani, M. T., Jamshidi, A. & Irani, S. (2013) Nano-hydroxyapatite reinforced polyhydroxybutyrate composites: A comprehensive study on the structural and *in vitro* biological properties. *Materials Science and Engineering C*. 33 (5), 2776–2787.

Saito, M., Inoue, Y. & Yoshie, N. (2001) Cocrystallization and phase segregation of blends of poly (3-hydroxybutyrate) and poly(3-hydroxybutyrate-co-3-hydroxyvalerate). *Polymer*. 42 (13), 5573–5580.

Saldias, C., Bonardd, S., Quezada, C., Radic, D. & Leiva, A. (2017) The role of polymers in the synthesis of noble metal nanoparticles: A review. *Journal of Nanoscience and Nanotechnology*. 17 (1), 87–114.

Sandoval, Á., Arias-Barrau, E., Arcos, M., Naharro, G., Olivera, E. R. & Luengo, J. M. (2007) Genetic and ultrastructural analysis of different mutants of *Pseudomonas putida* affected in the poly-3-hydroxy-n-alkanoate gene cluster. *Environmental Microbiology*. 9 (3), 737–751.

dos Santos, A. J., dalla Valentina, O. V., Hidalgo-Schulz, A. A. & Tomaz-Duarte, M. A. (2017) From Obtaining to Degradation of PHB:Material Properties. Part I. *Ingeniería y Ciencia*. 13 (26), 269–298.

Santos, M., Fonseca, A., Mendonça, P., Branco, R., Serra, A., Morais, P. & Coelho, J. (2016) Recent Developments in Antimicrobial Polymers: A Review. *Materials*. 9 (7), 599.

Sarath, C. C., Shanks, R. A. & Thomas, S. (2014) 'Polymer Blends', in *Nanostructured Polymer Blends*. Elsevier Inc. pp. 1–14.

Saska, S., Pires, L. C., Cominotte, M. A., Mendes, L. S., de Oliveira, M. F., Maia, I. A., da Silva, J. V. L., Ribeiro, S. J. L. & Cirelli, J. A. (2018) Three-dimensional printing and *in vitro* evaluation of poly(3-hydroxybutyrate) scaffolds functionalized with osteogenic growth peptide for tissue engineering. *Materials Science and Engineering C*. 89, 265–273.

Scholz, C., Wolk, S., Lenz, R. W. & Fuller, R. C. (1994) Growth and Polyester Production by *Pseudomonas oleovorans* on Branched Octanoic Acid Substrates. *Macromolecules*. 27 (22), 6358–6362.

Seok, Y., Woo, Hyung, Hee, S., Sook, K., Woo, Hyoung & Ha, Y. (2007) Preparation of alginate – quaternary ammonium complex beads and evaluation of their antimicrobial activity. *International Journal of Biological Macromolecules*. 41 (2), 36–41.

Sewalt, V., Shanahan, D., Gregg, L., La Marta, J. & Carillo, R. (2016) The Generally Recognized as Safe (GRAS) process for industrial microbial enzymes. *Industrial Biotechnology*. 12 (5), 295–302.

Sharifahmadian, O., Salimijazi, H. R., Fathi, M. H., Mostaghimi, J. & Pershin, L. (2013) Relationship between surface properties and antibacterial behavior of wire arc spray copper coatings. *Surface and Coatings Technology*. 233, 74–79.

Sheehy, E. J., Kelly, D. J. & O'Brien, F. J. (2019) Biomaterial-based endochondral bone regeneration: a shift from traditional tissue engineering paradigms to developmentally inspired strategies. *Materials Today Bio*. 3100009.

Sheshadri, P. & Shirwaiker, R. A. (2015) Characterization of material-process-structure interactions in the 3D Bioplotting of Polycaprolactone. *3D Printing and Additive Manufacturing*. 2 (1), 20–31.

Shetta, A., Kegere, J. & Mamdouh, W. (2019) Comparative study of encapsulated peppermint and green tea essential oils in chitosan nanoparticles: Encapsulation, thermal stability, *in-vitro* release, antioxidant and antibacterial activities. *International Journal of Biological Macromolecules*. 126, 731–742.

Shih, I. L., Shen, M. H. & Van, Y. T. (2006) Microbial synthesis of poly(Ɛ-lysine) and its various applications. *Bioresource Technology*. 97 (9), 1148–1159.

Shima, S., Matsuoka, H., Iwamoto, T. & Sakai, H. (1984) Antimicrobial action of epsilon-poly-L-lysine. *The Journal of antibiotics*. 37 (11), 1449–1455.

Siedenbiedel, F. & Tiller, J. C. (2012) Antimicrobial polymers in solution and on surfaces: Overview and functional principles. *Polymers*. 4 (1), 46–71.

Simon, J. L., Roy, T. D., Parsons, J. R., Rekow, E. D., Thompson, V. P., Kemnitzer, J. & Ricci, J. L. (2003) Engineered cellular response to scaffold architecture in a rabbit trephine defect. *Journal of Biomedical Materials Research*. 66A (2), 275–282.

Singh, A. K. & Mallick, N. (2009) Exploitation of inexpensive substrates for production of a novel SCL-LCL-PHA co-polymer by *Pseudomonas aeruginosa* MTCC 7925. *Journal of Industrial Microbiology and Biotechnology*. 36 (3), 347–354.

Singh, M., Patel, S. K. & Kalia, V. C. (2009) *Bacillus subtilis* as potential producer for polyhydroxyalkanoates. *Microbial Cell Factories*. 8 (1), 38.

Singh, M., Kumar, P., Ray, S. & Kalia, V. C. (2015) Challenges and Opportunities for Customizing Polyhydroxyalkanoates. *Indian Journal of Microbiology*. 55 (3), 235–249.

Sionkowska, A., Skrzyński, S., Śmiechowski, K. & Kołodziejczak, A. (2017) The review of versatile application of collagen. *Polymers for Advanced Technologies*. 28 (1), 4–9.

Slavin, Y. N., Asnis, J., Häfeli, U. O. & Bach, H. (2017) Metal nanoparticles: Understanding the mechanisms behind antibacterial activity. *Journal of Nanobiotechnology*. 15 (1), 1–20.

Snoch, W., Stępień, K., Prajsnar, J., Staroń, J., Szaleniec, M. & Guzik, M. (2019) Influence of chemical modifications of polyhydroxyalkanoate-derived fatty acids on their antimicrobial properties. *Catalysts*. 9 (6), 1–12.

Solaiman, D. K. Y., Ashby, R. D. & Foglia, T. A. (1999) Medium-chain-length poly(β-hydroxyalkanoate) synthesis from triacylglycerols by *Pseudomonas saccharophila*. *Current Microbiology*. 38 (3), 151–154.

Solaiman, D. K. Y., Ashby, R. D. & Foglia, T. A. (2002) Physiological characterization and genetic engineering of *Pseudomonas corrugata* for medium-chain-length polyhydroxyalkanoates synthesis from triacylglycerols. *Current Microbiology*. 44 (3), 189–195.

Sombatmankhong, K., Sanchavanakit, N., Pavasant, P. & Supaphol, P. (2007) Bone scaffolds from electrospun fiber mats of poly(3-hydroxybutyrate), poly(3-hydroxybutyrate-co-3-hydroxyvalerate) and their blend. *Polymer*. 48 (5), 1419–1427.

Son, B., Yeom, B.-Y., Song, S. H., Lee, C.-S. & Hwang, T. S. (2009) Antibacterial electrospun chitosan/poly(vinyl alcohol) nanofibers containing silver nitrate and titanium dioxide. *Journal of Applied Polymer Science*. 111 (6), 2892–2899.

de Souza, L. & Shivakumar, S. (2019) Polyhydroxyalkanoates (PHA) – Applications in Wound Treatment and as Precursors for Oral Drugs, in *Biotechnological Applications of Polyhydroxyalkanoates*, Springer, Singapore, pp. 227-270.

St-Pierre, J. P., Gauthier, M., Lefebvre, L. P. & Tabrizian, M. (2005) Three-dimensional growth of differentiating MC3T3-E1 pre-osteoblasts on porous titanium scaffolds. *Biomaterials*. 26 (35), 7319–7328.

Stanford, C. M., Jacobson, P. A., Eanes, E. D., Lembke, L. A. & Midura, R. J. (1995) Rapidly forming apatitic mineral in an osteoblastic cell line (UMR 106-01 BSP). *Journal of Biological Chemistry*. 270 (16), 9420–9428.

Stewart, P. S. (2002) Mechanisms of antibiotic resistance in bacterial biofilms. *International journal of medical microbiology : IJMM*. 292 (2), 107–113.

Stewart, P. S. & William Costerton, J. (2001) Antibiotic resistance of bacteria in biofilms. *The Lancet*. 358 (9276), 135–138.

Straccia, M. C., D'Ayala, G. G., Romano, I. & Laurienzo, P. (2015) Novel zinc alginate hydrogels prepared by internal setting method with intrinsic antibacterial activity. *Carbohydrate Polymers*. 125, 103–112.

Su, P., Tian, Y., Yang, C., Ma, X., Wang, X., Pei, J. & Qian, A. (2018) Mesenchymal stem cell migration during bone formation and bone diseases therapy. International Journal of Molecular Sciences 19 (8).

Suchitra, M. (2004) Thermal Analysis of Composites Using DSC. *Advanced Topics in Characterization of Composites*. 11–33.

Sudesh, K., Abe, H. & Doi, Y. (2000) Synthesis, structure and properties of polyhydroxyalkanoates: Biological polyesters. *Progress in Polymer Science (Oxford)*. 25 (10), 1503–1555.

Sukan, A., Roy, I. & Keshavarz, T. (2017) A strategy for dual biopolymer production of P(3HB) and γ-PGA. *Journal of Chemical Technology and Biotechnology*. 92 (7), 1548–1557.

Sukan, A., Roy, I. & Keshavarz, T. (2014) Agro-Industrial Waste Materials as Substrates for the Production of Poly(3-Hydroxybutyric Acid). *Journal of Biomaterials and Nanobiotechnology*. 5 (4), 229–240.

Sultana, N. & Khan, T. H. (2012) *In vitro* degradation of PHBV scaffolds and nHA/PHBV composite scaffolds containing hydroxyapatite nanoparticles for bone tissue engineering. *Journal of Nanomaterials*. 2012.

Sun, Z., Ramsay, J. A., Guay, M. & Ramsay, B. A. (2007) Fermentation process development for the production of medium-chain-length poly-3-hyroxyalkanoates. *Applied Microbiology and Biotechnology*. 75 (3), 475–485.

Sun, Z., Shi, C., Wang, X., Fang, Q. & Huang, J. (2017) Synthesis, characterization, and antimicrobial activities of sulfonated chitosan. *Carbohydrate Polymers*. 155, 321–328.

Sung, H. J., Meredith, C., Johnson, C. & Galis, Z. S. (2004) The effect of scaffold degradation rate on three-dimensional cell growth and angiogenesis. *Biomaterials*. 25 (26), 5735–5742.

Šupová, M. (2015) Substituted hydroxyapatites for biomedical applications: A review. *Ceramics International*. 41 (8), 9203–9231.

Tack, K. & Sabath, L. (1985) Increased minimum inhibitory concentrations with anaerobiasis for tobramycin, gentamicin, and amikacin, compared to latamoxef, piperacillin, chloramphenicol, and clindamycin. *Chemotherapy*. 31 (3), 204–210.

Tai, H. Y., Fu, E., Cheng, L. P. & Don, T. M. (2014) Fabrication of asymmetric membranes from polyhydroxybutyrate and biphasic calcium phosphate/chitosan for guided bone regeneration. *Journal of Polymer Research*. 21 (412), 1–11.

Takagi, Y., Hashii, M., Maehara, A. & Yamane, T. (1999) Biosynthesis of polyhydroxyalkanoate with a thiophenoxy side group obtained from *Pseudomonas putida*. *Macromolecules*. 32 (25), 8315–8318.

Tan, G. Y. A., Chen, C. L., Li, L., Ge, L., Wang, L., Razaad, I. M. N., Li, Y., Zhao, L., Mo, Y. & Wang, J. Y. (2014) Start a research on biopolymer polyhydroxyalkanoate (PHA): A review. *Polymers*. 6 (3), 706–754.

Tao, O., Kort-Mascort, J., Lin, Y., Pham, H. M., Charbonneau, A. M., ElKashty, O. A., Kinsella, J. M. & Tran, S. D. (2019) The Applications of 3D Printing for Craniofacial Tissue Engineering. *Micromachines*. 10 (7), 480.

Tasdemir, M., Kenet, I. H. & Pazarlioglu, S. (2017) Hydroxyapatite Reinforced Polypropylene Bio Composites. *Academic Journal of Science* , 6(1), 461-462.

Tawfik, S. M. & Hefni, H. H. (2016) Synthesis and antimicrobial activity of polysaccharide alginate derived cationic surfactant-metal(II) complexes. *International journal of biological macromolecules*. 82, 562–572.

Thandapani, G., Radha, E., Jayashri, J., Annie Kamala Florence, J. & Sudha, P. N. (2018) 'Bioactive metallic surfaces for bone tissue engineering', in *Fundamental Biomaterials: Metals*. Elsevier. pp. 79–110.

Thawabteh, A., Juma, S., Bader, M., Karaman, D., Scrano, L., Bufo, S. A. & Karaman, R. (2019) The Biological Activity of Natural Alkaloids against Herbivores, Cancerous Cells and Pathogens. *Toxins*. 11 (656), 1–28.

Thomas, M. V. & Puleo, D. A. (2011) Infection, inflammation, and bone regeneration: A paradoxical relationship. *Journal of Dental Research*. 90 (9), 1052–1061.

Tian, L., Zhang, Z., Tian, B., Zhang, X. and Wang, N. (2020). Study on antibacterial properties and cytocompatibility of EPL coated 3D printed PCL/HA composite scaffolds. *RSC Advances*, 10(8), 4805-4816.

Timofeeva, L. & Kleshcheva, N. (2011) Antimicrobial polymers: Mechanism of action, factors of activity, and applications. *Applied Microbiology and Biotechnology*. 89 (3), 475–492.

Tite, T., Popa, A. C., Balescu, L. M., Bogdan, I. M., Pasuk, I., Ferreira, J. M. F. & Stan, G. E. (2018) Cationic substitutions in hydroxyapatite: Current status of the derived biofunctional effects and their *in vitro* interrogation methods. *Materials*. 11 (11), 1–62.

Tortajada, M., da Silva, L. F. & Prieto, M. A. (2013) Second-generation functionalized mediumchain-length polyhydroxyalkanoates: The gateway to high-value bioplastic applications. *International Microbiology*. 16 (1), 1–15.

Torun-Köse, G., Kenar, H., Hasirci, N. & Hasirci, V. (2003) Macroporous poly(3-hydroxybutyrate-co-3-hydroxyvalerate) matrices for bone tissue engineering. *Biomaterials*. 24 (11), 1949–1958.

Toyofuku, M., Inaba, T., Kiyokawa, T., Obana, N., Yawata, Y. & Nomuro, N. (2015) Environmental factors that shape biofilm formation. *Bioscience,Biotechnology, and Biochemistry*. 80 (1), 7–12.

Trachtenberg, J. E., Mountziaris, P. M., Miller, J. S., Wettergreen, M., Kasper, F. K. & Mikos, A. G. (2014) Open-source three-dimensional printing of biodegradable polymer scaffolds for tissue engineering. *Journal of Biomedical Materials Research - Part A*. 102 (12), 4326–4335.

Trampuz, A. & Widmer, A. F. (2006) Infections associated with orthopedic implants. *Current Opinion in Infectious Diseases*. 19 (4), 349–356.

Tsuge, T. (2016) Fundamental factors determining the molecular weight of polyhydroxyalkanoate during biosynthesis. *Polymer Journal*. 48 (11), 1051–1057.

Tsuge, T. (2002) Metabolic improvements and use of inexpensive carbon sources in microbial production of polyhydroxyalkanoates. *Journal of Bioscience and Bioengineering*. 94 (6), 579–584.

Turnbull, G., Clarke, J., Picard, F., Riches, P., Jia, L., Han, F., Li, B. & Shu, W. (2018) 3D bioactive composite scaffolds for bone tissue engineering. *Bioactive Materials*. 3 (3), 278–314.

Turner, B. N., Strong, R. & Gold, S. A. (2014) A review of melt extrusion additive manufacturing processes: I. Process design and modeling. *Rapid Prototyping Journal*. 20 (3), 192–204.

Turner, R. J., Weiner, J. H. & Taylor, D. E. (1998) Selenium metabolism in Escherichia coli. *BioMetals*. 11, 223–227.

Ungureanu, C., Ionita, D., Berteanu, E., Tcacenco, L., Zuav, A. & Demetrescu, I. (2015) Improving Natural Biopolymeric Membranes Based on Chitosan and Collagen for Biomedical Applications Introducing Silver. *Journal of the Brazilian Chemical Society*. 26 (3), 458–465.

Ural, E., Kesenci, K., Fambri, L., Migliaresi, C. & Piskin, E. (2000) Poly(D,L-cactide/ε-caprolactone)/hydroxyapatite composites. *Biomaterials*. 21 (21), 2147–2154.

Uskokovic, V., Iyer, M. & Wu, V. M. (2017) One Ion to Rule Them All: Combined Antibacterial, Osteoinductive and Anticancer Properties of Selenite- Incorporated Hydroxyapatite. *Journal of Materials Chemistry B*. 25 (5), 1032–1057.

Utracki, L. A. & Wilkie, C. A. (2014) 'Polymer blends handbook', in *Polymer Blends Handbook*. Springer Science. pp. 1203–2378.

Vaidya, A. A., Collet, C., Gaugler, M. & Lloyd-Jones, G. (2019) Integrating softwood biorefinery lignin into polyhydroxybutyrate composites and application in 3D printing. *Materials Today Communications*. 19286–296.

Valappil, S. P., Misra, S. K., Boccaccini, A. & Roy, I. (2006) Biomedical applications of polyhydroxyalkanoates, an overview of animal testing and *in vivo* responses. *Expert Review of Medical Devices*. 3 (6), 853–868.

Valentini, F., Dorigato, A., Rigotti, D. & Pegoretti, A. (2019) Polyhydroxyalkanoates/Fibrillated Nanocellulose Composites for Additive Manufacturing. *Journal of Polymers and the Environment*. 27 (6), 1333–1341.

VanEpps, J. S. & Younger, J. G. (2016) Implantable Device Related Infection. *Shock*. 46 (6), 597–608.

Vasić, S., Radojević, I., Pešić, N. & Čomić, L. (2011) Influence of sodium selenite on the growth of selected bacteria species and their sensitivity to antibiotics. *Kragujevac Journal of Science*. (33), 55–61.

Veleirinho, B., Coelho, D. S., Dias, P. F., Maraschin, M., Ribeiro-do-valle, R. M. & Lopes-da-silva, J. A. (2012) Nanofibrous poly(3-hydroxybutyrate-co-3-hydroxyvalerate)/chitosan scaffolds for skin regeneration. *International Journal of Biological Macromolecules*. 51 (4), 343–350.

Ventola, C. L. (2015) The antibiotic resistance crisis: causes and threats. *P & T journal*. 40 (4), 277–283.

Versace, D. L., Ramier, J., Grande, D., Andaloussi, S. A., Dubot, P., Hobeika, N., Malval, J. P., Lalevee, J., Renard, E. & Langlois, V. (2013) Versatile Photochemical Surface Modification of Biopolyester Microfibrous Scaffolds with Photogenerated Silver Nanoparticles for Antibacterial Activity. *Advanced Healthcare Materials*. 2 (7), 1008–1018.

Vinh, D. C. & Embil, J. M. (2005) Device-Related Infections: A Review. *Journal of Long-Term Effects of Medical Implants*. 15 (5), 467–488.

Visscher, L. E., Dang, H. P., Knackstedt, M. A., Hutmacher, D. W. & Tran, P. A. (2018) 3D printed Polycaprolactone scaffolds with dual macro-microporosity for applications in local delivery of antibiotics. *Materials Science and Engineering C*. 87 (2017), 78–89.

Vu, D. H., Åkesson, D., Taherzadeh, M. J. & Ferreira, J. A. (2019) Recycling strategies for polyhydroxyalkanoate-based waste materials: An overview. *Bioresource Technology*. 122393.

Van Vugt, T. A. G., Geurts, J. & Arts, J. J. (2016) Clinical Application of Antimicrobial Bone Graft Substitute in Osteomyelitis Treatment: A Systematic Review of Different Bone Graft Substitutes Available in Clinical Treatment of Osteomyelitis. *BioMed Research International*. 2016, 1–9.

Walsh, C. (2000) Molecular mechanisms that confer antibacterial drug resistance. *Nature*. 406 (6797), 775–781.

Wang, Q. & Nomura, C. T. (2010) Monitoring differences in gene expression levels and polyhydroxyalkanoate (PHA) production in *Pseudomonas putida* KT2440 grown on different carbon sources. *Journal of Bioscience and Bioengineering*. 110 (6), 653–659.

Wang, R., Xu, D., Liang, L., Xu, T., Liu, W., Ouyang, P., Chi, B. & Xu, H. (2016a) Enzymatically crosslinked epsilon-poly-l-lysine hydrogels with inherent antibacterial properties for wound infection prevention. *RSC Adv*. 6 (11), 8620–8627.

Wang, R., Zhou, B., Liu, W., Feng, X. H., Li, S., Yu, D. F., Chang, J. C., Chi, B. & Xu, H. (2015a) Fast *in situ* generated ε-polylysine-poly (ethylene glycol) hydrogels as tissue adhesives and hemostatic materials using an enzyme-catalyzed method. *Journal of Biomaterials Applications*. 29 (8), 1167–1179.

Wang, S., Chen, W., Xiang, H., Yang, J., Zhou, Z. & Zhu, M. (2016b) Modification and potential application of short-chain-length polyhydroxyalkanoate (SCL-PHA). *Polymers*. 8 (8), 1–28.

Wang, Y., Ma, J., Zhou, L., Chen, J., Liu, Y., Qiu, Z. & Zhang, S. (2012) Dual functional selenium-substituted hydroxyapatite. *Interface Focus*. 2 (3), 378–386.

Wang, Y., Zhao, F., Fan, X., Wang, S. & Song, C. (2016c) Enhancement of medium-chain-length polyhydroxyalkanoates biosynthesis from glucose by metabolic engineering in *Pseudomonas mendocina*. *Biotechnology Letters*. 38 (2), 313–320.

Wang, Y., Bian, Y. Z., Wu, Q. & Chen, G. Q. (2008) Evaluation of three-dimensional scaffolds prepared from poly(3-hydroxybutyrate-co-3-hydroxyhexanoate) for growth of allogeneic chondrocytes for cartilage repair in rabbits. *Biomaterials*. 29 (19), 2858–2868.

Wang, Y. W., Wu, Q., Chen, J. & Chen, G. Q. (2005) Evaluation of three-dimensional scaffolds made of blends of hydroxyapatite and poly(3-hydroxybutyrate-co-3-hydroxyhexanoate) for bone reconstruction. *Biomaterials*. 26 (8), 899–904.

Wang, Y., Wang, Yanmei, Guo, X., Xiong, Y., Guo, M., Wang, Yifeng, Wang, Yanmei, Guo, X., Xiong, Y., Guo, M. & Wang, X. I. A. (2015b) Microbial Transglutaminase and Tyrosinase Modified Gelatin-Chitosan Material Microbial Transglutaminase and Tyrosinase Modified Gelatin-Chitosan Material. *Soft Materials*. 13 (1), 32–38.

Watson, E., Tatara, A. M., Kontoyiannis, D. P. & Mikos, A. G. (2017) Inherently Antimicrobial Biodegradable Polymers in Tissue Engineering. *ACS Biomaterials Science and Engineering*. 3 (7), 1207–1220.

Wei, G. & Ma, P. X. (2004) Structure and properties of nano-hydroxyapatite/polymer composite scaffolds for bone tissue engineering. *Biomaterials*. 25 (19), 4749–4757.

Wei, W., Zhou, Y., Chang, H., Yeh, J., Wei, W. E. I., Zhou, Y. & Chang, H. (2015) Antibacterial and Miscibility Properties of Chitosan / Collagen Blends Antibacterial. *Journal of Macromolecular Science, Part B: Physics*. 54, 143–158.

WHO (2014) Antimicrobial resistance: global report on surveillance. World Health Organization (WHO), 2014.

WHO (2015) Global action plan on antimicrobial resistance. World Health Organization (WHO), 2015.

Wichai, S., Chuysinuan, P., Chaiarwut, S., Ekabutr, P. & Supaphol, P. (2019) Development of bacterial cellulose/alginate/chitosan composites incorporating copper (II) sulfate as an antibacterial wound dressing. *Journal of Drug Delivery Science and Technology*. 51, 662–671.

Williams, S. F., Rizk, S. & Martin, D. P. (2013) Poly-4-hydroxybutyrate (P4HB): A new generation of resorbable medical devices for tissue repair and regeneration. *Biomedizinische Technik/Biomedical Engineering*. 58 (5), 439–452.

Williams, S. F., Martin, D. P. & Moses, A. C. (2016) The History of GalaFLEX P4HB Scaffold. *Aesthetic surgery journal*. 36, S33–S42.

Winkler, T., Sass, F. A., Duda, G. N. & Schmidt-Bleek, K. (2018) A review of biomaterials in bone defect healing, remaining shortcomings and future opportunities for bone tissue engineering: The unsolved challenge. *Bone and Joint Research*. 7 (3), 232–243.

Von Wintersdorff, C. J. H., Penders, J., Van Niekerk, J. M., Mills, N. D., Majumder, S., Van Alphen, L. B., Savelkoul, P. H. M. & Wolffs, P. F. G. (2016) Dissemination of antimicrobial resistance in microbial ecosystems through horizontal gene transfer. *Frontiers in Microbiology*. 7, 1–10.

De Witte, T. M., Fratila-Apachitei, L. E., Zadpoor, A. A. & Peppas, N. A. (2018) Bone tissue engineering via growth factor delivery: From scaffolds to complex matrices. *Regenerative Biomaterials*. 5 (4), 197–211.

Wong, C. T., Lu, W. W., Chan, W. K., Cheung, K. M. C., Luk, K. D. K., Lu, D. S., Rabie, A. B. M., Deng, L. F. & Leong, J. C. Y. (2004) *In vivo* cancellous bone remodeling on a Strontium-containing hydroxyapatite (Sr-HA) bioactive cement. *Journal of Biomedical Materials Research - Part A*. 68 (3), 513–521.

Woodard, L. N. & Grunlan, M. A. (2018) Hydrolytic Degradation and Erosion of Polyester Biomaterials. *ACS Macro Letters*. 7 (8), 976–982.

Woodruff, M. A., Lange, C., Reichert, J., Berner, A., Chen, F., Fratzl, P., Schantz, J. T. & Hutmacher, D. W. (2012) Bone tissue engineering: From bench to bedside. *Materials Today*. 15 (10), 430–435.

Wrobel, J. K., Power, R. & Toborek, M. (2016) Biological activity of selenium: Revisited. *IUBMB Life*. 68 (2), 97–105.

Wu, C., Hsu, Y., Liao, H. & Cai, Y. (2015a) Antibacterial activity and *in vitro* evaluation of the biocompatibility of chitosan-based polysaccharide / polyester membranes. *Carbohydrate Polymers*. 134, 438–447.

Wu, D., Chen, X., Chen, T., Ding, C., Wu, W. & Li, J. (2015b) Substrate-anchored and degradation-sensitive anti-inflammatory coatings for implant materials. *Scientific Reports*. 5 (1), 1–12.

Wu, S., Wang, J., Zou, L., Jin, L., Wang, Z. & Li, Y. (2018) A three-dimensional hydroxyapatite/polyacrylonitrile composite scaffold designed for bone tissue engineering. *RSC Advances*. 8 (4), 1730–1736.

Xie, H. & Kang, Y. (2009) Role of Copper in Angiogenesis and Its Medicinal Implications. *Current Medicinal Chemistry*. 16 (10), 1304–1314.

Xue, Y., Xiao, H. & Zhang, Y. (2015) Antimicrobial polymeric materials with quaternary ammonium and phosphonium salts. *International Journal of Molecular Sciences*. 16 (2), 3626–3655.

Yan, X. Z., Yang, W., Yang, F., Kersten-Niessen, M., Jansen, J. A. & Both, S. K. (2014) Effects of continuous passaging on mineralization of MC3T3-E1 cells with improved osteogenic culture protocol. *Tissue Engineering - Part C: Methods*. 20 (3), 198–204.

Yang, D., Xiao, J., Wang, B., Li, L., Kong, X. & Liao, J. (2019) The immune reaction and degradation fate of scaffold in cartilage/bone tissue engineering. *Materials Science and Engineering C*. 104109927.

Yang, E., Miao, S., Zhong, J., Zhang, Z., Mills, D. K. & Zhang, L. G. (2018) Bio-Based Polymers for 3D Printing of Bioscaffolds. *Polymer Reviews*. 58 (4), 668–687.

Yang, S., Wang, J., Tang, L., Ao, H., Tan, H., Tang, T. & Liu, C. (2014) Mesoporous bioactive glass doped-poly (3-hydroxybutyrate-co-3-hydroxyhexanoate) composite scaffolds with 3-dimensionally hierarchical pore networks for bone regeneration. *Colloids and Surfaces B: Biointerfaces*. 116, 72–80.

Yanhua, W., Hao, H., Li, Y. & Zhang, S. (2016) Selenium-substituted hydroxyapatite nanoparticles and their *in vivo* antitumor effect on hepatocellular carcinoma. *Colloids and Surfaces B: Biointerfaces*. 140, 297–306.

Yoshie, N., Menju, H., Sato, H. & Inoue, Y. (1996) Crystallization and melting behavior in blends of poly(3-hydroxybutyrate-co-3-hydroxyvalerate)s with a narrow composition distribution. *Polymer Journal*. 28 (1), 45–50.

You, Y., Min, B. M., Lee, S. J., Lee, T. S. & Park, W. H. (2005) *In vitro* degradation behavior of electrospun polyglycolide, polylactide, and poly(lactide-co-glycolide). *Journal of Applied Polymer Science*. 95 (2), 193–200.

Yu, J., Xu, Y., Li, S., Seifert, G. V. & Becker, M. L. (2017) Three-Dimensional Printing of Nano Hydroxyapatite/Poly(ester urea) Composite Scaffolds with Enhanced Bioactivity. *Biomacromolecules*. 18 (12), 4171–4183.

Zahran, M. & Marei, A. H. (2019) Innovative natural polymer metal nanocomposites and their antimicrobial activity. *International Journal of Biological Macromolecules*. 136, 586–596.

Zarins, J., Pilmane, M., Sidhoma, E., Salma, I. & Locs, J. (2019) The role of Strontium enriched hydroxyapatite and tricalcium phosphate biomaterials in osteoporotic bone regeneration. *Symmetry*. 11 (2), 1–17.

Zdraveva, E., Mijović, B., Govorčin Bajsić, E., Slivac, I., Holjevac Grgurić, T., Tomljenović, A., Zubin Ferri, T. & Ujčić, M. (2019) Electrospun PCL/cefuroxime scaffolds with custom tailored topography. *Journal of Experimental Nanoscience*. 14 (1), 41–55.

Zeng, J. H., Liu, S. W., Xiong, L., Qiu, P., Ding, L. H., Xiong, S. L., Li, J. T., Liao, X. G. & Tang, Z. M. (2018) Scaffolds for the repair of bone defects in clinical studies: A systematic review. *Journal of Orthopaedic Surgery and Research*. 13 (1), 1–14.

Zhan, J., Chen, Y., Tang, G., Pan, H., Zhang, Q., Song, L. & Hu, Y. (2014) Crystallization and melting properties of poly(butylene succinate) composites with titanium dioxide nanotubes or hydroxyapatite nanorods. *Journal of Applied Polymer Science*. 131 (11), 1–10.

Zhang, H., Lv, X., Zhang, X., Wang, H. & Deng, H. (2015) Antibacterial and hemostatic performance of chitosan-organic rectorite/alginate composite sponge. *Royal Society of chemistry advances*. 5, 50523–50531.

Zhang, J., Liu, W., Schnitzler, V., Tancret, F. & Bouler, J. M. (2014) Calcium phosphate cements for bone substitution: Chemistry, handling and mechanical properties. *Acta Biomaterialia*. 10 (3), 1035–1049.

Zhang, J., Xia, W., Liu, P., Cheng, Q., Tahi, T., Gu, W. & Li, B. (2010) Chitosan Modification and Pharmaceutical / Biomedical. *Marine Drugs*. 8 (7), 1962–1987.

Zhang, K., Fan, Y., Dunne, N. & Li, X. (2018) Effect of microporosity on scaffolds for bone tissue engineering. *Regenerative Biomaterials*. 5 (2), 115–124.

Zhang, Z., Chen, G.-Q., Tian, W., He, W. & Zhang, G. (2006) Production of novel polyhydroxyalkanoates by *Pseudomonas stutzeri* 1317 from glucose and soybean oil . *FEMS Microbiology Letters*. 169 (1), 45–49.

Zhang, Z. H., Sun, Y. S., Pang, H., Munyendo, W. L. L., Lv, H. X. & Zhu, S. L. (2011) Preparation and evaluation of berberine alginate beads for stomach-specific delivery. *Molecules*. 16 (12), 10347–10356.

Zhao, K., Deng, Y., Chun Chen, J. & Chen, G.-Q. (2003) Polyhydroxyalkanoate (PHA) scaffolds with good mechanical properties and biocompatibility. *Biomaterials*. 24 (6), 1041–1045.

Zhao, S., Zhu, M., Zhang, J., Zhang, Y., Liu, Z., Zhu, Y. & Zhang, C. (2014) Three dimensionally printed mesoporous bioactive glass and poly(3-hydroxybutyrate-co-3-hydroxyhexanoate) composite scaffolds for bone regeneration. *Journal of Materials Chemistry B*. 2 (36), 6106.

Zheng, Y., Chen, J. C., Ma, Y. M. & Chen, G. Q. (2019) Engineering biosynthesis of polyhydroxyalkanoates (PHA) for diversity and cost reduction. *Metabolic Engineering*. 1–12.

Zheng, Z., Bei, F. F., Tian, H. L. & Chen, G. Q. (2005) Effects of crystallization of polyhydroxyalkanoate blend on surface physicochemical properties and interactions with rabbit articular cartilage chondrocytes. *Biomaterials*. 26 (17), 3537–3548.

Zhou, C., Li, P., Qi, X., Sharif, A. R. M., Poon, Y. F., Cao, Y., Chang, M. W., Leong, S. S. J. & Chan-Park, M. B. (2011) A photopolymerized antimicrobial hydrogel coating derived from epsilon-poly-l-lysine. *Biomaterials*. 32 (11), 2704–2712.

Zhou, F. L., Parker, G. J. M., Eichhorn, S. J. & Hubbard Cristinacce, P. L. (2015) Production and cross-sectional characterization of aligned co-electrospun hollow microfibrous bulk assemblies. *Materials Characterization*. 109, 25–35.

Zhou, H. & Lee, J. (2011) Nanoscale hydroxyapatite particles for bone tissue engineering. *Acta Biomaterialia*. 7 (7), 2769–2781.

Zhu, D., Cheng, H., Li, J., Zhang, W., Shen, Y., Chen, Shaojun, Ge, Z. & Chen, Shiguo (2016) Enhanced water-solubility and antibacterial activity of novel chitosan derivatives modified with quaternary phosphonium salt. *Materials Science and Engineering C*. 61, 79–84.

Ziebuhr, W. (2001) *Staphylococcus aureus* and *Staphylococcus epidermidis* : Emerging Pathogens *in Nosocomial Infections*. 8, 102–107.

Zinn, M., Witholt, B. & Egli, T. (2001) Occurrence, synthesis and medical application of bacterial polyhydroxyalkanoate. *Advanced Drug Delivery Reviews*. 53 (1), 5–21.

Zinn, M. & Hany, R. (2005) Tailored material properties of polyhydroxyalkanoates through biosynthesis and chemical modification. *Advanced Engineering Materials*. 7 (5), 408–411.

Zou, F., Jiang, J., Lv, F., Xia, X. and Ma, X. (2020). Preparation of antibacterial and osteoconductive 3D-printed PLGA/Cu (I)@ ZIF-8 nanocomposite scaffolds for infected bone repair. *Journal of Nanobiotechnology*, 18(1), 1-14.